The Search for Very High Energy γ-rays from Misaligned AGN

CHEESEBROUGH, ALISTAIR

The Search for Very High Energy γ-rays from Misaligned AGN

Alistair Cheesebrough

A Thesis presented for the degree of
Doctor of Philosophy

Very High Energy γ-ray Astronomy Group
Department of Physics,
Durham University,
England
January 2013

For Mum

The Search for Very High Energy γ-rays from Misaligned AGN

Alistair Cheesebrough

Submitted for the degree of Doctor of Philosophy
January 2013

Abstract

The aim of this work is to study the potential for emission at very high energies ($\gtrsim 100$ GeV) by misaligned active galactic nuclei (AGN) and the future prospects for observations of these objects with the next generation imaging atmospheric Cherenkov telescope, the Cherenkov Telescope Array (CTA). Initially, data collected by the H.E.S.S. array was used to study fourteen Seyfert galaxies and two other AGN with Seyfert-like properties and no new detections were reported. For each object upper limits were calculated, assuming a similar spectral shape to M87.

Further work focused on modelling the GeV spectra of misaligned AGN (AGN with angles of inclination to the line of sight $\gtrsim 5^\circ$) detected in 2010 with the *Fermi Space Telescope*. The modelling was carried out using a multiblob model that had previously been used to model the very high energy emission of M87 and Centaurus A. This work was used to investigate the capacity of the model to reproduce the high energy spectra observed for each object, while also allowing predictions of the potential very high energy fluxes to be produced. In each case the multiblob model was able to reproduce the observed GeV spectrum.

The spectral energy distributions produced were then compared to predicted sensitivity curves for a number of possible CTA configurations to determine the likelihood of detection of these misaligned AGN with the array. It was found that detection of the objects within 50 hours of observations with CTA using standard Durham analysis is unlikely, but that 3C 111 may be detectable using the Paris analysis method.

Declaration

The work in this thesis is based on research carried out in the very high energy γ-ray astronomy group, the Department of Physics, Durham University, England. No part of this thesis has been submitted elsewhere for any other degree or qualification and it all my own work unless referenced to the contrary in the text.

Acknowledgements

The course of my PhD has not been smooth and without assistance I doubt I would have ever submitted my thesis. I owe so much to so many people who helped me over the years, particularly my Mum, who passed away in August 2011 but always believed in me. I have to thank Paula Chadwick, my supervisor, who remained convinced that I could complete even when things seemed bleak and the staff of the College of St. Hild and St. Bede, with special mention of the senior tutor, Laura Wilson, the chaplain, Jonathan Lawson and the student support officer, Elaine Franklin who provided much needed emotional support after the loss of my Mum. I should also thank the University Counselling service who helped me find the strength to continue.

Obviously I could never have reached this point without the love and support of my sister, Helen, and my father who found the strength to help me despite also feeling the loss of my mother keenly. Additional thanks should also be sent the way of all of my close friends who both supported me and stayed by me even when my work was consuming almost all of my energies.

Contents

List of Figures

List of Tables

Chapter 1

γ-ray Emission Mechanisms and Detection Techniques

1.1 Introduction

In 1912, experiments carried out by Victor Hess using gold-leaf electroscopes carried in balloons to altitudes of up to 5 km showed that there is a source of ionising radiation that increases in intensity with altitude. It was posited that the origin of such radiation must be cosmological. This ionising radiation is known as cosmic rays and consists of high-energy charged particles, the bulk of which are believed to come from within the Milky Way; however, the spectrum extends out to energies of over 10^{20} eV indicating that at least some of the radiation must be of extragalactic origin, since the Galactic magnetic field is not strong enough to contain such particles within the local Galaxy. Of the particles in cosmic rays, approximately 86% are protons, 11% alpha particles and 2% electrons, the remaining 1% are nuclei of heavier elements up to uranium (Perkins, 2003). The charged nature of cosmic rays makes it impossible to track those originating from distant sources or with lower energies, as their paths are deflected by Galactic and intergalactic magnetic fields. These sources of cosmic rays are obviously high-energy particle accelerators, and the accelerated particles emit radiation across the entire electromagnetic spectrum, being the primary source of very high energy (VHE) γ-rays in the Universe. As these γ-rays are not deflected by magnetic fields, determining the source of such high-energy radiation should allow the determination of the origins of cosmic rays.

Definitions of what constitutes a γ-ray vary, but a general definition is that they are photons with energies from around 100 keV to $>$ 100 EeV (10^{20} eV) (Weekes, 2003). This is greater

than the energy range of the rest of the electromagnetic spectrum from very long wavelength radio waves through to hard X-rays. This part of the spectrum is further divided into the region between 100 keV and $\sim$ 100 GeV, which can be observed directly with space-based instruments, and energies above $\sim$ 100 GeV known as VHE γ-rays, the main subject of this work. At such high energies direct observations of incoming photons becomes extremely difficult and the ground-based Cherenkov technique, discussed in Section 1.4, is used. Observations in the γ-ray part of the electromagnetic spectrum allow a greater understanding of nonthermal processes in the Universe to be developed, many of which are difficult, if not impossible, to reproduce in a terrestrial laboratory.

Studying photons at these energies relies on the fact that during absorption of the photon by the atmosphere, which has an optical thickness at these wavelengths similar to that of 1 m of lead (Weekes, 2003), a number of secondary particles are produced and the products resulting from further interactions with the atmosphere by these secondary particles can be detected at ground level. As the techniques to detect these secondary products have advanced, the number of objects known to emit at high energies has increased dramatically and, since the construction of the current generation of ground-based γ-ray telescopes, the number of different classifications of objects has almost equalled the total number of objects detected by previous generations. The aim of this work is to investigate the expansion of the catalogue into Seyfert galaxies and other misaligned AGN.

In this chapter, the mechanisms by which such very high energy photons are emitted, the methods by which they are detected, and the current status of experiments relating to their detection will be discussed in detail.

1.2 γ-ray Emission Mechanisms

Emission from many objects at up to X-ray energies can be satisfactorily explained through thermal processes; however, to emit γ-rays at energies $\gtrsim$ 100 GeV thermally would require extremely high temperatures, far above those generally observed in the Universe (e.g., for the emission from a thermal blackbody source to peak at $\sim$ 100 GeV would require a temperature of $\sim 2.4 \times 10^{14}$ K). It is therefore clear that other, non-thermal, processes must be behind the emission of VHE γ-rays. Six processes potentially important for the emission of TeV photons are discussed here: *synchrotron radiation*, *curvature radiation*, *inverse-Compton scattering*, *Bremsstrahlung emission*, *pion decay* and *dark matter annihilation*.

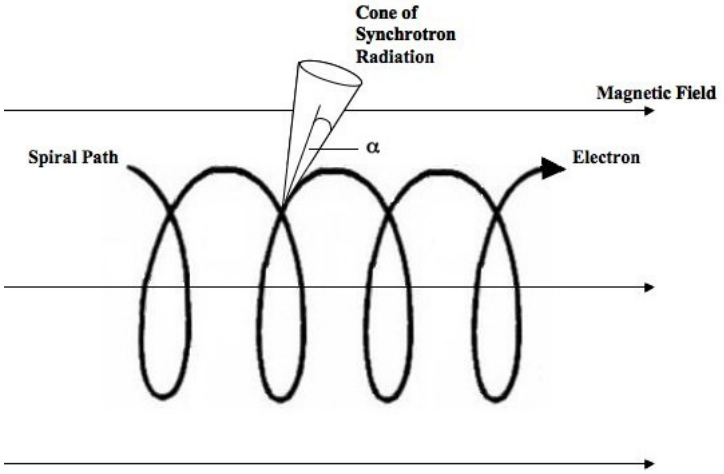

Figure 1.1: Synchrotron emission from a charged particle moving in a magnetic field, showing the motion of the particle, direction of the magnetic field and opening angle, α, of the cone of emission.

1.2.1 Synchrotron Radiation

Synchrotron emission is emission by relativistic charged particles that have been accelerated in a magnetic field of strength, B. A complete treatment of synchrotron radiation can be found in Rybicki & Lightman (1979).

In this work, a brief summary of its important properties will be given. In a constant, uniform magnetic field the motion of a particle in a magnetic field composes a constant velocity component along the field and circular motion in a plane perpendicular to it. The motion of the particle is described by its velocity, $|\mathbf{v}|$, and the pitch angle, α, which is the angle between the magnetic field and the velocity (see Figure 1.1); $\mathbf{v}$ and α are both constants of motion. The power emitted by a relativistic electron gyrating in a magnetic field is given by Hughes (1991):

$$P_S = 2\sigma_T c \sin^2 \alpha \gamma^2 U_B \tag{1.1}$$

where σ_T is the Thomson cross section, calculated using $\sigma_T = e^4/(6\pi m_e^2 \epsilon_0^2 c^4)$, where m_e is the electron mass, and U_B is the magnetic energy density. The relativistic motion of the particle results in beaming of the emitted radiation into a cone of semi-angle $1/\gamma$ radians, where γ is the Lorentz factor, defined as $\gamma = 1/\sqrt{1 - \frac{v^2}{c^2}}$. A consequence of this is that the observer will only detect the emitted radiation when the angle between the magnetic field and the line of sight is approximately equal to the pitch-angle of the particle being considered. The $\sin^2 \alpha$ term in Equation 1.1 results in the power radiated by a particle increasing as the pitch-angle approaches 90° and so suggests that the maximum emitted power will be observed if the angle between the line of sight and the magnetic field is also 90°, which, in turn, implies that for a significant flux of radiation to be

observed from a source, the source must have a significant component of the magnetic field in the plane of the sky. If the pitch-angle distribution of electrons in the source is isotropic, then averaging the power over all pitch-angles results in the $\sin^2\alpha$ term in Equation 1.1 becomes 2/3 (Rybicki & Lightman, 1979).

If the electron moves nonrelativistically in a magnetic field, then most of the power is radiated at a frequency ω_B/γ, where ω_B is the gyration frequency in a magnetic field, given by $\omega_B = eB/\gamma_e c$, and γ_e is the Lorentz factor of the electron. In the case of relativistic motion, this must be modified: most of the power is radiated near the characteristic frequency, ω_c, related to the ω_B multiplied by a factor of γ to account for the small opening angle of the cone of emission, a factor of γ^2, arising from the difference between 'emission' and 'arrival' times of the pulse, by $\sin\alpha$ and a constant equal to $3c/2$. This leads to the conclusion that most of the power emitted by a moving charge is emitted at an angular frequency close to:

$$\omega_c = 3/2\gamma^3\omega_B c\sin\alpha \tag{1.2}$$

A detailed calculation of the field of a moving charge (Rybicki & Lightman, 1979), shows that the power actually peaks at $\omega = 0.29\omega_c$, and that the spectrum shows different behaviour in the low-frequency and high-frequency regimes:

$$\begin{aligned} P_S(\omega) &\propto (\omega/\omega_c)^{\frac{1}{3}} & \omega \ll \omega_c \\ P_S(\omega) &\propto (\omega/\omega_c)^{\frac{1}{3}} e^{\frac{-\omega}{\omega_c}} & \omega \gg \omega_c \end{aligned} \tag{1.3}$$

where $P_S(\omega)$ is the synchrotron power at angular frequency ω. The characteristic frequency of emitted radiation is also the median frequency, with half the power being radiated above and half below this value. Synchrotron emission from a monoenergetic population of many electrons produces a spectrum as shown in Figure 1.2. The assumption that the electrons follow an isotropic pitch-angle distribution can be used, as scattering from plasma waves should ensure that this is the case. As shown in Figure 1.2, the power emitted drops off dramatically at high frequencies. This means that it is extremely unlikely that emission of γ-rays with energies $\sim$1 TeV is due to synchrotron emission, as it would require magnetic fields and γ factors far higher than those believed to be found in astrophysical sources. However, for a γ-ray of this energy, synchrotron emission is important as it provides the seed photons for later upscattering through the inverse-Compton process discussed in Section 1.2.3.

In the case of a compact source, it is important to take into account reabsorption of synchrotron photons by the medium; this process is known as synchrotron self-absorption and can lead to

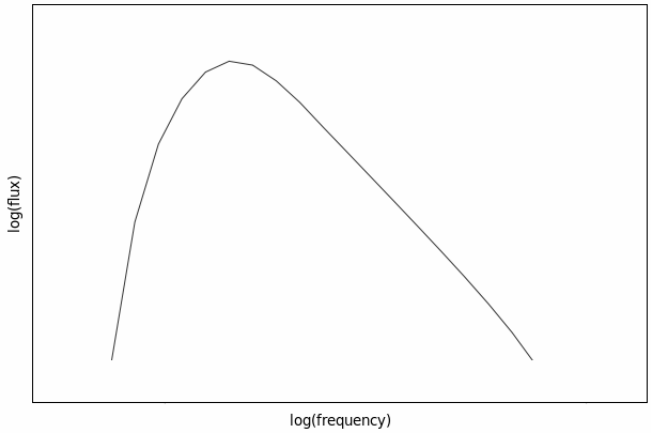

Figure 1.2: A synchrotron spectrum as produced by a monoenergetic population of many electrons. The turnover where the spectrum goes from absorption-dominated to emission-dominated can clearly be seen.

observation of a low-frequency turnover in the spectrum. To describe the effect that synchrotron self-absorption has on the observed spectrum, a self-absorption coefficient, κ_ν, is introduced (a derivation can be found in Padmanabhan, 2000). This is related to the frequency of the synchrotron radiation, ν, and the synchrotron emissivity j_ν by (Hughes, 1991):

$$\kappa_\nu \propto j_\nu \nu^{-\frac{5}{2}} \tag{1.4}$$

Equation 1.4 is true for all frequencies as κ_ν is a property of the medium and is not dependent on the line-of-sight thickness of the source. Defining ν_1 as the frequency at which the optical depth becomes unity allows the intensity at the surface of the source to be calculated. In the case of a power-law electron distribution, $j_\nu = j_0(\nu/\nu_0)^{-\alpha}$, Hughes (1991) shows that:

$$I_\nu = I_0 \left(\frac{\nu_1}{\nu_0}\right)^{-\alpha} \left(\frac{\nu}{\nu_1}\right)^{\frac{5}{2}} \left\{1 - \exp\left[-\frac{\nu_1}{\nu}^{\alpha+\frac{5}{2}}\right]\right\} \tag{1.5}$$

where I_0 is the surface-brightness measured at a frequency ν_0 where the optical depth is negligible.

1.2.2 Curvature Radiation

Curvature radiation and synchrotron radiation are closely related in that both are emitted by a charged particle moving in a curved path in a strong magnetic field. In the case of curvature radiation, however, the emission arises by virtue of the longitudinal motion of the particle along curved magnetic field lines, so it is related to a change of the longitudinal (along $\boldsymbol{B}$) energy of

the particle, as opposed to synchrotron radiation where it results from a change in the particle's transverse energy (with respect to $\boldsymbol{B}$). Curvature radiation is important in rotation-powered pulsars and is generally seen in regions with strong magnetic fields with high curvature (Mészáros, 1992). The emission gives a spectrum, for electrons, around a characteristic frequency ν_c:

$$\nu_c = \frac{3}{4}\frac{c\gamma^3}{\pi r_c} \tag{1.6}$$

where γ is the Lorentz factor of the electrons emitting the curvature radiation and r_c is the radius of curvature. For typical pulsar values of $B \sim 10^{12}$ G, $r_c \sim 10^6$ cm and electron energies $10^{12} - 10^{13}$ eV, the characteristic frequencies for curvature radiation correspond to energies in the GeV range, just below the very high energy band. The magnetic fields in AGN are unlikely to display the high curvature required for curvature radiation to contribute significantly to the emission from such objects, however it may be important in other sources of VHE γ-rays.

1.2.3 Inverse-Compton Scattering

Inverse-Compton scattering is the scattering of a photon in an encounter with a highly relativistic particle, usually an electron, and is believed to be the primary mechanism for VHE γ-ray emission in the Universe. Inverse-Compton scattering can be viewed as the consequence of two successive Lorentz transformations, one into the rest frame of the relativistic particle and the other back into the laboratory frame. In the frame of the relativistic particle, Compton scattering behaves as Thompson scattering and the photon frequency ν' is preserved. Because Compton scattering exhibits forward-backward symmetry, the mean scattering angle is 90°; at 90°, the photon of frequency ν before collision is upscattered by a factor of γ as a consequence of transforming into the particle's rest frame, resulting in $\nu' = \gamma\nu$. After collision and transferring back into the laboratory frame, the photon is further upscattered by another factor of $\sim \gamma$ resulting in $\nu'' \sim \gamma\nu' = \gamma^2\nu$, these transformations are illustrated in Figure 1.3. In encounters between relativistic electrons with Lorentz factors of γ and photons of frequency ν from an isotropic radiation field of energy density U_P, the mean frequency of the upscattered photons is $\approx \frac{4}{3}\gamma^2\nu$. The angle-averaged power, $\overline{P_C}$, emitted due to inverse-Compton scattering involving the interaction of relativistic electrons with an isotropic photon field of energy density U_P is given by (Rybicki and Lightman, 1979):

$$\overline{P_C} = \frac{4}{3}\beta^2\gamma^2 c\sigma_T U_P \tag{1.7}$$

for photon energies $\ll m_e c^2$. In the regime where photon energies approach $m_e c^2$, the Thomson cross section must be replaced with the Klein-Nishina cross section, and the maximum possible

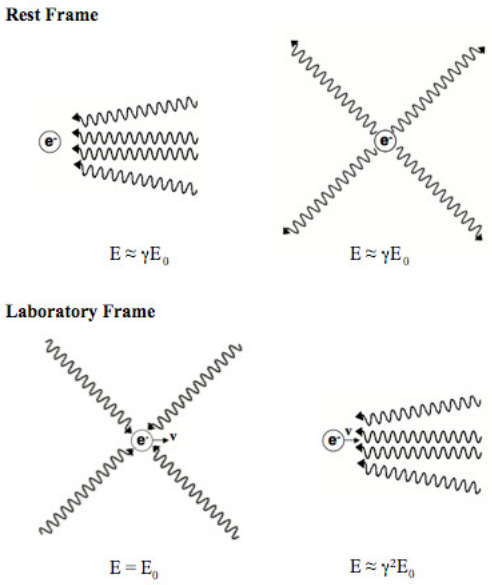

Figure 1.3: Interaction of a relativistic electron with a photon field, showing the Lorentz transforms leading to the upscattering of the incident photons.

photon energy is limited by the energy of the incident electrons. The Klein-Nishina cross section takes the form (see, for example, Padmanabhan, 2000):

$$\sigma_{\rm KN} = \frac{3}{8}\sigma_T \frac{1}{\epsilon}\left\{\left[1 - \frac{2(\epsilon+1)}{\epsilon^2}\right]\ln(2\epsilon+1) + \frac{1}{2} + \frac{4}{\epsilon} - \frac{1}{2(2\epsilon+1)^2}\right\} \tag{1.8}$$

where $\epsilon = (\hbar\omega/m_e c^2)$. This reduces to $\sigma_{\rm KN} \approx \sigma_T$ for $\epsilon \ll 1$, as expected; when $\epsilon \gg 1$, $\sigma_{\rm KN} \approx (3/8)(\sigma_T/\epsilon)(\ln 2\epsilon + 0.5)$. Comparing the power emitted via inverse-Compton scattering in equation 1.7 with the averaged form of equation 1.1, which assumes an isotropic distribution of electron pitch angles, allows the relative luminosity due to the two mechanisms to be found (Shu, 1991). This leads to the result that:

$$\frac{L_C}{L_S} = \frac{U_P}{U_B} \tag{1.9}$$

where L_C and L_S are the inverse Compton luminosity and the synchrotron luminosity, respectively, and U_P and U_B the energy densities in the photon field and in the magnetic field, respectively. Assuming a uniform model in which U_P and U_B have constant values throughout the source (see Shu, 1991), it can be shown that the ratio between the inverse Compton and synchrotron luminosities depends on the brightness temperature of the synchrotron radiation at the turnover frequency, ν_m. The brightness temperature at ν_m is the maximum brightness temperature of the source, $T_b(m)$. The numerical estimate found in Shu (1991), which is only applicable when

the source remains static in bulk, is:

$$\frac{L_C}{L_S} \sim \left[\frac{T_b(m)}{10^{12}\mathrm{K}}\right]^5 \left(\frac{\nu_m}{10^{8.5}\mathrm{Hz}}\right) \tag{1.10}$$

In astrophysical sources photons produced via synchrotron emission can then undergo a process known as synchrotron self-Compton emission. In this process the synchrotron photons are upscattered, via inverse-Compton scattering, by the population of relativistic electrons responsible for the initial synchrotron emission. Taking into account synchrotron self-Compton emission, Equation 1.10 leads to the conclusion that losses due to Compton scattering in sources with a maximum brightness temperature of $\sim 10^{12}$ K or below are relatively small and sustainable within the source, but become catastrophically large in a source with a maximum brightness temperature above this value. In a source with such a high maximum brightness temperature, a large percentage of the radio photons will be upscattered to higher frequencies (reaching far beyond the optical regime), and the density of low-energy photons available for scattering will become much lower, reducing the radio brightness of the source to more modest values. This leads to the conclusion that no compact radio source should have a brightness temperature $\gtrsim 10^{12}$ K; however, it is important to note that jets in astrophysical sources, which are observed to be undergoing bulk expansion, lead to sources exhibiting brightness temperatures above this limit (Band and Grindlay, 1986). It is believed that most sources of VHE γ-rays exhibit relativistic jets, suggesting that in the case of such objects, the ratio of Compton losses to synchrotron losses would likely be reduced from that given in equation 1.10.

The spectrum produced through inverse Compton scattering depends strongly on both the incident photon spectrum and the energy distribution of the electrons responsible for the scattering. In synchrotron self-Compton emission, this results in the shape of the inverse-Compton peak strongly resembling the synchrotron spectrum, just shifted to higher energies, and it is this that is responsible for the distinctive double-humped shape seen in the spectra of blazars (see Figure 1.4).

1.2.4 Bremsstrahlung Emission

Bremsstrahlung (literally, *braking radiation*) emission is a result of inelastic scattering of charged particles off atomic nuclei, see Figure 1.5. When a charged particle passes close enough to an atomic nucleus, it will be deflected by the electric field of the nucleus; during this interaction, radiation will be emitted with an amplitude proportional to the acceleration that caused the deflection. Classically, the acceleration produced by an ion of charge Ze on an incident particle of charge ze and mass M is $\propto Zze^2/M$, and so the intensity (which is proportional to the product of the

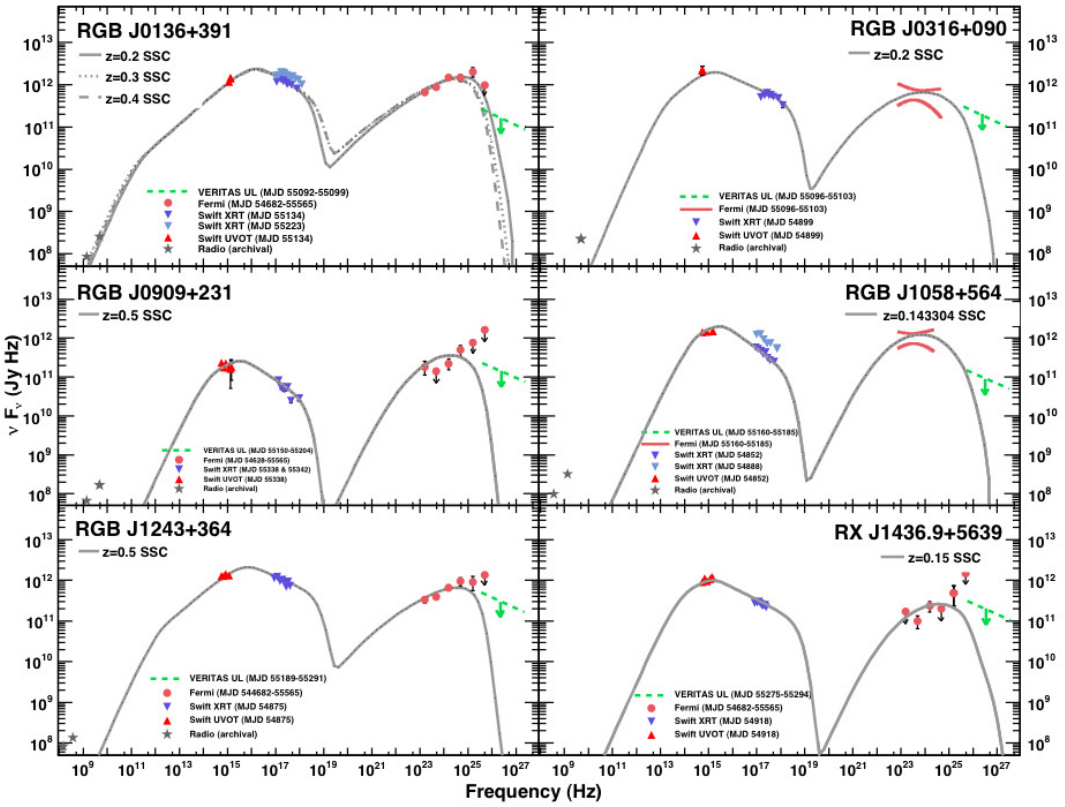

Figure 1.4: The spectral energy distributions (SEDs) of 6 BL Lacs (discussed in Section 3.3) observed with the VERITAS VHE γ-ray telescope (discussed in Subsection 1.5.2), showing non-contemporaneous data across a number of wavelengths displaying the typical "double-hump" shape seen from such objects. The grey lines show the results of modelling of the spectra of the objects using the model of Böttcher & Chang (2002). Taken from Aliu et al. (2012).

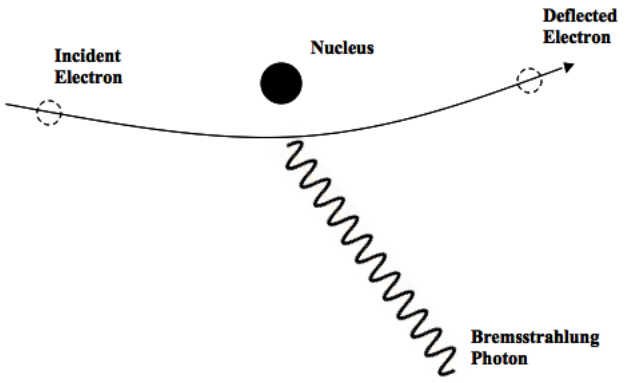

Figure 1.5: Interaction of an electron with the electric field of an atomic nucleus, resulting in the emission of a Bremsstrahlung photon.

amplitude squared and the charge ze) will vary as $Z^2z^4e^6/M^2$ (Evans, 1955). As can be seen, the intensity of the emitted Bremsstrahlung depends on the inverse square of the mass of the incident particle, so the intensity of the emission for a proton is a factor of $\sim 3 \times 10^6$ smaller than the intensity of the emission from an electron incident with the same nucleus. Thus Bremsstrahlung emission from particles other than electrons is generally negligible. The maximum amount of energy that can be radiated in an interaction between a charged particle and a nucleus is equal to the the total kinetic energy of the incident particle, and, classically, every interaction should result in the release of a photon.

The quantum-mechanical approach to Bremsstrahlung emission considers the interaction between a plane wave (representing the electron) and the Coulomb field of the nucleus. During this interaction, the electron has a small but finite probability of emitting a photon, and, if a photon is emitted, the electron will also be acted on by the electromagnetic field of the photon. This process, involving the coupling of the electron with the electromagnetic field of the photon, has a cross-section equal to the fine structure constant, $\alpha = e^2/(2\epsilon_0 hc) \sim 1/137$, times the cross section for elastic scattering; therefore, most of the deflections of incident electrons by atomic nuclei are elastic, and photons are emitted in only a small percentage of these interactions. During a radiative collision, the momentum of the incident electron is shared between the electron, the photon and the ion, and therefore the photon can have any momentum and corresponding energy, up to the kinetic energy of the electron, K. In the case of highly relativistic electrons, the momentum carried away by the photon approaches that carried by the electron, and, after scattering, both the photon and electron tend to proceed in the same direction as the incident electron, with the average angle between them being $\sim m_e c^2/K$.

Thermal Bremsstrahlung is emission via the Bremsstrahlung process that takes place in a

thermal plasma, temperature T, in which the ionised particles follow a Maxwell-Boltzmann distribution. In this case, screening electrons do not have an impact on the cross section, and the power output from Bremsstrahlung emission, P_b, can be found (Duric, 2004). For $h\nu/k_BT \gg 1$:

$$P_b(\nu) \approx E_1(1)e^{-h\nu/k_BT} \tag{1.11}$$

while for $h\nu/k_BT \ll 1$:

$$P_b(\nu) \approx \ln\left[\gamma\left(\frac{m_eZ^2e^4}{2\hbar^2h\nu}\right)\left(\frac{m_eZ^2e^4}{2k_BT\hbar^2}\right)^{\frac{3}{2}}\right] - \frac{3}{2}\gamma \tag{1.12}$$

where:

$$\gamma = -\int_0^\infty \ln x\, e^{-x}\, dx \tag{1.13}$$

The energies of γ-ray photons emitted by thermal Bremsstrahlung are of the same order as the energies of the electrons incident on the ions; this means that if the electron population is characterised by a power law with spectral index Γ_e, the resulting γ-ray spectrum has an index $\Gamma_\gamma \approx \Gamma_e$. Bremsstrahlung emission is generated by the secondary particles produced when a VHE γ-ray interacts with the atmosphere and so is important in TeV astronomy, where the properties of the emission from these particles allows information about the incident photon to be inferred, as discussed in Section 1.4.

1.2.5 Pion Decay

In objects that accelerate protons to very high energies, interactions can occur which result in the emission of γ-rays through the production and decay of pions can occur. The dominant pγ interaction is through the Δ-resonance:

$$p + \gamma \rightarrow \Delta^+ \rightarrow \begin{cases} p\pi^0 & \text{fraction } 2/3 \\ n\pi^+ & \text{fraction } 1/3 \end{cases} \tag{1.14}$$

and the pions produced in the interactions then decay. It is important to note that pions can also be produced in interactions between protons, for example:

$$p + p \rightarrow \pi^{+,\ 0 \text{ or } -} + X \tag{1.15}$$

where X refers to decay products consistent with the initial state. Charged pions have a mean lifetime of 2.6 $\times$ 10^{-8} s and primarily decay leptonically into muons and neutrinos through the

following interactions, mediated by the weak force:

$$\pi^+ \rightarrow \mu^+ + \nu_\mu \tag{1.16}$$

$$\pi^- \rightarrow \mu^- + \bar{\nu_\mu} \tag{1.17}$$

These muons then decay via:

$$\mu^+ \rightarrow e^+ + \nu_e + \bar{\nu_\mu} \tag{1.18}$$

$$\mu^- \rightarrow e^- + \bar{\nu_e} + \nu_\mu \tag{1.19}$$

A second, far less likely path of decay also exists, in which the charged pions decay into (Vaks & Ioffe, 1958):

$$\pi^+ \rightarrow e^+ + \nu_e \tag{1.20}$$

$$\pi^- \rightarrow e^- + \bar{\nu_e} \tag{1.21}$$

The π^0 has a lifetime of 0.83×10^{-16} s and decays, mediated by the electromagnetic force, into two photons, whose energy depends on the energy of the pion (Griffiths, 1987). This means that even though the rest energy of a π^0 is 135 MeV, which is shared by the emitted photons, more energetic pions will emit more energetic photons, with energies potentially extending to 100s of GeV, allowing detection with very high energy instruments (Sahu, Zhang & Fraija, 2012).

1.2.6 Dark Matter Annihilation

Work on the nature of dark matter in the 1990s led to the hypothesis that indirect detection through the products of annihilation reactions might be possible (Bergström, 1999). It is commonly assumed that cold dark matter (CDM) is made up of currently undiscovered weakly interacting massive particles (WIMPs), candidates for which are usually particles predicted by models beyond the standard model of particle physics. The annihilation of these WIMPs may lead to detectable VHE γ-rays at energies $\gtrsim$ 100 GeV via continuum emission (from hadronisation of gauge-bosons and heavy quarks) or γ-ray lines (through loop-induced processes) (Aharonian et al., 2008). The predicted γ-ray flux and continuum shape depend strongly on the nature of the WIMP being con-

sidered as a prospective candidate for the CDM and its annihilation interactions. For neutralino dark matter, predicted by supersymmetric theories, it is expected that loop-induced annihilation processes will lead to a series of monoenergetic spectral lines. In Kaluza-Klein scenarios, hypercharge gauge-boson pairs annihilate preferentially into charged lepton pairs, which radiate γ-rays with hard spectra; additionally, cascading decays of quark-antiquark final states lead to secondary γ-rays.

1.3 γ-ray Absorption Mechanisms

Despite the penetrative power of γ-rays, there are two main mechanisms by which they are absorbed, which obviously impacts on whether or not an object can be detected at very high energies. The first of these, involves the interaction of γ-rays with matter and is extremely important for ground-based VHE γ-ray astronomy (discussed in Section 1.4) as it is through this process that γ-rays are absorbed by the atmosphere. In interactions with matter, the γ-rays produce electron-positron pairs and are absorbed in the process. Over interstellar and even intergalactic distances, the typical matter density of the interstellar or intergalactic medium is far too low to have a significant effect on the emission observed (Weekes, 2003). In objects where significant accretion is occurring or where the emission passes through a region of high matter density, absorption by matter can have a non-negligible effect on the observed spectra.

Another means by which γ-rays can be absorbed is through γ-γ photoabsorption. This occurs when a high-energy photon, of energy ϵ_1, passes through a region with a high density of lower-energy photons, with energies ϵ_2 that fulfil:

$$\epsilon_2 \gtrsim \frac{m_e^2 c^4}{\epsilon_1} \tag{1.22}$$

as derived in Longair (1981). At this energy, a collision between the two photons will lead to pair production through $\gamma + \gamma \rightarrow e^+ + e^-$. The cross section for this process peaks at

$$\epsilon_1 \epsilon_2 (1 - \cos\theta) \sim 2(m_e c^2)^2 \tag{1.23}$$

where θ is the collision angle between the two photons (Weekes, 2003). For incident photons with energies $\epsilon_1 = 1$ TeV, the cross section peaks in the near-infrared at 0.5 eV ($\lambda = 2.5$ μm). Photons of this energy are common in the Universe, leading to significant γ-ray absorption on intergalactic scales. This infrared photon field is known as the extragalactic background light (EBL). The consequences for VHE γ-ray astronomy are discussed in Section 3.5.

1.4 Ground-based very high energy γ-ray Astronomy

VHE γ-rays are generally considered to be those photons with energies $\gtrsim 100$ GeV. At such high energies the total flux observed from even the brightest objects is very low; for the Crab Nebula, which is considered the brightest constant[1] source in the VHE γ-ray sky, the flux detected above 1 TeV is only 2×10^{-11} photons cm^{-2} s^{-1} (Aharonian et al., 2006a). For a 2.5 m^2 detector (a reasonable size for a space-based instrument) with 100% efficiency, this implies a detection rate of only $\sim$16 photons yr^{-1}, which obviously makes direct detection very difficult. However, when a VHE γ-ray photon interacts with the Earth's atmosphere, the products of the interaction generate Cherenkov emission as discussed in Section 1.4.1. This leads to the use of the atmosphere as a very large detector through the atmospheric Cherenkov technique discussed in Section 1.4.3 with the construction of arrays of ground based telescopes to make use of the effect.

1.4.1 Cherenkov Radiation

Cherenkov radiation is the light emitted by a charged particle, such as an electron, moving through an insulating medium at a velocity greater than the phase velocity of light in the medium. As an electron moves through an insulating medium, its electric field distorts nearby atoms by displacing the electrons and polarising the medium around the moving electron (see Figure 1.6). These distorted atoms behave like elementary electric dipoles with the negative poles pointing away from the passing electron. If the electron is moving more slowly than the phase velocity of light in the medium, then the polarisation field around the electron will be symmetric and there will be no net field at large distances and, therefore, no radiation. In the case where the electron is moving at a speed comparable to that of light, however, the polarisation field is no longer completely symmetrical, and as the atoms revert to their original state a pulse of electromagnetic radiation will be emitted (Jelley, 1958). The threshold velocity, $\beta_{\min}c$, above which Cherenkov emission will take place in a medium with refractive index n is given by $\beta_{\min} = 1/n$; at this velocity, the direction of the emission will correspond with that of the particle, while higher velocities will result in a cone of radiation up to the angle θ_c, the Cherenkov angle, defined by:

$$\cos\theta_c = \frac{1}{\beta n} \tag{1.24}$$

where the velocity of the particle is βc, (Jelley, 1958).

The classical theory of Cherenkov radiation was developed by Frank and Tamm in 1937 (Frank

[1] It is important to note that recently variability has been observed at GeV energies (Tavani et al., 2011) and that some possible hints of variability at very high energies have also been claimed (Bednarek & Idec, 2011).

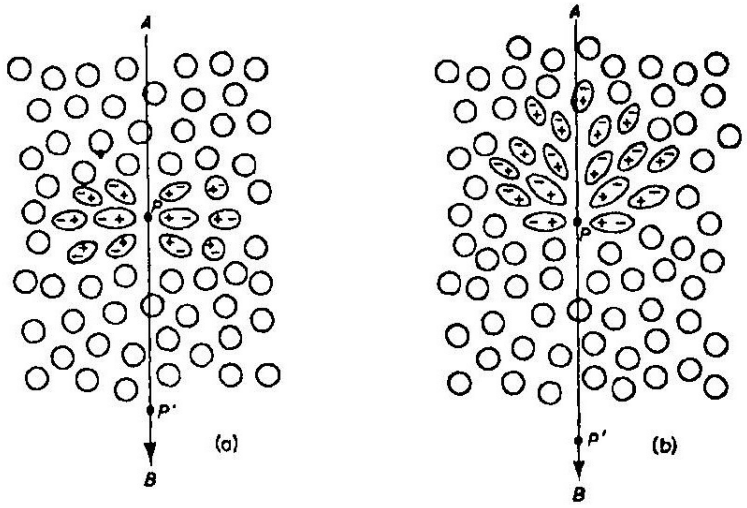

Figure 1.6: The polarisation set up in a dialectric medium by the passage of a charged particle at (a) a velocity lower than that of light in the medium, (b) a velocity greater than that of light in the medium. Taken from Jelley (1958).

& Tamm, 1937); the formulae are derived in Jelley (1958). It is found that the output of radiation per unit length, dW/dl, at a specified frequency, ω, is

$$\frac{dW}{dl} = \frac{e^2}{c^2} \int_{\beta n > 1} \left(1 - \frac{1}{\beta^2 n^2}\right) \omega d\omega \tag{1.25}$$

When deriving the spectrum, Jelley (1958) notes that no frequency cut-off is imposed, which implies that the radiation output is infinite. In reality there are two factors which set an upper limit to the frequency spectrum and cause the radiation output to remain finite. The first is that a real medium is always dispersive, which restricts radiation to those frequency bands where $n(\omega) > 1/\beta$, whereas, in the treatment by Frank and Tamm, dispersion is ignored to the first order. No emission can be observed for X-rays, because $n(\omega) > 1$ in the X-ray regime, and in media which are transparent at optical wavelengths the absorption bands are found at shorter wavelengths, limiting radiation to the near ultraviolet and longer wavelengths. A further limiting factor is the classical diameter of the electron, $d_e = e^2/2\pi\epsilon_0 m_e c^2 = 5.6 \times 10^{-15}$ m, because to satisfy coherence conditions the angular wavelengths (angular wavelength = $\lambda/2\pi$) of the emitted photons must be greater than this. This leads to the constraint that the radiation must have a wavelength greater than $\lambda_{min} = 2\pi d_e = 3.5 \times 10^{-15}$ m, which falls in the γ-ray region of the spectrum. The total energy lost by a relativistic particle per unit length via Cherenkov emission is given by:

$$\frac{dW}{dl} = \frac{e^2\omega_0^2}{2c^2}(\epsilon - 1)\ln\left(\frac{\epsilon}{\epsilon - 1}\right) \tag{1.26}$$

where ω_0 is the frequency of the first resonance of the spectrum and ϵ is the dielectric constant of the medium. Using this it can be seen that for a relativistic particle in a typical medium where $\omega_0 = 6 \times 10^{15}\text{s}^{-1}$, dW/dl is of the order of several keV per cm, which is $\sim 0.1\%$ of the energy lost by ionisation for the particle.

To find the duration of the light flash, Jelley considered dispersion within the medium. In a nondispersive medium, the wavefront is infinitely thin and the duration of the light pulse must therefore be infinitely short. In a dispersive medium, however, the Cherenkov angle depends on the wavelength of the emission, and the duration, Δt, of the light flash as seen by a given detector is

$$\Delta t = \frac{\rho}{\beta c}(\tan\theta_2 - \tan\theta_1) \tag{1.27}$$

where θ_1 and θ_2 are the Cherenkov angles for the frequency limits of the detector, and ρ is the distance from the path of the particle. This means that for a fast electron moving through the upper atmosphere ($\beta = 1$, $n = 1.000292$, $\theta_c = 1.403°$), observed from 100 m away by a detector which can detect radiation with wavelengths between 180 nm (where $n = 1.000346$ and $\theta_c = 1.507°$) and 750nm (where $n = 1.000275$ and $\theta_c = 1.345°$), the Cherenkov emission will have a pulse length of $\sim 10^{-6}$ s.

Thus far, the formulae given above have assumed that the relativistic particle is moving at a constant speed, but as the particle traverses the medium it will lose energy via Bremsstrahlung and ionisation, which will also affect its direction of motion (as will non-radiative Coulomb scattering). To ensure that coherence is preserved despite the change in β (and hence θ_c), the deceleration must not be too rapid and must satisfy

$$T.\left(\frac{dv}{dt}\right) \ll \frac{c}{n} \tag{1.28}$$

where T is one period of the wave emitted and dv/dt is the deceleration of the electron. At visible wavelengths, this condition is easily satisfied where ionisation is the dominant form of energy loss. As the energy loss via Cherenkov emission is so small, the energy of the emitted photon must also be small when compared to the energy of the interacting particle; this means that quantum effects can generally be ignored and the classical treatment by Frank and Tamm, is generally valid.

1.4.2 Air Showers

When a photon of energy greater than ~ 10 MeV or a high-energy charged particle (a cosmic ray) enters the atmosphere, it will interact with atoms in the atmosphere and result in the production of an air-shower. In the case of a photon, the dominant interaction is pair production, in which the γ-ray is annihilated and an electron-positron pair produced. For pair production to occur, the photon must have an energy greater than that of the particles produced. Additionally, energy and momentum considerations mean that it cannot occur in free space, but it can occur in the electric field of a nucleus or an electron. The electron-positron pair is strongly beamed in the direction of the initial γ-ray, but, as the energy from the γ-ray is not necessarily shared equally between the two particles, the mean of their emission angles is not always equal to the initial trajectory of the photon (Weekes, 2003). The cross section for this interaction σ_{pp} depends on the energy of the initial photon; for photon energies in the range $1 \ll \hbar\omega/m_e c^2 \ll 1/\alpha_f Z^{\frac{1}{3}}$:

$$\sigma_{pp} = \alpha_f r_e^2 Z^2 \left[\frac{28}{9}\ln\left(\frac{2\hbar\omega}{m_e c^2}\right) - \frac{218}{27}\right] \mathrm{m}^2 \text{ atom}^{-1} \tag{1.29}$$

and for photon energies $\hbar\omega/m_e c^2 \gg 1/\alpha_f Z^{\frac{1}{3}}$:

$$\sigma_{pp} = \alpha_f r_e^2 Z^2 \left[\frac{28}{9}\ln\left(\frac{183}{Z^{\frac{1}{3}}}\right) - \frac{2}{27}\right] \mathrm{m}^2 \text{ atom}^{-1} \tag{1.30}$$

where ω is the angular frequency of the photon, Z is the atomic number of the nucleus involved, α_f is the fine-structure constant and r_e is the classical electron radius. In both cases the cross section for pair production is $\sim \alpha_f \sigma_T$ (where σ_T is the Thomson cross section). Using the cross sections above, it is then possible to find the mean distance a γ-ray will travel before interacting with the atmosphere; this distance is given by $\lambda_{pp} = 1/N\sigma_{pp}$, where N is the number of target nuclei per unit volume.

The electron-positron pair produced in pair production will then interact with the atmosphere further, resulting in an air shower. The positron generally annihilates later with an electron to produce a pair of photons, and both the electron and positron can interact with the atmosphere via Bremsstrahlung also resulting in the emission of photons. In both cases, the angle of emission for the photons will be $\propto\ m_e/E$ radians, where E is the energy of the particle. These photons can then go through the pair-production process in the same manner as the initial incident photon, and this process can continue until a critical energy, E_c is reached. Below E_c there is too little energy remaining in the products of the interaction for this process to take place and further energy losses then proceed via ionisation rather than pair production or Bremsstrahlung. On average, the air shower consists of $\frac{2}{3}$ electrons and positrons and $\frac{1}{3}$ photons, and it reaches maximum lateral

extension when the average energy of the cascade particles is $\sim E_c$. The number of particles and high-energy photons in the shower, at maximum lateral extension, is $\sim E_0/E_c$, where E_0 is the initial photon energy.

The high-energy electrons and positrons in the shower emit radiation via Cherenkov emission as described in Section 1.4.1. In the case of an air shower initiated by a high-energy γ-ray, a fraction of $\sim 10^{-6}$ of the primary energy is observed as Cherenkov emission in the optical part of the spectrum and this emission is coherent (Weekes, 2003). At energies greater than about 100 GeV, the radiation emitted via Cherenkov emission closely follows the trajectory of the initial photon, allowing the direction of the source to be calculated.

Air showers initiated by an incident high-energy nucleon or heavier nucleus are known as hadronic showers; these contain a large number of other particles, including pions, muons and kaons, in addition to the electrons, positrons and photons seen in showers initiated by γ-rays. The nucleons and heavier nuclei that initiate hadronic air showers are more penetrating than purely electromagnetic cascades initiated by photons; their interaction length in air is approximately 2.5 times that of photons. In the case of a nucleon-initiated air-shower, a large fraction (between 25% and 50%) of the nucleon energy is transferred to secondary mesons during the first interaction. Around 90% of these secondary particles are pions, with all three types (π^+, π^- and π^0) produced in approximately equal quantities while the remaining 10% are kaons. Neutral pions produced in the air shower then decay to produce γ-ray pairs, which in turn initiate electromagnetic showers as discussed above; the electrons and positrons created in these showers reach a maximum intensity at an altitude of approximately 15km and are easily absorbed by the atmosphere, although radiation produced via Cherenkov emission can be detected down to sea level. The leptonic decay of charged pions produces the highly penetrating muons and neutrinos seen in hadronic showers. The muons produced then go on to decay into electrons and neutrinos, although most reach sea level before decaying, and, as few are absorbed, this leads to muons accounting for almost 80% of the secondary particles observed at sea level.

The profiles of electromagnetic and hadronic air showers are noticeably different in the lateral direction due to different distribution of momentum during the cascade. In an electromagnetic shower, the lateral extension of the cascade is determined by the momentum of the secondary electrons and positrons, which are produced via pair production and which undergo multiple scattering as they travel through the atmosphere. In a hadronic shower, the lateral extension is determined by the transverse component of momentum at the production of secondary particles in the nuclear interactions (typically ~ 0.3 GeV/c). The result of this is that hadronic showers are more laterally extended than electromagnetic showers and tend to be more irregular in shape, as shown in Figure

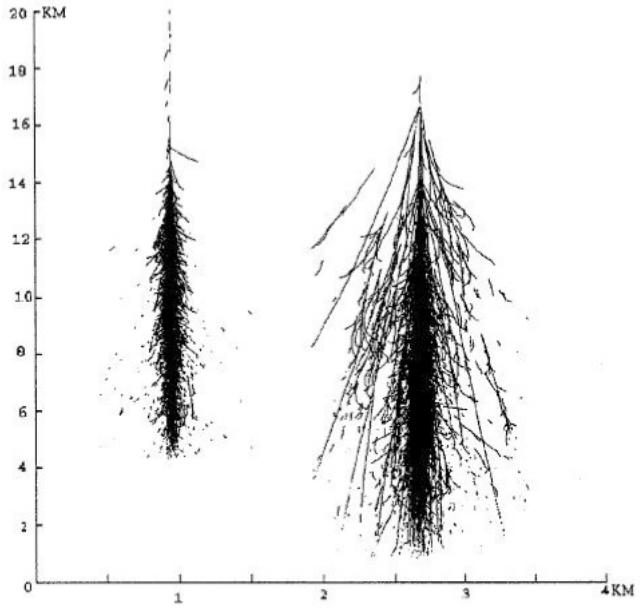

Figure 1.7: Monte Carlo simulation of the development in the atmosphere of a 300 GeV γ-ray shower (left) alongside a 900 GeV proton initiated shower. Note the more compact nature of the γ-ray shower. The horizontal axis has been exaggerated for clarity of illustration. Taken from Fegan (1997).

1.7. Using this information, it is possible to distinguish between γ-ray primaries and hadronic primaries, as discussed in Chapter 2.

1.4.3 Detection Techniques

A simple atmospheric Cherenkov telescope requires a single light detector (typically a photomultiplier tube, PMT), placed in the focal plane of a mirror and coupled to low latency electronics. In 1953 Jelley and Galbraith detected Cherenkov radiation from the atmosphere for the first time, using a simple detector constructed from a signalling mirror, a dustbin and a PMT (Jelley, 1987). Using this rather primitive device, Jelley and Galbraith detected light pulses at a rate of between 1 and 2 per minute, distributed randomly in time, showing a broad zenith-angle dependence and (after control experiments to determine that the source of these pulses was indeed the sky) a correlation with detections of shower particles detected by an extended air-shower array. The first imaging atmospheric Cherenkov telescope was constructed by Hill and Porter in 1960 using an image-intensifier camera system, which had been adapted from a particle-physics experiment, coupled to a small mirror. The system had a threshold energy for cosmic rays of >500 TeV and successfully detected the Cherenkov light from an incident cosmic ray, thereby demonstrating the potential of the technique (Weekes, 2003).

The simple atmospheric Cherenkov detector described earlier is characterised by the collection area of the mirror, A, the reflectivity, R, the solid angle, Ω and the integration time, τ. If the integration time of the photomultiplier counting system, τ, is greater than the duration of the Cherenkov light flash, then the signal (in photoelectrons) detected by an atmospheric Cherenkov telescope can be calculated using:

$$S = \int_{\lambda_2}^{\lambda_1} C(\lambda)\eta(\lambda)Ad\lambda \tag{1.31}$$

where $\eta(\lambda)$ is the response function of the PMT, λ_1 and λ_2 are the wavelength sensitivity bounds of the PMT, and $C(\lambda)$ is the Cherenkov photon flux as a function of wavelength. The Cherenkov photon flux can be calculated using:

$$C(\lambda) = kE(\lambda)T(\lambda) \tag{1.32}$$

where $E(\lambda)$ is the shower Cherenkov emission spectrum, which is $\propto 1/\lambda^2$, $(T\lambda)$ is the transmission function of the atmosphere, and k is a constant which depends on the number of particles in the shower, and on the geometry of the emitting particles and detector. To detect the Cherenkov light from an air shower, it must be possible to detect the pulse above the fluctuations in the night sky background, B, in the time interval, τ. The signal-to-noise ratio, SNR, is given by:

$$SNR = \frac{S}{B^{0.5}} = \int_{\lambda_2}^{\lambda_1} C(\lambda) \left[\frac{\eta(\lambda)A}{\Omega B(\lambda)\tau}\right]^{\frac{1}{2}} d\lambda \tag{1.33}$$

With current detectors the SNR must be above 5 to allow it to be identified as originating from something other than extreme background fluctuations.

Unlike other areas of astronomy where the atmosphere tends to make image collection more difficult, it is a fundamental part of the detector in a very high energy γ-ray telescope, as focusing of such high energy photons is impossible by any currently known means. Unfortunately, the atmosphere is variable, and it's transmissivity depends on a large number of factors including temperature, humidity and pressure, thereby affecting the quality of the data returned by ground-based telescopes. Moreover the transmission properties of the atmosphere can change, resulting in changing extinction rates for the Cherenkov light. Currently, a section of the very high energy γ-ray astronomy community is engaged in experiments to find the effect the changing atmosphere has on the sensitivity of the telescopes, with a view to improving the quality of the data collected (Nolan, Pühlhofer & Rulten, 2010). Despite the lack of a complete understanding of these effects, the current generation of telescopes has been extremely successful, suggesting that the overall

impact is a second order effect.

The Cherenkov radiation emitted by an air shower arrives at sea level in a broad but thin disc of diameter ∼120 m, and so the collection area of an imaging atmospheric Cherenkov telescope (IACT) does not rely on the size of the mirror collection area (which only determines the minimum intensity of the Cherenkov flash detectable and therefore the minimum detectable γ-ray energy). This means that an IACT has an effective air shower detection area of $\sim 5 \times 10^4$ m^2. The construction and design of such telescopes will be further discussed in Section 1.5.

The optimum optical waveband for Cherenkov light detection is in the blue and near-ultraviolet, between 300nm and 450nm; this is a part of the spectrum in which sensitive photomultiplier tubes are available, and a region where the background light from the night sky is near minimum (in the 300nm - 400nm band the night sky background flux is $\sim 2.5 \times 10^{-4}$ erg s^{-1} cm^{-2} ster^{-1}). However, background light nonetheless limits the energy threshold of the telescope, and sites must be chosen where this is kept to a minimum. Two sources of background light, starlight and airglow, both have a broadband emission spectrum similar to that seen from Cherenkov light and must be accounted for. Airglow peaks in the ultraviolet, and its effect is minimised by selecting detectors with a quantum efficiency that peaks in the blue, which is consistent with atmospheric transmission.

A major limiting factor in very high energy γ-ray observations is the background Cherenkov light from cosmic ray interactions with the atmosphere, which cause hadronic air showers as discussed in Section 1.4.2. Cosmic rays are high-energy particles, mostly protons. In the energy range of interest to very high energy γ-ray astronomers, these protons are 10^3-10^4 times more numerous than the photons from the diffuse γ-ray background and $\sim 10^3$ times more numerous than the photons from the strongest steady discrete source of very high energy γ-rays. The observed background of cosmic rays is isotropic, as the paths of the charged particles are affected by the Galactic magnetic field, and so a discrete γ-ray source of sufficient strength (a few percent of the cosmic ray background) is distinguishable from this background. Unfortunately, this is a very strong requirement and it limited the field of very high energy γ-ray astronomy for many years. To get useful data on γ-ray sources requires that the cosmic ray background be distinguished from the γ-ray signal.

Fortunately, there are a number of differences between hadronic and electromagnetic air showers which make it possible to distinguish between the two to a certain extent. As discussed in Section 1.4.2, the lateral profiles of hadronic and electromagnetic air showers are very different, and current methods of separating the cosmic ray background from the signal rely on this for accurate background rejection. The lateral profile of a hadron-initiated air shower is far larger than that of an air shower initiated by an incident γ-ray, as the secondary products emitted within

the core of the hadronic cascade are produced with a wide variation in angle. The result of this is that the Cherenkov light distribution a proton initiated air shower seen in the focal plane of an IACT is broader and less well-defined than that from a very high energy γ-ray initiated air shower. Using this, Hillas (1985) defined image parameters that can be used to reject most of the cosmic ray background, as discussed in greater detail in Section 2.2.

Additionally, the Cherenkov light from a hadron-initiated air shower is also more spread out in time than that from a purely electromagnetic shower, as the penetrating particles and their local Cherenkov light arrive early. Cosmic electrons also provide background noise, about 100-1000 times smaller than that for hadronic cosmic rays, decreasing with increasing energy. Unfortunately this background cannot be discriminated via the method set out by Hillas, as electrons also produce electromagnetic cascades leaving a virtually irreducible background which may constitute the limiting factor at energies below a few GeV.

1.5 Imaging Atmospheric Cherenkov Telescopes (IACTs)

As described in the previous section, IACTs detect the Cherenkov light emitted by charged particles produced in air showers initiated by cosmic rays or very high energy γ-rays. In this section, the construction and design of such telescopes will be described in greater depth, and the current state of very-high energy γ-ray astronomy around the world will be discussed. As of the middle of 2012, there are currently three arrays of IACTs operational: H.E.S.S. (the High Energy Stereoscopic System) in Namibia, MAGIC on the Canary island of La Palma, and VERITAS (Very Energetic Radiation Imaging Telescope Array System) in Arizona, USA. Further discussion of these telescopes can be found in Subsections 1.5.1, 1.5.2 and 1.5.3, with greatest emphasis on the H.E.S.S. array.

The optical quality of an IACT can afford to be much lower than of telescopes that operate in the visible part of the electromagnetic spectrum, as the angular size of the Cherenkov image of an air shower is 0.5°-1.0° and the structure in the image is of the order of a few arcmin. This allows large collection areas, required to increase the sensitivity of the telescope to lower-energy γ-rays ($\sim$ 100 GeV), to be obtained at relatively low cost through the use of large tessellated arrays of spherical mirrors of the same focal length, mounted on an optical support with the same radius of curvature as the focal length; this arrangement is known as the Davies-Cotton design (Davies & Cotton, 1957; Aharonian et al., 2006a). One drawback of this design is that it introduces a spread in the time of arrival of the light in the focal plane; however, this is outweighed by the increase in off-axis performance. A camera, made up of an array of photomultiplier tubes, is then mounted in the focal plane of the telescope to record the optimum optical image. Photomultiplier tubes are

used due to their fast response times, blue-sensitivity and reasonable cost. The Cherenkov light is focused onto the photomultiplier tubes using Winston-cone light collectors. A Winston-cone light collector is an off-axis parabola with reflective inner seurface designed to maximise collection of incoming rays within a field of view by funnelling all wavelengths passing through the large entrance aperture through to the smaller exit aperture (Fernow, 1989).

IACTs can be used to find the position of a source of a few hundred detected γ-rays to within a few arcmin, (Aharonian et al., 2006a). To do this, the image of the Cherenkov light pool is recorded; in the case of a γ-ray shower, this image is reasonably elliptical in shape and the direction of its semimajor axis allows the trajectories of the emitting particles to be deduced. The trajectory of the core of the shower, from which most of the Cherenkov light is emitted, is generally very close to the trajectory that the primary γ-ray would have followed had it not interacted with the atmosphere. Using this method, the arrival direction of the shower can be found to within 0.1° with a single detector, while an array of two or more detectors can be used to fix the direction to within $\sim 0.05^\circ$.

The number of secondary particles at shower maximum is proportional to the energy of the initial γ-ray over a wide range of energies, while the height of shower maximum also depends on the initial energy, so to find the energy of the primary γ-ray using these facts would require the particle density to be sampled at various heights. A more practical method relies on the fact that most of the particles that emit Cherenkov light in the shower are found at the shower maximum and that this Cherenkov light is only lightly attenuated. Thus, a good estimate of the number of particles at shower maximum can be found by measuring the intensity of the Cherenkov light pool, allowing the energy of the initial γ-ray to be calculated. The chief uncertainty in this measurement comes about due to uncertainty in the measurement of the distance to the centre of the Cherenkov light pool; however, if the measurement is made within 50 m-130 m from this, then this effect is small. A single detector can achieve an energy resolution of between 30% and 40%, while an array of parallel detectors can achieve an energy resolution of 10%-15% (Weekes, 2003).

Current-generation IACTs are generally built as arrays, as this increases the overall performance. In an array of telescopes, each shower is observed by all of the telescopes lying within the Cherenkov light pool, giving multiple images of the same shower. The multiple images taken by different telescopes can then be used to improve angular resolution, energy resolution, background discrimination, energy threshold (by increasing the effective area) and shower-axis location. To achieve this the separation between the IACTs should be large enough to have a low correlation between images while being small enough that multiple cameras can be triggered by the lateral extension of local air showers. The optimum separation has been found to be between 50m and

100m, with closer spacing increasing low-energy sensitivity at the expense of effective collection area at higher energies (and vice versa) (Weekes, 2003).

1.5.1 H.E.S.S.

The H.E.S.S. (High Energy Stereoscopic System) telescopes are situated in the Khomas Highlands of Namibia, near the table mountain, the Gamsberg, at an altitude of 1800 m above sea level, and a position of 23°16′18″ S, 16°30′00″E. The telescopes were constructed in the Southern hemisphere to allow for thorough studies of Galactic sources to be carried out as well as studies of extragalactic objects. At completion, the system had a threshold energy of $\approx$ 100GeV and a sensitivity of around 1% of the Crab Nebula flux above 1 TeV for a 5σ detection in 25 hours of operation. The angular resolution of the telescopes is $\sim 5'$.

Until recently, the H.E.S.S. array consisted of four 13m IACTs, which are made up of 382 round quartz-coated mirror facets, each of diameter 60cm, so each telescope has a total reflector area of 107 m^2 (Bernlöhr et al., 2003). The mirror facets are mounted using a Davies-Cotton layout in which the facets are arranged on a sphere of radius 15m, equal to the focal length of the facets, giving a focal ratio $\approx$ 1.2. One consequence of the Davies-Cotton layout is that there is a spread in the photon-arrival times at the camera, which, for the H.E.S.S. telescopes is $\approx$ 1.4 ns rms, of the same order as the intrinsic time spread in the shower photons. On construction, the average reflectivity of the mirrors was 80% - 85% over the relevant wavelength range (300 nm to 600 nm), and the system was designed so that 80% of the reflected light from a point source is concentrated in a circle of 0.4 mrad in diameter. The telescopes are focused to an object distance of around 10 km, which is the typical distance to an air shower from the telescope. A diagram of one of the telescopes is shown in Figure 1.8.

Each camera is made up of 960 photomultiplier tubes, which have a quantum efficiency of $\sim$ 25%. Each photomultiplier tube and its Winston-cone light collector forms a pixel with a 0.16° field of view, leading to a total field of view of 5° for each telescope; this allows observations to be made of extended sources with extensions of a few degrees. These pixels are then arranged into groups of 16, with the associated read-out and triggering electronics contained within the camera body. This avoids the signal loss and broadening of the Cherenkov pulses which would occur if the signals were transmitted over a long distance. The electronics are sampled every 1 ns and the camera is triggered when 3-5 pixels in overlapping 8 $\times$ 8 pixel sectors detect a signal of $\sim$ 5 photoelectrons within a narrow coincidence window. The setup provides an effective coincidence window of $\sim$ 1.5 ns and allows for efficient background rejection of night-sky photons. If two or more telescopes are triggered simultaneously, then the data are read out, providing stereoscopic

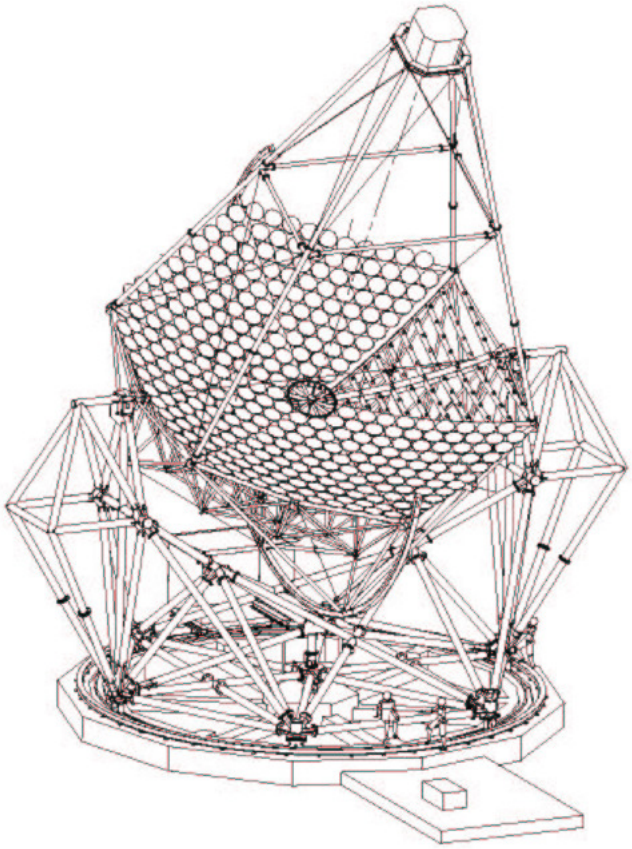

Figure 1.8: Diagram of a H.E.S.S. telescope, showing the steel space frame of the dish and the telescope mount. Mirrors are removed in one section of the dish to view the support beams. Taken from Bernlöhr et al. (2003).

images of the air-shower.

The dish is supported in an altitude-azimuth mount in a rotating base-frame, giving freedom to move the full 360° in azimuth and from −30° (for easy camera maintenance and parking) to +180° in altitude. The telescope can slew in both axes at up to 100° per minute with arcsecond pointing resolution. The cameras are supported by four masts attached to the dish; these cause some shadowing of the reflective area and reduce the effective area of the mirrors to ~ 95 m^2. The support structures of the telescopes are painted red: this helps to minimise stray reflected light in the blue part of the spectrum where the observations are carried out, while limiting heat absorption (and hence distortion) of the telescopes during the day. The mirrors are mounted on the structure in such a manner so as to minimise the stress imparted and are attached to motor-driven actuators to allow position adjustments to be carried out remotely.

At the end of July 2012, a fifth, larger, telescope was brought online as part of H.E.S.S. phase 2. This telescope has a diameter of 28 m, and the structure is similar in design to the 12 m telescopes. At its focal plane is a 2048-pixel camera, utilising similar pixels to those in the smaller telescopes. The telescope is sensitive to photons with energies as low as 10 GeV (Moudden et al., 2011).

Thus far, the H.E.S.S. telescopes have been extremely successful in detecting both Galactic and extragalactic sources and have helped to change the field of very high energy γ-ray astronomy dramatically. The H.E.S.S. Galactic plane survey, carried out between 2004 and 2009, uncovered more than 50 new TeV γ-ray sources, including supernova remnants, pulsar wind nebulae, X-ray binary systems, a young star cluster, the γ-ray source at the centre of the Milky Way and a number of dark sources (sources for which counterparts cannot be identified at other wavelengths). Nearly all of the sources detected by the survey are extended, with rms sizes up to 0.3° (Chaves, 2009). H.E.S.S. has also been successful in the detection of extragalactic objects including blazars, the radio galaxy M87 (for which variability on timescales of days was observed, Aharonian et al, 2006c), Centaurus A (Aharonian et al., 2009b) and the starburst galaxy NGC 253 (Acero et al., 2009).

1.5.2 VERITAS

Of the other operational IACTs of the current generation, the closest in design philosophy to H.E.S.S. is probably the VERITAS (Very Energetic, Radiation Imaging Telescope Array System) array in Arizona, located at 31°40′30″ N, 110°57′07″ W and 1280 m above sea level (Beilicke, 2009). It consists of four 12 m diameter IACTs, separated by a typical baseline of ∼100 m, each of which is made up of 350 individual hexagonal, spherical mirrors giving a total reflector area of 110 m^2. The cameras are made up of 499 photomultiplier tubes, each with a field of view of 0.15°, and are mounted in the focal plane of the telescope at a distance of 12 m from the mirrors. The

total field of view of the telescopes is 3.5°, slightly less than that for the H.E.S.S. array. VERITAS operates in a similar energy range to H.E.S.S., with a threshold energy of ∼100 GeV (Weinstein, 2011). The angular resolution of the array is $< 0.1°$ for small zenith angles, the pointing accuracy is < 50" and the energy resolution (above 200GeV) is 15%-20%. In the summer of 2009, the first constructed telescope was moved to improve the array configuration, and the alignment of the mirrors on the individual telescopes was refined, after which the γ-ray point source sensitivity of VERITAS corresponds to the detection of a γ-ray source with a flux 1% of that of the Crab Nebula at 5σ in less than 25 hours. One major advantage of the array is that unlike the H.E.S.S. array it can collect scientifically useful data under partial moonlight, leading to an increase of around 30% in the average yearly data yield.

Regular observations with all four of the VERITAS telescopes began in September 2007, and since then it has made a number of interesting observations. The weakest source detected by VERITAS thus far is the starburst galaxy M82 (Acciari et al., 2009a), which was observed between January 2008 and April 2009 and is one if two such sources detected at TeV energies. VERITAS collected 137 hours of good data, resulting in a detection at a significance of 4.8σ with a flux level of only 0.9% that of the Crab Nebula. VERITAS has detected four intermediate-frequency BL Lacs (IBLs). The first of these W Comae, was detected over four nights in March 2008 while the source was flaring, reaching a maximum flux of 9% that of the Crab Nebula. W Comae appears to be highly variable, but is also seen as a weak steady source (Majumdar, 2011). VERITAS has also been successful in detecting high-frequency BL Lacs (HBLs), both those previously discovered with other instruments and a number of previously unreported objects; the new discoveries include 1ES 0806+524 detected using observations carried out during construction of the telescopes and incorporating data collected using two, three and four telescopes (Beilicke, 2009). Observations of possible Galactic sources have also been successful, with the collaboration reporting detections of a number of supernova remnants, the first of which were Cassiopeia A and IC443 (Beilicke, 2009). VERITAS has also been used to carry out studies of X-ray/γ-ray binaries, with the detection of LSI +61 306 confirming a previous detection in 2006 by MAGIC (Acciari et al., 2008).

1.5.3 MAGIC

The MAGIC (Major Atmospheric γ-ray Imaging Cherenkov) telescopes are two 17 m IACTs separated by 85m, located at the Roque de los Muchachos Observatory on the Canary Island of La Palma at 2200m above sea level (Cortina, 2011). The telescopes were, until the construction of the H.E.S.S. phase 2 telescope, the largest IACTs in the world; the first began operation in 2004, while the second was completed in 2009. Each telescope has a total reflective area of 236 m^2: this large

size enables the array to observe energies as low as 50 GeV, the lowest energy detectable by any currently operational IACT (Tibolla, 2012; Aleksić et al., 2012a). The reflectors of the telescopes are parabolic to minimise the time spread of the Cherenkov light flashes in the camera plane, and each telescope has a focal length of 17 m. The reflector of the first telescope is constructed of 956 0.5m × 0.5m spherical mirrors, each with a radius of curvature tuned to its position on the paraboloid. These are mounted, as groups of four mirrors, on two motors to allow for the orientation of the groups of mirrors to be adjusted. The second telescope is made up of 247 square tiles of 1 m^2, which are also mounted in groups on pairs of motors.

Since the summer of 2011, the telescopes have been equipped with cameras made up of 1039 photomultiplier tubes, each with a field of view of 0.1° and a response time of ∼0.1 ns. Both telescopes are designed to be relatively lightweight and are constructed out of carbon fibre. This enables rapid movement so they can be repositioned up to 180° within 20 seconds; this permits rapid response to gamma ray burst alarms so as to increase the probability of a very high energy component being detected (Tibolla, 2012). Unfortunately, the light weight of the telescopes means that they are more prone to mechanical distortion due to gravity, atmospheric conditions and weather; to counteract this the telescopes employ an elaborate computer control system for the motors on the mirrors, helping to keep them in the optimal position for photon collection (Aleksić, 2012a). The sensitivity of the array is such that it can detect a source with flux $0.76 \pm 0.03\%$ of the Crab Nebula flux in 50 h at energies > 290 GeV.

The MAGIC telescopes were the first to detect TeV γ-ray emission from the X-ray binary LSI +61 303 (Albert et al., 2006) and claimed the initial detection of the shell-type supernova remnant IC 443 alongside the VERITAS array (Albert et al., 2007a). Work on the Crab nebula with the MAGIC telescopes has been used in an attempt to detect pulsed TeV emission from the Crab pulsar and potential variability from the nebula itself, the suggestion being that its low energy threshold may make detection possible. The telescope has conducted ∼132 hours of observations of the pulsar and has successfully detected pulsed emission from the object at energies between 50 and 400 GeV (Aleksić, 2012b). Observations of the Crab nebula with MAGIC during flares at other wavelengths have shown no evidence for variability above 400 GeV (Tibolla, 2012). A hint of a signal from the X-ray binary Cygnus X-1 with a significance of 4.1σ was reported in 2007, during a flare observed at both hard and soft X-rays with numerous space-based instruments (Albert et al., 2007b).

Since the beginning of 2005, MAGIC has been following up gamma ray burst alerts but so far no detections have been made; however, upper limits have been successfully constructed for a number of events (Cortina, 2011). Other observations have been undertaken of a number of

different AGN classes, including blazars, Seyfert galaxies and radio galaxies. MAGIC has claimed the detection of TeV γ-rays from the 3C 66A/B region with a significance of 5.4σ (Aliu et al., 2009). Interestingly, the MAGIC collaboration found that the distant blazar 3C 66A was unlikely to be the source of the TeV emission, which appeared to be coincident with the Seyfert 1 galaxy 3C 66B with a probability of 85.4%. This may represent the first possible detection of VHE γ-rays from a Seyfert galaxy, although the subsequent detection of 3C 66A by VERITAS casts some doubt on this claim (Acciari, 2009a). The detection of IC 310 was reported in 2010 (Aleksić et al., 2010). This object was initially classified as a radio galaxy, although there is some evidence to suggest it may in fact be an HBL (Kadler et al., 2012).

1.6 Space-based Instruments

The atmospheric Cherenkov technique discussed in Section 1.4.3 allows γ-rays of energies $\gtrsim 50$ GeV to be studied in great detail; however, to study γ-rays with energies below this threshold, the effects of the atmosphere must be eliminated. In the past, this was done using instruments in balloons, but since 1973 this energy band has been studied using space-based telescopes. Unfortunately, γ-rays cannot be reflected or focused, which limits the collection area to the size of the detector; owing to the relatively low fluxes, long exposure times are therefore required. Currently, there are 3 main space-based γ-ray observatories in operation: *INTEGRAL*, *AGILE* and the *Fermi* γ-ray Space Telescope; these are discussed in the following sections.

1.6.1 *INTEGRAL*

The *INTEGRAL* (INternational γ-Ray Astrophysics Laboratory) observatory is operated by the European Space Agency (ESA) and was launched in October 2002. It had an initial operational lifetime of 2 years which has since been extended; the satellite is now funded until 31 December 2012, with mission operations extended until 31 December 2014 (Winkler, 2011). The instrument is designed to gather spectroscopic data primarily in the energy range of 15 keV to 10 MeV, with monitoring capabilities both at X-ray energies between 3 keV and 35 keV and in the optical band at 550 nm. It has an angular resolution between 15 keV and 10 MeV of 12 arcmin full width at half maximum (FWHM).

INTEGRAL has two γ-ray instruments, the first of which, the spectrometer for INTEGRAL (SPI), is optimised for high-resolution spectroscopy between 20 keV and 8 MeV and has the widest field of view of any of the instruments on board (16° corner to corner). The second instrument, the imager on-board the INTEGRAL satellite (IBIS), is designed for γ-ray imaging and so has a

better angular resolution than SPI. IBIS operates over a slightly wider band, between 15 keV and 10 MeV; however, it has a smaller field of view ($9° \times 9°$). In addition to the γ-ray instruments the satellite also carries two monitors, JEM-X, which operates in the 3 keV to 35 keV X-ray band, and the optical monitor, OMC.

Data collected using the *INTEGRAL* satellite have led to a number of important discoveries about the Universe in soft γ-rays. Prior to the launch of *INTEGRAL*, the origin of $\sim 50\%$ of the emission between 50 keV and 500 keV had been attributed to diffuse emission, as earlier missions had difficulty in resolving point sources. Since *INTEGRAL* began observations, the greater imaging accuracy and good sensitivity have led to the detection of a large number (> 90) of point sources; the energy output of these accounts for $\sim 90\%$ of the unexplained diffuse soft γ-ray emission in the inner Galaxy (Winkler, 2007). The telescope has been used to observe the 1809 keV line emission from ^{26}Al, which is a key tracer for nucleosynthesis from massive stars, allowing the star-formation rate in the Galaxy to be estimated at ~ 4 $M_\odot$ yr^{-1}. Using data from *INTEGRAL*, it has been possible to localise the 511 keV electron-positron annihilation line (which is the brightest γ-ray line in the galaxy), towards the Galactic centre (Knödlseder et al., 2005). Although the source of positrons for this annihilation is currently unknown, the data collected have allowed greater constraints to be placed on any potential sources of this emission.

Observations of the centre of the Galaxy with the satellite led to the first detection of a persistent hard X-ray source within the central 10 arcmin of the Milky Way (Bélanger et al., 2006). This source is coincident with Sgr A*, believed to be the counterpart of the supermassive black hole at the centre of the Galaxy, but has a flux eight orders of magnitude lower than that expected for a maximally accreting black hole of the currently accepted mass. By using *INTEGRAL* to study the scattering of past hard X-rays from the molecular cloud Sgr B2, 350 light years away from Sgr A*, it has been possible to determine that the centre of the Galaxy was about 10 000 times more luminous at energies above 20 keV 350 years ago than is seen today. Additionally, *INTEGRAL* has detected a large number of both Galactic and extragalactic sources of soft γ-rays, leading to the construction of the IBIS soft γ-ray catalogue (Winkler, 2007).

1.6.2 *AGILE*

AGILE (Astro-rivelatore γ a Immagini LEggero) is an Italian mission supported by the Italian Space Agency (ASI), and was launched in April 2007 (Tavani et al., 2009a). The scientific payload of the satellite is made up of three detectors combined into a single instrument: a γ-ray imaging detector (GRID), a hard X-ray imager (super-*AGILE*) and a mini-calorimeter which is part of the GRID. *AGILE* was the first γ-ray telescope to use solid-state silicon detector technology similar to

that used on the *Fermi* satellite discussed in Subsection 1.6.3. The GRID instrument is sensitive to photons between $\sim$ 30 MeV and 50 GeV and consists of a silicon-tungsten tracker, a caesium iodide calorimeter and an anticoincidence system for efficient background rejection. It has a field of view of $\sim$ 3 sr and an angular resolution of 0.1° - 0.2° (Pittori, 2012). Super-*AGILE* is a hard X-ray detector sensitive in the 18 keV-60 keV band, with an angular resolution of 1-2 arcmin. The mini-calorimeter is capable of independently detecting transient sources in the range 350 keV - 100 MeV with excellent timing capabilities.

Since its launch, *AGILE* has successfully spent time studying a wide variety of objects. In December 2009, the satellite detected the strongest γ-ray flare for energy greater than 100 MeV observed to date from the flat-spectrum radio quasar (FSRQ) 3C 454.3. Analysis of the data from the flare showed a rapid increase of $\sim$ 80% in the flux $>$ 100 MeV over a 24-hour period, (Striani et al., 2010a). The flaring of another FSRQ, 4C 21.35, in June 2010 was also detected by the satellite; this flare was detected by the *Fermi* satellite and at energies $>$ 100 GeV by the MAGIC telescopes, while also displaying an increase in near-infrared flux (Pittori, 2012). The detection of the flare by *AGILE* led to six Swift (a satellite with instruments covering energy ranges from optical to γ-rays, primarily designed for observations of gamma-ray bursts) target of opportunity observations, as well as optical observations both during and after the flare providing good multiwavelength coverage of the source.

Observations with *AGILE* have confirmed detection of the six pulsars previously detected with *EGRET* (energetic γ-ray experiment telescope) as well as two further pulsars, and timing analysis has led to the detection of a further seven (Pellizzoni et al., 2009). Additionally, the detection of the Vela pulsar wind nebula is the first experimental confirmation of such a source at energies in the range 100 MeV $< E <$ 50 GeV (Pellizzoni et al., 2010). Studies of binary systems with the telescope have led to interesting discoveries of episodes of transient γ-ray emission from both a colliding-wind massive binary system in the eta-Carinae region (Tavani et al., 2009b) and from two microquasars, Cygnus X-1 (Pittori, 2012) and Cygnus X-3; *AGILE* also detected weak persistent emission from Cygnus X-3 for the first time (Tavani et al., 2009c). *AGILE* was the first instrument to report detection of γ-ray flares from the Crab Nebula, long believed to be constant across all energies (Tavani et al., 2011). Super-*AGILE* detects GRBs at a rate of about one per month (Del Monte et al., 2008), while the mini-calorimeter detects them in its energy range at a rate of about one per week (Marisaldi et al., 2008). GRBs have also been detected at the higher energies observed with GRID, displaying a high energy component $E >$ 50 MeV (Giuliani et al., 2008).

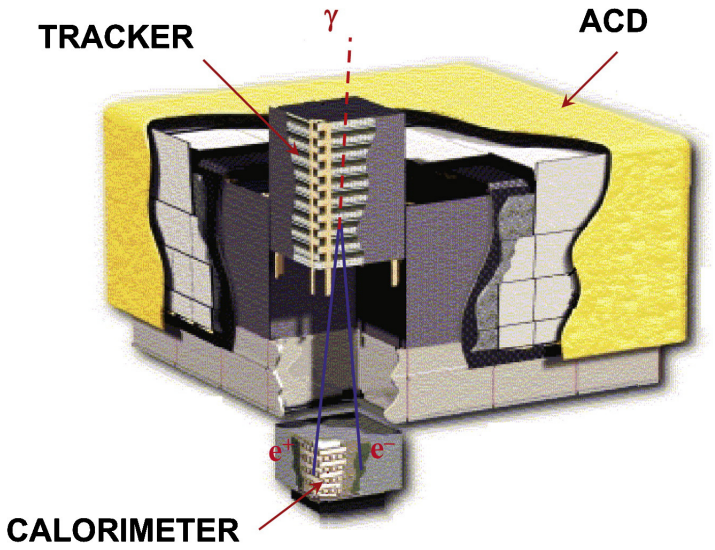

Figure 1.9: Schematic diagram of the LAT aboard the *Fermi* satellite showing the Anticoincidence Detector (ACD), the tracker and the calorimeter. Taken from Moiseev (2011).

1.6.3 The *Fermi* γ-*ray Space Telescope*

The *Fermi* γ-*ray Space Telescope* was launched on the 11th June 2008 to observe the universe at energies from 8 keV to 300 GeV. The telescope contains two instruments, the Large Area Telescope (LAT), an imaging high-energy γ-ray telescope which covers the energy range from 20 MeV to 300 GeV, and the GLAST Burst Monitor (GBM), which is sensitive to X-rays of energy 8 keV through to γ-rays of energy 40 MeV and is used to study transient sources such as γ-ray bursts. The LAT has a field of view that covers 20% of the sky ($>$ 2 steradians), and a complete scan of the sky is completed every 3 hours (Moiseev, 2011).

The LAT is a pair-conversion telescope. This means that it detects γ-rays through the electrons and positrons generated when the γ-ray interacts with the medium through which it passes. Until the launch of *AGILE* in April 2007, pair-production telescopes used a spark chamber to detect γ-rays. In both *AGILE* and *Fermi*-LAT, this has been replaced with a solid-state detector with which the incoming γ-ray interacts. A major benefit of solid-state detectors over spark chambers is that the gas in a spark chamber gradually becomes contaminated and needs replenishing, whereas the silicon in a solid-state detector remains functional for a a far longer period of time. The part of the telescope in which this occurs is known as the tracker, which in the *Fermi*-LAT telescope is made up of a four-by-four array of tower modules, each consisting of layers of silicon strip particle tracking detectors interleaved with thin tungsten converter foils. The direction of the incoming γ-ray is measured by studying the tracks of pair-produced electrons and positrons, while the energy is determined using a calorimeter, which is mounted at the bottom of the tower module and absorbs

all of the particles produced during the γ-ray's passage through the silicon. Surrounding the assembly is an anticoincidence detector which provides charged particle background rejection. The LAT has an effective area for γ-ray detection of 9500 cm^2, an energy resolution between 6% and 18% depending on the angle of incidence and the energy of the incident γ-ray, and a point-source sensitivity for photons with energy > 100 MeV of 3×10^{-9} ph cm^{-2} s^{-1} (Atwood et al., 2009). The structure of the LAT can be seen in Figure 1.9.

The GBM is mounted so as not to block the field of view of the LAT or interfere with the solar cells. It comprises 12 sodium iodide (NaI) scintillation detectors each directly coupled to a photomultiplier tube, to cover the energy range 8 keV to 1 MeV, and two bismuth germanate scintillation detectors, each coupled to two photomultiplier tubes, to cover energies from 150 keV to 40 MeV. The GBM has a field of view of 9.5 steradians, an energy resolution of 12% at 511 keV, a detection area of 12 cm^2 for both the high-energy and low-energy energy detectors and a trigger sensitivity of 0.74 photons cm^2 s^{-1} between 50 keV and 300 keV (Meegan et al., 2009).

The first discovery made using the *Fermi*-LAT was the detection of a pulsar in the CTA 1 supernova remnant (Abdo et al., 2008). The pulsar at the centre of the supernova remnant is the first discovered to emit pulses only at at γ-ray wavelengths. This pulsar has a pulsation period of 316.86 ms. Further work on pulsars has led to the detection of 24 radio-quiet neutron stars pulsating in γ-rays, γ-ray emission from rapidly spinning pulsars with periods ~ 0.01, s and pulsed γ-ray emission from ~ 30 other pulsars (Caraveo, 2012). In 2010, a transient source was detected coincident with Nova V407 Cyg, suggesting the first detection of γ-rays from a nova (Sitarek & Bednarek, 2012). Both instruments on board the *Fermi γ-ray Space Telescope* detected the γ-ray burst GRB 080916C in the constellation Carina, the first time such a phenomenon has been observed at such high energies (Abdo et al, 2009a). Since detection of GRB 080916C, a large number of other γ-ray bursts have been detected, allowing the high-energy spectra of these phenomena to be studied in detail (Bissaldi, 2011). Additionally, the *Fermi* satellite has detected emission from a number of other Galactic sources, pulsar wind nebulae, binary systems, globular clusters and potentially even two massive stars; these results are included in the 2nd *Fermi* catalogue (Nolan et al., 2012).

Fermi-LAT studies of extragalactic sources have also revealed interesting results. In July 2009, the *Fermi* Collaboration reported the detection of PMN J0948+0022, a radio-loud narrow-line Seyfert 1 galaxy (NLSy1) at a redshift of $z = 0.586$ (Abdo et al. 2009b) which is the first detected at such high-energy; since then, a further three radio-loud NLSy1s have been detected: PKS 1502+036 at $z = 0.409$, 1H 0323+342 at $z = 0.061$, and PKS 2004-447 at $z = 0.24$ (Abdo et al., 2009c). These sources will be discussed in more detail in Section 4.3. Thus far, the *Fermi*-LAT

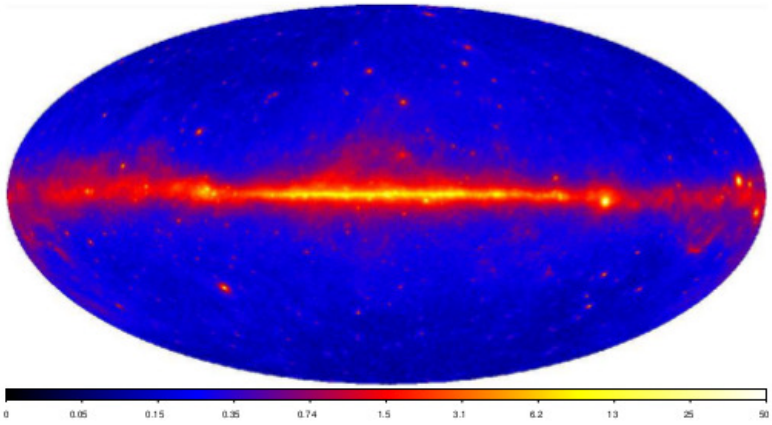

Figure 1.10: Sky map of the γ-ray energy flux between 100 MeV and 10 GeV as derived from *Fermi*-LAT data over 24 months of observations, in units of 10^{-7} erg cm^{-2} s^{-1} sr^{-1}. The map uses the Aitoff projection in Galactic coordinates. The highest concentration of sources can be seen across the middle of the map corresponding to the position of the Galactic plane. Taken from Nolan et al. (2012).

has detected $>$ 900 sources associated with AGN, of which 894 are blazars; in addition to the Seyfert galaxies discussed above, nine radio galaxies have also been detected as well as nine other AGN (Nolan et al., 2012). Interestingly, the *Fermi*-LAT has discovered seven sources associated with galaxies not hosting an AGN, including both the Large and Small Magellanic Clouds, four starburst galaxies and the Andromeda Galaxy, M31. An image of the γ-ray sky as seen by the *Fermi*-LAT in the energy range 20 MeV - 300 GeV is shown in Figure 1.10.

1.6.4 Lower energy space telescopes

There are a number of telescopes operating in the X-ray and lower energy γ-ray regimes of relevance to VHE γ-ray astronomy two of them are briefly described here.

The *Swift Gamma-Ray Burst Explorer* is a NASA mission launched to observe gamma-ray bursts in the Universe. To do this it has the capability to rapidly slew to point at newly detected gamma-ray bursts and carries three co-aligned telescopes at wavelengths from the optical and ultraviolet (170 - 650 nm), X-rays (0.2 - 10 keV) and low energy γ-rays (15 - 150 keV). The low energy γ-ray telescope has a wide field of view to enable it to survey as much of the sky as possible for gamma ray bursts so the telescope can quickly slew to any new events (Romano P., 2012).

XMM-Newton is an ESA mission, sensitive at X-ray energies betweem $\sim$ 1.0 keV - $\sim$ 10.0 keV. The telescope has a relatively large field of view enabling it to be used for survey work (Jansen F. & Parmar A. N., 2001).

1.7 Current Status of Very High Energy γ-ray Astronomy

As of late 2012, 143 VHE γ-ray sources have been observed (http://tevcat.uchicago.edu/ accessed on 20/12/2012). Of these, 88 are Galactic sources, some of which were discovered by the H.E.S.S. Galactic plane scan, which was carried out between 2004 and 2009 and covered $-85^\circ < l < 60^\circ$, $-2.5^\circ < b < 2.5^\circ$, where l is the Galactic longitude and b is the Galactic latitude (Hinton, 2009). The Galactic sources identified can be separated further into four categories: *pulsar wind nebulae*, *supernova remnants*, *star clusters* and *binary systems*.

Pulsar wind nebulae, also known as plerions, are nebulae powered by a pulsar contained within it. As the pulsar wind expands out from the pulsar into the ambient medium, it creates a standing shock where particles are accelerated to high energies, allowing for the production of γ-rays. The data collected thus far on such sources imply that energy may be transferred from the spin-down of the pulsar into TeV γ-rays with an efficiency of $\sim 1\%$. In the pulsar wind nebula HESS J1825-137, the VHE spectrum is observed to soften with increasing distance from the pulsar (known as an energy dependent morphology) and the γ-ray flux increases with increasing distance from the pulsar (Aharonian et al., 2006b). An excess map of the sky region around the object in very high energy γ-rays is shown in Figure 1.11. Recently a pulsar wind nebula has been detected outside of the Galaxy in the Large Magellanic Cloud at a distance of 48.1 kpc (Abramowski et al., 2012a).

Supernova remnants were long suspected to be sources of very high energy γ-rays. The first confirmed detections were of RX J1713.73946 (Muraishi et al., 2000), by the CANGAROO Collaboration (shown in Figure 1.12), and Cassiopeia A (Aharonian et al., 2001) by the HEGRA Collaboration. There are currently two basic sets of theories that have been put forward to explain very high energy emission from such sources (Hinton, 2009). In the first, the TeV γ-ray emission is due to inverse-Compton scattering from the same relativistic electron population as is responsible for synchrotron emission from the source (as described in Section 1.2.3). In the second theory, emission is thought to be due to hadronic interactions between protons and nuclei, which lead to γ-ray emission via decay of neutral pions (see Section 1.2.5).

Some *binary systems* have been observed to emit at very high energies. These systems contain a massive star and a compact object, and may be either microquasars, in which TeV emission occurs in a relativistic jet, or binary pulsar wind nebulae, where the spin-down of the pulsar provides the energy for the very high energy γ-ray emission (Hinton, 2009). LS 5039, a γ-ray binary thought to be made up of a black hole and massive star, shows periodicity at TeV energies with a period equal to the orbital period of the system, 3.9 days (Aharonian et al., 2006c). The object can be seen as the southern-most source in Figure 1.11.

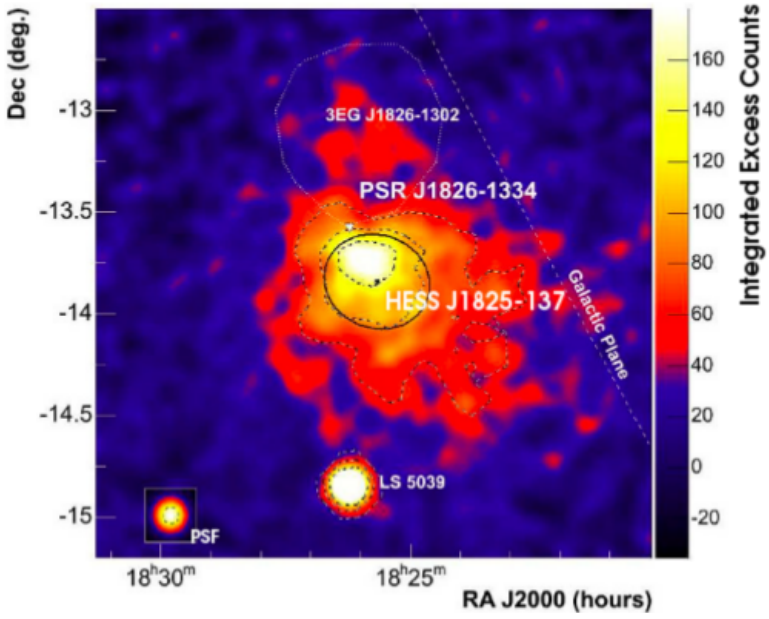

Figure 1.11: A smoothed excess map of the sky region around the pulsar PSR J1826-1334 (the white triangle), showing the pulsar wind nebula HESS J1825-137 and the γ-ray binary LS 5039, constructed with data from the H.E.S.S. array. The linear colour scale is in units of integrated excess counts within the smoothing radius of 2.5'. The best fit position of HESS J1825-137 is denoted by the black circle, and the dashed contours represent the 5σ, 10 σ and 15 σ significance levels with the outermost contour corresponding to the 5σ significance level. The inset circle in the bottom left hand corner shows the point spread function of the dataset. LS 5039 is the bright source to the south of HESS J1825-137. From Aharonian et al. (2006b).

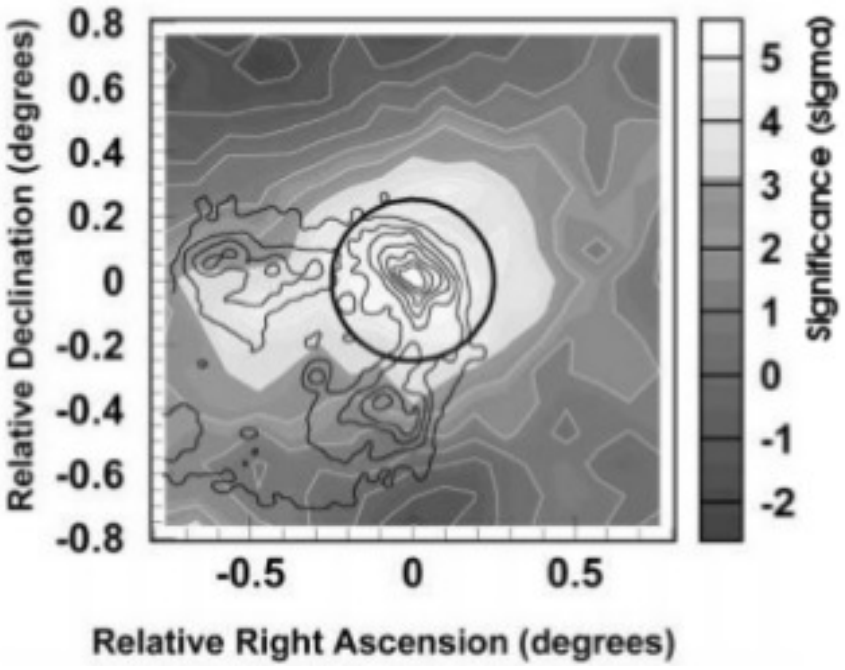

Figure 1.12: Contour map of significance at very high energies around RX J1713.7-3946, centred on the sky region brightest in hard X-rays (R.A. 17h 11m 56.7s Dec -39° 31' 52") constructed with data from the CANGAROO VHE γ-ray telescope as presented in Muraishi et al. (2000). The white contours represent significance and the black contours are X-ray data between 0.5 and 10 keV. The solid circle represents the point-spread function of the telescope.

Finally, a number of TeV γ-ray sources have also been associated with *stellar clusters* of massive young stars, where collisions between the strong stellar winds may produce standing shocks capable of accelerating particles up to the required energies for very high energy γ-ray emission (Abramowski et al., 2012b). One such object reported recently is Westerland 1, although it is suggested that some of the emission may originate from a spatially adjacent pulsar, PSR J1646-458. An excess map of the sky region in VHE γ-rays is shown in Figure 1.13.

The remaining 55 very high energy γ-ray sources are all extragalactic in origin, they are all point sources and they have generally been detected through targeted observation campaigns, making identification far easier than with Galactic sources. Thus far all bar two of the detected extragalactic sources are coincident with AGN which will be more fully discussed in Chapter 3. The remaining two, both reported in 2009, are starburst galaxies, NGC 253 (Aharonian et. al., 2009a) and M82 (Acciari et al., 2009b). A starburst galaxy is one in which there is a boosted formation rate of massive stars, and consequently of supernovae, in localised regions which also exhibit very high densities of gas and radiation fields. These galaxies are considered favourable for the production of cosmic rays (believed to be produced in shocks such as those seen in supernovae) which can then produce TeV γ-rays via inelastic collisions with gas particles and subsequent π^0

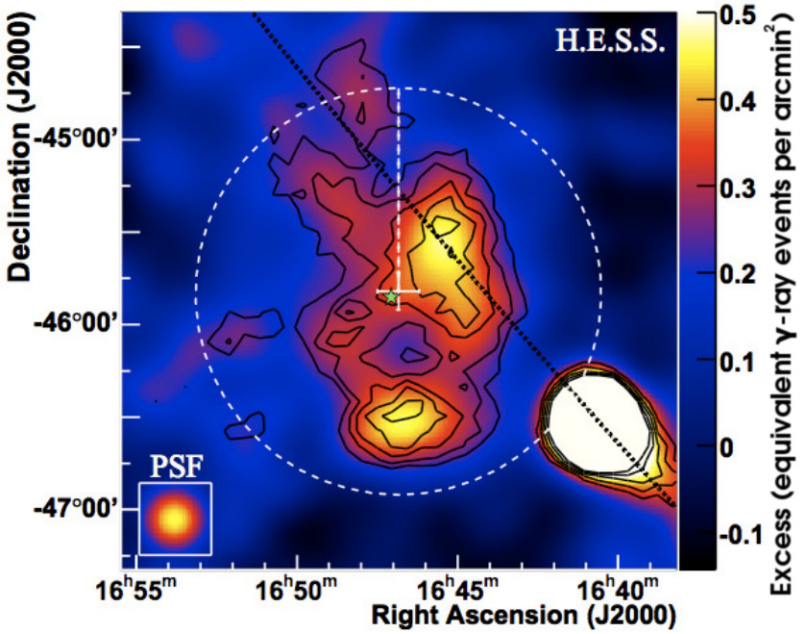

Figure 1.13: H.E.S.S. excess map of the sky region around Westerlund 1 in units of equivalent γ-ray events per arcmin^2. Significance contours between 4σ and 8σ are overlaid in black. The green star represents the position of Westerlund 1 and the white cross the best-fit position of the γ-ray source, while the black dotted line is the Galactic plane. The bright region in the lower right corner is the pulsar wind nebula HESS J1640-465, detected during the H.E.S.S. Galactic plane scan. Taken from Abramowski et al. (2012b)

decay. Of the AGN detected, most are of the blazar subclass, with the relativistic jet at a small angle of inclination to the line of sight; however, three are misaligned, M87 (Aharonian et al., 2006d), Centaurus A (Aharonian et al., 2009b) and NGC 1275 (Aleksić et al., 2012c). Thus far, all extragalactic sources detected have been at relatively low redshift ($z \lesssim 0.5$), because of attenuation of very high energy γ-rays by the extragalactic background light which will be discussed in Section 3.5.

1.8 Conclusions

The study of γ-rays opens up a new window on the Universe, and over the last decade great strides have been made towards revealing the nature of the objects responsible for such high-energy emission. To emit photons at energies $E \gtrsim 1$ GeV requires nonthermal processes such as those described in Section 1.2, and the conditions of the source will determine which of these processes is dominant. Currently, the field is relatively healthy, with three very high energy ($E \gtrsim$ 100 GeV ground-based arrays of telescopes in operation, all using the atmospheric Cherenkov technique. This technique detects the Cherenkov light emitted by secondary particles produced by the interaction of γ-rays in the atmosphere. This light is then used to infer both the trajectory

and energy of the initial γ-ray. These ground-based installations have been extremely successful in detecting large numbers of new sources of very high energy γ-rays, with the number of such objects now significantly above 100. At slightly lower energies, observations must be carried out in orbit and there are currently three operational satellites studying the Universe in γ-rays. Of these, the oldest is *INTEGRAL*, launched in 2002 and is scheduled to remain operational until $\sim$2014; *AGILE* and *Fermi*, launched in 2007 and 2008 respectively are expected to be collecting data for some time yet.

Chapter 2

Analysis of Data from IACTs

2.1 Introduction

Unlike many other fields of astronomy where it is possible to directly count the photons incident upon the detector, very high energy γ-ray astronomy relies on detecting the Cherenkov emission from particles released in air-showers as discussed in Section 1.4.2. This makes analysing the data collected by IACTs relatively complex and this is further compounded by the extremely high background of Cherenkov light emitted by cosmic ray initiated air-showers. Over the decades, however, methods have been developed to allow almost all of this background to be rejected through analysis of the properties of the Cherenkov light pools. By studying the properties of these light pools, it is possible to differentiate between those air-showers initiated by cosmic rays and those initiated by γ-ray photons, while also determining the properties of the primary. This enables the source of any detected γ-rays to be determined and its flux and spectrum at very high energies to be calculated. In the case of observations of an object that does not show significant TeV γ-ray emission, an upper limit on the flux from it can be calculated.

2.2 Parameters Used for γ-ray/Hadron Separation

As discussed in Section 1.4.3 the overwhelming majority of air showers are initiated by a cosmic ray incident on the atmosphere rather than a γ-ray photon. Despite this, very high energy γ-ray astronomy has been able to flourish thanks to work reported in Hillas (1985) which made it possible to distinguish between the two forms of air shower with a high degree of accuracy (achieving greater than 98% rejection of proton-initiated air showers). It had been noted that a number of astrophysical objects appeared to be potential point sources of TeV cosmic rays,

presumed to be γ-rays, but that they did not stand out clearly from the isotropic cosmic ray background; however, it was hoped that if any differences between air showers initiated by TeV photons and those initiated by protons could be documented, it might be possible to reject the background cosmic rays. Hillas used a Monte Carlo simulation to model the development of air showers with both proton and γ-ray primaries, using a program that had been previously used to model other interactions. The Cherenkov light released in these showers was assumed to be received by a collector, 10 m in diameter, and the predicted images were recorded. To describe these images Hillas used a total of six image parameters, which are described mathematically in Fegan (1997) and reproduced here. The first two parameters are the length, l, and width, w, of the ellipsoid, defined as:

$$l = \sqrt{\frac{\sigma_{x^2} + \sigma_{y^2} + s}{2}} \qquad\qquad w = \sqrt{\frac{\sigma_{x^2} + \sigma_{y^2} - s}{2}} \tag{2.1}$$

where:

$$\sigma_{x^2} = \langle x^2 \rangle - \langle x \rangle^2 \qquad\qquad \sigma_{y^2} = \langle y^2 \rangle - \langle y \rangle^2 \tag{2.2}$$

and

$$s = \sqrt{(\sigma_{y^2} - \sigma_{x^2})^2 + 4(\sigma_{xy})^2} \tag{2.3}$$

where

$$\sigma_{xy} = \langle xy \rangle - \langle x \rangle \langle y \rangle \tag{2.4}$$

σ_{x^2}, σ_{y^2} and σ_{xy} are the spreads of the image in different directions defined in terms of the image moments. These image moments are related to the number of counts in a pixel, n_i, and the position of this pixel, described, to second order, using the Cartesian coordinates x_i and y_i, through:

$$\langle x \rangle = \frac{\Sigma n_i x_i}{\Sigma n_i} \qquad \langle y \rangle = \frac{\Sigma n_i y_i}{\Sigma n_i} \tag{2.5}$$

$$\langle x^2 \rangle = \frac{\Sigma n_i x_i^2}{\Sigma n_i} \qquad \langle y^2 \rangle = \frac{\Sigma n_i y_i^2}{\Sigma n_i} \tag{2.6}$$

$$\langle xy \rangle = \frac{\Sigma n_i x_i y_i}{\Sigma n_i} \tag{2.7}$$

The third parameter is the distance, d, from the centroid of the image to the centre of the field of view, this is calculated using:

$$d = \sqrt{\langle x \rangle^2 + \langle y \rangle^2} \tag{2.8}$$

Fourth is the miss, m, the perpendicular distance between the major axis of the image and the centre of the field of view of the camera, evaluated as:

$$m = \sqrt{\left(\frac{u\langle x \rangle^2 + v\langle y \rangle^2)}{3}\right) - \left(\frac{2\sigma_{xy}\langle x \rangle \langle y \rangle}{s}\right)} \tag{2.9}$$

where

$$u = 1 + \frac{\sigma_{y^2} - \sigma_{x^2}}{s} \tag{2.10}$$

and

$$v = 2 - u \tag{2.11}$$

Fifth is the azimuthal width, A_w, which is the rms spread of light perpendicular to the line connecting the centroid of the image to the centre of the field of view, defined mathematically:

$$A_w = \sqrt{\frac{\langle x \rangle^2 \langle y^2 \rangle - 2\langle x \rangle \langle y \rangle \langle xy \rangle + \langle x^2 \rangle \langle y \rangle^2}{d^2}} \tag{2.12}$$

The final parameter is the degree of light concentration determined using the ratio of the two largest pixel signals to the sum of all signals. The length, width and distance are shown in Figure 2.1.

It was found that the images of hadronic showers tend to be longer and wider (due to the emission angles of pions, not present in γ-ray showers), fluctuate more in intensity across the image, and are not systematically aligned with the source. Using the parameters described above,

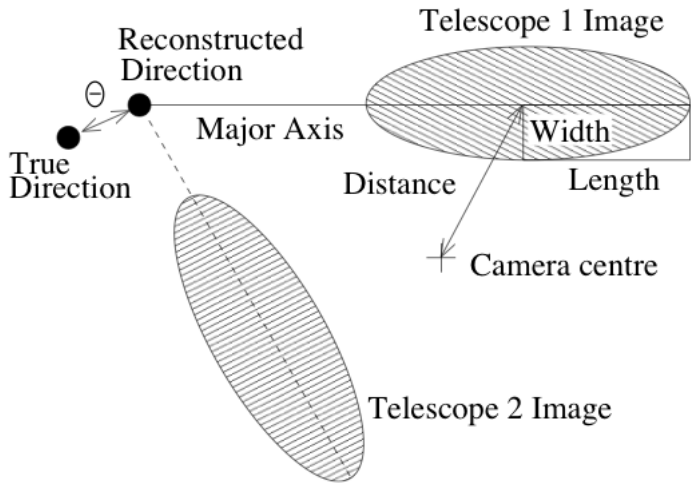

Figure 2.1: Diagram illustrating simple Hillas parameters, calculated for a γ-ray image, approximated as an ellipse. An image from a second telescope is superimposed to demonstrate the geometrical technique for source position reconstruction. The magnitude of the angular offset in shower direction reconstruction is the parameter, θ. Taken from Aharonian et al. (2006a).

Hillas was able to define a region of parameter space containing showers mostly initiated by a γ-ray primary and only a small percentage of proton-initiated showers. By requiring that any four out of the six parameters for a shower lie in this region, Hillas found that it was possible to accept 60%-70% of γ-ray-initiated air showers while rejecting more than 98% of background proton-initiated showers.

In practical situations, the image must be "cleaned" before the Hillas parameters can be calculated. This involves selecting only the pixels which contain Cherenkov light while rejecting those containing only night-sky background (Aharonian et al., 2006a). For the H.E.S.S. telescopes, a two-level filter is used: pixels in the image are required to be above 5 photoelectrons with a neighbour above 10 photoelectrons and vice versa. This method successfully selects spatially correlated features which correspond to air shower light and smooths out shower fluctuations in a simple and repeatable manner. After this the Hillas parameters can then be calculated.

For arrays of more than one telescope, hadron-like events are primarily separated from γ-ray-like events using mean-scaled parameters, p_{sc}, for both the width and length of the detected air shower (Aharonian et al., 2006a). A lookup table, calculated using Monte Carlo simulations, is used to predict the mean value and scatter expected for the parameter being considered in the case of a γ-ray-initiated air shower, as a function of the amplitude of the shower image on the camera, the impact parameter (the projected distance of the extrapolated shower track to a telescope) and the zenith angle. The value of p_{sc} is then calculated using:

$$p_{sc} = \frac{(p - \langle p \rangle)}{\sigma_p} \tag{2.13}$$

where $\langle p \rangle$ is the mean value of the parameter from the lookup tables, σ_p is the scatter taken from the lookup tables and p is the measured value of the parameter from the air shower. The smaller the calculated value for p_{sc}, the more likely the event is to be a γ-ray initiated air shower. Using the calculated value for p_{sc} the mean reduced scaled width (MRSW) and mean reduced scaled length (MRSL) are then calculated by averaging over those telescope images which pass the image-amplitude selection cut for each event.

2.3 Reconstruction of the Origin of a TeV Event

The arrival direction of an air shower can be reconstructed by tracing the direction of the semimajor axis of the image to the point of origin of the particle. Using a single telescope the point of origin of the particle must be estimated using the energy of the particle inferred from the shower size in addition to the asymmetry in the image, which introduces a large amount of inaccuracy in the calculation. By using multiple telescopes, as in the H.E.S.S. array, it is possible to find the intersection of the major axes of the shower images in multiple cameras, giving a simple geometric method of accurately measuring the shower direction, as can be seen in Figure 2.1. Requiring more than one telescope to be triggered for an event to be recorded therefore allows improved accuracy in determining the point of origin of the air shower, with the added benefit of rejecting detections of the Cherenkov light from single muons passing within $\sim$ 100 m of the camera of one of the telescopes.

The point-spread function (PSF) of an array of telescopes is defined as the distribution of events around the location of a point source. In very high energy γ-ray astronomy, the distribution of reconstructed shower directions is usually plotted as a function of θ^2. The PSF defines the accuracy of the reconstructed arrival directions from a point source and can be approximated as the sum of two one-dimensional Gaussian functions

$$\mathrm{PSF} = A\left(\exp\left(\frac{-\theta^2}{2\sigma_1^2}\right) + A_{\mathrm{rel}}\exp\left(\frac{-\theta^2}{2\sigma_2^2}\right)\right) \tag{2.14}$$

where A is the absolute amplitude, which is proportional the number of events, A_{rel} is the relative amplitude of the second Gaussian, and σ_1 and σ_2 are the standard deviation parameters (Aharonian et al., 2006a). The values for these parameters at set zenith angles are calculated by fitting the function to the θ^2 distributions for simulated Monte Carlo γ-rays, and have also been

Cuts	MRSL Min/Max	MRSW Min/Max	$\theta^2_{\rm cut}$ Max (deg^2)	Image Amp. Min (photoelectrons)	Distance Max (°)	γ acc. ($Z = 20°$) %	BG acc. ($Z = 20°$) %
Standard	-2.0/2.0	-2.0/0.9	0.0125	80	2.0	35	9×10^{-3}
Hard	-2.0/2.0	-2.0/0.7	0.01	200	2.0	13	8×10^{-4}
Loose	-2.0/2.0	-2.0/1.2	0.04	40	2.0	68	0.11

Table 2.1: Selection cuts optimised for various sources as described in the text. Cuts are applied on MRSW, MRSL and the distance, θ, from the reconstructed shower position to the source. A minimum of two telescopes passing the per-telescope cuts on image amplitude and distance from the source is also required. The γ-ray acceptance and background rejection for each set of cuts are also displayed for a zenith angle $Z = 20°$. Taken from Aharonian et al. (2006a).

verified by fitting to Crab Nebula data.

2.4 H.E.S.S. Selection Cuts

Selection cuts are the ranges of values of the parameters discussed in Sections 2.2 and 2.3 for which an event is assumed to be initiated by a γ-ray primary. The selection cuts used by the H.E.S.S. array are optimised to maximise the detection significance for sources with typical fluxes and energy spectra, and have been calculated using a mixture of γ-ray simulations and background data (Aharonian et al., 2006a). The significance achieved for a given source increases with the square root of the observation time, and the optimised cuts yield the maximum significance for a source of that type. The optimum cuts to use for a specific source are strongly dependent on the spectrum of the object being observed and so several different sets of cuts may be used in analysis; however, multiple sets of cuts are not used in source searches in order to preserve the *a priori* nature of the analysis. The cuts used in H.E.S.S. analysis are displayed in Table 2.1.

The *standard* cuts described in Table 2.1 are optimised to give the maximum significance for a source with a flux 10% of the Crab Nebula and displaying a similar spectrum. As shown in the table, these cuts reject all bar 9×10^{-3}% of background events, while successfully selecting 35% of photon-initiated air showers. *Hard* cuts are optimised for fainter sources, with flux ∼1% of the Crab flux and steeper spectra than the Crab Nebula. These cuts are particularly useful for analysing data from weak, hard-spectrum sources, returning higher significances than *standard* cuts, while also rejecting a higher percentage of background events (8×10^{-4}%) at the cost of retaining only 11% of γ-ray-initiated events. *Loose* cuts are optimised to give the maximum significance for sources displaying similar fluxes to the Crab Nebula and softer spectra. The lower intensity cut when compared to the *standard* cuts reduces the energy threshold of the analysis, and more γ-ray-initiated events (68%) pass selection; however, the percentage of background events selected (0.11%) is also higher. When conducting source searches, the standard cuts are always

used, unless there is a reason to suspect a very hard or very soft γ-ray spectrum from the object. In addition for large extended sources, the cut on θ^2 is usually set to be larger than the known or assumed extension of the source, so that all γ-rays from the object should pass this cut.

2.5 Calculating the Significance of a Detection

After cuts have been applied, it is necessary to find the significance of a potential detection when compared to the residual background. To do this, the method proposed in Li & Ma (1983) is used, where the statistical significance, S, of a potential detection is shown to be:

$$S = \frac{N_{on} - \alpha N_{off}}{\sqrt{\alpha(N_{on} + N_{off})}} \tag{2.15}$$

where N_{on} is the number of counts on the source position, N_{off} is the number of off-axis counts and α is the normalisation constant between the *on* and *off* regions, taking into account any difference in the size of the effective areas (which depends on zenith angle and photon energy) of the regions considered and in observation times. The *on* signal for a given object is determined by selecting events within a circle with radius $\theta_{\rm cut}$ around that object. Calculating the value of N_{off} is done by measuring the background across a different region of the field of view of the telescope. The region over which this background is measured depends on the background model used. For the H.E.S.S. telescopes, this is either the reflected-background model or the ring-background model.

The reflected-background model uses a number of small circular regions, of the same distance from the centre of the camera as the source being observed. The combined events from these regions are used to estimate N_{off}, and α is then the ratio of the solid angles of the *on* to *off* regions. The method cannot be used for sources closer to the centre of the field of view than the radius of the *on* region, as the background positions would overlap with the source position. The ring-background model calculates the background in a ring around the source position with an internal radius chosen to be significantly larger than the *on* region. This avoids any potential signal leakage from the source. The outer radius of the ring is generally chosen such that the ratio between the area of the *on* and *off* regions is close to 7, as this makes a good compromise between the size of the region being used to calculate the background and distance from the *on* region. In this case, α not only takes into account the ratio between the solid angles of the *on* and *off* regions, but, as the regions being considered are different distances from the centre of the camera, must also take into account the radial background acceptance (which is a radial profile describing the rate of background events passing the shape cuts) in the camera. A comparison of the two methods is shown in Figure 2.2. Using the background methods discussed a sky map displaying

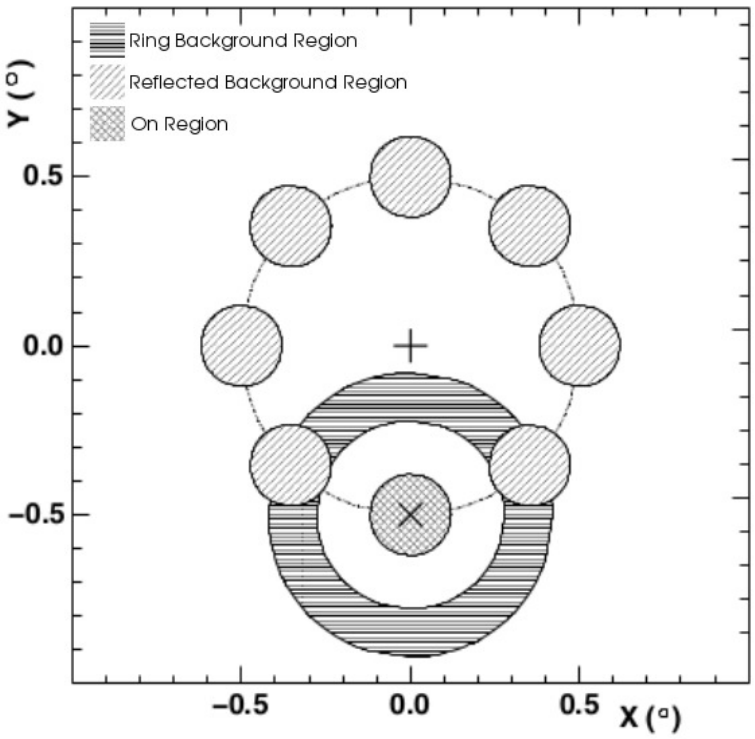

Figure 2.2: Illustration of the background models described in Section 2.5. The centre of the field of view of the telescopes is marked by a cross while the source position is marked with an X The total field of view of the camera is 5° with the diagram only covering a $2° \times 2°$ region. The region used to calculate N_{off} for the ring-background method is indicated with horizontal lines, while the regions used in the case of the reflected-background method are indicated with diagonal lines. The region in which N_{on} is calculated is indicated with a cross-hatch filled circle. Taken from Aharonian et al. (2006a).

the significance of the events detected at each region across the field of view can be constructed. To do this each part of the sky map is treated as a test position and the background around it calculated using either of the methods described leading to a calculation of the significance across the field of view.

2.6 Calculating the γ-ray Flux and Spectra

The flux of an object at very high energies is of great interest when studying the properties of the source involved, and calculating it allows a light curve of the γ-ray flux from the object to be constructed. To generate a light curve the integrated flux above a chosen threshold energy, $E_{\rm th}$ is calculated for each time period ($t_{\rm start}$ to $t_{\rm stop}$). To do this a spectral form, dN/dE, for the emission from the object must be assumed or measured; in the case of a power law spectrum this takes the form (Benbow et al., 2005):

$$\frac{dN}{dE} = I_0(E)^{-\Gamma} \tag{2.16}$$

where Γ is the photon index and I_0 the flux normalisation. The excess number of events seen from a source, δ, is then given by

$$\delta = \int_{E_{\rm th}}^{E_c} \int_{t_{\rm start}}^{t_{\rm stop}} I_0 \left(\frac{dN}{dE}\right)^{-\Gamma} A_{\rm eff}(E, Z(t)) dt dE \tag{2.17}$$

where $A_{\rm eff}$ is the effective area as a function of zenith angle, Z and true photon energy, E (Aharonian et al., 2006a). The effective area is defined as the area over which an incoming γ-ray will trigger the detector and pass selection cuts. Monte Carlo simulations have been used to determine the fraction of simulated γ-rays that fulfil both of these conditions over a range of energies and zenith angles and the calculated values for effective areas for each set of parameters have been recorded in lookup tables. Equation 2.17 is then solved for the flux normalisation in the differential spectrum in Equation 2.16 by integrating up to a cutoff energy E_c (the upper bound of the Monte Carlo simulations) from $E_{\rm th}$ and over the observation time, using the lookup tables discussed to provide values for the effective areas. The integral flux above the threshold energy can then be calculated using:

$$I = \int_{E_{\rm th}}^{E_c} \frac{dN}{dE} dE = \int_{E_{\rm th}}^{E_c} I_0(E)^{-\Gamma} dE \tag{2.18}$$

The energy of each event is calculated using the mean of the energies estimated for each telescope (Aharonian et al., 2006a). The energies estimated take into account the image size, the impact parameter of the event and the zenith angle of the observation, and are taken from lookup tables based on results from Monte Carlo γ-ray simulations. To determine the energy spectrum the events that pass selection cuts are then placed in bins, i, of width ΔE_i and the differential flux, dF_i/dE, is calculated by summing over the on source events $N_{\rm on}$, weighted by the inverse of the effective area, $A_{\rm eff}$, for each event. The normalised sum of the weighted off events $N_{\rm off}$ is then subtracted and the difference is weighted by the live-time for the bin, T and the bin width:

$$\frac{dF_i}{dE} = (T \Delta E_i)^{-1} \left(\sum_{j=0}^{N_{on}} (A_{\rm eff})^{-1} - \alpha \sum_{k=0}^{N_{off}} (A_{\rm eff})^{-1} \right) \tag{2.19}$$

where α is the normalisation constant discussed in Section 2.5. As the estimation of the effective area depends weakly on the assumed spectral shape, an iterative procedure is then followed starting with assumed parameter values fitted to the spectrum. The effective area is then adjusted for the fitted spectrum and the spectrum re-fit. This is repeated until convergence (Aharonian et al.,

1999).

2.7 Calculating Upper Limits

In a situation where no signal is detected from an object, it is often useful to calculate an upper limit on its γ-ray flux. To do this, the method proposed in Feldman & Cousins (1998) is used; this method relies on classical statistical theory (as opposed to the Bayesian approach) and was developed to analyse data from neutrino-oscillation experiments. The method constructs confidence intervals in such a manner that it unifies the treatment of upper confidence limits in the case of non-detection and two-sided confidence intervals (i.e. the error on the result to a given confidence level) for positive results.

Considering a probability distribution, $P(x|\mu)$, which describes the probability of obtaining x for a given value of μ, where μ is the true value of the quantity being measured and x the result obtained by direct measurement, it is possible to select an interval such that the probability that μ is contained within it is $\alpha_{\rm con}$. This interval is referred to as the acceptance region and is bounded by x_1 and x_2. It is expressed as:

$$P(x \in [x_1, x_2]|\mu) = \alpha_{\rm con} \tag{2.20}$$

In order to specify uniquely the acceptance region, auxiliary criteria must be specified. In the case of upper confidence limits:

$$P(x < x_1|\mu) = 1 - \alpha_{\rm con} \tag{2.21}$$

which satisfies $P(\mu > \mu_1) = 1 - \alpha_{\rm con}$, where μ_1 is the upper bound on the true value μ given the acceptance region. To calculate the upper limit:

$$\int_{x_2}^{x_1} P(x|\mu)dx = \alpha_{\rm con} \tag{2.22}$$

must be evaluated; x_2 is set to 0 as only non-negative values of x are physically allowed. In very high energy γ-ray astronomy, it is assumed that $P(x|\mu)$ follows a Gaussian distribution:

$$P(x; \mu, \sigma^2) = \frac{1}{\sqrt{2\pi\sigma^2}} \exp\left(-\frac{(x-\mu)^2}{2\sigma^2}\right) \tag{2.23}$$

where $x = N_{on}$ and $\sigma = \alpha N_{off}$ (α is as described in Section 2.5). The integral in Equation 2.22 is generally evaluated iteratively until $\alpha_{\rm con} = 99\%$. As the α depends weakly on photon energy,

an initial spectral shape and the parameters describing it must be assumed.

2.8 Conclusions

The method proposed by Hillas in 1985 to distinguish between cosmic ray initiated air-showers and γ-ray-initiated air-showers, as described in Section 2.2, has proved invaluable in furthering the study of objects at very high energies. By measuring the properties of the Cherenkov light pool on the ground, more than 99% of air showers with cosmic ray primaries can be rejected. The path of the initial γ-ray photon can be derived from the direction of the semimajor axis of the Cherenkov light pool, and by combining the data from multiple telescopes this can be found far more accurately than for a single telescope, allowing the source of the γ-rays to be determined. The statistical significance of a potential detection depends on the number of events detected in a region around the object, which pass the cuts on the parameters of the light pool compared with to the number of events in other regions of the telescope field of view which pass the cuts, normalised to take into account differences in effective area between the two regions. In the case of a significant detection (above 5σ), the flux of an object can then be calculated by finding the energy of each event, which depends on a number of variables found using Monte Carlo simulations, and determines the number of events within a specified energy range. By taking the effective area into account, the flux over each energy range can then be calculated. If no significant signal is detected, upper limits on the flux can be found using the method of Feldman & Cousins (1998).

Chapter 3

Very High Energy γ-rays from Active Galactic Nuclei (AGN)

3.1 Introduction

The term active galactic nuclei (AGN) refers to energetic phenomena observed in the central regions of some galaxies with emission that cannot be attributed to stellar activity or gas heated by stellar processes. It is widely believed that the very high luminosities observed are due to the energy released as matter is consumed by the central supermassive black hole. The taxonomy of AGN is complex, and many of the subdivisions are more historical than based on physical differences between the objects, although as more data on the properties of such sources have become available and their spectral energy distributions determined over a wide range of energies, more meaningful classifications have become possible. Many AGN are very luminous across the entire electromagnetic spectrum (although in some cases they can be outshone by their host galaxy at optical through to X-ray wavelengths) and display strong radio and potentially γ-ray emission. To date, AGN are by far the most numerous extragalactic sources of very high energy γ-rays, and studies at these energies have helped to increase our understanding of the properties of these highly energetic sources. In this chapter, the current status of these studies will be reviewed with particular emphasis on the misaligned objects M87 and Centaurus A. The difficulties presented by γ-ray absorption over the long distances involved will also be discussed.

3.2 Classification of AGN

AGN display luminosities anywhere from $\sim 10^{11} L_{\odot}$ to $\sim 10^{13} L_{\odot}$, depending on the type of AGN (Peterson, 2003). Of the 46 extragalactic sources detected in TeV γ-rays to date, 44 are AGN and the first extragalactic object observed in the very high energy regime was the blazar Mrk 421 in 1992 (Punch et al., 1992). Such objects are most luminous in the optical through to the γ-ray regime and between 15% and 20% are radio-loud, with ratios of radio flux at 5GHz to optical flux in the B-band ($\sim$687nm) of ~ 10 (Kellerman et al. 1989). To produce the high luminosities observed in AGN, it is believed that the central engine must be a black hole of mass $\sim 10^{6} M_{\odot}$ to $\sim 10^{9} M_{\odot}$ which is accreting matter at an extremely high rate and emitting close to the Eddington luminosity, L_{Ed}. The Eddington luminosity is the maximum luminosity achievable for an object, such as a black hole, balancing radiation pressure against gravitational force, it is calculated using $L_{\mathrm{Ed}} = 4\pi G M m_p c/\sigma_T$, assuming the matter falling towards the body is pure ionised hydrogen, where M is the mass of the central object, m_p is the proton mass, G is the gravitational constant and σ_T is the Thomson cross section. AGN are relatively rare in the universe and are found at all distances, although they appear more common at higher redshifts, and their luminosity is generally seen to increase with higher redshift (Weekes, 2003).

The observational study of AGN began in 1908 at the Lick Observatory in California with work carried out by Edward Fath (Osterbrock & Ferland, 2006). During the study of absorption lines in the spectra of the nuclei of what were known as "spiral nebulae" and are now known to be galaxies, Fath noted that these could be understood as resulting from the integrated light of a large number of unresolved stars. Additionally Fath, also recognised six emission lines in the spectrum of the nucleus of NGC 1068. Around 30 years later Carl Seyfert published a paper (Seyfert, 1943) detailing the observed properties of a number of galaxies (including NGC 1068), which he recognised as displaying many high-ionisation emission lines. He noted that these objects were highly luminous, that they made up a very small fraction of galaxies, and that their emission lines were wider than those seen in other galaxies. The characteristics noted by Seyfert are now used to classify *Seyfert galaxies*, which are the most common kind of AGN and will be discussed in detail in Chapter 4. Discussions of the different classes of AGN can be found in the following Subsections.

3.2.1 Radio Galaxies

The advent of radio astronomy saw the detection of a number of unknown radio sources, and advances made in the field in the decade after the Second World War led to optical counterparts to

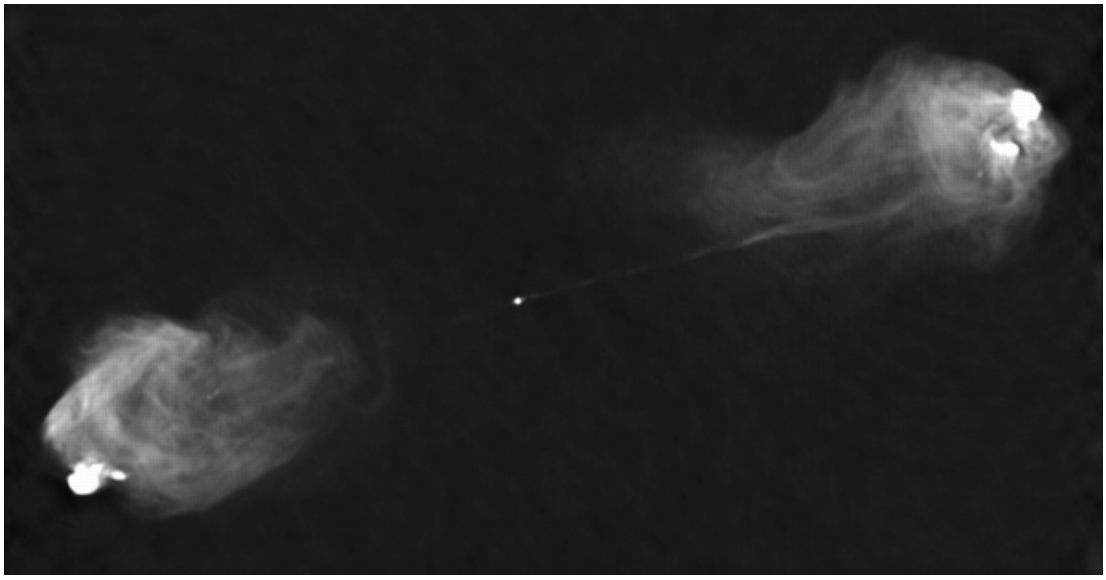

Figure 3.1: Radio image of Cygnus A at a wavelength of 20 cm. Two narrow radio jets can be seen emanating from the central core, channelling matter and energy into the large radio lobes. Taken from Perley et al. (1984).

some of them being identified. One of these sources was Cygnus A (a galaxy at $z = 0.057$), which was found to have a similar emission-line spectrum to the Seyfert galaxies previously identified, but unlike those sources, it was radio-loud (Baade & Minkowski, 1954). Identification of other similar sources quickly followed, and they were classified as "radio galaxies".

Radio galaxies are some of the brightest radio sources in the sky and have radio luminosities of greater than $\sim 10^8 L_\odot$, with the most powerful displaying overall luminosities as high as $\sim 10^{12} L_\odot$ (Sparke & Gallagher, 2000). Radio galaxies are highly structured. They are seen to have twin radio-bright, optically-thin, lobes on opposite sides of the galaxy, which are related in size to the strength of the radio source at the nucleus; the largest lobes are ~ 3 Mpc across (Sparke & Gallagher, 2000). To fill out such lobes, a radio galaxy must have been active for at least 10-50 million years. Within the lobes, there are luminous hot spots with sizes ~ 1 kpc; these hot spots are observed to emit polarised visible light via the synchrotron process. The core of a radio galaxy is a radio source only a few parsecs across, which is optically thick and varies in luminosity on timescales of years, suggesting an emission region at most a few light years across. The radio galaxies observed with large radio lobes are generally giant elliptical or cD galaxies (giant ellipticals that have a large halo of stars) and are in many cases the brightest galaxies in their clusters. Many radio galaxies have been observed to be blue in colour and show other signs of recent star formation. Strong radio emission appears to be favoured in radio galaxies with relatively low amounts of cool gas (Sparke & Gallagher, 2000).

Emerging from deep within the central core of a radio galaxy are narrow, bright jets. In some cases, these are observed on only one side of the galaxy, while in others two-sided jets are detected. The matter in these jets is relativistic and is focused into a beam within the central parsec of the galaxy. These jets channel energy and matter into the radio lobes of the galaxy. The jets of radio galaxies emit via synchrotron radiation at all wavelengths from radio to X-rays and they have also been observed to emit γ-rays.

Radio galaxies can be divided into narrow-line radio galaxies, which make up around two-thirds of the population, and broad-line radio galaxies, which account for the rest. In narrow-line radio galaxies, the emission lines seen in the spectrum are relatively narrow (between $\sim$400 km s^{-1} and $\sim$800 km s^{-1}, characterised using velocities as the broadening is due to to the range of Doppler factors observed for the emitting gas), and a very wide range of ionisation states is observed from [OI] (neutral oxygen) to [FeX] (the ninth ionised state of iron). The emission lines detected are very similar to those seen in planetary nebulae and HII regions, suggesting that the elemental abundances, temperatures and densities near the core of narrow-line radio galaxies are similar to such objects. Absorption lines are generally similar to those seen in elliptical galaxies not hosting an AGN, although with stronger HI lines in the ultraviolet, suggesting a larger population of young stars than would be expected for such objects. Broad-line radio galaxies show broad recombination lines, such as HI, HeI and HeII, although the forbidden line widths are similar to those seen in narrow-line galaxies. The narrow-line spectra in broad line radio galaxies are similar in relative intensity to those seen in narrow line radio galaxies. This suggests that all these objects have similar physical conditions in the narrow-line emission region, but that, in the case of broad-line radio galaxies an additional region is observed which contains matter with a much larger range of velocities.

In addition to being classified on the basis of detected emission lines, the cores of radio galaxies can also be separated into two categories depending on the properties of the jet, Fanaroff-Riley class 1 (FRI) and Fanaroff-Riley class 2 (FRII). Radio galaxies hosting FRI cores (henceforth FRI galaxies) have lobes which are brightest in the centre, with the ends showing "edge-darkening" and steeper radio spectra. Generally the jets are double sided, continuous and brighter than the radio lobes. FRI cores appear to be hosted in by the most luminous ellipticals and cD galaxies (giant ellipticals with a large halo of stars) (Phillips, 2005). The brighter radio galaxies, such as Cygnus A, show lobes which are "edge-brightened", with steeper radio spectra near the centre of the lobes, and are classified as FRII hosting galaxies (henceforth FRII galaxies). Inside the lobes of FRII galaxies are usually a number of smaller, kpc-sized, radio hotspots. The jets of such objects are usually one-sided or at least asymmetric and, although brighter than the jets in FRI galaxies, show

less contrast with the brightness of the radio lobes. FRII cores are hosted at the core of normal giant elliptical galaxies (Phillips, 2005).

3.2.2 Quasars and QSOs

Some optically identified radio sources were stellar in appearance (point-sources with no obvious galaxy in their images), but their spectra were continuous in nature with no absorption lines and with broad emission lines at unidentifiable wavelengths. In 1963, emission lines in 3C 273 were identified, a radio source with what was at the time an unusually large redshift of $z = 0.158$ (Schmidt, 1963), and similar lines were soon identified in 3C 48 with a redshift of $z = 0.367$ (Greenstein, 1963). These redshifts were larger than those for even the faintest galaxies known at the time, and made it clear that the objects were extremely luminous and definitely not stellar in nature, despite the lack of an identifiable host galaxy. These sources are now understood to be AGN and are known as quasi-stellar radio sources (quasars); with the advent of CCDs, many have had their host galaxies resolved. Soon afterwards, similar radio-quiet sources were observed and these, along with quasars are termed QSOs or quasi-stellar objects.

The active nuclei in QSOs are so bright that they outshine their host galaxies, and most are so distant that they appear quasi-stellar in optical images. They are the most luminous known objects, with typical luminosities $\sim 2.6 \times 10^{12} L_{\odot}$ (Peterson, 1997). Around 5-10% of these objects are quasars (radio loud) and appear to be predominantly hosted in elliptical galaxies, while the remaining QSOs appear to be mostly found in spiral galaxies (Peterson, 1997). The radio power in a radio-quiet QSO is $\sim 1\%$ that seen in quasars. Thus far, QSOs have been observed at redshifts up to and exceeding $z \approx 5$, suggesting that light emitted by them was emitted when the Universe was as little as one-sixth of its current age. Evidence from the relative intensities of broad emission lines suggests that the ratio of metals to hydrogen and helium in these objects is similar to that in the sun, suggesting that the metal content in the interstellar medium in QSOs has already been enriched by a first generation of stars (Sparke & Gallagher, 2000).

Low-redshift QSOs have broad HI, HeI and HeII absorption lines and narrow, collisionally excited lines over a wide range of ionisation from [OI] to [NeV], with [OIII] λ 5007 (which denotes emission at a wavelength of 5007 $\mathring{A} = 500.7$ nm) the strongest. In many of these objects, the MgII λ 2800 line is shifted to the observable region and has a broad spectrum profile. In higher redshift QSOs, strong [CIII] λ 1909, CIV λ 1549, NV λ 1240, OVI λ 1034 and Lyα λ 1216 emission lines are observed (Hazard & Mitton, 1979). The continuous spectra of such sources do not show any stellar absorption lines and appear to follow a pure power law, with a local emission maximum near the rest wavelength λ 3650. Most of the quasars detected at high energy have been observed

to be highly polarised at optical wavelengths and are generally only detected when the flux at high radio frequencies is increasing (Valtaoja & Teräsranta, 1995).

The maximum energy that can be extracted from a mass M falling into a black hole is about 43% of Mc^2, as suggested in Li & Paczyński (2000); however, in practice it is expected that $\sim 0.1Mc^2$ will emerge as radiation while the rest is permanently added to the mass of the black hole. In the case of a QSO with a luminosity of $\sim 10^{12} L_\odot$, approximately $0.1 M_\odot$ must be converted into energy every year, and to maintain that power the black hole mass must grow by $\sim 0.9 M_\odot$ per year. Activity in a quasar or QSO is thought to continue for at least 100 million years, suggesting that a black hole with a mass of at least $10^8 - 10^9 M_\odot$ should remain. This is supported by observations of local galaxies, where central black holes with masses $\gtrsim 10^{10} M_\odot$ have not been found (Sparke & Gallagher, 2000).

3.2.3 Unification of AGN

Attempts to unify AGN usually assume that they are similar objects viewed from different angles on the sky; the proposed structure in the central region of such objects is shown in Figure 3.2. This is suggested by the fact that radio sources have axial rather than spherical symmetry and would thus appear different when viewed from different angles. The most widely accepted model posits that the central core of an AGN is a supermassive black hole, as previously discussed, and that surrounding this is an accretion disc of hot gas and dust that emits radiation all the way up to X-ray frequencies. Surrounding this in turn is a dusty, optically-thick torus which absorbs radiation passing through it and re-emits it at longer wavelengths. In around 10% of AGN, jets are observed emanating from the central core, roughly perpendicular to the accretion disc.

As previously stated, viewing an AGN from a different angle results in different observable properties. Assuming a smooth-density torus, the objects are divided in type 1 and type 2 AGN based on the extent to which the nuclear region is visible; see (a) and (b) Figure 3.3. In the case of a clumpy torus, the difference between type 1 and type 2 AGN is not merely an issue of orientation but of the probability of drawing a direct line of sight to the nucleus as shown in (c) in Figure 3.3.

It is believed that orbiting relatively close to the central AGN are a number of clouds of gas or dust, which produce the broad emission lines, with FWHM $\sim$ 4000 km s^{-1}, observed in the UV/optical spectra (Netzer & Laor, 1993), and the strong absorption features seen in the X-ray/UV spectra of type 1 AGN. This is known as the broad-line region (BLR) and is directly observed in type 1 AGN; however, it can be indirectly detected in type 2 AGN in polarised light (Anonucci, 1993). To date, very little can be said with certainty about the BLR because even in the case of the closest AGN it remains spatially unresolved; however, it would appear to be dense by nebular

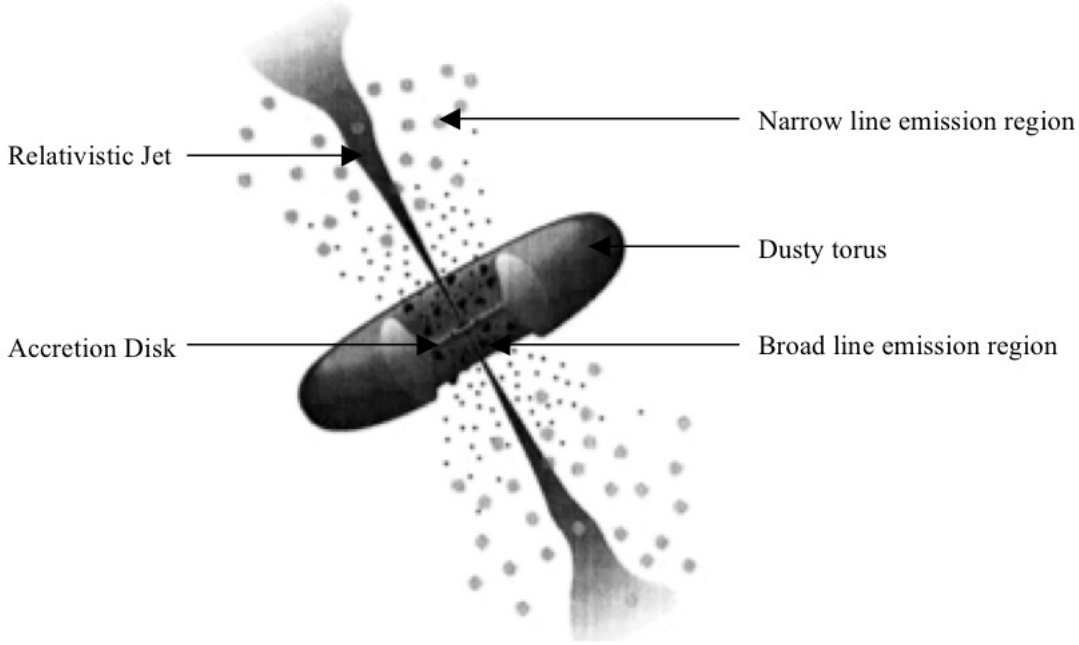

Figure 3.2: Diagram of the currently supported model for the unification of AGN. The central engine, assumed to be a supermassive black hole, is surrounded by an accretion disk of luminous material; beyond the accretion disc is an obscuring dusty torus. Broad emission lines are produced by clouds orbiting the disc close to the central black hole while narrow emission lines are produced in clouds orbiting further from the central supermassive black hole. Radio jets are observed to emanate from the region near the black hole, initially at relativistic speeds. Taken from Urry (1995).

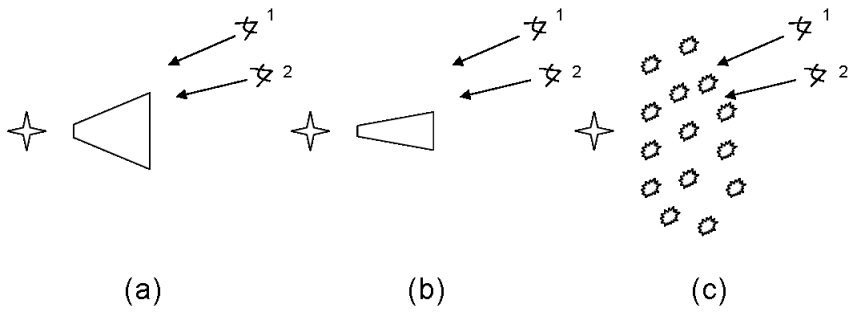

Figure 3.3: Classification of AGNs in unified schemes. For simplicity each diagram shows only the central black hole (the four pronged star), a cross-section of one side of the torus (the structure to the right of the black hole in each diagram) and the observers, labelled 1 and 2. In a smooth-density torus, as in (a), any observer located in such a manner that their line of sight to the central black hole will not pass through the torus, such as observer 1, will see a type 1 source. Those with a line of sight to the central black hole passing through the torus, such as observer 2, will see a type 2 source. If the torus covering factor is decreased, such as in (b), this will lead to the object appearing as a type 1 source to most observers. In the case of (c), a clumpy, soft-edge torus, the probability of a direct view of the AGN decreases away from the horizontal axis, but is always finite. After Elitzur (2011).

standards, $n_e > 10^9$ cm^{-3}, and at temperatures of $T \approx 10^4$ K (Peterson, 2006). The dynamics of the BLR are currently debated, but it is likely that the gravitational acceleration from the central object is dominant to such a degree that it is possible to use the size and the velocity dispersion of the region to provide an estimate of the central black hole mass to within a factor of ~ 3. The size of the BLR scales simply with relation to luminosity, both on an object-to-object basis and within a single AGN as its luminosity varies with time (Peterson, 2006).

Further from the centre of the AGN, at distances of $\sim 50 - 100$ pc are further clouds of gas or dust (Peterson, 2006). These are believed to be the origin of the narrow emission lines, with FWHM ~ 500 km s^{-1}, observed in the spectra of both type 1 and type 2 AGN (Netzer & Laor, 1993); this region is known as the narrow line region (NLR). The gas or dust in the NLR is at a similar temperature to that found in the BLR ($T \approx 10^4$) but at much lower density ($10^2 - 10^6$ cm^{-3}), and the dimensions of the region scale with the square root of the luminosity of the source (Netzer & Laor, 1993).

Based on evidence collected from galaxy counts and the host galaxies of AGN it is widely believed that over time quasars evolve into radio galaxies and from there into normal elliptical galaxies, while radio-quiet QSOs evolve into Seyfert galaxies and then into normal spiral galaxies. Current evidence suggests that the rate of evolution of AGN is dependent on their luminosity. Early optical surveys demonstrated that QSOs undergo significant evolution from $z \sim 0$ up to $z \sim 2$ and that beyond $z \sim 2$ the space density of QSOs starts to decline (e.g., Schmidt & Green, 1983). More recent surveys using X-rays, which can more robustly select fainter AGN such as Seyfert nuclei, have found that faint AGN evolve at a more modest rate with respect to redshift than QSOs; in contrast, bright AGN appear to evolve at a similar rate to QSOs. Current observations in soft X-rays provide evidence that the comoving spatial density of bright AGN peaks at higher redshifts ($z \sim 2$) than fainter AGN ($z < 1$) (Fanidakis et al., 2012). This differential evolution of AGN depending on luminosity has been described as "downsizing" (Barger et al., 2005; Hasinger, Miyaji & Schmidt, 2005), and leads to the conclusion that AGN activity in the low-z Universe is dominated by either high-mass black holes accreting at low rates or smaller-mass black holes accreting rapidly. Hopkins et al. (2005) have proposed that the faint end of the luminosity function is composed of high-mass black holes experiencing quiescent accretion, while the bright end corresponds to black holes accreting close to the Eddington luminosity. Approximate space densities of the different classes of AGN can be seen in Table 3.1.

Support for hierarchical models of AGN evolution is provided both by surveys, as previously stated, and through semianalytic modelling, such as that in Fandiakis et al. (2012). It was found that at high redshift ($z \sim 6$) most of the active black holes have masses of $10^6 - 10^7$ M$_\odot$ and

Object Type	Number Mpc^{-3}
Field Galaxies	10^{-1}
Luminous Galaxies	10^{-2}
Seyfert Galaxies	10^{-4}
Radio Galaxies	10^{-6}
QSOs	10^{-7}
Quasars	10^{-9}

Table 3.1: Approximate space densities of different AGN in the Universe. From Osterbrock and Ferland (2006).

accrete at a rate of $\dot{m} \approx 0.3$, where $\dot{m}$ is the rate of mass accretion onto the object in units of the Eddington accretion limit (the rate of mass falling onto the black hole that would lead to emission at the Eddington luminosity). At lower redshifts, the accretion activity peaks for 10^7-10^8 $M_\odot$ black holes accreting at a rate of $\dot{m} \approx 0.05$. Using the results found for accretion rates and black-hole masses, and assuming that accretion takes place in two distinct regimes, a thin disc which is radiatively efficient, and an advection-dominated accretion flow which is not, Fandiakis et al. (2012), predict that the brightest AGN ($L \gtrsim 10^{46}$ erg s^{-1}) should be found in dark matter haloes with masses $\sim 10^{12} - 10^{13}$ $M_\odot$ in the low-redshift Universe ($z \lesssim 2$). These intermediate-mass haloes provide gas for intense black-hole growth as they are typical environments for instabilities in gas-rich galaxies and for galaxy mergers. In the case of more massive dark matter haloes, there is generally less gas available as they are usually in quasistatic equilibrium and subject to feedback from the AGN, leading to lower accretion rates. The assumption of two distinct accretion channels leads naturally to the downsizing observed in surveys, which is further accentuated when obscuration is taken into account.

3.3 Blazars

Blazars, the most luminous objects in the Universe, are AGN with a jet at a small angle of inclination to the line of sight. This means that the radiation detected is highly beamed and relativistically boosted, to the extent that the jets in some blazars show apparent superluminal motion. Blazars are further separated into three categories: BL Lacertae objects, optically violent variables (OVVs) and flat spectrum radio quasars (FSRQs) (Weekes, 2003). BL Lacertae objects are named after the prototype for this galaxy, BL Lacertae, and are characterised by rapid and large flux variability, significant optical polarisation and a spectrum dominated by a featureless non-thermal continuum, with no strong emission or absorption lines. Where emission and absorption lines are detectable in BL Lacertae objects, they are invariably weak relative to the continuum and typically show relatively small redshifts of $z \lesssim 0.1$ (Peterson, 1997). OVVs show very short

timescale variations ($<$ 1 day) at visible wavelengths, faster than those seen in other blazars, and have high polarisation ($\gtrsim$ 3%-4% as opposed to $\sim$1% in other AGN) which varies both in magnitude and in position angle. In OVVs, the spectrum observed tends to show broad emission lines except when the continuum is at its brightest, where the emission-line equivalent widths become small as the line flux changes very little while the continuum flux increases dramatically. The redshifts of OVVs are generally larger than those of BL Lacs, with $z \gtrsim 0.5$ (Peterson, 1997). FSRQs show strong and broad optical emission lines and have higher total bolometric luminosities than BL Lacs, exhibiting signs of thermal activity in their optical through to ultraviolet spectra (Sambruna, 1997). All known blazars are radio-loud and have highly variable radio emission, while the overall emission of the object is dominated by the core.

The spectral energy distributions (SEDs) of blazars show two peaks, one at lower energy, attributed to synchrotron emission, and the other at higher energy, likely due to Comptonisation of the synchrotron photons. Additionally, most blazar SEDs show an absence of characteristic features seen in thermal emission from other AGN, such as a local minimum around 1 μm which is thought to represent the minimum between a hot thermal spectrum and a cool thermal spectrum due to emission by warm ($T \lesssim 2000$ K) dust grains, which precludes a thermal origin for the continuum. Further evidence that the emission is nonthermal comes from the magnitude of continuum variations and polarisation of emission from the blazar (Peterson, 1997).

BL Lac objects can be further classified into three subtypes based on their SED: low-frequency peaked, intermediate-frequency peaked and high-frequency peaked BL Lacs (LBL, IBL and HBL respectively). In all three subtypes, the shape of the SEDs are approximately the same, but the position of the peaks changes, as shown in Figure 3.4. For LBLs, the lower-frequency peak is observed in the infrared or the optical, and in HBLs it is observed in the ultraviolet through to the hard X-ray band; IBLs are those sources that have their lower-frequency peak in the crossover region between HBLs and LBLs (Tang et al., 2010). The lower-frequency peaks in FSRQs are generally observed at radio frequencies (Tang et al., 2010).

As you move from FSRQs through to HBLs, the ratio of the γ-ray flux to the low-frequency flux increases. The variability of some HBLs in X-rays displays spectral hysteresis in hardness-intensity diagrams, such as those shown in Zhang (2002), which can be interpreted as the synchrotron signature of gradual injection or acceleration of ultrarelativistic electrons in the emitting region, with subsequent radiative cooling (Böttcher and Chiang, 2002). Spectral hysteresis has been clearly observed only in HBLs (Böttcher, 2007), although it should occur in the soft X-ray part of the spectrum of LBLs if their synchrotron component extends into the soft X-ray regime.

Although blazars are believed to be relatively rare in the Universe, at energies $>$ 100 MeV and

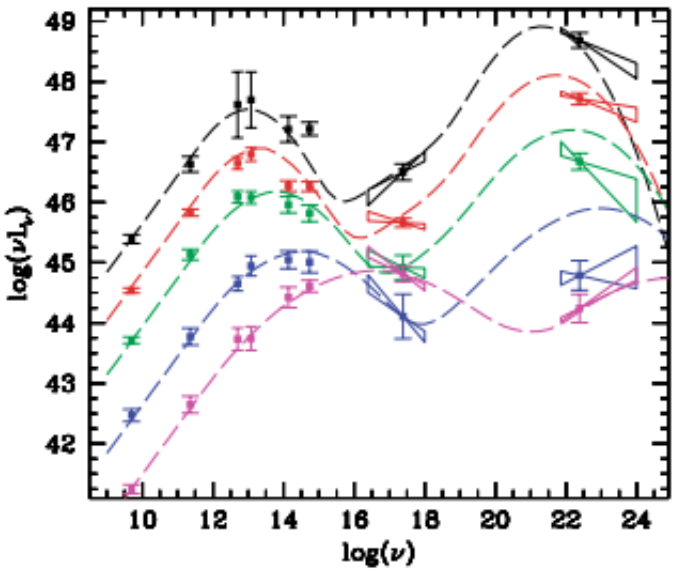

Figure 3.4: The average overall SEDs of blazars studied in Fossati et al. (1998), that have been separated according to radio luminosity. Empty bow ties represent uncertainties in the spectral shapes in the X-ray and γ-ray bands. The dashed curves are analytic approximations that assume that luminosity of the second peak is proportional to the radio luminosity and that the ratio of the two peak frequencies is constant. As they are separated by radio luminosity the different curves represent different points in the blazar sequence, with the black curve represents LBLs and the fuschia curve represents HBLs, with those in between showing transitional objects. The low frequency peak in the SEDs is due to synchrotron radiation and is anticorrelated with the source luminosity, moving from the ultraviolet or X-ray regime ($\sim 10^{16}$-10^{17} Hz) for less luminous sources to the infrared ($\sim 10^{13}$-10^{14} Hz) for the most luminous ones. The higher frequency peak, possibly Compton emission, of the SEDs is similarly anticorrelated with luminosity and is found at $\sim 10^{24}$-$\sim 10^{25}$ Hz for less luminous sources and $\sim 10^{21}$-$\sim 10^{22}$ Hz for the most luminous ones. Adapted from Fossati et al. (1998) by Ghisellini et al. (2004).

in VHE γ-rays they are the most numerous of extragalactic sources. In most cases, the high-energy luminosity of a blazar tends to dominate the power output of the source. At energies > 100 MeV, most of the detected extragalactic sources are FSRQs, while at VHE, BL Lac objects are more numerous. One interpretation of the different classes of blazars is known as the blazar sequence, in which it is postulated that there is an evolutionary process from FSRQs to LBLs to IBLs and finally to HBLs (Beckmann et al., 2003). If the blazar sequence, as postulated, is a real effect then it can be readily explained by the models discussed below; however, it is not predicted by them.

To date ~ 50 blazars have been detected in VHE γ-rays; of these 39 are HBLs, 7 are IBLs, 1 is an LBL and 3 are FSRQs, (see Table 3.2). As at all other wavelengths, the TeV emission from such sources is highly variable, often on timescales of days or less. Until the middle of the last decade, the only blazars detected at energies >100 GeV were those with fairly hard spectra and in a high state; however, observations with the current generation of IACTs have made it possible to detect many more blazars, allowing a more wide-ranging study of blazars as a category of TeV-emitting object, with much smaller selection bias to be carried out by Wagner (2008). This synoptic study of 17 TeV blazars was carried out in an attempt to find common properties shared by the blazars that had been detected at very high energies. It was found that there was no correlation between the inferred black hole masses of the TeV blazars and their redshifts, and that none of them had inferred black hole masses of $\lesssim 10^8$ $M_\odot$, whereas AGN in general have been found with black hole masses as low as $\sim 10^6$ $M_\odot$. This raises the question of whether there is a physical reason for the lack of TeV blazars with relatively small black hole masses. Some studies have shown a similar connection between radio loudness and black hole mass, suggesting that radio loudness occurs only above some threshold mass (Laor, 2000; Metcalf & Magliocchetti, 2006).

Emission models for blazars can be separated into those that suggest that the observed emission is due to leptonic interactions and those that assume that the emission has a hadronic origin. In some hadronic models, such as that of Tang, Dai & Zheng (2010), protons are assumed to accumulate in the source and then produce electron-positron pairs through interactions with the ambient photon field and with each other. The pairs produced then emit high-energy photons through synchrotron emission (as discussed in Section 1.2.1), and inverse-Compton scattering (Section 1.2.3). Some of these high-energy photons escape the source, while others interact to produce more electron-positron pairs, which, generate more high-energy photons. This process is referred to as a proton-initiated cascade. Another hadronic model, that of Böttcher (2007), considers the situation where the kinetic power of the jet is large enough to accelerate protons to the threshold required for proton-photon pion production. In this case, synchrotron-supported pair cascades will form as the pions decay. Further hadronic models consider the possibility of synchrotron emission

Object	RA (J2000)	Dec (J2000)	Type	Redshift
PKS 1510-089	15h 12m 50.5s	-09° 06' 00"	FSRQ	z = 0.36
4C +21.35	12h 24m 54.4s	+21° 22' 46"	FSRQ	z = 0.432
3C279	12h 56m 11.1s	-05° 47' 22"	FSRQ	z = 0.5362
BL Lacertae	22h 02m 43.3s	+42° 16' 40"	IBL	z = 0.069
W Comae	12h 21m 31.7s	+28° 13' 59"	IBL	z = 0.102
S5 0716+714	07h 21m 53.4s	+71° 20' 36"	IBL	z = 0.31
3C66A	02h 22m 41.6s	+43° 02' 35.5"	IBL	z = 0.444
PKS 1424+240	14h 27m 00s	+23° 47' 40"	IBL	
MAGIC J2001+435	20h 01m 13.5s	+43° 53' 02.8"	IBL	
1ES 1440+122	14h 42m 48.3s	+12° 00' 40"	IBL	
VER J0521+211	05h 21m 55s	+21° 11' 24"	IBL	
AP Lib	15h 17m 41.8s	-24° 22' 19"	LBL	z = 0.049
IC 310	03h 16m 43.0s	+41° 19' 29"	HBL	z = 0.0189
Mrk 421	11h 04m 19s	+38° 11' 41"	HBL	z = 0.031
Mrk 501	16h 53m 52.2s	+39° 45' 37"	HBL	z = 0.034
1ES 2344+514	23h 47m 04.9s	+51° 42' 17"	HBL	z = 0.044
Mrk 180	11h 36m 26.4s	+70° 09' 27"	HBL	z = 0.045
1ES 1959+650	19h 59m 59.8s	+65° 08' 55"	HBL	z = 0.048
1ES 1727+502	17h 28m 18.6s	+50° 13' 10"	HBL	z = 0.055
PKS 0548-322	05h 50m 38.4s	-32° 16' 12.9"	HBL	z = 0.069
PKS 2005-489	20h 09m 27.0s	-48° 49' 52"	HBL	z = 0.071
RGB J0152+017	01h 52m 33.5s	+01° 46' 40.3"	HBL	z = 0.08
1ES 1741+196	17h 43m 57.8s	+19° 35' 09"	HBL	z = 0.083
SHBL J001355.9-185406	00h 13m 56.0s	-18° 54' 07"	HBL	z = 0.095
1ES 1312-423	13h 15m 03.4s	-42° 36' 50"	HBL	z = 0.105
PKS 2155-304	21h 58m 52.7s	-30° 13' 18"	HBL	z = 0.116
B3 2247+381	22h 50m 06.6s	+38° 25' 58"	HBL	z = 0.1187
RGB J0710+591	07h 10m 26.4s	59° 09' 00"	HBL	z = 0.125
H 1426+428	14h 28m 32.6s	+42° 40' 21"	HBL	z = 0.129
1ES 1215+303	12h 17m 52.1s	+30° 07' 01"	HBL	z = 0.13
1ES 0806+524	08h 09m 59s	+52° 19' 00"	HBL	z = 0.138
1ES 0229+200	02h 32m 53.2s	+20° 16' 21"	HBL	z = 0.14
1RXS J101015.9-311909	10h 10m 15.03s	-31° 18' 18.4"	HBL	z = 0.142639
H 2356-309	23h 59m 09.42s	-30° 37' 22.7"	HBL	z = 0.165
RX J0648.7+1516	06h 48m 45.6s	+15° 16' 12"	HBL	z = 0.179
1ES 1218+304	12h 21m 26.3s	+30° 11' 29"	HBL	z = 0.182
1ES 1101-232	11h 03m 36.5s	-23° 29' 45"	HBL	z = 0.186
1ES 0347-121	03h 49m 23.0s	-11° 58' 38"	HBL	z = 0.188
RBS 0413	03h 19m 47s	+18° 45' 42"	HBL	z = 0.19
PKS 0447-439	04h 49m 29.9s	-43° 50' 09"	HBL	z = 0.2
1ES 1011+496	10h 15m 04.1s	+49° 26' 01"	HBL	z = 0.212
1ES 0414+009	04h 16m 52.96s	+01° 05' 20.4"	HBL	z = 0.287
1ES 0502+675	05h 07m 56.2s	+67° 37' 24"	HBL	z = 0.341
1ES 0647+250	06h 50m 46.5s	+25° 03' 00"	HBL	z = 0.45
PG 1553+113	15h 55m 44.7s	+11° 11' 41"	HBL	z = 0.5
1ES 1440+122	14h 42m 48.3s	+12° 00' 40"	HBL	
RGB J0136+391	01h 36m 32.5s	+39° 06' 00"	HBL	
PKS 0301-243	03h 03m 26.5s	-24° 07' 11"	HBL	
KUV 00311-1938	00h 33m 34.2s	-19° 21' 33"	HBL	
HESS J1943+213	19h 43m 55s	+21° 18' 08"	HBL	
1ES 0033+595	00h 35m 52.63s	+59° 50' 04.56"	HBL	

Table 3.2: Table of currently detected TeV blazars taken from tevcat.uchicago.edu accessed on 20/12/2012, organised first by type and then by redshift.

from extremely high energy protons and from secondary muons and mesons. Both of these models require extremely strong magnetic fields of at least several tens of gauss.

If protons are not accelerated to sufficiently high energy to generate high-energy emission, then the source of the high-energy radiation will be dominated by ultrarelativistic electrons and electron-positron pairs. High-energy emission in this case is produced via inverse-Compton scattering of ambient photons off the ultrarelativistic electrons and electron-positron pairs (Böttcher, 2007). Potential photon fields could be provided by the synchrotron photons emitted by the ultrarelativistic electrons and electron-positron pairs in which case the process is referred to as synchrotron self-Compton (SSC), or by external photons, where the process is referred to as external Comptonisation (EC). In EC, the seed photons can originate in the accretion disc and enter the jet either directly or after being reprocessed by circumnuclear material, in which case they could be jet synchrotron emission reflected off clouds in the circumnuclear material or infrared photons emitted by the dust torus around the central engine. In leptonic models, it is important to consider particle injection and acceleration, in addition to subsequent radiative and adiabatic cooling, particle escape from the jet, and potential deceleration of the jet. Such models require large numbers of parameters to be estimated or calculated from observations of the source; many of the parameters used in modelling blazars can be constrained by the broadband spectrum. In most cases, however, it is not possible to constrain all of the parameters, and so over the past few years progress has been directed into using both spectral and variability data to model the emission of blazars more successfully (e.g., Böttcher & Reimer, 2004). Leptonic models have been used successfully to model SEDs of several blazars for which contemporaneous data across many wavebands were available and the results appear to suggest that FSRQs have a high EC contribution to the γ-ray spectrum, but that this lower for LBLs and lowest for HBLs (Böttcher, 2007). Most FSRQs can be successfully modelled by pure EC models (models in which the photons scattered to high-energies only originate from outside the jet) while HBLs are usually easier to model using pure SSC models. It has been found that modelling the observed spectra of HBLs requires higher average electron energies and lower magnetic fields than LBLs or FSRQs to provide the synchrotron photons to seed the inverse-Compton scattering in the jet (Böttcher, 2007).

In reality, it is unlikely that either of the two extremes, purely leptonic or purely hadronic origin for emission from blazars, is entirely correct, as a blazar jet is likely to contain large numbers of both hadrons and leptons at extremely high energy. What is more likely is that both types of process play a substantial part in emission of radiation from the jets of blazars (Böttcher, 2007). Observations of TeV flares without simultaneous X-ray flares (known as "orphan flares") in 1ES 1959+650 (Krawczynski et al., 2004) and in Mrk 421 (Błażejowski et al., 2005) may provide

support for the importance of hadronic processes in sources that are otherwise well reproduced by leptonic SSC models. Leptonic SSC models predict a close temporal flux correlation between the synchrotron and inverse-Compton components of the spectrum, so a lower-energy flare would be expected to occur close in time to a high-energy flare.

The synoptic study carried out by Wagner (2008), discussed earlier, also attempted to identify links between TeV emission and emission in the radio, optical and X-ray wavebands. In the case of objects such as Mrk 421 a clear link between TeV emission and X-ray emission was observed by a number of authors (e.g. Krawczynski et al., 2001); however, Albert et al. (2007c) found only a weak link in the case of Mrk 501, and for orphan flares such as that observed from 1ES 1959+650 no link was observed (Daniel et al., 2005) . In the synoptic study, it is argued that there is some correlation between the X-ray luminosities of the sources at 1 keV and their TeV luminosities. In the optical waveband a very weak correlation is noted between optical flux at 550 nm and TeV flux, but no correlation is observed at radio frequencies (5 GHz). This strongly suggests that flares in blazars can be caused by both leptonic and hadronic interactions.

In SSC models, the very high energy peak is identified with the inverse-Compton peak and resembles the form of the synchrotron peak, but displaced in frequency by $\sim \gamma^2$, where γ is the Lorentz factor of the electrons responsible for the emission. Wagner (2008) found a correlation between the position of the peak in the synchrotron spectrum and the photon index of the γ-ray spectrum, but no correlation was found between the former and the γ-ray luminosity of the source. It is generally believed that very high energy emission takes place at shock fronts inside the AGN jets, very close to the central black hole; if this is the case, the properties of the black hole should have an effect on the TeV γ-ray emission from the source. However, no correlation has been found between the mass of the central black hole and either the photon index or the luminosity of very high energy emission, but it is important to note that the measurements of the black hole masses have large uncertainties. The limited data currently available mean that it is impossible to determine whether there is a link between black hole spin, accretion rate or properties of the acceleration region and the very high energy properties of the TeV blazars. Additionally, it appears that there is no correlation between black hole mass and the LBL-HBL transition for the very high energy blazars studied (Wagner, 2008).

3.3.1 PKS 2155-304: The Archetypal TeV Blazar

PKS 2155-304 is one of the most highly-studied active galactic nucleus at very high energies and is an HBL at a redshift of $z = 0.117$ that can only be observed from the southern hemisphere; it is positioned at R.A. 21h 58m 52.7s, Dec. -30° 13' 18" (J2000). It was initially detected in X-rays

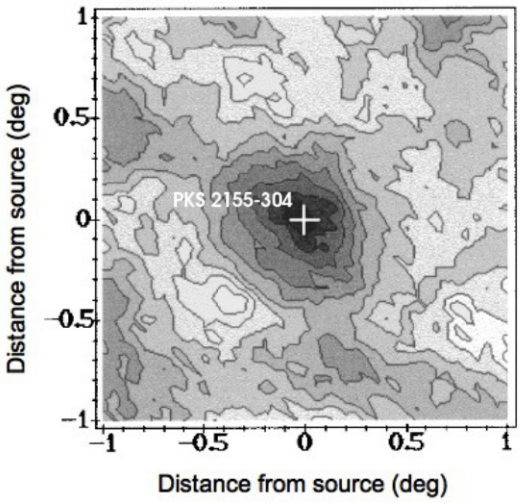

Figure 3.5: Initial detection of PKS 2155-304 in TeV γ-rays from Chadwick et al. (1999a). The grey scale is such that black corresponds to a detection significance of $> 6\sigma$. Contours are at 0.7σ intervals and the position of PKS 2155-304 is marked with a white cross.

by Griffiths et al. (1979) using the HEAO-1 X-Ray satellite and is one of the brightest objects in the sky at X-ray wavelengths. It is associated with a compact flat-spectrum radio source and its spectrum is essentially featureless from radio through to X-ray frequencies. Detection of γ-rays from PKS 2155-304 was first reported using the *EGRET* satellite (Vestrand et al., 1995). The broadband variability of the source is well documented and has been observed at all energies. The maximum power emitted by the source is between the ultraviolet and soft X-ray range, and it is the brightest BL Lac detected in the ultraviolet regime (Wandel & Urry, 1991).

The data collected by *EGRET* showed that in the energy range 30 MeV to 10 GeV PKS 2155-304 has a hard energy spectrum that follows a power law with photon index 1.71 ± 0.24 (Vestrand, Stacy & Sreekumar, 1995), which pointed to a high probability of it being a TeV γ-ray source and made it a prime target for IACTs. The first reported detection of PKS 2155-304 at very high energies (above 300 GeV) was made with the University of Durham Mark 6 Telescope in 1996 and 1997 (Chadwick et al., 1999a) (see Figure 3.5); attempts to detect it with the same telescope in 1998 failed, possibly due to the object being in a lower TeV γ-ray state, supported by evidence that it was in a lower X-ray state (Chadwick et al., 1999b). Observations with the CANGAROO telescopes were carried out in 1997, 1999, 2000 and 2001, but again no detection was made (Roberts et al., 1999; Nishijima et al., 2001; Nakase et al., 2003). The upper limits reported by CANGAROO in 1997 are consistent with the flux detected by the Durham Mark 6 in 1996-1997, and the lack of detection in subsequent years is consistent with the fact that emission from blazars is known to be highly variable.

H.E.S.S. observations of PKS 2155-304 began while the array was under construction in 2002, and so the observations of the object were taken with varying numbers of telescopes. The first observations in 2002 were taken with a single telescope, most of those taken in 2003 consist of observations made in a 2-telescope configuration, while from September 2003 to December 2003 a 3-telescope configuration was used. The final H.E.S.S. telescope was brought online in December 2003 after the end of the observation season for PKS 2155-304. Over the course of these early H.E.S.S. observations, PKS 2155-304 was strongly detected in all dark periods during which it was observed, except in November 2002 when the total exposure time was less than one hour; the total significance of the detection was 44.9σ (Aharonian et al., 2005a). PKS 2155-304 is the brightest blazar detected by the H.E.S.S. telescopes at TeV energies and has a very high energy flux which is typically $\sim 15\%$ that of the Crab Nebula flux above 200 GeV.

During July 2006, the average very high energy γ-ray flux detected from PKS 2155-304 was more than 10 times its typical value. In particular , a very bright flare was observed in the early hours (starting around midnight UTC) of July 28th 2006. During the flare, the TeV flux was observed to vary on timescales $\sim$3 minutes (Aharonian et al., 2007). This has important implications for the size of the emission region within PKS 2155-304. Causality arguments imply that γ-ray variabilty of a source, on a timescale t_{var}, is related to the radius of the emission region, R, and the Doppler factor, δ, by $R \leq ct_{var}\delta/(1+z)$. The observed variability of the source therefore limits the size of the emission region to $R\delta^{-1} \leq 4.65 \times 10^{12}$ cm ≤ 0.31 AU. The variability at very high energies observed during the flare in July 2006 is the fastest ever observed from a blazar, $\sim$5 times as fast as that previously measured from Mrk 421 (Gaidos et al., 1996) and $\sim$6-12 times more constraining for the light crossing time than the results from Mrk 421. Unfortunately, this flare occurred before already triggered but not yet started X-ray observations which began the night after, leaving this flare without multiwavelength coverage (Aharonian et al., 2009c).

Two days after the first major γ-ray flare from PKS2155-304 observed by H.E.S.S., a second large flare was detected on the night of July 29th-30th 2006 (Aharonian et al., 2009c). This occurred in coincidence with the planned Chandra-H.E.S.S. target-of-opportunity program, with further coverage in the optical band by the Bronberg Observatory in South Africa and some data provided by snapshot observations of around a few ks taken with RXTE and the *Swift* satellite. As can be seen in Figure 3.6, this outburst reached fluxes of $\sim$ 11 times that seen from the Crab Nebula, and as a result it was possible to carry out an extremely sensitive X-ray/TeV comparison during one of the brightest states ever observed from an HBL. During the flare very high energy flux variations of more than an order of magnitude were accompanied by smaller changes in the flux in X-rays, which varied by a factor $\sim$2, and optical flux variations of less than 15%. On subhour and

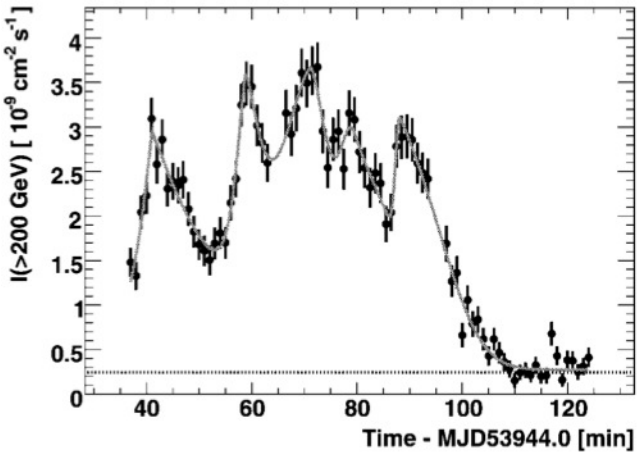

Figure 3.6: Integral flux above 200 GeV observed from PKS 2155-304 on the night of 29th-30th July, 2006 against time with data binned in 1-minute intervals, clearly showing rapid variability of the object. The dotted horizontal line represents the flux above 200 GeV from the Crab Nebula. From Aharonian et al. (2007).

longer timescales, the X-ray and γ-ray variations correlate strongly, although there is no evidence of a time lag between the two; on very short timescales of a few minutes or less the behaviour appears more complex. The optical flux began increasing simultaneously with the γ-ray flare but varied on a much longer timescale, showing no correlation with the flare at other wavelengths and reaching a plateau $\sim$2 hours later than the very high energy peak flux. During the flare, the spectral evolution of the VHE γ-ray spectrum and the X-ray spectrum are correlated although, as with the changes in flux, the amplitude of the variations in photon index was far greater at very high energies. Despite the changes in luminosity, the positions of the peaks in the SED do not change significantly, but the ratio between the Compton luminosity and the synchrotron luminosity increases dramatically from the usual values of $\lesssim 1$ to $\gtrsim 8$.

The correlation between X-ray flux and VHE γ-ray flux would appear to lend support to a simple SSC model. However, the TeV flux decreases as the cube of the X-ray flux, a relation which holds both during the overall decaying phase and when considering shorter intervals separately, which cannot be easily accounted for with a simple, one-zone SSC model. This indicates that a single particle population cannot be responsible for both peaks in the SED during the flare. Aharonian et al. (2009c) interpret the data as the emergence of a new Compton-dominated component in the SED, with a synchrotron luminosity that is too small to be detected against the "persistent" synchrotron emission from PKS 2155-304. If a pure SSC model is used then the data suggest that the emitting region of this new component must be extremely compact (of the order of a few times r_s, the Schwarzschild radius[1] of the central black hole) otherwise it must be EC dominated, as

[1]The radius around a body, mass M, such that the escape velocity is equal to the speed of light, calculated using

would be expected in models with a strong interplay between different parts of the jet. The data collected across all wavebands have helped to provide an important testbed for modelling PKS 2155-304 and other blazars. As similar emission mechanisms are likely to dominate in misaligned blazars as well, in-depth study of objects such as PKS 2155-304 can be used to help further the development of models to explain the emission from radio galaxies such as M87.

3.4 Radio Galaxies at TeV Energies

Of the extragalactic TeV γ-ray sources detected, all except five are blazars, as discussed in Section 3.3. Of the five non-blazar sources detected, two are starburst galaxies, NGC 253 and M82, and are not relevant to this work; however, the other three are radio galaxies: M87 (Aharonian et al., 2006d), Centaurus A (Aharonian et al., 2009b) and the recently detected NGC 1275 (Aleksić et al., 2012c). These will be discussed in further detail in the following sections with greatest emphasis placed upon M87 and Centaurus A, as only limited work has so far been carried out on NGC 1275 at very high energies. In the case of blazars, the TeV emission from the object is strongly Doppler-boosted to higher energies as the line of sight points down the jet; however, due to the greater angle to the line of sight seen in radio galaxies any Doppler boosting must be relatively minimal. Assuming that the unified model of AGN is valid, the detection of VHE emission from misaligned objects such as M87 and Cen A raises a number of important questions about the mechanism behind such emission in all AGN (Aharonian, 2006d). It is impossible to detect the site of TeV emission in radio galaxies directly even though the base of the jet is visible, as the spatial resolution of Cherenkov telescopes is relatively limited; however, a number of variability studies have enabled limits to be placed on the size of the emission region in M87 by studying the variability timescales during flares in 2008 (Tavecchio & Ghisellini, 2009) and more recently in 2010 (Abramowski et al, 2011). As more data become available for TeV radio galaxies, it should be possible to impose stronger constraints on the emission mechanisms involved.

3.4.1 M87

M87 is a giant elliptical galaxy located at the centre of the Virgo cluster, at a distance of 16.7 Mpc away. Spectroscopy carried out with the *Hubble Space Telescope* gives strong evidence for a rapidly rotating, ionised gas disc orbiting a massive black hole at the centre (Ford et al., 1994; Harms et al., 1994). The black hole at the centre is estimated to have a mass of $3.2(\pm 0.9) \times 10^9$ $M_\odot$ (Macchetto et al., 1997). Emanating from the core is a one-sided relativistic jet at an angle of

$r_s = 2GM/c^2$.

between 20° and 40° to the line of sight. This was the first extragalactic jet ever discovered and was initially reported by Curtis (1918). An optical image taken with the *Hubble Space Telescope* showing the jet can be seen in Figure 3.7. The power of the relativistic jet is estimated to be as high as 10^{44} ergs s^{-1} (Owen et al., 2000). M87 has been observed at all wavelengths ranging from radio through to very high energy γ-rays, and the jet has been observed from radio through to X-rays. The proximity and jet angle of M87 mean that the jet can be resolved at radio, optical and X-ray wavelengths and a similar morphology is displayed at each wavelength, suggesting a common origin for the emission. The non-thermal emission from the jet is almost certainly synchrotron in nature, as radio and optical emission are polarised and the X-ray spectrum is steeper than the radio spectrum (Le Bohec et al., 2004). Within the context of blazar unification models, it is believed that M87 can be considered a BL Lac type object viewed at a higher inclination angle, although the specific BL Lac classification (LBL, IBL or HBL) is currently unknown (Le Bohec et al., 2004). The detection of the source at γ-ray energies does, however, lend support to the argument that it is a misaligned HBL.

Observations made with the Hubble Space Telescope between 1994 and 1998 studied the motions of 12 features within the first 500 pc from the core of the jet of M87 (Biretta et al., 1999). This study detected apparent superluminal motion in ten of the observed features, eight of which have apparent velocities ranging from $4c$ to $6c$; the two observed to have subluminal velocities were those closest to the base of the jet. These findings would appear to be challenged by data reported by Ly et al. (2007), collected using the Very Long Baseline Array (VLBA); these data suggested that jet components detected by the array were moving at velocities between $0.25c$ and $0.4c$, although it is noted within the paper that this could be due to misidentification of the components and that such values should be treated as lower limits for the velocity. The same observations also confirmed the existence of a radio counterjet which appears to move away from the core (Ly et al., 2004). As radio observations in the late 1980s failed to detect the counterjet (Biretta et al., 1989; Reid et al., 1989), it is suggested that the counterjet is variable, partly due to its outward motion. In optical studies carried out by Sparks et al. (1992) and Stiavelli et al. (1992), a bright hotspot was observed 24" away from the core. Sparks et al. (1992) detected optical emission coming from a site almost exactly opposite the jet, at an angle of $182° \pm 1°$. This emission had a polarisation of 30% and was theorised to be synchrotron radiation from continuously accelerating electrons at the site of the emission. The authors argue that this is likely due to an optical counterjet in M87 and that the asymmetry between the jet and counterjet is probably due to interaction between the counterjet and the interstellar medium. The arguments put forward are supported by the data from Stiavelli et al (1992).

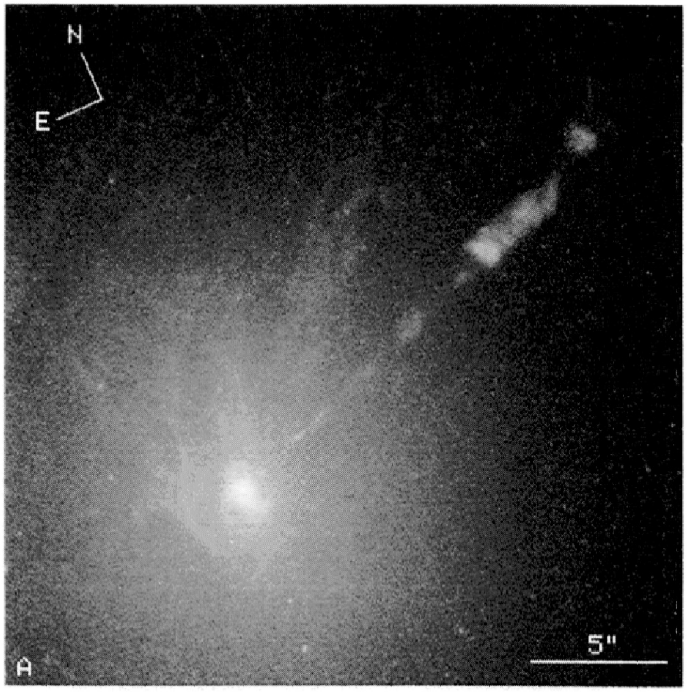

Figure 3.7: Image of M87 taken with the *Hubble Space Telescope*. The jet originates from the centre of a disc-like structure with a semimajor axis of ∼1". Taken from Ford et al. (1994)

On parsec scales, the jet is quite narrow and has an opening angle with full-width-quarter-maximum of $\phi \approx 9°$, comparable with that measured on kiloparsec scales where the full-width-quarter-maximum is $\phi \approx 6°$ (Biretta & Junor, 1995). The brightness of the jet at 18 cm radio wavelengths decreases smoothly with distance from the core, although there are a number of prominent features, or knots, that stand out above this smooth emission. Within the jet, narrow elongated structures, or filaments, that can be traced along much of the parsec-scale jet were also observed. From parsec scales out to kiloparsec scales, the jet is highly collimated and shows limb-brightening along one or both edges of the jet. The brightness centroid of the jet appears to fluctuate from side to side depending on the position within the jet. It is suggested that this and the narrow elongated structures could be interpreted as helical filaments within the jet or wrapped around its surface. The collimation of the jet appears likely to occur on scales of > 0.1 pc which corresponds to $\approx 300 r_s$ from the central black hole, suggesting that the initial collimation is provided by electromagnetic processes associated with the black hole and accretion disc. At scales of < 0.1 pc, the opening angle observed is $\sim 60°$ (Junor et al., 1999) and is seen to get progressively larger closer to the core of M87. Results from Walker et al. (2008), with a resolution ~ 0.02 pc, suggest that the inner part of the jet of M87 is a fast-moving and rapidly evolving structure. Components observed within the subparsec-scale jet have been detected with apparent velocities near $2c$, which contrasts with the value of $0.07c$ within the first 1.6 pc of the jet (Kovalev

et al., 2007); however, this is probably because the observations used in the earlier work were not sensitive enough to the faster motions due to undersampling. The disparity in measured velocities between these studies could also be due to some components being density enhancements or other structures moving with the jet, while others are shocks or instabilities through which the jet travels, that have their own intrinsic, lower velocity. Interestingly, the value of $2c$ found by Walker et al. (2008) is far lower than the velocities of up to $6c$ reported for the jet on larger scales as discussed earlier (Biretta et al., 1999).

It has been proposed that the observed large opening angle of the jet may be due to the core of M87 not being associated with the brightest part of the jet and that the core may be offset from this region by up to ∼2 mas (Ly, Walker & Junor, 2007). If this were the case, the actual opening angle of the jet would be $\approx 15°$, and the counterjet would then be part of the inner jet of the galaxy; however, the observed motion would appear to indicate that it is travelling in the wrong direction. This hypothesis has been supported by results published by Batcheldor et al. (2010) using data collected by the *Hubble Space Telescope*. It is reported that the supermassive black hole in M87 is displaced by a projected distance of 6.8 ± 0.8 pc in the direction of the counterjet. It is concluded that the most likely causes of this displacement may be a moderate (a few hundred km s^{-1}) kick that occurred $\sim$ 1 Myr ago (which would explain the alignment of the jet axis and the disturbed nature of the nuclear gas disc) or supermassive black hole oscillations following a kick that occurred $\lesssim$ 1 Gyr ago. A less likely possibility is that the displacement is caused by jet acceleration, but this requires that the jet age be $\gg$ 1 Myr and that the restoring force of the galaxy be small.

Biretta et al. (1999) also reported detecting a region, appearing as a linear chain of compact components, extending along the jet of M87 at a distance of $\sim$ 80 pc from the nucleus. As these results were based on data from the *Hubble Space Telescope*, they designated the feature HST-1. HST-1 was observed to have both slow-and fast-moving features, some moving with apparent superluminal motion of velocities up to $6c$. It also showed the birth of new components and the fading of older ones. Since then, further study has shown HST-1 to be active in radio, optical and X-ray regimes (Chang et al., 2010), and it is now identified as a knot in the jet of M87. An X-ray view of M87 showing HST-1 taken the *Chandra X-ray Observatory* can be seen in Figure 3.8. Observations of HST-1 with the *Chandra X-ray Observatory* (Harris et al., 2006) show X-ray variability on timescales of approximately one month. During the observations, the feature was observed to undergo an X-ray outburst in which the X-ray luminosity increased by a factor of 50. During this flare variability was also detected in the ultraviolet and radio, suggesting that the input spectrum of reativistic particles did not change its shape, only its amplitude. Using radio data

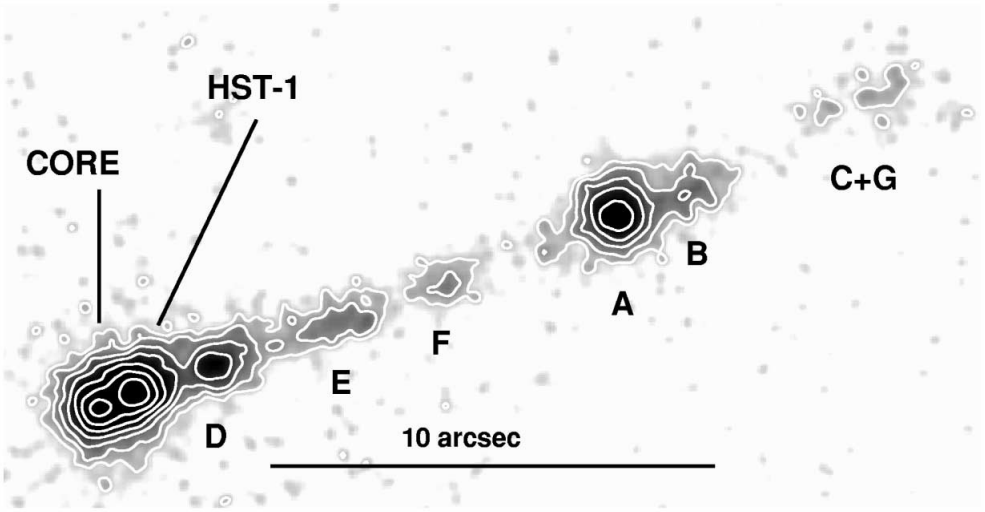

Figure 3.8: Image of M87 taken in the 0.2-6 keV band with the *Chandra X-ray Observatory*, using data taken in July 2000 and during 2002, showing the many knots in the jet and HST-1 close to the nucleus. The contours increase by a factor of two in brightness with darker regions signifying higher brightness; the lightest areas display a flux of 1×10^{-16} ergs cm^{-2} s^{-1} pixel^{-1}. Taken from Harris et al. (2003).

from the VLBA collected in 2005 and 2006, Cheung et al. (2007) confirmed apparent velocities of 4.3c inside HST-1 and used this to constrain the angle of the jet at this location to 26° ± 4°. Using these data, the authors were able to determine that HST-1 must be $\gtrsim$ 120 pc from the core of M87 rather than the 80pc as initially determined by Biretta et al. (1999), much farther than had previously been thought for the formation of such knots in a relativistic jet source.

The nature of HST-1 is currently unknown; however, it has been suggested by Stawarz et al. (2006a) that it could be a reconfinement shock within the jet of M87. They suggest that, although the inner part of the jet within an AGN may be dominated by the electromagnetic jet flux in the case that the initial collimation is due to a dynamic magnetic field (Gracia et al., 2005), at greater distances this must be converted to a dominant particle flux as large-scale jets appear to be primarily particle-dominated (Sikora et al., 2005). Stawarz et al. (2006a) speculate that at sufficiently large distances from the nucleus, the radio jet of M87 is already particle-dominated and starts to expand freely. As the jet expands, this causes a rapid decrease in the thermal pressure with distance, r, from the core. In cold (nonrelativistic) jet matter with a ratio of specific heats (ratio of the heat capacity of the jet matter at constant pressure to its heat capacity at constant volume) of 5/3 (as in classical hydrodynamics) the pressure varies as $r^{-10/3}$ (Sanders, 1983). The ambient gas pressure, however, decreases at a much slower rate with respect to distance from the nucleus, varying as $r^{-0.6}$ for $r < 235$ pc. This, combined with the results found in Komissarov & Falle (1997), implies that the initially free jet of M87 will become reconfined at a point upstream

where it is suggested that the jet will develop a reconfinement shock at its boundary. This will lead to limb-brightening of the reconfining outflow. The distance from the core at which the whole jet will reach equilibrium with the surrounding medium is designated r_{cr} and occurs at the point where the converging reconfinement shock reaches the jet axis. If it is assumed that the jet in M87 is ultrarelativistic at the reconfinement shock then HST-1 is found to be coincident with the position calculated for r_{cr} (see Appendix A of Stawarz et al., 2006a). Using this model and assuming an ultrarelativistic jet, Stawarz et al. (2006a) find that the kinetic power of the jet, L_j, is related to the viewing angle, θ, the ambient gas pressure, $p_G(r)$, and the break radius, r_B (the radius at which the brightness profile of the galaxy ceases to obey a power law). For M87, $r_B \approx 0.3$ arcsec and the authors assume that the ambient gas pressure profile follows $p_G(r) \propto r^{-0.6}$ with $p_0 = 1.5 \times 10^{-10}$ pa. This relation is given in Appendix A of Stawarz et al. (2006a) and is:

$$L_j \sim 3c\pi p_0 r_B^{0.6} r_{cr}^{1.4} \sim 0.4 \times 10^{44} (\sin\theta)^{-1.4} \text{ erg s}^{-1} \tag{3.1}$$

Using equation 3.1 and an assumed inclination angle of $\theta = 20°$, the implied luminosity is $L_j \approx 10^{44}$ erg s^{-1}, which is consistent with the jet power (of $\sim$ a few $\times 10^{44}$) estimated in Owen et al. (2000) and greater than the $\sim 10^{42}$erg s^{-1} required to power the radio lobes (Bicknell & Begelman, 1996). The total luminosity, from radio to X-ray wavelengths, of the jet in M87 is calculated to be $\sim 3.7 \times 10^{42}$ erg s^{-1}, giving an efficiency of approximately 1% for the source (Owen et al., 2000). This is consistent with the currently held view that radio galaxies are low-efficiency radiators. In the case of a *cold* jet, the total kinetic power of the jet is calculated to be an order of magnitude lower. Previous studies of reconfinement shocks propose that they are found at much greater distances from the central engine, coincident with the brightest knots $\sim$ 1 kpc from the active nucleus (Laing & Bridle, 2002). For M87, this would place a reconfinement shock at knot A (Wilson & Falle, 1985), which is entirely feasible if the jet breaks free again after the HST-1 complex and reconfines at a later point; however, in Bicknell & Begelman (1996), the knots beyond HST-1 are adequately described as oblique shocks formed by helical modes of Kelvin-Helmholtz instabilities, characterised by a growing amplitude along the jet and finally disrupting the outflow at knot C.

The first indication of very high energy γ-ray emission from M87 was reported by the HEGRA Collaboration using 83.4 hours of data collected during 1998 and 1999 (Aharonian et al., 2003). The detection was marginal, with a significance of only 4.1 σ above the background, and as only a limited number of excess events were detected, the origin of the detected TeV γ-rays could not be determined with any confidence. Later attempts by the Whipple Collaboration between 2000

and 2003 failed to detect any γ-ray excess in 39 hours of observations (Le Bohec et al., 2004). Confirmation that M87 does emit at very high energies was eventually found by the H.E.S.S. Collaboration (Aharonian et al., 2006d). The study used data collected by the H.E.S.S. telescopes between 2003 and 2006, yielding a total of 89 hours of data and a significance of 13σ above the background. The detection of M87 at TeV energies was the first confirmation of very high energy γ-ray emission from an AGN other than a blazar. Aharonian et al. (2006d) found the luminosity of M87 in VHE γ-rays to be relatively modest, at $L_\gamma \approx 3 \times 10^{40}$ erg s^{-1}. The position of the detected excess is nominally coincident with the nucleus of M87 and it is consistent with a point-like object; however, the angular resolution of the H.E.S.S. telescopes makes it impossible to positively identify the nucleus as the source of the emission, and the upper limit for a Gaussian surface brightness profile of 3' (99.9% confidence level) corresponds to a radial distance of 14 kpc at M87 (Beilicke et al., 2008), about two orders of magnitude larger than the core-HST1 separation. The upper limit on the angular size of the TeV γ-ray emission region does, however, exclude the core of the Virgo cluster of galaxies and the outer radio regions of the jet as possible sources. The energy spectra of M87 measured in both 2004 and 2005 are well fitted by power-law functions, with photon indices of $\Gamma = 2.62 \pm 0.35$ and $\Gamma = 2.22 \pm 0.15$, respectively (Aharonian et al., 2006d).

The data collected by the H.E.S.S. telescopes showed variability from M87 on timescales of $\sim$ 1 day with a significance of 4 σ, faster than the variability seen in the source at any other wavelength. This rapid variability allows the size of the emission region to be constrained to $R \leq c\Delta t\delta \approx 5\delta R_s \approx 0.022\delta$ pc, where δ is the relativistic Doppler factor of the source of the γ-ray emission and R_s is the Schwarzshchild radius of the supermassive black hole in M87 ($R_s \approx 10^{15}$ cm). More recent observations with VERITAS during a flare period of M87 in 2010 showed doubling times for the VHE flux of $\tau_d^{\rm rise} = 1.69 \pm 0.30$ days while the flux was increasing and $\tau_d^{\rm decay} = 0.611 \pm 0.080$ days while it was decaying. This is the first detection of a significantly asymmetric VHE flare profile from M87 and the most rapid variability observed from it to date, with the decay timescale leading to an upper bound on the size of the emission region of ≈ 0.0005 pc (Abramowski et al., 2012c). For reasonable values for the Doppler factor ($1 < \delta < 50$), a number of possible areas and mechanisms for TeV emission can be excluded. The regions excluded include the most likely candidate for efficient particle acceleration, the entire extended kiloparsec-scale jet. Although knot A, (the brightest knot in the jet) is compatible with the position of the very high energy γ-ray source, the size of the knot, $\sim$ 80 pc (Perlman & Wilson, 2005), would appear to exclude it as the source of the TeV emission. The possibility that the emission is due to cosmic ray interaction with matter in M87 or to dark matter annihilation can be excluded. This leaves two sites as possible sources for the very high energy emission from M87: the core or the knot HST-1.

Current theories posit that the most likely source of very high energy emission within M87 is close to the core of the galaxy, where the restrictions on the size of the emission region placed by the observed rapid variability can easily be met. In TeV blazars, the very high energy γ-ray emission is believed to be Doppler-boosted to higher energies as the material within the jet is moving at relativistic velocities almost directly towards the observer; in M87, however, the jet is at an angle of $\sim 30^{\circ}$ to the line of sight, so any Doppler boosting will be modest at best. This poses some problems for understanding the nature of emission at TeV energies close to the core, although, due to the proximity of the source, both leptonic and hadronic models predict detectable TeV emission at these energies (Georganopoulos et al., 2005; Reimer et al., 2004). These models do not fully account for the observed emission as they generally predict a soft energy spectrum, which contradicts the hard spectrum measured by H.E.S.S. and Veritas, but both leptonic and hadronic models can be adapted in ways that successfully model the behaviour of M87. It is therefore difficult to determine the most likely emission method, even if the assumption is made that the VHE γ-ray flux emanates from close to the black hole. In leptonic models, the jet is assumed to have additional structure. One such model argues that it may be sensible to consider that in the jet-formation zone the jet is dominated by a number of relativistic blobs of plasma, with different Doppler factors and moving in different directions with respect to the line of sight (Lenain et al., 2008). If this assumption is made, it is possible to produce a spectrum for M87 that agrees with observations, although this requires a large number of variables that are difficult to constrain with current data. Two possible mechanisms for emission via hadronic interactions are synchrotron emission by ultrahigh-energy protons, which requires that the jet be able to accelerate protons up to energies as high as 10^{20} eV, and curvature radiation from similarly energetic protons in the immediate vicinity of the supermassive black hole. In the case of curvature radiation, assuming that the black hole in the centre of M87 is rapidly rotating, protons could be accelerated up to energies of 10^{20} eV by the electric field generated by rotation of the black hole in the magnetic field supported by the accretion disc (Levinson, 2000; Boldt & Loewenstein, 2000). The main weakness with the curvature radiation model is that it requires the horizon threading magnetic field to be $\sim 10^4$ G, which is orders of magnitude larger than the field expected from the accretion process given the low accretion rate predicted from the bolometric luminosity of the core. A further possiblilty for the origin of TeV γ-ray emission from M87 is disc-dominated external inverse-Compton (EIC) radiation (Cui et al., 2012); the model presented suggests that the soft radiation, which is upscattered to TeV energies, originates in the accretion disc rather than within the jet as with SSC models, leading to lower $\gamma\gamma$ absorption. In this case, the low $\gamma\gamma$ absorption leads to the EIC spectra inheriting the original power-law index of the very high energy electrons in the jet. In such an EIC model, no

correlation is expected with infrared-ultraviolet emission during a TeV flare, but unfortunately no data are currently available to allow this prediction to be tested. Currently available data cannot discount this model, but neither do they provide additional support over other models (Cui et al., 2012).

Initially, it was thought unlikely that the TeV emission from M87 originated in the HST-1 knot, as the size of the region has been estimated at between 0.1 pc and 1 pc (Stawarz et al., 2006a; Harris et al., 2006), which is too large for any reasonable Doppler factor. However, data collected by the VLBA show compact knots within HST-1 that are essentially unresolved and therefore have semiminor axes of < 0.15 pc, implying that they can approach the size limits imposed by the observed variability of the TeV emission region (Cheung et al., 2007). The maximum flux for TeV emission coincides with the peak of the radio-X-ray activity observed in HST-1 and the luminosities are comparable, suggesting a possible link between the two flares. Additional support is lent by similarities in the spectra of very high energy emission, which is described by a power law of index $\Gamma_\gamma = 1.2 \pm 0.15$, and optical emission, described by a power law of index $\Gamma_\mathrm{o} = 0.99 \pm 0.03$. More recent joint observations; however, carried out by the H.E.S.S., VERITAS and MAGIC Collaborations during which M87 was also observed by the Very Long Baseline Interferometer (VLBI) and the *Chandra X-ray observatory*, detected a very high energy γ-ray flare from M87 which coincided with low X-ray flux from HST-1, but increased X-ray activity in the core unlike the previous flare observed in 2005 (Wagner et al., 2009). The information gathered from these two flares presents different conclusions as to the likely source of origin for the VHE emission leaving the actual location of the emission region open to debate.

The most recent flare from M87 observed in VHE γ-rays in 2010 initially by Veritas (Aliu et al., 2012b) triggered further VHE observations with both MAGIC and H.E.S.S., X-ray observations with the *Chandra X-ray Observatory* and radio observations by the VLBA (Abramowski, 2012c). This flare shared a similar peak flux and VHE spectrum with the previously observed flares but had an asymmetric flare profile and more rapid variability as previously discussed; while the large amount of data gathered allowed unprecedented sampling of the light curve. During the flare no increased radio flux from the innermost core regions was detected; however, the X-ray flux was observed to increase dramatically ~ 3 days after the VHE maximum. During this flare, no increased multiwavelength emission was observed from HST-1 suggesting, as with the 2008 flare, that it is unlikely to be associated with the increased activity. Despite this extra data, the precise location of VHE emission from M87 is still unknown; however, it is possible that the core provides the dominant emission as implied by the 2008 and 2010 flare events and that HST-1 only has a minimal effect on the VHE flux, unless it too is also undergoing a flare event as in 2005.

3.4.2 Centaurus A

At a distance of ≈ 3.8 Mpc, Centaurus A is the closest giant elliptical galaxy exhibiting activity in its nucleus (Israel, 1998). It is undergoing a late-stage merger with a small spiral galaxy. Radio observations of the galaxy show a complex morphology, consistent with that of a FRI galaxy and displaying extended diffuse emission. The core of Centaurus A is extremely bright and emerging from it are a subparsec-scale jet and a fainter counterjet, a one-sided kiloparsec jet and two radio lobes extending out to a distance of 250 kpc (Tingay et al., 1998; Tingay & Murphy, 2001; Horiuchi et al., 2006). The bright central source is not the nucleus itself, because at radio wavelengths the emission is absorbed via synchrotron self-absorption processes in a disc or torus of ionised gas (Jones et al., 1996; Tingay and Murphy, 2001). At a distance of around 5 kpc from the nucleus, the jets expand into plumes and the position angle of the radio features relative to the line of sight changes dramatically (Israel, 1998). Observations of the subparsec-scale jet indicate that Centaurus A is a non-blazar source with a jet inclination angle $\theta \gtrsim 50^\circ$ (Tingay et al., 1998), although Hardcastle et al. (2003) argue that the inclination angle could be as low as $\sim 15^\circ$. At the centre of the galaxy is a supermassive black hole with a mass inferred to be in the range $M_{\rm BH} \approx (0.5 - 1.2) \times 10^8 M_\odot$ corresponding to a Schwarzschild radius of $r_{\rm s} \approx (1.5 - 3.6) \times 10^{13}$ cm (Marconi et al., 2006; Häring-Neumayer et al., 2006). A prominent feature of the galaxy are the dust lanes along its minor axis, composed of a large amount of gas and dust within a warped disc-like structure which is seen almost edge on. Between about 1 kpc and 7 kpc from the centre of the galaxy, there is an HI mass of $(10 \pm 3) \times 10^8 M_\odot$ (van Gorkom et al., 1990; Schiminovich et al., 1994; Israel, 1998). Orbiting the black hole is a compact accretion disc, not aligned with the principal axis of the galaxy but perpendicular to the parsec-scale jets (Israel, 1998). Variability at radio frequencies has been observed both from the nucleus of Centaurus A and within the inner jet structures; however, these variations do not appear connected as they do not occur in tandem. At 1.4 GHz, considerable variability is observed near the nucleus on timescales of $\sim$100 days or longer (Romero, Benaglia & Combi, 1997). As the centre of the galaxy is strongly self-absorbed, such large variability cannot originate from activity in the nucleus itself; this probably indicates instead the presence of shocks interacting with inhomogeneities in the subparsec-scale jet (Israel, 1998). Variability has also been observed at X-ray energies on timescales of $\sim$ a few days first in soft X-rays by Winkler & White (1975) and more recently in hard X-rays (Jourdain et al., 1993). The X-ray variability is most pronounced at ~ 8 MeV. At X-ray energies below 100 keV the spectral shape is independent of luminosity; however, at higher energies this is not the case (Steinle et al., 1998).

The SED of the nucleus of Centaurus A consists of two peaks, one at $\sim 10^{13}$ Hz and the other

at 0.1 MeV (Chiaberge, Capetti & Celotti, 2001; Meisenheimer et al., 2007). To date Centaurus A is the only non-blazar type AGN detected at both MeV (Steinle et al., 1998) and GeV energies (Sreekumar et al., 1999). The SED of Centaurus A below 1 GeV has been successfully modelled using a simple jet SSC framework (Chiaberge, Capetti & Celotti, 2001), assuming that the object is a misaligned blazar. At X-ray energies observations between 2 keV and 7 keV made with the *Chandra X-ray Observatory* and *XMM-Newton* suggest that the X-ray continuum spectrum from the nucleus may be composed of both a disc component and a jet component, consistent with a hybrid disc configuration where the inner accretion disc is advection-dominated and becomes a standard geometrically thin, but optically thick, disc moving in Keplerian motion at some distance r_l from the black hole (Evans et al., 2004). This model is supported by the absence of the large ultraviolet bump expected in a more basic accretion disc model such as that proposed by Marconi et al. (2001). To date, the accretion rate of Centaurus A remains uncertain, with estimates varying by about an order of magnitude, from $\sim 10^{-4}\ \dot{m}_{\rm Edd}$ to $\sim 10^{-3}\ \dot{m}_{\rm Edd}$ (Rieger & Aharonian, 2009). Taking the measured nuclear X-ray luminosity as an upper limit to the contribution made by the advection-dominated part of the disc allows an upper limit of $\dot{m} \lesssim 0.004\ \dot{m}_{\rm Edd}$ to be derived for the accretion rate (Rieger & Aharonian, 2009).

A number of models proposed since the detection of M87 at TeV energies have predicted VHE emission from Centaurus A; these include models favouring jet-based emission mechanisms, such as that proposed by Lenain et al. (2008), and more exotic emission mechanisms that focus on the magnetosphere of the central supermassive black hole as proposed by Neronov & Aharonian (2007). The first hint of very high γ-ray emission from Centaurus A was reported by Grindlay et al. (1975) at a significance level of 4.5σ above background using data collected with the optical intensity interferometer operated by Sydney University between 1972 and 1974. During the observation period, Centaurus A was observed to be in a state of high X-ray flux; however, data collected in the late 1990s and early to mid 2000s by the CANGAROO telescopes and the H.E.S.S. Collaboration produced only upper limits, as discussed in Rowell et al. (1999), Kabuki et al. (2007) and Aharonian et al. (2005b). The first solid detection of Centaurus A was made by the H.E.S.S. Collaboration, using 120 hours of data collected between April 2004 and July 2008 (Aharonian et al., 2009b). The smoothed excess sky map in Figure 3.9 shows a clear excess at the position of Centaurus A, and the overall significance of the detection is 5σ.

Aharonian et al. (2009b) fitted the data with the point-spread function of the H.E.S.S. telescopes (as derived from Monte Carlo simulations) and found a best-fit position compatible with the radio core and inner kpc-scale jet region. The extension of the emitting region is found to have an upper limit of 0.2° at the 95% confidence level. The spectrum at $E > 250$ GeV is well

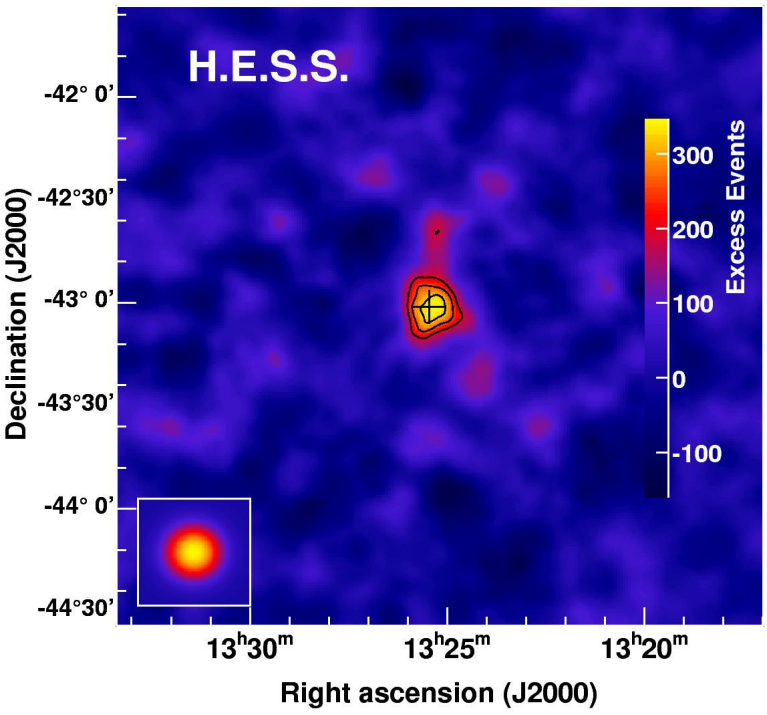

Figure 3.9: Smoothed excess sky map centered on the position of Centaurus A (marked with a cross). The contours correspond to significances of 3σ, 4σ and 5σ. The point-spread function of the H.E.S.S. telescopes is displayed in the bottom left-hand corner, the integration radius is 0.1225° and the data is smoothed using a radius of 0.02° to reduce the effect of statistical variations. Taken from Aharonian et al. (2009b).

fitted by a simple power law with a photon index of $\Gamma = 2.73 \pm 0.65$, although the relatively low statistics result in a large uncertainty. The apparent luminosity of the source at $E > 250$ GeV is $L \approx 2.6 \times 10^{39}$ erg s^{-1}, assuming a distance of 3.8 Mpc to the source; this is $\sim 0.8\%$ that of the Crab nebula at these energies. No variability has been detected, but, due to the low flux of the source, variability above a factor of $\sim 15 - 20$ on daily timescales would be required before any hints of this could be observed. The flux detected by the H.E.S.S. telescopes agrees with all previously published upper limits, and extrapolating the spectrum measured with the *EGRET* satellite in the GeV regime to TeV energies roughly matches the spectrum observed (although the softer end of the error range on the *EGRET* spectral index is preferred). It has been suggested by Stawarz et al. (2006b) that, due to the relative closeness of Centaurus A, a phenomenon known as a pair halo might be observable leading to slightly extended VHE emission. It is theorised that VHE γ-rays emitted in the vicinity of the central black hole could be partly absorbed by the starlight radiation from the host galaxy, creating e^+e^- pairs. In this scenario, the e^+e^- pairs would be quickly become isotropic and would radiate very high energy γ-rays by inverse-Compton scattering of the starlight, generating a pair halo. If such a model is true, then the isotropic pair halo would have an angular size of ~ 4 arcmin, which is fully consistent with a point-like source for H.E.S.S. but could potentially be resolved by a future IACT instrument.

As the significance of the detection is relatively low, determining the origin of the TeV γ-ray emission is extremely difficult, although a number of possible sources are currently being considered. The simplest possibilities are that emission originates at the base of the jet or very close to the black hole; however, as in the case of M87, there are other possibilities that cannot currently be ruled out. The detection of nonthermal X-ray synchrotron emission from a shock in the southwest inner radio lobe ~ 5' from the nucleus, showing edge-brightened X-ray emission (Croston et al., 2009), suggests that this site could be a possible source; although this location is 3σ away from the best-fit position of the very high energy excess, it is still within the upper limit of the extension. It is suggested that very high energy γ-ray emission could occur via inverse-Compton scattering of starlight and cosmic microwave background off the high-energy particles within this lobe. This scenario predicts TeV emission compatible with the H.E.S.S. results; if correct, this would suggest that Centaurus A is analogous to a very large supernova remnant. One further suggestion was that the very high energy γ-ray emission from Centaurus A could originate from sources within the host galaxy. Kraft et al. (2001) detected more than 200 X-ray point sources in Centaurus A and the detection of large numbers of TeV sources in our Galaxy, many associated with X-ray sources, could lend support to this suggestion. However, Aharonian et al. (2009b) note that the sum of such contributions would require an unrealistically large number of galactic sources with

Centaurus A (assuming a typical luminosity of $\sim 10^{35-35}$ erg s $^{-1}$). It is argued by Aharonian et al. (2009b) that with a sensitivity increase of about an order of magnitude, better astrometric accuracy ($\sim$ 5") and better angular resolution ($\sim$ 1') it would become possible to determine the emission site within Centaurus A which could potentially lead to a much greater understanding of both radio galaxies and blazars as a source of TeV emission.

Out of 27 ultrahigh-energy cosmic ray (UHECR) protons above 57 EeV detected with the Pierre Auger cosmic ray observatory, four may be associated with the location of Centaurus A (Abraham et al., 2008). As sites of cosmic ray acceleration are also expected to be sources of TeV γ-ray emission, an understanding of the origin of such high-energy protons could allow for a better understanding of the nature of very high energy emission within Centaurus A. Unfortunately, it is extremely difficult to account for UHECR protons at energies beyond 10^{19} eV using conventional acceleration concepts. Rieger & Aharonian (2009) argue that protons could not be accelerated to the energies observed, either in the vicinity of the black hole, or in the accretion disc. It is also argued that, if radio observations are a reliable tracer of fluid velocities within the jet of Centaurus A, then internal shocks cannot account for cosmic ray emission beyond 50 EeV, either on subparsec or on hundred-parsec scales, as the jet seems at most mildly relativistic (not exceeding $0.5c$ by much) thereby severely limiting shock speeds (Tingay et al., 2001; Hardcastle et al., 2003), severely limiting shock speeds. The most likely explanation (Rieger & Aharonian, 2009) is shear acceleration of the protons along the large-scale jet, in which high-energy seed particles are accelerated by a factor of an order of magnitude or more in energy as they pass from a stratification within the jet (Rieger & Duffy, 2004). One further possibility, put forward by Hardcastle et al. (2009), is that the particle acceleration could occur within the giant radio lobes of Centaurus A on scales of R $\sim$ 100 kpc. It is unknown whether the conditions required for such high energy acceleration to take place in these areas exist within Centaurus A; however, the northern lobe does show continuous acceleration of electrons implying that magnetic turbulence is present which could theoretically accelerate the different species of cosmic rays although a relatively optimistic scenario must be assumed for these particles to reach ultrahigh energies.

3.4.3 NGC 1275

NGC 1275 is the dominant galaxy in the Perseus cluster and is situated at a redshift of $z = 0.0179$ (Aleksić et al., 2012c). It displays a number of properties reminiscent of Seyfert galaxies and has been classified as a Seyfert 1.5 (Veron-Cetty & Veron, 1998); it has also been classified as a FRI due to the morphology of the extended radio jet (Buttiglione et al., 2010). The nucleus of the object is very bright at radio wavelengths and highly variable in the optical regime, where the emission

is highly polarised, suggesting a significant contribution from the jet. The angle of inclination changes from $10° - 20°$ on milliarcsecond scales up to $40° - 60°$ at arcsecond scales (Krichbaum et al., 1992).

Prior to the detection of the object with the MAGIC telescopes, it was reported as a γ-ray emitter in the 100 MeV - 100 GeV range by Abdo et al. (2009b), using data collected with the *Fermi*-LAT during its first four months of operation. Since the initial detection of NGC 1275 with the *Fermi*-LAT the collection of more data has led to very strong evidence for variability of the source on timescales of days at energies > 800 MeV (Brown & Adams, 2011). The detection of NGC 1275 at TeV energies with the MAGIC telescopes was reported in Aleksić et al. (2012c) with a significance of 6.6σ, based on observations performed between August 2010 and February 2011. The spectrum of the source at very high energies can be fitted between 70 GeV and 500 GeV by a simple power law with a spectral index of $\Gamma = -4.1 \pm 0.7_{\mathrm{stat}} \pm 0.3_{\mathrm{sys}}$. No flux or spectral variability at these energies is detected. When compared to the *Fermi*-LAT spectrum above 100 MeV, which displays a much lower spectral index of $\Gamma = -2.1$, a break or cut-off at an energy of a few tens of GeV is implied.

3.5 The Extragalactic Background Light (EBL)

The EBL is the faint diffuse background radiation permeating across the Universe and consists of the sum of the radiation emitted by galaxies throughout the history of the Universe, including an important contribution from the very first stars to form. It is dominated from the optical through to ultraviolet by direct emission from stars and at infrared wavelengths by absorption and re-radiation by gas and dust. The spectrum of the EBL takes the form of a hump at infrared energies and a second hump at ultraviolet energies. The properties of this radiation field are of great interest to astronomers, as it can be used to study the star-formation history of the Universe.

Direct measurements of the EBL are complicated as it is strongly dominated (by a factor of ~ 100) by local emission both from within the solar system and the Galaxy at large. At infrared and ultraviolet wavelengths a major contribution to the background light that must be estimated and subtracted comes from sunlight scattered and reprocessed by the zodiacal dust (dust in the solar system). Correcting for Galactic sources is relatively simple for resolved objects, but the reprocessed emission from interstellar dust is difficult to measure leading to uncertainties on EBL measurements. Despite these difficulties direct detection of the EBL has been claimed at infrared (e.g. Gorijan, Wright & Chary (2000), with the Diffuse Infrared Background Experiment (DIRBE) on board the *Cosmic Background Explorer (COBE)* satellite) and at optical and soft ultraviolet

(e.g. Bernstein, Freedman & Madore (2002) with the *Hubble Space Telescope*). In addition to direct measurements of the EBL it is possible to place a lower limit on it's spectrum by summing the contribution of galaxies in galaxy surveys (e.g. Fazio et al. (2002)).

The spectrum of the EBL can also be estimated using empirical models of the evolutionary histories of galaxies and these models can be separated into a number of classes. One class of models use infrared data from local galaxies and extrapolate the evolution of these galaxies to higher redshifts and shorter wavelengths (e.g. Stecker et al. (2006)). Another approach uses semianalytic models of galaxy formation and evolution to determine the star formation history of the Universe and use this to calculate the contribution to the EBL (e.g. Gilmore et al. (2009)). A further approach focuses primarily on the stars themselves, using star formation rates and stellar properties to estimate the EBL spectrum (e.g. Finke, Razzaque & Dermer (2010)).

When a very high energy γ-ray photon comes into contact with a photon from the EBL, there is a chance that it will interact via the pair-production process $\gamma + \gamma \rightarrow e^+ + e^-$, as discussed in Section 1.3, resulting in the γ-ray being absorbed. This process has a cross-section, σ_{EBL}, as given in Vassiliev (2000):

$$\sigma_{EBL}(q) = \frac{3}{8}\sigma_T f(q) \tag{3.2}$$

where

$$f(q) = q\left[\left(1 + q - \frac{q^2}{2}\right)\ln\left(\frac{1+\sqrt{1-q}}{1-\sqrt{1-q}}\right) - (1+q)\sqrt{1-q}\right] \tag{3.3}$$

and

$$q = \frac{m_e^2}{E\epsilon}\frac{2}{1-\cos(\theta)} \tag{3.4}$$

In Equation 3.2, $\sigma_T = 6.67 \times 10^{-25}$ cm^2 is the Thomson scattering cross section, E and ϵ are the energies of the interacting photons, and θ is the collision angle. The function, $f(q)$ in equation 3.3 reaches its maximum at $q = 0.508$, which indicates that, for a head-on collision, the peak of the interaction cross section for a γ-ray photon of energy $E \sim 1$ TeV corresponds to pair production with a photon of energy $\epsilon \sim 0.5$ eV ($\lambda \sim 2.5$ μm) in the infrared regime, as found in Section 1.3. However a head-on collision is unlikely, and for the case of an isotropic radiation field, attenuation of 1 TeV γ-rays actually peaks for interactions with infrared photons of energy $\sim \epsilon 0.9$ eV (Vassiliev, 2000). The impact on the observed flux, $F_{obs}(E)$, is such that:

$$F_{obs}(E) = F_{int}(E)\exp[-\tau_{\gamma\gamma}(E)] \tag{3.5}$$

where F_{int} is the unabsorbed source flux as a function of observed energy E and $\tau_{\gamma\gamma}$ is the EBL

absorption optical depth (Finke, Razzaque & Dermer, 2010). If F_{int} is known for a specific object, then observations of that object would enable the EBL absorption optical depth to be determined from Equation 3.5. Unfortunately the intrinsic TeV spectra of AGN observed at these energies are not known. However, by using models or extrapolation from lower energies to estimate the unattenuated spectrum then upper limits can be found to the absorption, providing another means to constrain the spectrum of the EBL. Plots of a range of direct measurements, upper limits from VHE observations, lower limits from galaxy counts and empirical models from the last 15 years can be seen in Figure 3.10. An in depth discussion of current upper and lower limits and direct measurements of the EBL can be found in Dwek & Krennrich (2012).

A major issue in using TeV blazars to constrain the EBL is that, although they are persistent sources, they are generally variable and their intrinsic spectra are difficult to model accurately. In spite of this, theoretical models can be used to determine the maximum possible intrinsic spectrum of a very high energy blazar, by assuming that γ-rays are produced by Compton scattering off electrons so that the hardest possible photon index is $\Gamma_{max} = 1.5$. For very high energy γ-ray astronomers, the EBL has a large impact on the distance out to which extragalactic sources can be observed before enough of their TeV emission is absorbed for detection to be impossible. To date the most distant extragalactic source detected at TeV energies is at a redshift of $z = 0.5$.

3.6 Conclusions

AGN are some of the most luminous phenomena in the Universe and display emission across the entire electromagnetic spectrum. It is currently believed that the various types of AGN are similar objects viewed at different angles, leading to the different properties observed. At very high energies, the vast majority of extragalactic sources are AGN and, of these, all except three are blazars, i.e., AGN with jets closely aligned to the line of sight. The small angle of inclination of the jets in blazars leads to strong Doppler boosting of emission in the jet, resulting in detection of higher energy emission than would otherwise be expected.

The detection at very high energies of three radio galaxies, M87, Centaurus A and NGC 1275, has raised interesting questions about potential emission mechanisms in such objects, as the jets in these sources are not aligned with the line of sight, resulting in very limited, if any, Doppler boosting of the emission.

When studying extragalactic objects at very high energies, it is important to take into account the extragalactic background light, which is a faint, diffuse radiation field consisting of contributions from the radiation emitted from all galaxies throughout the age of the Universe. This radiation field

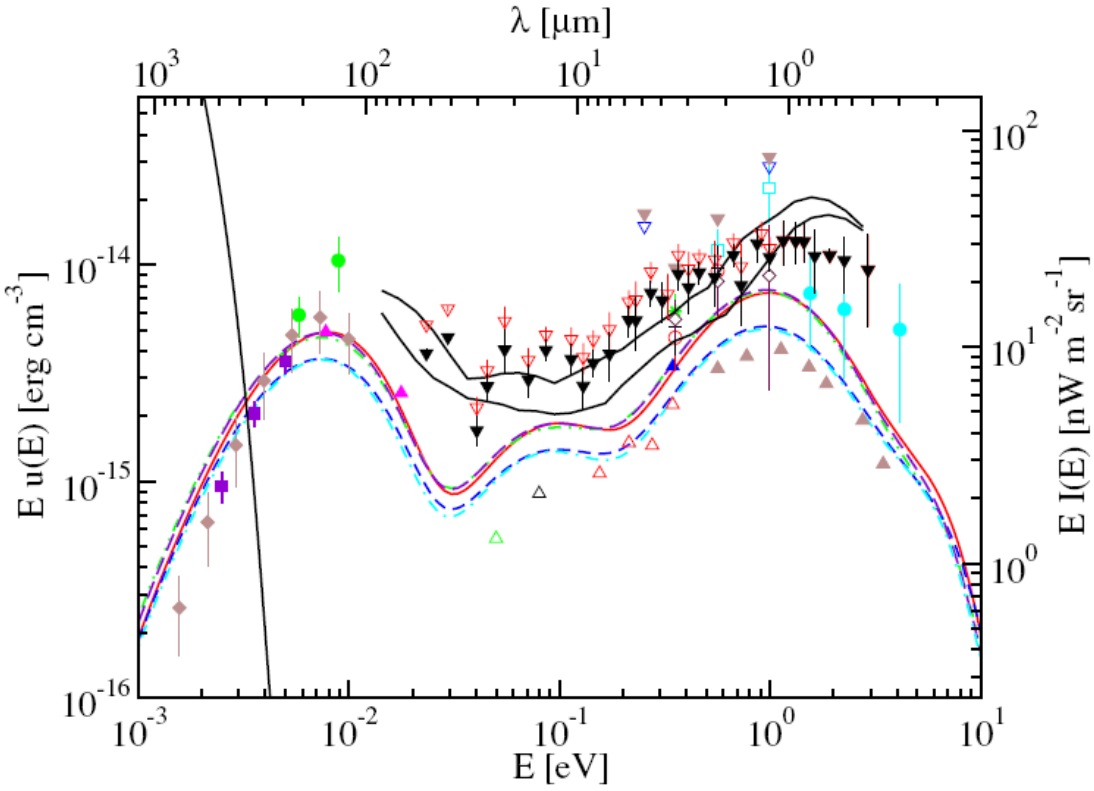

Figure 3.10: EBL models, measurements and constraints from a number of sources. The model of Finke, Razzaque & Dermer (2010)(solid black curve), the best-fit model of Kneiske et al. (2004) (red dotted curve), the fiducial model of Gilmore et al. (2009) (long dashed blue curve) and the fast evolution and baseline model from Stecker et al. (2006) (upper and lower dot-dashed violet curves, respectively). The double dot-dashed and the dot double-dashed black curves are the single power-law Model B and Model C from Razzaque et al. (2009). Measurements from Bernstein et al. (2002)(cyan points), Gorjian et al. (2000) (empty red circle), Dwek & Arendt (1998) (green asterisk), Cambrésy et al. (2001) (empty cyan square), Wright & Reese (2000) (black cross), Levenson et al. (2007)(maroon diamonds), Hauser et al. (1998) (green filled circles), Fixsen et al. (1998) (brown filled diamonds) and Marsden et al. (2009) violet filled squares). Lower limits are from Fazio et al. (2004)(red empty triangles), Madau & Pozzetti (2000) (brown filled triangles), Levenson & Wright (2008) (blue filled triangle), Dole et al. (2006)(magenta filled triangles), Metcalfe et al. (2003)(black empty triangle), and Papovich et al. (2004, green empty triangle). Upper limits are from Hauser et al. (1998)(brown filled inverted triangles), Dwek & Arendt (1998)(blue empty inverted triangles), Mazin & Raue (2007)(upper and lower black curves $\Gamma_{int}^{min} = 0.67$ and $\Gamma_{int}^{min} = 1.5$ upper limits, respectively), and red empty and black filled inverted triangles are the $\Gamma_{int}^{min} = 1.0$ and $\Gamma_{int}^{min} = 1.5$ upper limits, respectively, from Finke & Razzaque (2009). The black curve at long wavelengths is the cosmic microwave background. Taken from Finke, Razzaque & Dermer (2010).

peaks at infrared energies, leading to $\gamma\gamma$ photoabsorption of very high energy γ-rays, as discussed in Section 1.3, and limiting the distance from which such high energy emission can be detected.

Chapter 4

Searching for Very High Energy γ-rays from Seyfert Galaxies

4.1 Introduction

The detection of M87 and Centaurus A at very high energies has helped change current understanding of such emission from extragalactic sources. The detection of these sources shows that even in cases where the jet is misaligned to the line of sight, it is possible for very high energy emission to be detected, dramatically increasing the potential number of extragalactic objects available for study at such energies. Further to this, the recent detection of NGC 253 and M82 open up a whole new class of galaxies for study, those without obvious nonthermal emission from the nucleus but with very high star-formation rates. Seyfert galaxies have seen little interest at high energies until recent results from the *Fermi*-LAT confirmed the detection of a number of such objects in the GeV γ-ray regime as discussed later in Section 4.3; however, they are interesting objects that, in many cases, show evidence of nonthermal emission, possible jet structures and starburst regions, making them prime candidates for further study with ground-based very high energy γ-ray telescopes.

In this chapter archival H.E.S.S. data are used to determine whether there is evidence for emission from a number of γ-ray-and X-ray-selected Seyfert galaxies observable with the H.E.S.S. telescopes. In the event that emission is not detected, upper limits on the flux are calculated using the procedure described in Section 2.7.

4.2 Seyfert Galaxies

Seyfert galaxies are the most luminous type of active galaxy observed in the local Universe ($z \lesssim 0.1$), displaying bolometric luminosities of $\sim 10^{43}$ - 10^{45} erg s^{-1} (Deo et al., 2006). As with all AGN, they are characterised by nonthermal continuum emission across the entirety of the electromagnetic spectrum, from radio right through to γ-ray energies, and the overall SED can be described as a power law of the form $F_\nu \propto \nu^{-\alpha}$ interspersed with bumps and dips. The spectra of the nuclei of such sources display prominent emission lines in the optical and ultraviolet. Seyfert galaxies are distinguishable from quasars by their lower luminosity which is of the order of 10^2 lower. Early work that separated Seyfert galaxies into classes based on the observed spectra of their nuclei was carried out by Khachikian and Weedman (1974), who divided them into two distinct classes based on the relative widths of their forbidden and Balmer lines, type 1 Seyfert galaxies (displaying broader Balmer lines than forbidden lines and referred to as Sy1s henceforth) and type 2 Seyfert galaxies (displaying Balmer lines and forbidden lines of approximately equal width and referred to as Sy2s henceforth). Sy1 nuclei show broad permitted emission lines with FWHM $>$ 1000 km s^{-1}, superposed with narrow emission lines from permitted and forbidden transitions, displaying FWHM $\lesssim$ 500 km s^{-1}, whereas Sy2 nuclei display only narrow emission lines. Further classifications were introduced by Osterbrock (1977, 1981), who classified Sy1s from 1.2-1.9 according to the ratio of the strength of the broad-line components to that of the narrow-line components, with numerically larger types displaying smaller broad-line to narrow-line ratios. By the end of the 1970s (Osterbrock, 1978), it had been suggested that the different properties observed in Sy1s and Sy2s might be due to an orientation effect, in which, for Sy2s, the broad-line region was obscured. Early evidence that the central continuum source is similar in all Seyfert galaxies, supporting Osterbrock's idea, was reported by Miller and Antonucci (1983) with detection of polarised emission from (what would be) the broad-line region of the Sy2 NGC 1068 (the brightest Seyfert galaxy). This was interpreted as probable synchrotron emission from the nucleus as seen in other AGN, as scattering by surrounding gas and dust would require a very unlikely distribution of clouds with appropriate behaviour of optical depth to explain the approximately flat continuum with the constant polarisation of $\sim 16\%$ observed.

The discovery that the source of emission within the two types of Seyfert galaxies was likely to be the same helped to further the unified model of AGN discussed in Chapter 3. This led to the conclusion that Sy2s are merely Sy1s viewed edge on, with the line of sight to the broad-line region (which is closer to the central black hole than the narrow-line region) obscured by an optically thick torus made up of gas and dust. In this model, the polarised light detected is attributable

to emission from the broad-line region reflected off ionised material above the torus but within its opening angle. At X-ray energies, the spectra of both Sy1s and Sy2s follow power laws with typical spectral indices of $\Gamma \sim 1.5-3.0$, and often show a break at ~ 100 keV (Zdziarski, 1999). This break would seem to support the conclusion that the high-energy emission from Seyfert galaxies originates from thermal Compton emission rather than having a nonthermal origin; however, similar features have been detected in Centaurus A, which is now known to be a source of TeV γ-rays (Section 3.4.2). Additionally, the detection of polarised optical emission from both Sy1s and Sy2s supports the conclusion that there is nonthermal synchrotron emission near the core of these galaxies.

At radio wavelengths, observations with arcsecond resolution (Ulvestad and Wilson, 1984a; Morganti et al., 1999; Thean et al., 2000) show resolved structures in a large fraction of Seyfert galaxies, with hints of jets and, in some cases, extended emission which is usually associated with star-forming regions. Several such objects, for example, NGC 1052 (Wrobel, 1984), NGC 1068 (Ulvestad et al., 1987), NGC 7674 (Momjian et al., 2003) and Mrk3 (Kukula et al., 1999), have radio morphologies similar to those seen in radio galaxies, with a core, collimated jets and hotspots; however, these are usually on smaller scales than in strong radio sources ($\sim$ a few kiloparsecs, compared with hundreds of kiloparsecs or even megaparsecs). Using arcsecond-scale observations, the parsec-scale structure of Seyfert nuclei can be resolved into a number of components, including structures resembling parts of a jet (NGC 4151, Ulvestad et al., 1998; Nagar et al., 2001) and, in some cases, extended emission. In many cases, comparisons between parsec-scale and kiloparsec-scale jets within Seyfert galaxies show misalignment between the jets on different scales, suggesting either a change in jet ejection axis, or bending of the jet by pressure gradients in the ambient medium (Middelberg et al., 2004). A large number of Seyfert nuclei display much fainter radio emission from the parsec-scale structures than is derived from observations at lower resolutions, even if the nucleus itself is unresolved, suggesting that in Seyfert galaxies the emission is not concentrated in the central source but is in fact dominated by emission on scales of tens or hundreds of parsecs (Sadler et al., 1995). This is not universal, however: some Seyfert nuclei such as Mrk 530 do not display "missing" flux on parsec scales, indicating that the radio emission is dominated by emission from the central compact source (Lal et al., 2004).

Using archival data from the Very Large Array (VLA) and the VLBA, Orienti and Prieto (2010) studied radio features of the nuclei of seven of the nearest Seyfert galaxies in the Southern hemisphere. For five of the Seyfert galaxies, data from the VLA were not of sufficient resolution to allow the nucleus to be resolved, but the remaining two, MGC-5-23-16 and NGC 7469, show a core-jet structure; at VLBA resolutions, the nucleus of Mrk 1239 is resolved into two separate components. In those Seyfert galaxies without known star-forming regions, no circumnuclear radio

emission was detected, except in the case of NGC 5506, which showed a radio halo surrounding the nucleus; however, for Seyfert galaxies with star-forming regions (detected at infrared wavelengths), radio emission from those regions was detected in ∼10% of cases. A suggestion that only star-forming regions with a high supernova rate may be detected at radio wavelengths is supported by the steep radio spectra observed in these regions. In six of the Seyfert galaxies studied, comparison between arcsecond and milliarcsecond resolutions revealed that a large percentage (∼ 80% for Mrk 1239 and NGC 3783) of the radio flux detected at VLA resolution was not observed at parsec-scale resolutions. This discontinuity in radio flux between parsec-scale and larger-scale observations is not found in elliptical radio galaxies, but appears to be common in Seyfert nuclei, which are mostly hosted in spiral galaxies. Orienti and Prieto (2010) suggest that this undetected flux component is probably due to AGN-related synchrotron emission and that if this is the case it may be split off from the jet, which could be distorted and/or disrupted by the dense interstellar medium at the nucleus of the host galaxy. It is concluded that in Seyfert galaxies with steep radio spectra, a significant portion of the radio emission arises from extended low-surface-brightness features. An important note is that in Seyfert galaxies displaying flat radio spectra, almost all of the flux density is contained within parsec scales, indicating that radio emission is most likely concentrated in the compact core, without evidence for a jet-like structure even on milliarcsecond scales.

The physical processes that produce the emission from Seyfert galaxies are open to interpretation. Gondek et al. (1996) report a study carried out on the average spectrum between 1 keV and 500 keV for seven radio-quiet Sy1s detected by both the Extra-Solar X-ray Observatory (EXOSAT) and the Oriented Scintillation Spectrometer Experiment (OSSE) on board the *Compton γ-ray Observatory*, and they present both thermal and nonthermal models of emission from such sources. The average Seyfert 1 spectrum found by Gondek et al. (1996) is fitted using a power law with exponential cut-off, with photon index $\Gamma = 0.90^{+0.09}_{-0.07}$ and cut-off energy $E_c = 510^{+4300}_{-250}$ keV. This average spectrum is consistent with thermal Comptonisation in optically thin, mildly relativistic plasmas as discussed in Zdziarski et al. (1994), where such a model is applied to the Sy1 galaxy IC4329A (ESO 445-50). The large value found for E_c by Gondek et al. (1996) discounts the possibility, proposed in the 1980s, that Sy1s could be modelled by Comptonisation in optically thick plasmas as suggested by Miyoshi et al. (1988), for example. One proposal is that the hot plasma in Seyfert nuclei forms mostly into a corona above the surface of the accretion disc and that most of the energy dissipation occurs in the corona (Haardt & Maraschi, 1993). Using this model, the plasma temperature can be calculated from the disc-corona energy balance, and this model can successfully account for the Compton-reflection spectral components observed in radio-quiet Sy1s. In this model, the hard corona emission reprocessed by the disc provides the soft ultraviolet

seed photons for Compton upscattering into the hard spectrum.

A flaw in the model proposed in Haardt & Maraschi (1993), pointed out by Haardt et al. (1994) would appear to rule out most of the dissipation occurring in the corona. In the model proposed by Haardt and Maraschi (1993), the ultraviolet emission is attributed to reprocessing of the X-ray and γ-ray emission directed towards the cold disc, which would result in the energy-scaled (EF_E) fluxes being of similar magnitude in both wavebands; however, this would appear not to be the case. Data from Gondek et al. (1996) show that the ratio of the fluxes, ($EF_E(9\text{ eV})/EF_E(2\text{ keV})$), in these two wavebands can vary widely between different Sy1s, and in four of the seven radio-quiet Sy1s studied this ratio is > 10. To explain the large ratios observed, it is suggested that the corona is patchy rather than being homogeneous and that coronal dissipation dominates the disc dissipation only in the vicinity of an active region (Haardt et al., 1994). Another assumption made in Haardt and Maraschi (1993) is that a pure $e^{\pm}$ pair corona could form a thin "slab"-type geometry above the surface of the accretion disc; however, hydrostatic equilibrium would appear to render this unfeasible. Further support for the idea of patchy coronae in Sy1s is provided by X-ray light curves measured with *EXOSAT*, in which some Sy1s show behaviour consistent with stochastic rather than deterministic chaos (Czerny and Lehto, 1997). These results imply that X-ray emission is due to multiple active regions rather than originating from a single extended source.

Further work on thermal Comptonisation models for both Sy1s and Sy2s was carried out by Zdziarski et al. (2000), using data from OSSE. As in the study by Gondek et al. (1996), these authors looked at the average spectra of the sources, 17 Sy1s and 10 Sy2s, at energies between 50 keV and 500 keV. In modelling the spectra of the Seyert galaxies, a spherical geometry was assumed, due to a lack of data on the overall geometry of the sources, resulting in thermal Compton spectra that are independent of the viewing angle. The corona was also assumed to be homogeneous. The results supported thermal Comptonisation and reflection as a valid model for the emission from the Seyfert galaxies observed, although a patchy corona as discussed previously cannot be ruled out. The average spectra of Sy1s appear to be softer than Sy2 spectra at 50 keV to 500 keV with photon indexes of $\sim 2.50 - 2.56$ and $\sim 2.05 - 2.21$ respectively. This difference in spectra between the two classes of objects cannot be due to changes in the strength of Compton reflection at different viewing angles for anything other than Sy2s with inclination $i < 72.5°$, and it cannot be accounted for in a slab geometry due to extra scattering of photons at large viewing angles. It is also unlikely to be due to absorption by a dusty torus at the wavelengths studied, as only one of the Sy2s included has a Thompson-thick absorber. This makes it impossible to rule out an intrinsic difference between Sy1s and Sy2s a conclusion supported when data from Sy1.5s (considered to be

systems viewed at angles between those of Sy1s and Sy2s) are included: these display spectra with photon indexes lying between those seen in the other Seyfert galaxies. One suggestion is that a complex structure in the torus around some Sy2s may lead to underestimation of the values of the photon indices found. The results found for the Seyfert galaxies studied do not rule out patchy coronae in the case of Seyfert galaxies with relatively soft spectra $\Gamma \sim 1.9$, but to produce the harder spectra observed requires the emitting region to be separated from the disc as suggested by Svensson (1996). In the case of objects with harder spectra, thermal Comptonisation models require that the emission is due to mildly relativistic blobs of plasma moving away from the disc in order to allow agreement with observed values for Compton reflection.

In addition to the thermal Comptonisation models discussed, attempts have been made to describe the X-ray and γ-ray emission from Seyfert galaxies using nonthermal models. In the study by Gondek et al. (1996) discussed earlier, the average spectrum from the Sy1s studied can be fitted using a number of different nonthermal models. The simplest model used consists of a seed population of electrons following a power law of index ≈ 2.8 that singly scatter some soft (ultraviolet) photons up to X-ray and γ-ray energies in the Thomson regime via inverse-Compton interactions. This model gives a spectral index for the high-energy emission of $\Gamma \approx 1.8$, but it does not predict the cut-off seen in the data at ~ 511 keV and so reproduces the spectra of the Seyfert nuclei studied with less accuracy than the thermal models discussed earlier. A more complicated model proposed by Zdziarski et al. (1990), attributes the X-ray spectral index between 1-30 keV of $\alpha \approx 0.7$ to reprocessing of the high-energy radiation produced by nonthermal pair cascades (of $alpha \approx 1.0$) by cold material in the central parts of Seyfert nuclei.

Although radio data have been important in the study of Seyfert galaxies, as noted above, Seyfert galaxies are generally radio-quiet. However, recent data suggest that the class of narrow-line Seyfert 1s (NLSy1) are more likely to be radio-loud than the other Seyfert classes. NLSy1s are Sy1 galaxies that display Balmer lines narrower than those seen in other Sy1s, with FWHM < 2000 kms^{-1} (Osterbrock and Pogge, 1985), and they also display other extreme observational properties such as relatively weak forbidden-line emission (Goodrich, 1989), strong permitted optical and ultraviolet FeII lines (Boroson and Green, 1992), steep soft-X-ray spectra (Wang et al., 1996), and rapid X-ray variability (Leighly, 1999). These galaxies are thought to be relatively young AGN hosting less-massive black holes with high accretion rates, with bolometric-to-Eddington luminosity ratios, $L_{\rm bol}/L_{\rm Edd} \sim 1$ (Boroson, 2002). The detection of radio-loud NLSy1s has changed the previously held views of such sources, and now it is believed that rather than being radio-quiet, such sources have a relatively low probability ($\sim 7\%$) of being radio-loud (Komossa et al., 2006), rather than 10%-15% for other broad-line AGN (Ivezić et al., 2002), and only a $\sim$2.5% chance of

being "very" radio loud (with a radio loudness, defined as the radio-to-optical flux density ratio, of $R > 100$). These radio-loud NLSy1s are generally compact sources and show steep radio spectra (Komossa et al., 2006); however, the loudest such radio sources display characteristics normally observed in blazars, and they harbour relativistic jets (Doi et al., 2007, Zhou et al., 2007, Yuan et al., 2008). A comprehensive study of 23 radio-loud NLSy1s (with radio loudness > 100), documented in Yuan et al. (2008), found that in all cases the region of radio emission was very compact and was unresolved on scales as small as several arcseconds. Some of the objects studied showed unusual radio to X-ray properties (reminiscent of blazars) that had previously only been seen in the most extreme radio-loud NLSy1s, and in six objects there is evidence for relativistic beaming. Those objects with evidence for relativistic beaming displayed flat radio spectra, large-amplitude flux and spectral variability, highly compact sources of radio emission, very high brightness temperatures, enhanced optical continuum emission, flat X-ray spectra, and blazar-like SEDs. In spite of the ever-increasing numbers of successful detections of NLSy1s, the mechanisms driving the radio properties are currently not clear; further work needs to be done to constrain the accretion rates, black hole spins, host-galaxy properties and merger histories of such sources in order to more fully understand their spectral properties (Zhou et al., 2006).

4.3 Detection of GeV γ-rays from Seyfert Galaxies

The blazar-like radio emission detected from Seyfert galaxies discussed previously and reported in articles such as Brunthaler et al. (2005) and Lister et al. (2009), along with inferences from multiwavelength data that there are some parallels between properties of Seyfert galaxies and blazars (see Section 4.2), has made these objects high-priority targets for observation with the *Fermi*-LAT. The first detection of GeV γ-rays from a Seyfert galaxy was the detection reported in Abdo et al. (2009b), of PMN J0948+0022, a Seyfert 1 galaxy at a redshift of $z = 0.585$ which displays narrow permitted lines at optical wavelengths. Previously, there was some evidence from radio observations for the presence of a relativistic jet (Doi et al., 2006). The detection of a bright γ-ray source associated with the Seyfert galaxy confirmed the existence of this jet and allowed a complete SED of the source to be constructed (shown in Figure 4.3). The data showed that PMN J0948+0022 displays characteristics normally associated with FSRQs, but with lower power than the FSRQs detected by the *Fermi*-LAT to date, relatively small mass ($1.5 \times 10^8 M_\odot$), and high accretion rates ($\approx 0.4 L_{\rm Edd}$). The detection of PMN J0948+0022, along with the previous evidence of nonthermal radio emission in Seyfert galaxies led to Abdo et al. (2009c) conducting a survey with the *Fermi*-LAT instrument of 29 radio-loud Seyfert 1 galaxies that display narrow

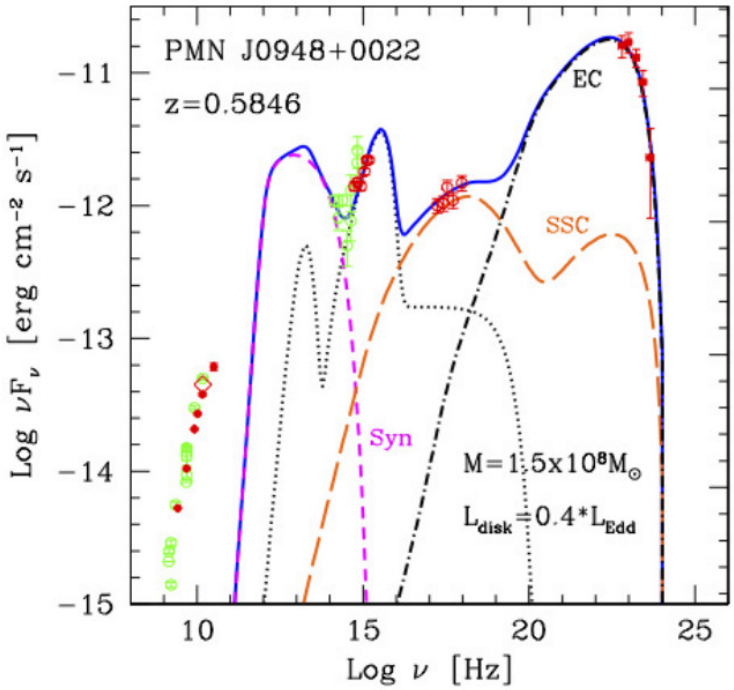

Figure 4.1: SED of PMN J0948+0022, taken from Abdo et al. (2009b). Red symbols represent data from *Fermi*-LAT (five months of data), *Swift* XRT and UVOT (2008 December 5), Effelsberg (2009 January 24) and OVRO (average in the five months of LAT data, indicated with a red diamond. Archival data are marked with green symbols. Radio data (1.4 to 15 GHz) is from Bennett et al. (1986), Becker, White & Edwards (1991), Gregory & Condon (1991), White & Becker (1992), Griffith et al. (1995), and Doi et al. (2006). Optical/IR data is from Monet et al. (2003) for USNO B1, B, R, I filters and Cutri et al. (2003) for 2MASS J, H, K filters. The modelling carried out by Abdo et al. (2009b) is shown on the figure with the contributions due to each component shown as a series of curves; the dotted line indicates the contributions from the infrared torus, the accretion disc, and the X-ray corona, the synchrotron emission, accounting for self absorption, is shown with a small dashed line and labelled Syn while the SSC and EC components are displayed with dashed and dot-dashed lines, labelled SSC and EC respectively. The continuous line indicates the sum of all the contributions.

permitted lines. This survey detected GeV γ-rays from three objects, PKS 1502+036 ($z = 0.409$), 1H 0323+342 ($z = 0.061$) and PKS 2004447 ($z = 0.24$). The detection of four such sources at GeV energies suggests that Seyfert 1 galaxies with narrow permitted lines form a new class of γ-ray-emitting AGN.

The spectrum of PMN J0948+0022 shown in Figure 4.3 strongly resembles those of high-power blazars, displaying two nonthermal emission peaks, one in the far infrared and the other at 40-400MeV. A peak in the ultraviolet can be attributed to emission from the disc and is well defined using data from the Ultraviolet and Optical Telescope (*UVOT*) aboard *Swift*. A lower limit of $\sim 10^8$ $M_\odot$ was found for the mass of the black hole (Abdo et al., 2009b). The jet power is estimated by Abdo et al. (2009b) by modelling the source using the model of Ghisellini and Tavecchio (2009). The jet is assumed to have conical geometry and most of the seed photons for inverse-Compton

scattering originate from the broad-line region. In this case, the bulk kinetic power carried by electrons in the jet is found to be $L_e = 5.0 \times 10^{44}$ erg s^{-1} and the Poynting flux $L_B = 1.8 \times 10^{44}$ erg s^{-1}, significantly lower than the radiative power of $L_{rad} = 2.0 \times 10^{45}$ erg s^{-1} seen in powerful blazars (Celotti & Ghisellini, 2008). This implies that the jet also contains protons, as the power available from the magnetic field and the electrons in the jet is too low to account for the radiative luminosity. Assuming one proton per electron results in a calculated jet power due to protons of $L_p = 4.8 \times 10^{46}$; however, if it is assumed that electron-positron pairs are present in the jet then the assumed number of protons would be reduced and hence the calculated power due to protons would also be reduced. Importantly, the systematic errors in the *Fermi*-LAT data do not have a significant effect on the values calculated for the luminosity. The jet power found for PMN J0948+0022 is relatively high and is comparable with that seen typically in powerful blazars (See Figure 4.3) (Celotti & Ghisellini, 2008). The parameters used to find the SED of PMN J0948+0022 are not fully constrained and so the authors suggest that detection of a typical variability timescale would allow discrimination between possible solutions.

The SEDs constructed by Abdo et al. (2009b) using the data available for the other three Sy1s show clear similarities with those of blazars as in the case of PMN J0948+0022. The SED of PKS 1502+036 suggests that the jet in the source carries comparable power to the jet in PMN J0948+0022 and is therefore also in the range typical of high-power blazars. The remaining two sources, PKS 2004-447 and 1H 0323+342, display significantly lower jet power than the other two objects, around two orders of magnitude for power from protons within the jets, which places them in the range typical of moderate power BL Lac objects. It is important to note, however, that unlike PMN J0948+0022, the data available at all wavebands is relatively limited and non-simultaneous. This leads to less tightly constrained parameters for PKS 1502+036, PKS 2004-447 and 1H 0323+342, and further multiwavelength studies will be required before this can be rectified. The masses of the central black holes in these sources are typical of those in Seyfert galaxies at $\sim 10^7$ M$_\odot$, 1-2 orders of magnitude lower than those typical of blazars (Ghisellini et al., 2010). This means that to display the luminosities observed they must have high accretion rates; in the cases of PKS 1502+036 and 1H 0323+342, the accretion rates are up to 80% and 90% of the Eddington luminosity, respectively. These values are the most extreme observed for any γ-ray-emitting AGN, but are within usual bounds for such Sy1s.

In three of the *Fermi*-detected Sy1s, the host galaxy is definitely spiral; however, in the case of 1H 0323+342 there are two possibilities. Observations of 1H 0323+342 with the *Hubble Space Telescope*, discussed in Zhou et al. (2007), show the existence of spiral arms, but Antón et al. (2008) using data collected with the ground-based Nordic Optical Telescope (NOT) suggest that

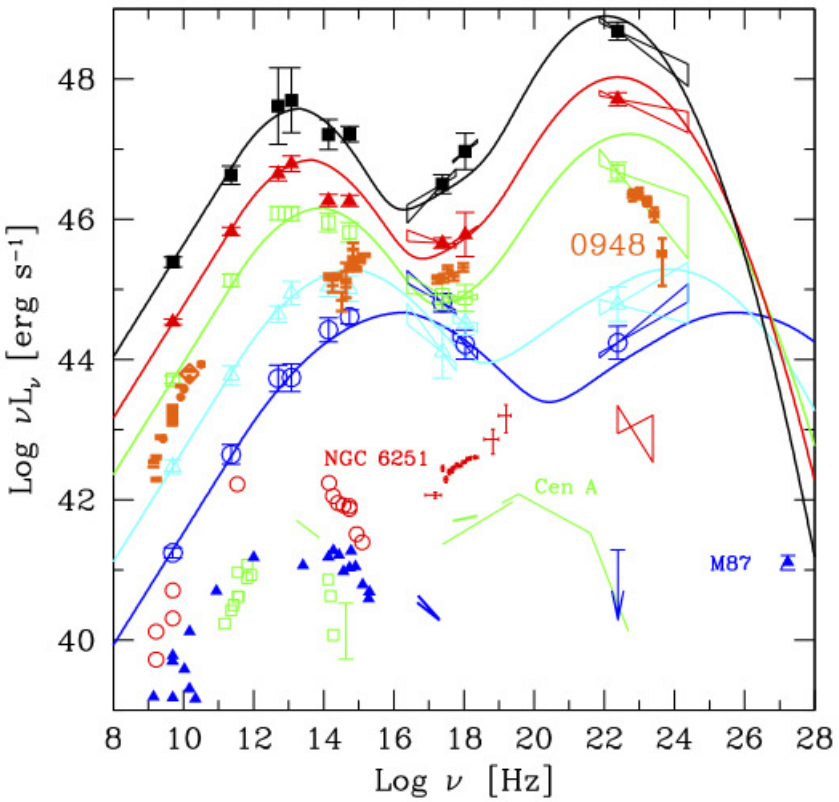

Figure 4.2: Comparison of the SED of PMN J0948+0022 (orange squares) with the blazar sequence from Figure 3.4; the black curve represents the SED of LBLs, the fuschia curve represents the SED of HBLs and the other curves represent transitional objects between them. Additionally the SEDs of three of the most powerful radiogalaxies, Cen A, M 87 and NGC 6251, are also marked as labelled on the figure. Taken from Foschini et al. (2010).

these structures are left over from a merger event that occurred sometime in the past 10^8 years. The detection of γ-rays from AGN hosted in spiral galaxies supports the hypothesis that relativistic jets can form independent of the nature of the host galaxy.

4.3.1 Seyfert 2 Galaxies Detected with the *Fermi* Space Telescope

The first reported detection of a Sy2 at *Fermi*-LAT energies was NGC 4945 which was noted in the 11-month *Fermi*-LAT catalogue (Abdo et al., 2010a). This object is at a redshift of $z = 0.001908$, exhibits strong starburst activity, was previously detected at soft γ-ray energies by the International Gamma-Ray Physics Laboratory (*INTEGRAL*) satellite (Petry et al., 2009), and is one of the brightest hard X-ray AGN (Itoh et al., 2008). Based on observations with the *INTEGRAL* (Beckmann et al., 2009) and *Ginga* (Iwasawa et al., 1993) satellites it is known to be a Compton-thick AGN. NGC 4945 is detected by the *Fermi*-LAT at a significance of 9.2σ above background; its high-energy spectrum is best described by a power law of index $\Gamma = 2.31 \pm 0.10$.

Also in the 11-month *Fermi*-LAT catalogue, a source, 1FGL J0242.7+0007, was detected in the region of NGC 1068 with no obvious counterpart in radio or lower energy γ-rays. Lenain et al. (2010) analysed 1.6 years of data from the *Fermi*-LAT to investigate the origin of this emission and concluded that 1FGL J0242+0007 is indeed associated with NGC 1068, with a significance of 8.4 σ. The γ-ray spectrum detected is consistent with a power law of index $\Gamma = 2.31 \pm 0.13$. NGC 1068 is the archetypal Sy2 galaxy: located at $z = 0.003786$, it is one of the closest Sy2s, and it is also one of the brightest. It exhibits both AGN and starburst activity in its central region; at infrared wavelengths, a circumnuclear starburst region at ~ 1 kpc dominates the SED. High-energy observations of the core of NGC 1068 by Chandra have shown that the X-ray emission from the source originates in the narrow-line emitting region from a primarily photoionised plasma (Ogle et al., 2003).

As NGC 4945 and NGC 1068 both display starburst activity, it is important to determine whether the γ-ray emission originates from this activity or from the hosted AGN. No conclusion was reached as to the source of γ-ray emission in NGC 4945 in Abdo et al. (2010a). To determine the origin of the γ-ray emission from both NGC 4945 and NGC 1068, Lenain et al. (2010) attempted to use the available data to look for significant variability in the γ-ray emission, as such variability would not be expected if the emission was due to starburst activity. No variability could be detected, but this result was not statistically significant. The γ-ray luminosities of NGC 4945 and NGC 1068 are 2.0×10^{40} erg s^{-1} and 1.7×10^{41} erg s^{-1} respectively, which are comparable to the luminosities at these energies of $\approx 10^{40}$ erg s^{-1} for the starburst galaxies NGC 253 and M82 (Abdo et al., 2010b), suggesting that starburst activity could account for the luminosities observed. To

investigate this possibility, the supernova rates ($R_{\rm SN}$) and total gas masses ($M_{\rm gas}$) of NGC 1068 and NGC 4945 were compared with those of NGC 253, M82, the Large Magellanic Cloud (LMC) and the Milky Way, along with their infrared and radio luminosities. Models that attribute the emission of γ-rays at these energies to starburst behaviour, and hence to cosmic ray processes, depend on the product $R_{\rm SN}M_{\rm gas}$. The γ-ray luminosity and supernova rate of NGC 4945 are comparable to those of NGC 253 and M82, so even though the object is a composite starburst/Sy2 galaxy its high-energy emission could be explained by starburst activity alone. In the case of NGC 1068, however, a more complex situation arises. The supernova rate in NGC 1068 (0.20 ± 0.08 yr^{-1}) is the same as in M82 (0.2 ± 0.1 yr^{-1}) and NGC 253 (0.2 ± 0.1 yr^{-1}), but its radio and γ-ray luminosities are higher by a factor of ~ 10. This would appear to support the hypothesis that the γ-ray emission in NGC 1068 probably originates from AGN activity rather than from starburst processes. Interestingly, when the product $R_{\rm SN}M_{\rm gas}$ is plotted against γ-ray luminosity, L_γ, for the previously mentioned galaxies, excluding NGC 1068, the relationship coefficient for a linear fit is as high as 0.95, rejecting the null hypothesis that there is no relationship between star formation and γ-ray luminosity in these objects with a probability of $\sim 99\%$. However, if NGC 1068 is included the probability that the null hypothesis is invalid drops to $\sim 62\%$, supporting the argument that γ-ray emission from this source is unlikely to originate from starburst activity (the plot is shown in Figure 4.3.1). Radio maps of NGC 1068 further support the conclusion of nonthermal emission within the object, as a structured jet can be detected on parsec and kiloparsec scales (Gallimore, Baum & O'Dea, 2004). In contrast, NGC 4945 shows extended emission consistent with the optical morphology of the edge-on galaxy, indicating likely starburst emission.

It is suggested by Lenain et al. (2010) that the high-energy emission from NGC 1068 could be due to a large, mildly relativistic zone of the wind-like outflow, at a few tens of parsecs from the core, which could emit GeV γ-rays by the external inverse-Compton process (EIC) discussed in Begelman & Sikora (1987). In this scenario, the infrared photons from the disc and from stellar emission are upscattered by high-energy electrons in the mildly relativistic zone of the outflow, resulting in the high-energy emission observed. At the distance from the core proposed for the relativistic zone, the infrared photon density is high enough to ensure significant emission while not being so high as to present high optical opacity from pair production. The model presented in Lenain et al. (2010) posits that the radio emission detected is due to synchrotron processes, while the γ-rays detected by the *Fermi*-LAT are interpreted as EIC emission with seed photons provided by thermal infrared emission from the accretion disc. The contribution from SSC processes is shown to be negligible in the SED of NGC 1068. The model as described has some trouble reproducing the hard X-ray spectrum observed with *INTEGRAL*, and it is proposed that this

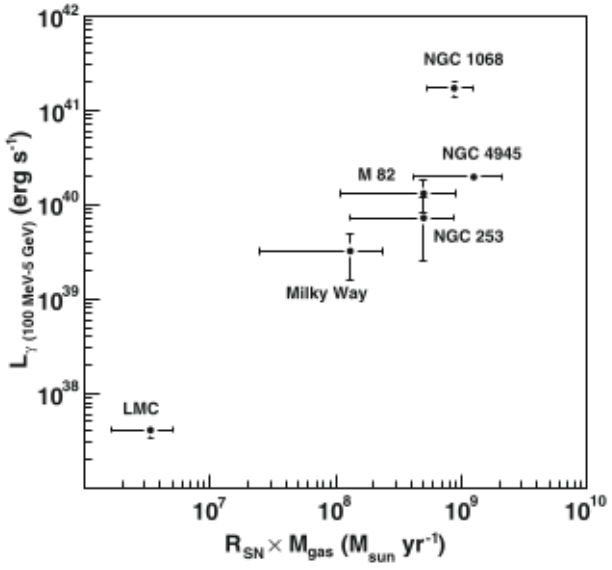

Figure 4.3: Plot of SN rate multiplied by total gas mass against -ray luminosity for NGC 1068, NGC 4945, NGC 253, M 82, the LMC and the Milky Way. Taken from Lenain et al. (2010).

originates from EIC processes on another population of leptons within the hot plasma located in the vicinity of the accretion disc. NGC 1068 is believed to have an accretion disc, because the soft X-ray spectrum, as measured by instruments such as *XMM-Newton* is dominated by thermal reflection emission (Kinkhabwala et al., 2002). Modelling the synchrotron and SSC emission from this component leads to the conclusion that the emission is negligible compared with that produced in the component responsible for the high-energy γ-ray emission. An alternative model (Lenain et al. 2010) posits that the hard X-ray emission observed with *INTEGRAL* and the high-energy γ-ray emission detected with *Fermi* originate from the same spacial component. This requires that the overall high-energy part of the SED be due to EIC processes from the same population of leptons and this would be tightly constrained by the available data; however, the particle energy distribution that results is unable to account for the SED in the radio domain.

The detection of both Sy1s and Sy2s at such high energies is of great interest to astronomers working in the TeV regime. The SEDs produced by Foschini et al. (2009) for the *Fermi*-detected Sy1s imply that two of the objects, PKS 1502+036 and 1H 0323+342, may emit at TeV energies, although the expected flux is relatively low. PKS 1502+036 is not a particularly promising prospect as it is situated at a redshift of $z = 0.49$, so any TeV emission is very likely to be strongly attenuated by the EBL. 1H 0323+342, however, is situated at a much lower redshift of $z = 0.061$ and so there is a much better chance of any very high energy emission being detectable.

4.4 Studying Seyfert Galaxies with the H.E.S.S. Telescopes

The detection of M87 in very high energy γ-rays, as discussed in Section 3.4.1, has led to the development of many different models to explain emission from such misaligned sources, but due to a lack of available dat, it has proved difficult to constrain many of the variables required by such complicated models (see Chapter 5). Due to the large angle of incidence between the line of sight and the jet in M87, these models must have a mechanism other than pure Doppler boosting to explain how radiation is emitted at energies in the TeV range, leading to the possibility that other misaligned AGN could also be sources of very high energy γ-rays. Detection of further misaligned AGN could be used to constrain some of the parameters in the proposed models and would open up a new avenue of investigation for IACTs. The recent detection of both Sy1s and a Sy2 at *Fermi*-LAT energies, discussed in Section 4.3, and the resulting predictions for TeV emission, would appear support this conclusion.

The study of Seyfert galaxies using the H.E.S.S. array, described in this chapter was initially carried out between 2008 and 2009, before the launch of the *Fermi* satellite, with further work carried out in October 2010. This means that no data from the *Fermi* satellite were used in the selection process. To find a list of Seyfert galaxies that might emit VHE γ-rays, a catalogue of sources detected at lower γ-ray energies with the *INTEGRAL* satellite was used (http://hea.iki.rssi.ru/rsdc/catalog/index.php?type=IGR&status=current accessed during August 2008). This catalogue contained data for 138 AGN which were then sorted by their location to determine those observable with the H.E.S.S. telescopes, which can observe objects with declinations between $\sim +20^\circ$ and $\sim -65^\circ$. This left a total of 92 potential sources to be studied. The identifiers of the remaining AGN were then used to determine the type and redshift of each using the SIMBAD astronomical database (http://simbad.u-strasbg.fr/simbad/ accessed throughout the study), and any with redshifts above 0.3 were excluded as any VHE emission is likely to be heavily attenuated by the EBL (see Section 3.5). The R.A. and Dec. of these objects were then used to determine those that had appeared in the field of view of the H.E.S.S. telescopes during previous observations (within $\sim 2^\circ$ of the centre of the telescopes), and any Seyfert galaxies for which data were unavailable were disregarded. Finally, the data were checked to determine whether the available telescope runs had been affected by adverse weather conditions or hardware faults, and runs failing these checks were omitted. This left a total of 10 Seyfert galaxies (6 Sy1, 1 Sy1.5 and 2 Sy2s), 1 Unclassified AGN (believed to be of type 2) and a quasar with Seyfert-like properties.

To increase the size of the sample the *XMM-Newton* X-ray catalogue was consulted using

Object	R.A. (J2000.0)	Dec. (J2000.0)	Class	Catalogue	Livetime (h)
Mrk 50	12h 23m 24.1s	+02° 40' 44.4"	Sy1	*INTEGRAL*	16.6
3C273	12h 29m 06.4s	+02° 03' 08.6"	Quasar	*INTEGRAL*	17.1
4U 1344-60	13h 47m 36.0s	-60° 37' 03.8"	Sy1.5	*INTEGRAL*	11.5
Circinus Galaxy	14h 13m 09.9s	-65° 20' 20.47"	Sy2	*INTEGRAL*	3.2
GRS 1734-292	17h 37m 24.3s	-29° 10' 48.0"	Sy1	*INTEGRAL*	149.3
IGR J14471-6319	14h 47m 14.9s	-63° 17' 19.2"	Sy2	*INTEGRAL*	41.7
IGR J17204-3554	17h 20m 21.8s	-35° 52' 48.2"	Uncl. AGN	*INTEGRAL*	30.8
IGR J17488-2353	17h 48m 55.1s	-32° 54' 52.1"	Sy1	*INTEGRAL*	7.2
IGR J22367-1231	22h 36m 46.5s	-12° 32' 42.63"	Sy1	*INTEGRAL*	3.6
NGC 1068	02h 42m 40.7s	-00° 00' 47.8"	Sy2	*INTEGRAL*	14.8
NGC 1365	03h 33m 36.3s	-36° 08' 27.8"	Sy1	*INTEGRAL*	14.5
NGC 7469	23h 03m 15.7s	+08° 52' 25.3"	Sy1	*INTEGRAL*	6.9
Mrk 1014	01h 59m 50.3s	+00° 23' 41.0"	Sy1	*XMM-Newton*	7.4
Mrk 1501	00h 10m 31.0s	+10° 58' 29.5"	Sy1	*XMM-Newton*	9.4
Mrk 573	01h 43m 57.8s	+02° 20' 59.7"	Sy2	*XMM-Newton*	21.1
3C 120	04h 33m 11.1s	+05° 21' 15.6"	Sy1	*XMM-Newton*	4.8

Table 4.1: List of AGN selected for study, including position (taken from the SIMBAD Astronomical Database), classification of the object, the catalogue from which the object was initially found, and the amount of H.E.S.S. data available.

the online facility Xcat (http://xcatdb.unistra.fr/2xmmidr3/catentries accessed during November 2008). This produced a list of $\sim$ 200 possible sources; however a large percentage of these were in close proximity to one another. The positions of the X-ray sources from the *XMM-Newton* catalogue were then cross correlated with the positions of known Seyfert galaxies using the SIMBAD astronomical database. It was found that many of the X-ray sources were associated with the same Seyfert galaxy and that, in some cases, the X-ray sources from the catalogue were further from the nearest Seyfert galaxy than the satellite's point-spread function of $\sim 4°$. Excluding these cases left 34 possible sources for four of which H.E.S.S. data were available (three Sy1s and one Sy2). The full set of AGN studied is listed in Table 4.1. For most of the objects studied this was the first time they had been investigated using VHE data.

The analysis of the objects was carried out using both the ring-background and reflected-background methods discussed in Section 2.5. Upper limits at the 99% confidence level were then calculated for each object above the threshold for the observations using the method described in Section 2.7, assuming a spectral shape similar to that of M87 with a spectral index $\Gamma \approx 2.2$ (Aharonian et al., 2006d). The runs analysed for each object are listed in Appendix A.

4.5 Discussion of Individual Sources

4.5.1 3C273

3C273 is one of only two objects in this study not classified as a Seyfert galaxy; however, it does display a number of Seyfert-like properties, including broad emission lines and the blue bump typical of Seyfert galaxies, making it an interesting object to study. The object, located in the constellation Virgo, is a flat-spectrum radio quasar, and is the nearest such object, with a redshift of $z = 0.158$. Its SED shows the twin humps typical of blazars (Pacciani et al., 2009). The object was first detected in γ-rays at energies > 100 MeV by the *COS-B* satellite in July 1976 (Swanenburg et al., 1978), and again in June 1978 (Bignami et al., 1981). During the operation of *EGRET*, the source was observed on many occasions, although it was not always detected; this suggested variability at high energies, later confirmed by the detection of a flux variation from $(22 \pm 5) \times 10^{-8}$ photons cm^{-2} s^{-1} to $(56 \pm 12) \times 10^{-8}$ photons cm^{-2} s^{-1}, for $E > 100$ MeV, during the campaign of October-November 1993 (von Montigny et al., 1997). Further observations of variability have shown correlation between flux variation at X-ray energies (using data from *RXTE/PCA*) and in the near infrared (with data taken by the UKIRT telescope), with X-ray lag < 1 day (Lawson et al., 1999).

Data collected with the H.E.S.S. telescopes between April 13th 2004 and May 10th 2007, made up of 44 runs with a total livetime of approximately 17 hours, were analysed. No significant detection was found using either the ring-background model, which returned a significance of only 0.98 σ above background variations, or the reflected-background, which returned a significance of 0.99 σ above background. Both methods of analysing the background are in agreement on the low significance observed in the vicinity of the object. The significance skymap (Figure 4.4) shows an area close to 3C273 with a significance of $\approx 3\sigma$; however, this is most likely an artifact of the analysis of the background as there are a number of other areas in the plot of similar significance. Since the area of higher significance is extended, even if it does represent a very marginal detection it is unlikely to be associated with 3C273 which would be expected to resemble a point source due to the extragalactic nature of the object. An upper limit for 3C273 of 4.5×10^{-12} photons cm^{-2} s^{-1} was calculated at a confidence limit of 99% with a threshold energy of 0.26 TeV. Additionally, the number of pixels of each significance (with a bin size of 0.05) is shown in Figure 4.5, plotted against significance and normalised such that the maximum number of pixels in a single bin is 1. This shows a good fit to a Gaussian function with a mean of 0, suggesting that the background is randomly distributed as would be expected, explaining the negative significances seen in Figure 4.4.

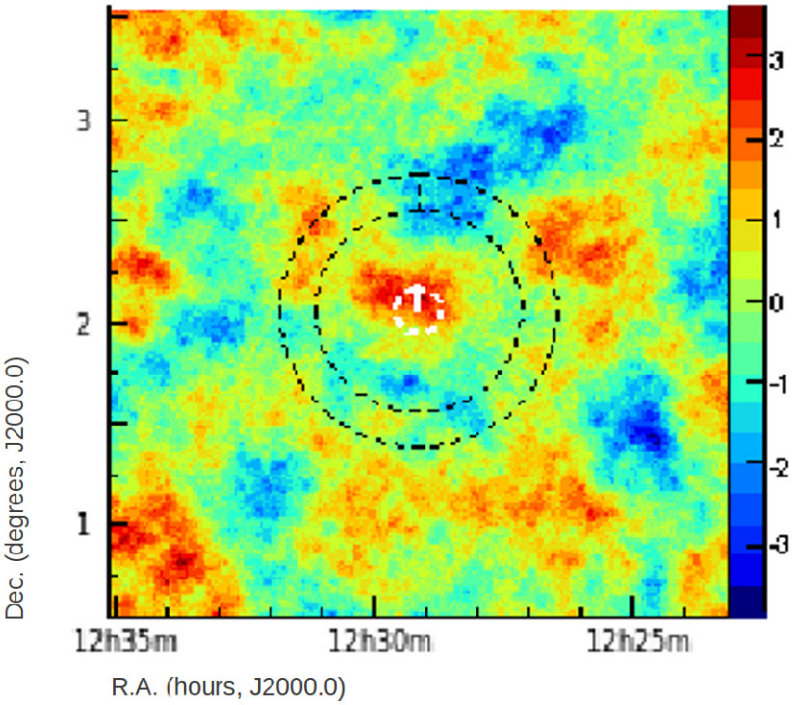

Figure 4.4: A γ-ray sky significance map of the area around 3C273. The right hand bar corresponds to measured significance above background in standard deviation units. The central white circle indicates the position of the object and the size of the PSF of the H.E.S.S. array, while the 2 outer circles indicate the area used during analysis of the background by the ring background method.

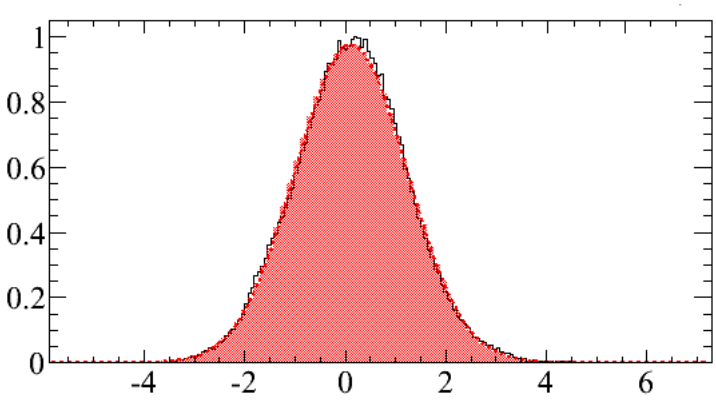

Figure 4.5: The number of pixels of each significance (with a bin size of 0.05) plotted against significance, the black line, showing a mean significance of 0.12, normalised such that the maximum number of pixels in a single bin is 1. The red shaded region represents a Gaussian function with a mean of 0.

4.5.2 Mrk 50

Mrk 50 is a Sy1 nucleus with a redshift $z = 0.023196$ (Paturel et al., 2002) located outside the Galactic plane. It is hosted in an elliptical galaxy with an extended halo (Adams, 1977). Despite being detected by the INTEGRAL satellite (Krivonos et al., 2007) there are no high energy studies of the object in the literature.

The H.E.S.S. data available for Mrk 50 were collected between 13th April 2004 and 10th May 2007, with just over 16 hours of usable livetime. The object was not detected using either the ring-background model or the reflected-background model; these analyses returned significances above background of 0.345 σ and -0.121 σ, respectively. The object observed to the northeast of Mrk 50 (See Figure 4.6) is a H.E.S.S. unidentified source; judging by the observed extension, it is probably Galactic. It is unlikely that this object will have had any effect on the calculation of the background via the ring background method as it is outside the ring used. An upper limit for Mrk 50 of 4.1×10^{-12} photons cm^{-2} s^{-1} was calculated, at a confidence limit of 99%.

4.5.3 4U 1344-60

4U1344-60, believed to be a Seyfert 1.5 galaxy, is situated at a redshift of $z = 0.012 \pm 0.001$ (Piconcelli et al., 2006). The object was first detected with the *Uhuru* X-ray Observatory while scanning the Galactic plane (Forman et al., 1978). The first accurate position of the object was reported by Warwick et al. (1988) using *EXOSAT* data. It was first detected above 10 keV in the 2nd *IBIS* survey (Bird et al., 2006). Owing to the object's position deep in the Galactic plane, it is relatively difficult to observe across a number of wavelengths (especially from the optical through to soft X-rays), but it was eventually optically identified as a type 1 Seyfert Galaxy by Masetti et al. (2006a). The X-ray spectral properties of the object were first studied in detail using data from *XMM-Newton*, and the source is included in the first INTEGRAL AGN catalogue (Beckmann et al., 2005). Piconcelli et al. (2006) found that 4U1344 displays a heavily absorbed X-ray spectrum even after correcting for the large Galactic extinction.

The H.E.S.S. data analysed for 4U 1334-60 were collected between 11th April 2005 and 18th May 2010, and totalled just over 11 hours of good quality livetime. Despite the object's position behind the Galactic plane, no H.E.S.S. sources are visible on the significance map (see Figure 4.7). Both background methods produced comparable significances, the ring-background model returning a significance of -0.11 σ above background and the reflected-background model returning -0.01 σ above background. The negative significance seen is likely due to fluctuations in the background. The spatial variation in the detected background can be seen in the significance map

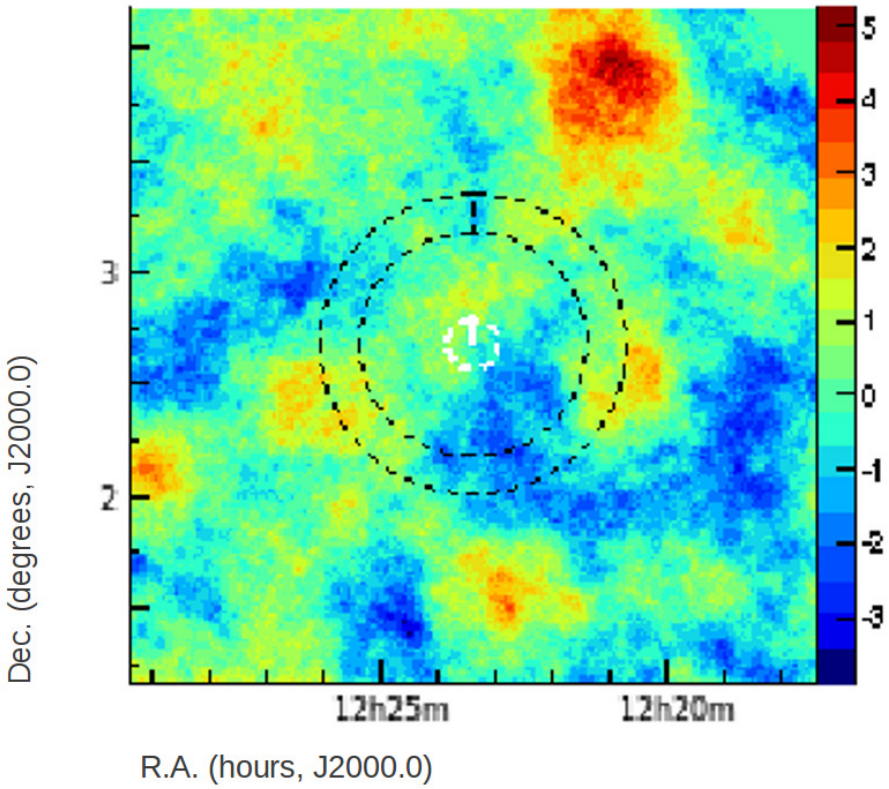

Figure 4.6: A γ-ray sky significance map of the area around MRK 50. The right hand bar corresponds to measured significance above background in standard deviation units. The central white circle indicates the position of the object and the size of the PSF of the H.E.S.S. array, while the 2 outer circles indicate the area used during analysis of the background by the ring background method.

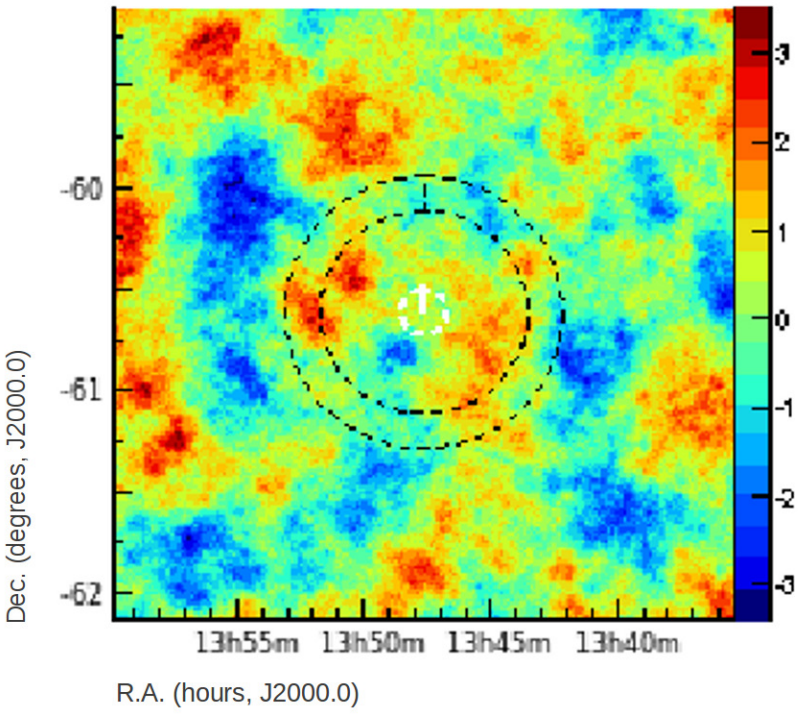

Figure 4.7: A γ-ray sky significance map of the area around 4U 1334-60. The right hand bar corresponds to measured significance above background in standard deviation units. The central white circle indicates the position of the object and the size of the PSF of the H.E.S.S. array, while the 2 outer circles indicate the area used during analysis of the background by the ring background method.

by the relatively large number of areas with significance $\gtrsim 2\sigma$. An upper limit for 4U 1334-60 of 2.6×10^{-12} photons cm^{-2} s^{-1} was calculated at a confidence level of 99% with a threshold energy of 0.51 TeV.

4.5.4 The Circinus Galaxy

The Circinus Galaxy is a large, nearby spiral galaxy with a redshift of $z = 0.001421$ (Paturel et al., 2002), situated behind the Galactic Centre where the high stellar density and dust extinction make it difficult to study at optical wavelengths. The object is at an inclination of $i = 64°$ (de Vaucouleurs et al., 1991). At its centre, it harbours a Seyfert 2 nucleus surrounded by a circumnuclear starburst region. X-ray spectra of the nucleus show a hard spectrum and high equivalent width Fe Kα emission, characteristic of Compton reflection from cold gas illuminated by a power-law continuum (Yang et al., 2009). This, combined with the detection of a Compton shoulder in Chandra observations (Bianchi et al., 2002) confirmed by XMM-Newton (Molendi et al., 2003), leads to the conclusion that Compton-thick matter is present at the centre of the object.

Compton-thick AGN provide a significant component of the hard cosmic X-ray background, due to their hard spectra which peak at 30-40 keV and drop off at higher energies (Setti & Woltjer, 1989; Madau et al. 1994). The Circinus Galaxy is the third-brightest Compton-thick AGN that can be studied in detail.

There are very little usable H.E.S.S. data available for the Circinus Galaxy, with only just over 3 hours of livetime available for the object, other observations taken of the region had to be discounted due to adverse weather conditions or hardware problems with the telescope. The data were collected between 15th May 2006 and 29th March 2007. Both background models report a lack of detection, as would be expected considering the very short livetime and the likely weak nature of any VHE γ-ray emission from the object, with the ring-background model reporting a significance of 0.08 σ above background (see Figure 4.8) and the reflected-background model reporting 0.50 σ above background. The slight discrepancy between the two methods may be due to a higher γ-ray background within the ring used by the ring background method than is present with the reflected background approach. To the northwest of the Circinus Galaxy is a region of relatively high significance ($\approx 4\sigma$) which is not associated with any known VHE γ-ray source; however there are large background fluctuations across the entire region, probably due to the position of the Circinus Galaxy close to the Galactic plane and this high significance region is likely an artifact of these background fluctuations. An upper limit for the Circinus Galaxy of 2.1×10^{-11} photons cm^{-2} s^{-1} was calculated at a confidence level of 99% with a threshold energy of 0.68 TeV.

4.5.5 GRS 1734-292

GRS 1734-292 is a Sy1 nucleus at a redshift of $z = 0.0214$ and is located 1.8° from the Galactic centre (Sazonov et al., 2004). It was first detected in 1990 with the Russian *GRANAT* X-Ray/γ-ray satellite (Pavlinsky et al., 1992). It was initially believed to be a Galactic X-ray binary, and an inferred X-ray luminosity of $\sim 10^{36}$ erg s^{-1} was calculated under this assumption. Subsequent optical observations (Martí et al., 1998) showed very strong broad emission lines, identifying the object as the nucleus of a Sy1 galaxy. Thus far, the host galaxy has not been directly detected at optical wavelengths owing to the high ($\approx$ 6 magnitude) visual absorption along the line of sight through the Galactic plane. Since the discovery of the nature of GRS 1734-292, the X-ray luminosity has been calculated to be $\sim 10^{44}$ erg s^{-1} (Sazonov et al., 2004), so it is one of the five or so most X-ray luminous AGN within 100 Mpc (Sazonov et al., 2004). Evidence of high energy emission from the object was provided by the detection of a potentially associated source with *EGRET* (Hartman et al., 1999). Owing to the high density of bright sources in the vicinity of the

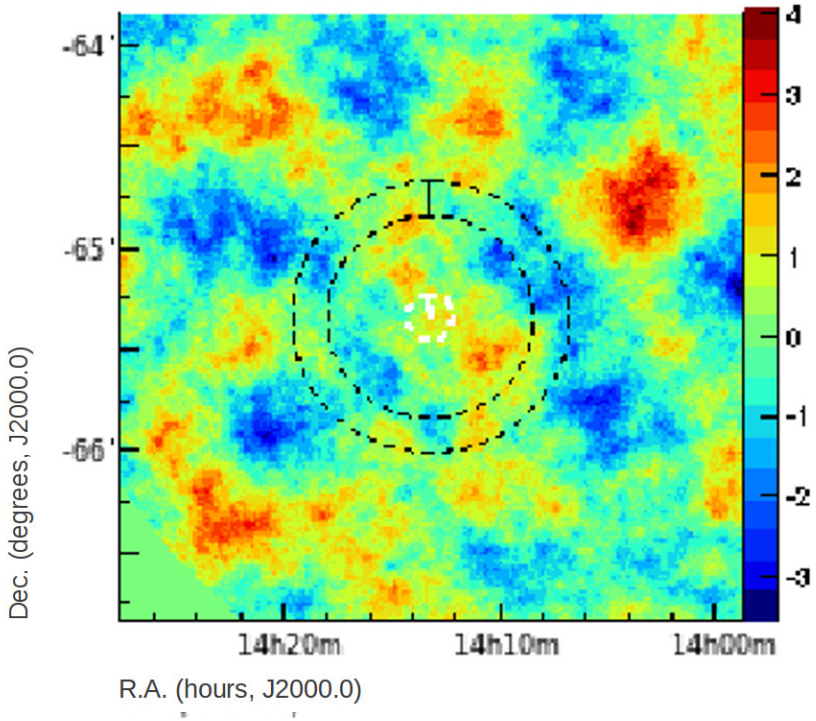

Figure 4.8: A γ-ray sky significance map of the area around the Circinus Galaxy. The right hand bar corresponds to measured significance above background in standard deviation units. The central white circle indicates the position of the object and the size of the PSF of the H.E.S.S. array, while the 2 outer circles indicate the area used during analysis of the background by the ring background method.

object, spectroscopy of GRS 1734-292 could not be carried out until the successful detection with the hard X-ray imager IBIS aboard the *INTEGRAL* satellite, when Sazonov et al. (2004) found that the spectrum is similar to that of other Seyfert galaxies.

There is a positional coincidence of GRS 1734-292 with the *EGRET* γ-ray source 3EG J17362908, a BL Lac object; however it is unlikely that it is connected with this object. There is a high probability ($\sim$ 50%) of finding an INTEGRAL source within the large error box of 3EG J1736-2908 (Sazonov et al., 2004), and the optical emission from GRS 1734-292 is strongly dominated by the broad lines typical of a Sy1 nucleus, which contrasts strongly with what is usually seen in a typical BL Lac where it is very difficult to discern any emission lines against the strong continuum. In addition, the radio flux observed from GRS 1734-292 is three orders of magnitude lower than what would be expected from the BL Lac object 3EG J1736-2908.

A large amount of H.E.S.S. data is currently available for GRS 1734-292, comprising over 149 hours between 29th March 2004 and 23rd April 2005. At the eastern edge of the significance map (see Figure 4.9) HESS J1745-303 can be seen with a significance of $\sim 7\sigma$ above background, while there is no evidence of a detection at the position of GRS 1734-292. The background models both return negative significances; the ring-background model returns a significance of -0.39 σ above background and the reflected-background model returns a significance of -0.96 σ above background. The negative significance and the discrepancy seen between the significances produced using the two models can be attributed to GRS 1734-292's proximity to the Galactic centre, resulting in a noisy background that is difficult to estimate. An upper limit for GRS 1734-292 of 1.4×10^{-12} photons cm^{-2} s^{-1} was calculated at a confidence level of 99% with a threshold energy of 0.22 TeV.

4.5.6 IGR J14471-6319

IGR J14471-6319 is a Seyfert 2 nucleus located behind the Galactic plane at a redshift of $z = 0.038$ (Malizia et al., 2007). Owing to its position in the Galactic plane, the object has not been studied in great detail. The *INTEGRAL* source is coincident with multiple soft X-ray sources detected by the *ROSAT* satellite; however, optical spectroscopy shows these to be ordinary Galactic stars and so unrelated to the INTEGRAL source (Masetti et al., 2006b). The object displays a photon index of $\Gamma = 1.7^{+1.04}_{-1.03}$ between 2 keV and 10 keV (Malizia et al., 2007).

Data available for IGR J14471-6319 have been collected throughout the life of the H.E.S.S. telescopes (between 25th April 2004 and 16th June 2010), with just over 41 hours of good quality data collected in total. The analysis fails to reveal a detection of the object, with a significance of -0.19 σ above background being returned via the ring-background method and -1.11 σ above

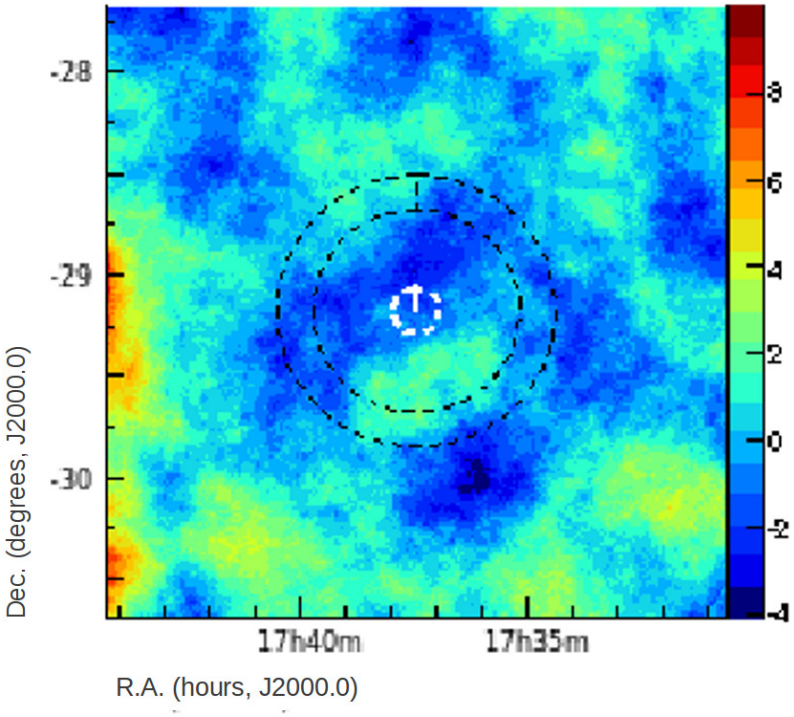

Figure 4.9: A γ-ray sky significance map of the area around GRS 1734-292. The right hand bar corresponds to measured significance above background in standard deviation units. The central white circle indicates the position of the object and the size of the PSF of the H.E.S.S. array, while the 2 outer circles indicate the area used during analysis of the background by the ring background method.

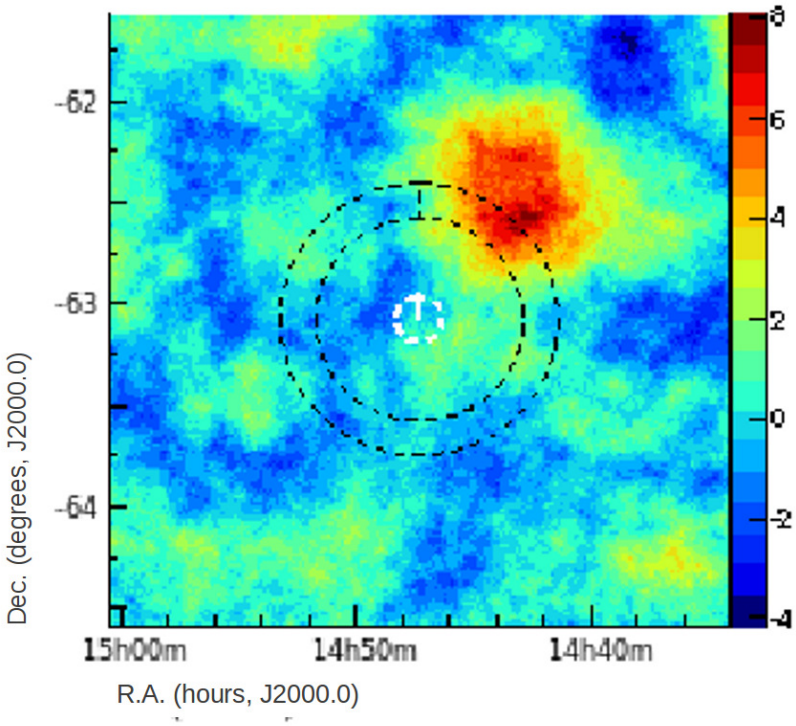

Figure 4.10: A γ-ray sky significance map of the area around IGR J14471-6319. The right hand bar corresponds to measured significance above background in standard deviation units. The central white circle indicates the position of the object and the size of the PSF of the H.E.S.S. array, while the 2 outer circles indicate the area used during analysis of the background by the ring background method.

background calculated using the reflected-background method. Slightly to the northwest of IGR J14471-6319 is the shell-type supernova remnant RCW 86, at a position of RA 14h 42m 42.96s Dec -62° 26' 41.6" (See Figure 4.10), which was detected in very high energy γ-rays using data collected by the H.E.S.S. telescopes and reported in Aharonian et al. (2009d). The presence of RCW 86 in the field of view probably accounts for the discrepancy between the significances calculated by the two methods. An upper limit for IGR J14471-6319 of 3.2×10^{-12} photons cm^{-2} s^{-1} was calculated at a confidence level of 99% with a threshold energy of 0.46 TeV.

4.5.7 IGR J17204-3554

The *INTEGRAL* source IGR J17204-3554 is an unclassified type 2 AGN (Bassani et al., 2005) believed to be situated at a redshift of only $z \sim 0.000021$. The object is situated behind the Galactic emission nebula NGC 6334, which has a complicated structure with a number of separated and localised star-formation sites established by radio and infrared observations (Bykov et al., 2006). The first hint of an obscured AGN behind NGC 6334 was the detection of the radio source,

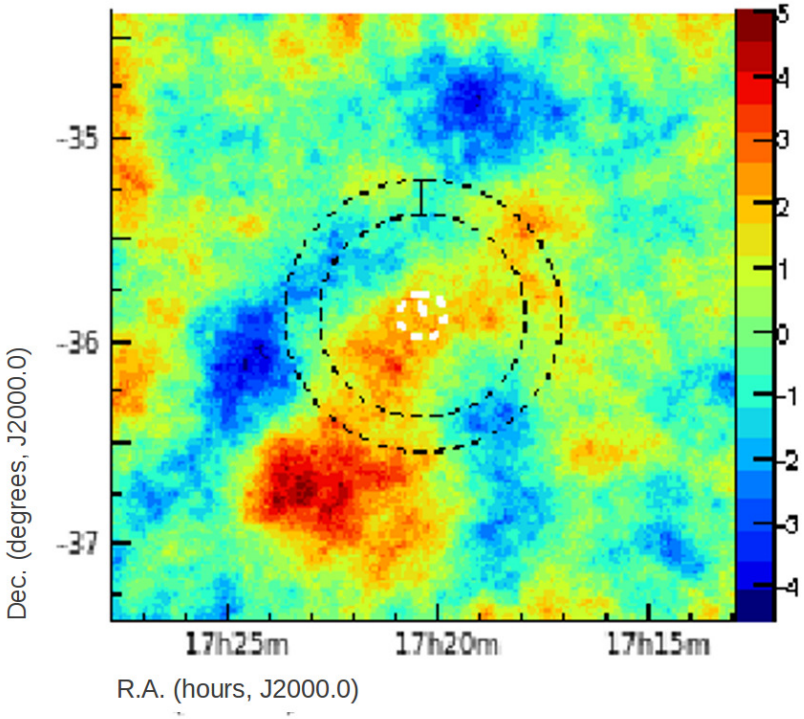

Figure 4.11: A γ-ray sky significance map of the area around IGR J17204-3554. The right hand bar corresponds to measured significance above background in standard deviation units. The central white circle indicates the position of the object and the size of the PSF of the H.E.S.S. array, while the 2 outer circles indicate the area used during analysis of the background by the ring background method.

NGC 6334B which is coincident with the *INTEGRAL* source. It was suggested by Moran et al. (1990) that NGC 6334B could be a background extragalactic source. The broadband spectral characteristics of NGC 6334B are consistent with those observed in obscured accreting sources associated with AGN, and it shows a nonthermal spectrum up to at least 100 keV (Bykov et al., 2006).

Observations of IGR J17204-3554 with the H.E.S.S. array were conducted between 22nd May 2004 and 20th August 2005 during which ∼30 hours of usable data was collected. Analysis of the data showed no evidence for detection of the object; the significance returned using the ring-background method is 0.49 σ above background, while that returned using the reflected-background method is 0.73 σ above background. The $\approx 5\sigma$ region southeast of IGR J17204-3554 in Figure 4.11 is HESS J1741-302, a H.E.S.S. unidentified source that may be associated with PSR B1737-30 (Tibolla et al., 2009). An upper limit for IGR J17204-3554 of 5.5×10^{-13} photons cm^{-2} s^{-1} was calculated at a confidence level of 99% with a threshold energy of 0.24 TeV.

4.5.8 IGR J17488-3253

The first detection of IGR J17488-3253 was made with *ROSAT* during the *ROSAT* all-sky survey performed in the period July 1990 to February 1991 (Voges, 1992), however the positional uncertainty on the source made it difficult to pinpoint a possible counterpart. The object was also observed with the HRI instrument aboard *ROSAT*, which was able to localise the object with an uncertainty of a few arcseconds; within this error box, however, no optical, radio or infrared counterpart was found (Stephen et al., 2005). Later observations of the region with *INTEGRAL* detected a high energy X-ray source associated with the *ROSAT* source (Stephen et al., 2005). The identification of the source was reported by Masetti et al. (2006b), who observed the source spectroscopically with the CTIO optical telescope of Cerro Tololo in Chile. The object was found to be a Sy 1, although a more accurate identification was impossible due to the low quality of the available spectrum. At energies between 17 keV and 60 keV, the flux detected with INTEGRAL is 1.06 ± 0.05 mCrab (Krivonos et al., 2007).

The H.E.S.S. data for the area around IGR J17488-3253 were collected between 14th June 2004 and 29th May 2009, and a total of ∼7.5 hours of usable livetime was available. The analysis found no evidence of a detection using either the ring-background model, which returned a significance of $-0.43\ \sigma$ above background (see Figure 4.12), or the reflected-background model, which returned a significance of $-1.2\ \sigma$ above background. The negative significances returned are likely due to background fluctuations. An upper limit for IGR J17488-3253 of 9.1×10^{-12} photons cm^{-2} s^{-1} was calculated at a confidence level of 99% with a threshold energy of 0.24 TeV.

4.5.9 IGR J22367-1231

IGR J22367-1231 is an INTEGRAL source associated with the Seyfert 1 galaxy Mrk 915, which is situated behind the Galactic plane at a redshift of $z = 0.024043$ situated behind the Galactic plane. Mrk 915 has a high inclination with respect to the line of sight, $i \sim 80°$ and has a companion galaxy 126" to the southeast (Keel, 1996). Exact classification of the object has been difficult. It has been suggested that it should be classified as a Seyfert 1.5 by Bennert et al. (2006), as during optical observations carried out in 2004 they detected easily recognised broad and superimposed narrow components of the Hα and Hβ spectral lines; however, CTIO spectra taken in June 2008 and reported by Trippe et al. (2010) show it to be a type 1.9 Seyfert galaxy. This is further complicated by a report by Goodrich (1995) who detected type variability between 1984 and 1993 during which period the object went from Seyfert 1.5 to Seyfert 1.9.

H.E.S.S. data on IGR J22367-1231 were collected between 21st July 2004 and 2nd July 2006,

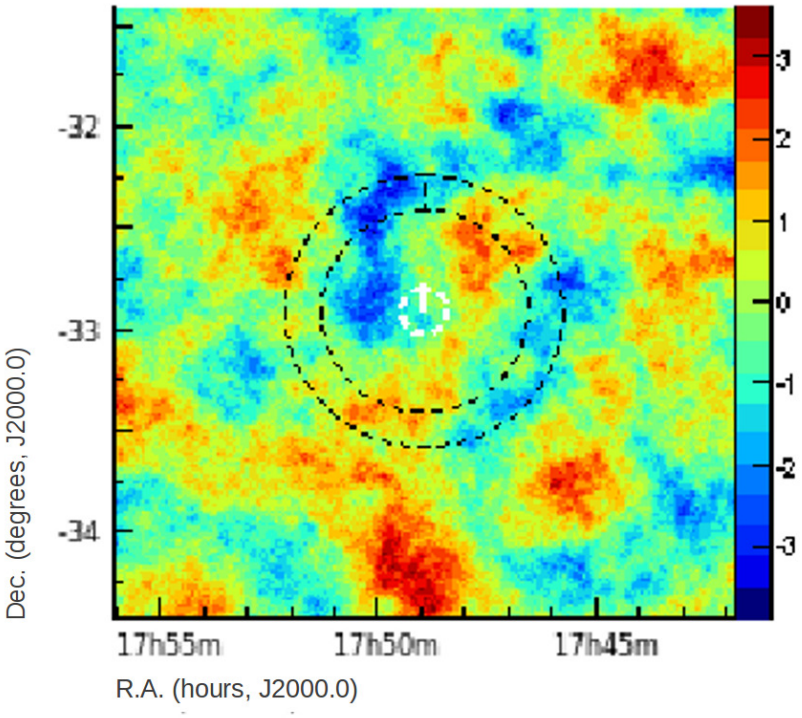

Figure 4.12: A γ-ray sky significance map of the area around IGR J17488-3253. The right hand bar corresponds to measured significance above background in standard deviation units. The central white circle indicates the position of the object and the size of the PSF of the H.E.S.S. array, while the 2 outer circles indicate the area used during analysis of the background by the ring background method.

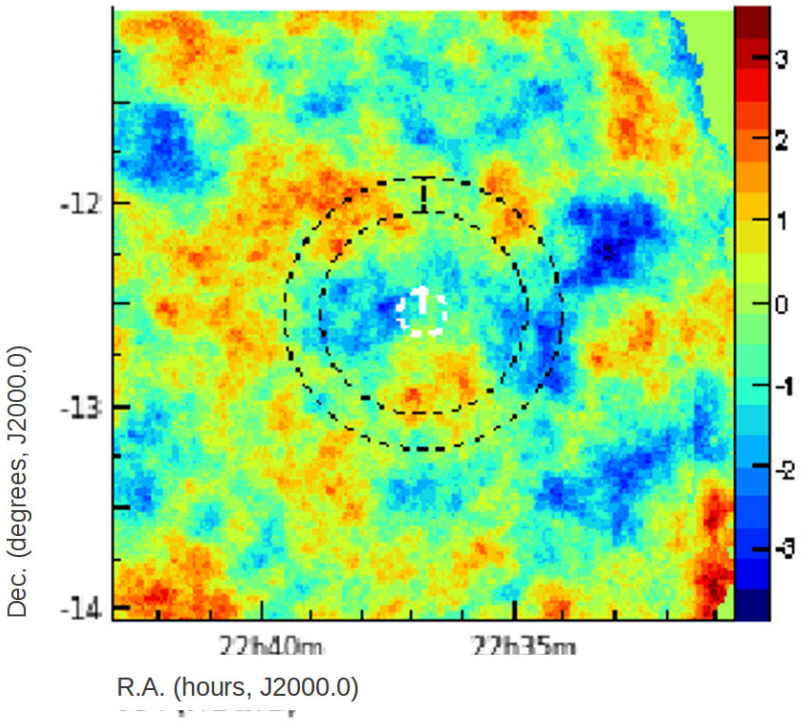

Figure 4.13: A γ-ray sky significance map of the area around IGR J22637-1231. The right hand bar corresponds to measured significance above background in standard deviation units. The central white circle indicates the position of the object and the size of the PSF of the H.E.S.S. array, while the 2 outer circles indicate the area used during analysis of the background by the ring background method.

although much of the available data were unusable due to poor weather conditions or technical problems with the telescopes, leaving only 3.5 hours of livetime. There is no evidence of a detection from the object, with the ring-background model returning a significance of -0.41 σ above background and the reflected-background model returning a significance of -0.70 σ above background (See Figure 4.13). The negative significances returned are probably due to the low statistics. An upper limit for IGR J22367-1231 of 5.8×10^{-12} photons cm^{-2} s^{-1} was calculated at a confidence level of 99% with a threshold energy of 0.24 TeV.

4.5.10 NGC 1068

NGC 1068 is the brightest known Seyfert 2 galaxy and is one of the oft-quoted "archetypes" of the class. It is located at a distance of $z = 0.003786$, making it also the closest Seyfert 2. As with all Seyfert 2 galaxies, it harbours an obscured Seyfert 1 core, as reported by Antonucci & Miller (1985) who used the data collected via spectropolarimetry to argue for the unification of AGN. Due to the object's relative proximity, the extension of the host galaxy is highly visible at

optical wavelengths. The centre of the object displays activity related to both starburst and AGN phenomena (eg. Lester et al., 1987; Jaffe et al., 2004), while the central nucleus is surrounded by a dusty torus that dominates the soft X-ray emission by reflection of radiation from the central nucleus. The starburst region is located at a distance of $\sim$ 1 kpc from the core and dominates the infrared emission (Thronson et al., 1989). Caproni et al. (2006) studied the morphology of the inner warped disc, coming to the conclusion that the 43 GHz central radio component is most likely dominated by thermal emission from the hot inner region of the obscuring torus; however, an earlier study by Gallimore et al. (2004), found evidence that the northeast radio component could be dominated by synchrotron emission, a view supported by more recent results from Hönig, Prieto & Beckert (2008), who suggested that the radio emission from the core could be dominated by synchrotron or free-free emission. At X-ray energies, data on NGC 1068 collected with the *Chandra* satellite show the existence of a hard power-law X-ray source, usually associated with Seyfert 1 galaxies (Young & Wilson, 2001), furthering the case for unification of the two types. High resolution X-ray studies of the object with Chandra have shown a large number of high energy emitting structures. At the centre of NGC 1068 is a very bright X-ray source coincident with the brightest radio and optical emission and about 550 pc northeast of this is an extended source of X-rays. This extended source of X-rays shows a large-scale structure reaching at least 6.6 kpc to the northeast and southeast including X-ray emission from the spiral arms and numerous point sources (Young et al., 2001); see Figure 4.14. It was discovered that the emission to the northeast of the nucleus is absorbed only by the Galactic column and thus is on the near side of the disc, while the southwestern emission region is more heavily obscured, suggesting that its origin is either inside or behind the disc.

Recently, a *Fermi*-LAT source, 1FGLJ0242+0007, was detected in the region of NGC 1068. Until Lenain et al. (2010) the *Fermi*-LAT source had no proposed counterpart in radio nor γ-rays. Lenain et al. (2010) concluded that this source is associated with NGC 1068 with a significance of 8.4σ (see Section 4.3.1). As has been mentioned, NGC 1068 harbours a starburst region, and such regions have also been detected in other objects at *Fermi* energies (Abdo et al, 2010b); however, the GeV luminosity of the object reported in Lenain et al. (2010) is far higher than that seen in M82 and NGC 253, in which the high-energy emission is dominated by starburst activity, suggesting a different explanation for the origin of such emission in NGC 1068.

Data available for analysis for NGC 1068 were collected by the H.E.S.S. array between the 11th October 2004 and the 6th September 2008, during which period $\sim$ 15 hours of usable data were collected. The significances returned by both background models are consistent with a lack of detection. The ring-background model returned a significance of 1.3 σ above background and

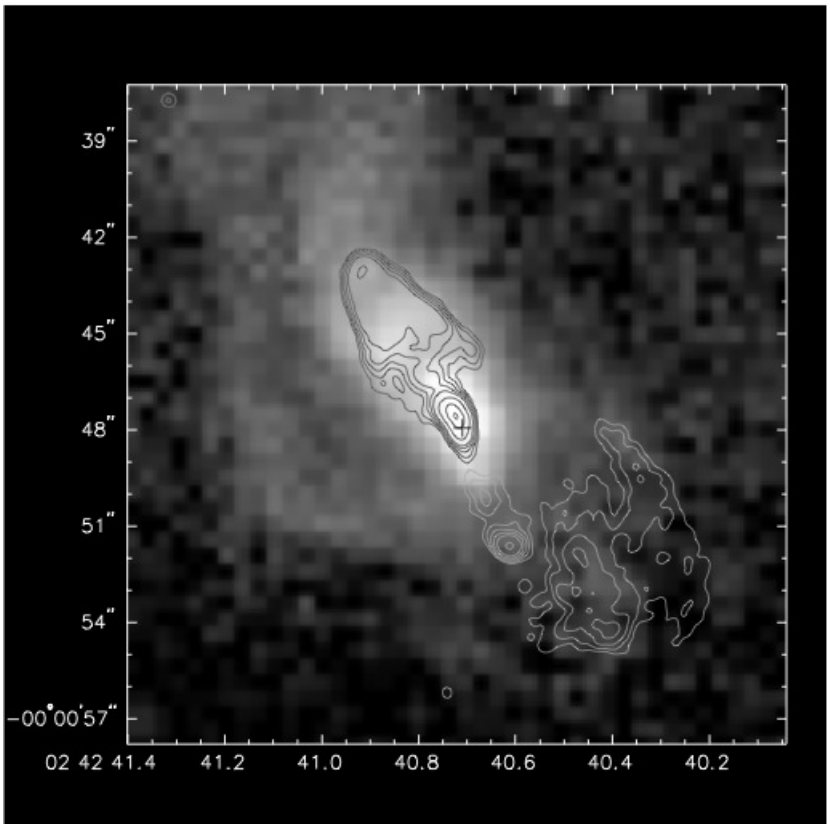

Figure 4.14: Superposition of the circumnuclear distribution of X-rays (gray scale) on a VLA 6 cm radio map (contours) for NGC 1068 with resolution 0.38" × 0.38". The cross marks the position of radio source S1, which is believed to coincide with the nucleus . Contours are plotted at 0.0005, 0.001, 0.002, 0.004, 0.008, 0.032, 0.128, and 0.256 Jy beam^{-1}. The gray scale is proportional to the logarithm of the X-ray intensity and ranges between log(counts pixel^{-1}) = 0 (black) and 3.0 (white). Taken from Young & Wilson (2001).

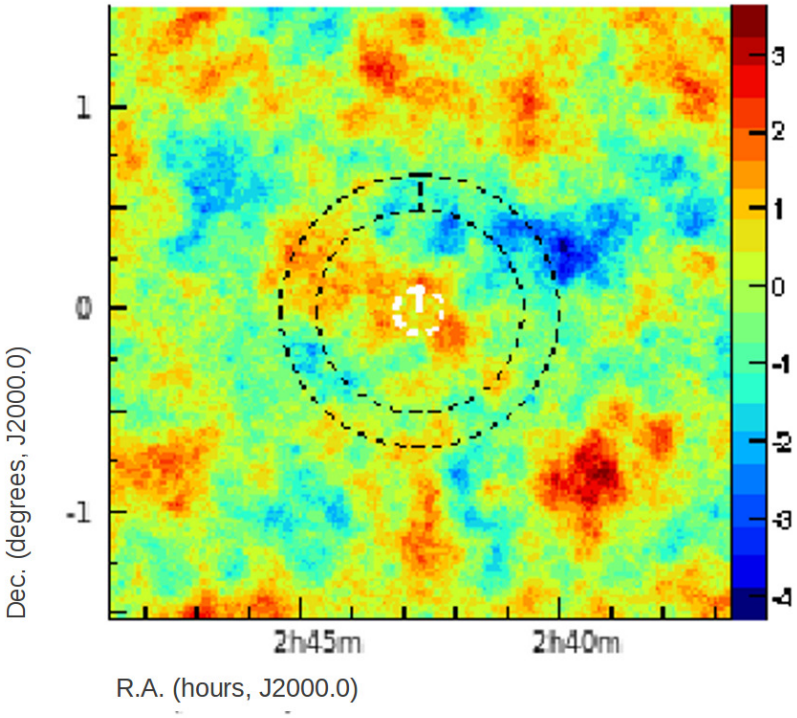

Figure 4.15: A γ-ray sky significance map of the area around NGC 1068. The right hand bar corresponds to measured significance above background in standard deviation units. The central white circle indicates the position of the object and the size of the PSF of the H.E.S.S. array, while the 2 outer circles indicate the area used during analysis of the background by the ring background method.

the reflected-background model returned a significance of 0.84 σ above background, consistent with one another. Southwest of the position of NGC1068, an area of relatively high background is observed ($\sim 3\sigma$), although this is consistent with background fluctuations (Figure 4.15). An upper limit for NGC 1068 of 5.1×10^{-12} photons cm^{-2} s^{-1} was calculated at a confidence level of 99% with a threshold energy of 0.26 TeV.

4.5.11 NGC 1365

NGC 1365 is a relatively nearby barred spiral galaxy at a redshift of $z = 0.0055$ (Risaliti et al., 2009) that harbours a Seyfert 1 nucleus at its core. Attempts to classify the Seyfert type have not been conclusive. Early results suggested that it could be a Seyfert 2 (Turner et al., 1993), but since then it has been suggested that it is more likely either a Seyfert 1.5 (Hjelm & Lindblad, 1996) or a Seyfert 1.8 (Risaliti et al., 2009). This difficulty in classification is due to the relatively complex multiwavelength properties of the object, many of which are unusual. NGC 1365 is at an inclination of 40° (Wang et al., 2009) and has a nuclear radio jet extending 5" southeast along the

galaxy's minor axis (Sandqvist et al., 1995). Around the nucleus of the galaxy is a star-forming ring with a diameter of ~ 1.3 kpc (Kristen et al., 1997).

At optical wavelengths, the degree of excitation of narrow emission lines is lower in the core region than in the extranuclear regions (Veileux et al., 2003); this observation cannot easily be explained as strong core absorption due to the presence of a broad component detectable in the Balmer lines (Schulz et al., 1999), usually indicative of a Seyfert 1.5 galaxy. X-ray observations with *ROSAT*, reported in Komossa & Schulz (1998), found a relatively low X-ray luminosity from the source, far lower than that expected from the infrared emission; this suggests either that the X-ray emission is almost completely obscured or that the infrared must originate elsewhere, possibly from the star-formation regions near the core, although in the latter case, the Hα line from the starburst region must be largely obscured. X-ray observations of the nucleus of NGC 1365 have revealed highly variable emission, with the object showing several spectral changes from Compton-thin to reflection-dominated states.

X-ray observations of the object have detected a compact central source that displays high absorption variability, with the optical depth varying from $N_H \sim 10^{23}$ cm^{-2} to $N_H > 10^{24}$ (Risaliti et al., 2007). This variability is suggested to be due to motion of a Compton-thick cloud crossing in front of the central source, at a distance comparable with that of the broad-line region ($\leq 10^{16}$ cm). X-ray emission has been detected using data from *Chandra* coincident with the position of the radio jet. This emission has been suggested as a candidate X-ray counterpart for the radio jet by Wang et al. (2009), although they remark that the X-ray spectrum observed is unusually soft for a radio jet and is best fitted by a model involving absorbed power-law emission with $\Gamma \sim 3.9$. Wang et al. (2009) theorise that the X-ray emission and radio jet are connected and likely represent synchrotron radiation from the same population of electrons. If this is the case, then the steep X-ray spectrum can be explained as the tail of the spectral distribution of the synchrotron emission.

The H.E.S.S. data analysed for NGC1365 were collected between 12th August 2005 and 12th October 2007. Over this period, $\sim$ 14.5 hours of usable data were collected. No evidence of a detection was found, with the ring-background model returning a significance of $-1.1\ \sigma$ above background and the reflected-background method returning a significance of $-0.78\ \sigma$ above background. The negative significances are consistent with background fluctuations, as is the relatively high significance ($\sim 3\ \sigma$) to the northwest of the position of NGC1365 (see Figure 4.16). An upper limit for NGC1365 of 2.8×10^{-12} photons cm^{-2} s^{-1} was calculated at a confidence level of 99% with a threshold energy of 0.29 TeV.

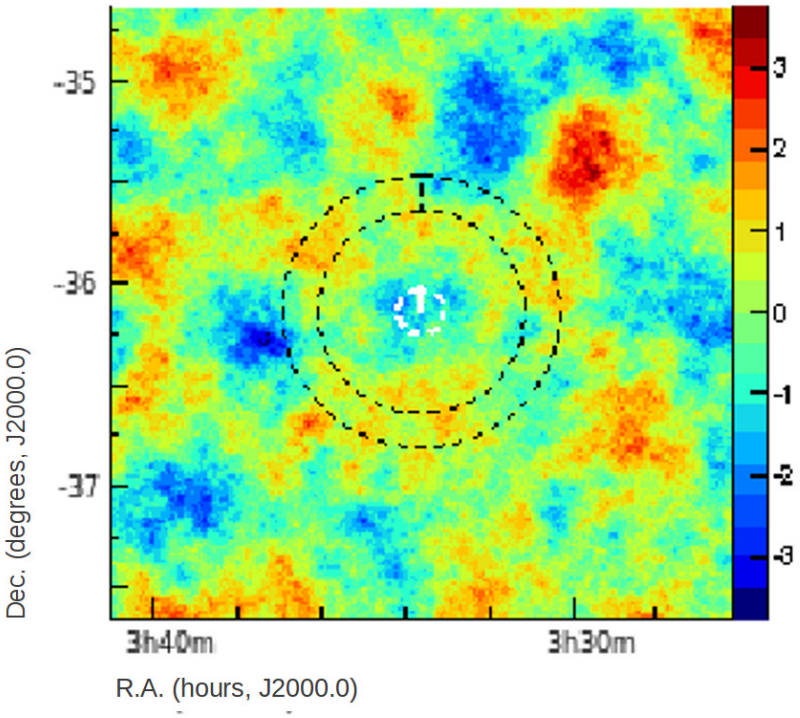

Figure 4.16: A γ-ray sky significance map of the area around NGC 1365. The right hand bar corresponds to measured significance above background in standard deviation units. The central white circle indicates the position of the object and the size of the PSF of the H.E.S.S. array, while the 2 outer circles indicate the area used during analysis of the background by the ring background method.

4.5.12 NGC 7469

NGC 7469 is a bright Seyfert 1 galaxy, with an angle of inclination $\theta = 18.2°$ (Nandra et al., 2000), situated relatively nearby at a redshift of $z = 0.0164$ (Artamonov et al., 2010). The host galaxy is a barred spiral of classification Sba. In most cases of ultraviolet and X-ray emission from Seyfert galaxies, a strong correlation is observed; however, for NGC 7469 this is not the case. During a ~ 1 month simultaneous *IUE* and *RXTE* monitoring campaign on the object performed in 1996, the correlation between ultraviolet and 1-10 keV X-ray fluxes was poor (Nandra et al., 1998). Strong, short-timescale variations were also detected at X-ray frequencies but not in ultraviolet. Correlation was detected, however, between the X-ray spectral index and the ultraviolet flux, with zero lag time. This was interpreted by the authors as strong support for the X-rays being produced by Compton upscattering of the ultraviolet photons. In the framework proposed, it is assumed that the observed variability of the ultraviolet flux is expected to directly modify the cooling rate of the corona, thus producing the observed X-ray spectral changes.

The H.E.S.S. data analysed for NGC 7469 were collected between 16th July 2004 and 23rd October 2006. Of the data available for NGC 7469, only 7 hours were of acceptable quality for analysis. No detection was found using either the ring-background method, which returned a significance of $-2.5\ \sigma$ above background, or the reflected-background method, which returned a significance of $-2.4\ \sigma$ above background. As can be seen in the significance sky map (Figure 4.17), the background is extremely variable across the sky, leading to the negative significances returned by the analysis. This apparent spatial variation in the background is most likely due to the low count statistics caused by the paucity of available data. An upper limit of 1.8×10^{-12} photons cm^{-2} s^{-1} was calculated at a confidence level of 99% with a threshold energy of 0.32 TeV.

4.5.13 Mrk 1014

Mrk 1014 is a Seyfert 1 galaxy, situated at a redshift of $z = 0.163$ (Boller et al., 2002). It is extremely bright in the far-infrared (Yun et al., 2001). It was first discovered as an ultraviolet-excess object in the Byurakan objective-prism survey (Markarian et al., 1977). It is radio-quiet, with a radio-loudness parameter of 2.1 (Kellermann et al., 1989), and the associated radio source was later resolved using data from the VLA as a triple source, composed of two radio knots within 3.1 kpc on either side of a central component corresponding to the nucleus of the object (Leipski & Bennert, 2006). There is evidence of strong jet-cloud interactions within the extent of the radio components (Fu & Stockton, 2009). *XMM-Newton* observations were analysed by Boller et al.

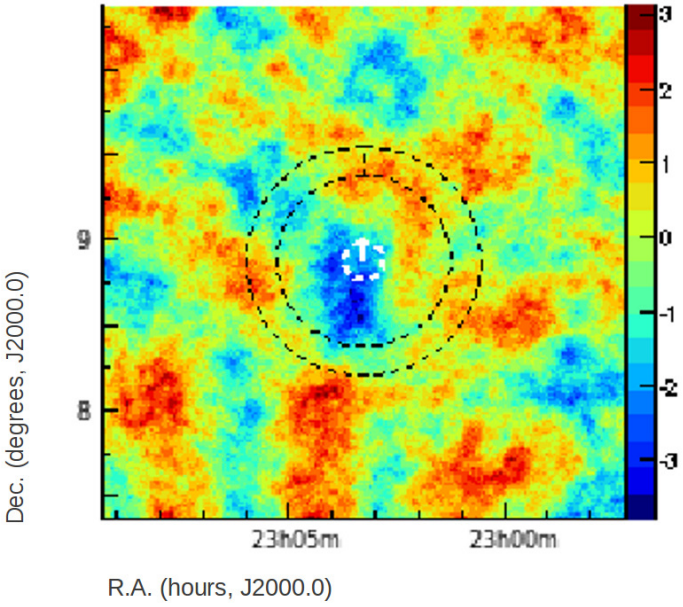

Figure 4.17: A γ-ray sky significance map of the area around NGC 7469. The right hand bar corresponds to measured significance above background in standard deviation units. The central white circle indicates the position of the object and the size of the PSF of the H.E.S.S. array, while the 2 outer circles indicate the area used during analysis of the background by the ring background method.

(2002) to determine whether the dominant process behind 0.3-8 keV emission from the object is driven by the central AGN or by starburst activity. The observations from *XMM-Newton* revealed a power-law-dominated spectrum which may be up to 30 times more luminous than the soft X-ray excess. After modelling the data, the authors concluded that the central emission was most likely dominated by the AGN, as the existence of an X-ray starburst seems highly unlikely due to the low temperature and high luminosity found in the models used; while further support for this conclusion was drawn from the variability in the light curve.

The H.E.S.S. data available for Mrk 1014 were collected between 2nd November 2007 and 1st November 2008. Only about 7 hours of the data collected were of sufficiently high quality to be analysed. The significances calculated using both the ring-background method and reflected-background method are consistent with no detection, returning $-1.4\ \sigma$ above background and $-1.2\ \sigma$ above background, respectively. The object is relatively close to the edge of the field of view of the telescopes, as can be seen in Figure 4.18. Additionally there is a region of relatively high significance towards the south of the significance map, however this does not appear to be associated with any H.E.S.S. sources and there are no obvious potential counterparts in the region, suggesting that the high apparent significance is likely an artifact of the analysis, caused by the closeness to the edge of the telescope. An upper limit for Mrk 1014 of 4.8×10^{-12} photons cm^{-2} s^{-1} was calculated at a confidence level of 99% with a threshold energy of 0.26 TeV.

4.5.14 Mrk 1501

Mrk 1501 is an AGN presenting the classic broad-line emission associated with Seyfert 1 galaxies (Arp, 1968) and is believed to be at a redshift of $z = 0.0898$ (Véron-Cetty & Veron, 2000). The object is the brightest at optical wavelengths in a triple group of galaxies. It is a bright X-ray source; Schnopper et al. (1978) reported a flux between 0.2 keV and 10 keV of $F \approx 4\times10^{-11}$ erg cm^{-2} s^{-1}. The luminosity between 0.2 keV and 10 keV was later calculated by Piccinotti et al. (1982) to be $L \approx 10^{45}$ erg s^{-1}, making it the most luminous Sy1 in their sample. In the early part of this century, superluminal motion of a radio-emitting plasma was detected by Brunthaler et al. (2000), the first detection of its kind in a spiral galaxy, indicating that at least some of the emission from the object must be nonthermal. At radio (Schnopper et al., 1978) and optical wavelengths (Lloyd, 1984), Mrk 1501 has been known to show large-amplitude flux variations, and smaller-amplitude variations (of less than 50%) have been detected in the infrared (Lebofsky & Rieke, 1980) and ultraviolet (Chapman et al., 1985). More recently, a study by Salvi et al. (2002) found large-amplitude (10-fold) variability in the X-ray flux over timescales of years, but no short-term variability on timescales of $\sim$ 1000 s. Salvi et al. (2002) propose that the high X-ray luminosity

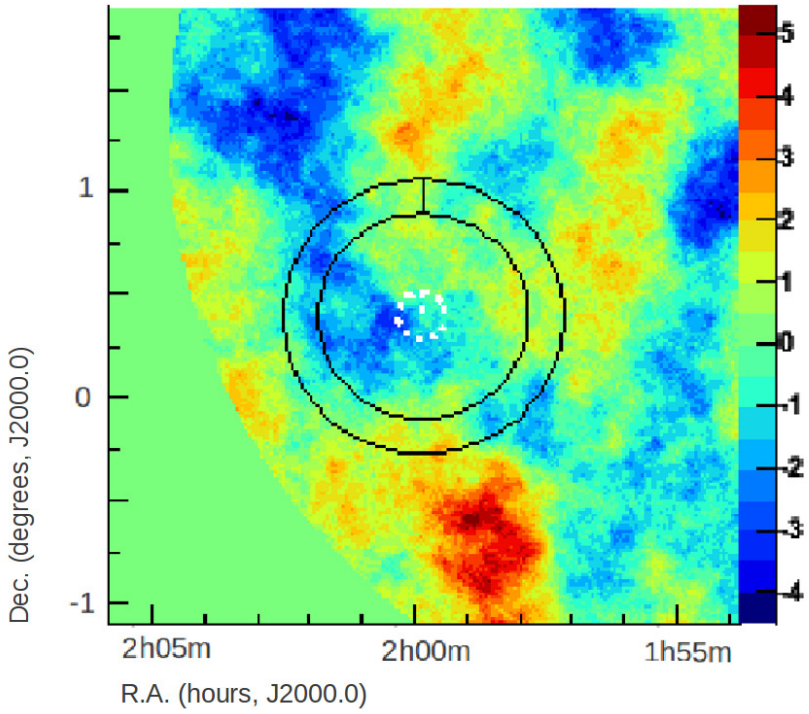

Figure 4.18: A γ-ray sky significance map of the area around Mrk 1014. The right hand bar corresponds to measured significance above background in standard deviation units. The central white circle indicates the position of the object and the size of the PSF of the H.E.S.S. array, while the 2 outer circles indicate the area used during analysis of the background by the ring background method. The smooth pale green region in the bottom left hand corner of the map is a region outside the field of view of the telescope.

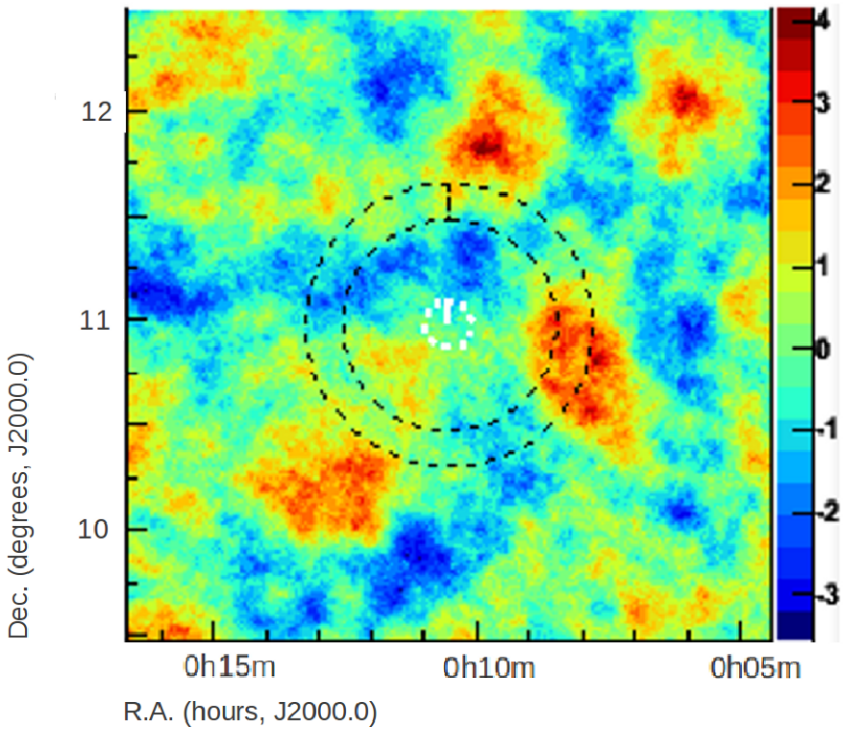

Figure 4.19: A γ-ray sky significance map of the area around Mrk 1501. The right hand bar corresponds to measured significance above background in standard deviation units. The central white circle indicates the position of the object and the size of the PSF of the H.E.S.S. array, while the 2 outer circles indicate the area used during analysis of the background by the ring background method.

and lack of short-term X-ray variability hint at the existence of a large central black hole of $\sim 10^9$ $M_\odot$. They argue that this view is supported by the lack of a thermal component at low X-ray energies, as a larger black hole would necessitate that the accretion disc form further away from the nucleus; this would lead to the temperature of the accretion disc being relatively low. The authors find a correlation between X-ray and optical flux variations, which they suggest could be explained if the X-ray emission is a result of inverse-Compton upscattering of synchrotron radio and optical photons.

The region around Mrk 1501 was observed with the H.E.S.S. telescopes on a number of occasions between 28th July 2006 and 21st August 2007. The data analysed totalled just over 9 hours of observations free of adverse weather conditions and technical issues with the telescopes. There is no evidence for VHE γ-ray emission from the object, with the ring-background method returning a significance of -0.05 σ above background (Figure 4.19) and the reflected-background method returning 0.22 σ above background. An upper limit for Mrk 1501 of 4.8×10^{-12} photons cm^{-2} s^{-1} was calculated at a confidence level of 99% with a threshold energy of 0.26 TeV.

4.5.15 Mrk 573

Mrk 573 is an opically bright Seyfert 2 galaxy at a redshift of $z = 0.0172$ (Bianchi et al., 2010). A triple radio source is associated with the galaxy, composing a central core and two spots, probably associated with nonthermal emission from a jet and counterjet (Ulvestad & Wilson, 1984b). Bianchi et al. (2010) note that the high-energy spectrum of Mrk 573 is typical of those observed in Compton-thick Sy2s, while the soft X-ray emission appears to originate through photoionisation of gas near the nucleus of the galaxy. The luminosity of the two jets is mainly due to nonthermal synchrotron emission, although the steep power-law radio spectrum makes any contribution to the X-ray emission from the Seyfert nucleus negligible (Falcke, Wilson & Simpsom, 1998). Bianchi et al. (2010) found that the radio emission was far more compact than the X-ray emission, but they were unable to determine the exact nature of the connection between the two spectra.

The H.E.S.S. data analysed for Mrk 573 were collected between 2nd November 2007 and 22nd October 2008 ∼20 hours were available with all four telescopes operational and no adverse weather conditions. There is no evidence of VHE γ-ray emission; the ring-background maker returns a significance of 1.3 σ above background and the reflected-background method returns a significance of -0.10 σ above background. The discrepancy in the significances calculated between the two background estimates is probably due to the substantial variation in the background across the field of view of the telescopes, as seen in Figure 4.20. An upper limit for Mrk 573 of 6.4×10^{-12} photons cm^{-2} s^{-1} was calculated at a confidence level of 99% with a threshold energy of 0.26 TeV.

4.5.16 3C 120

3C 120 is a nearby ($z = 0.033$) Sy1 galaxy that shows variability across a wide range of frequencies; however, despite displaying properties mostly associated with Seyfert galaxies it is also a strong and variable radio source (Doroshenko et al., 2009). Extending 100kpc from the central nucleus in the radio band is an inhomogeneous one-sided jet which appears to contain knots with apparent superluminal velocities (Ballantyne et al., 2004). It was noted by Marscher et al. (2002), and confirmed by Ogle et al. (2005), that new features appear in the jet after significant dips in the X-ray emission. It has been noted that, as with radio-quiet Seyfert galaxies, the X-ray spectrum becomes softer during periods of high X-ray flux, and analysis of the X-ray spectrum has led to the conclusion that only $\sim 5\%$ of the 2-10 keV X-ray emission is contributed by the emission from the jet (Ogle et al., 2005). Most of the X-ray emission is believed to be thermal in nature, emitted from a corona around the central black hole and reprocessed by the accretion disc (Doroshenko et

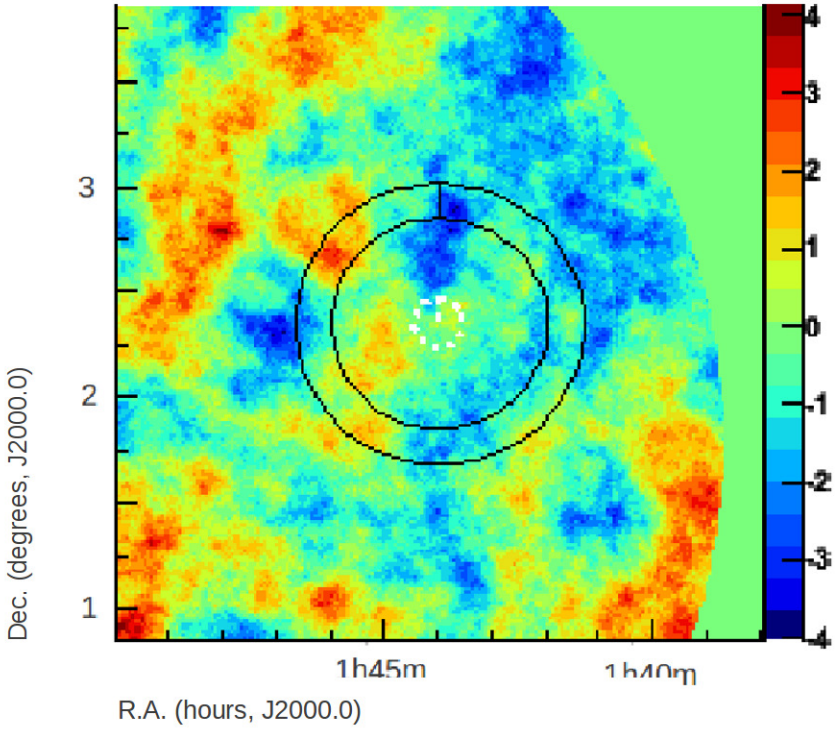

Figure 4.20: A γ-ray sky significance map of the area around Mrk 573. The right hand bar corresponds to measured significance above background in standard deviation units. The central white circle indicates the position of the object and the size of the PSF of the H.E.S.S. array, while the 2 outer circles indicate the area used during analysis of the background by the ring background method. The smooth pale green region to the right hand side of the map is a region outside the field of view of the telescope.

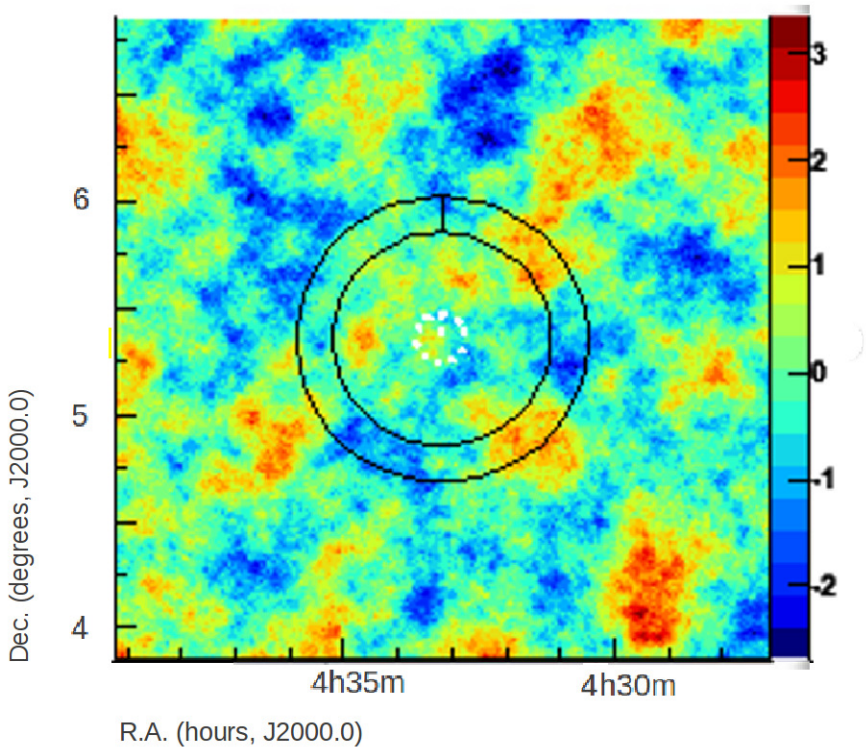

Figure 4.21: A γ-ray sky significance map of the area around 3C 120. The right hand bar corresponds to measured significance above background in standard deviation units. The central white circle indicates the position of the object and the size of the PSF of the H.E.S.S. array, while the 2 outer circles indicate the area used during analysis of the background by the ring background method.

al., 2009). Despite the likelihood that most of the X-ray emission is thermal in nature, recent observations by the *Fermi*-LAT have detected 3C 120 in GeV γ-rays, bringing into question previous understanding of the nature of the emission from the object (Abdo et al., 2010c).

H.E.S.S. data covering the region around 3C 120 were only collected between 6th November 2004 and 15th December 15th so it is unsurprising that there were less than 5 hours of observations of sufficient quality available for analysis. There is no evidence for VHE γ-ray emission from the object (see Figure 4.21) using either the ring-background method, which returned a significance of $-0.77\ \sigma$ above background, or the reflected-background method, which returned a significance of $-1.56\ \sigma$ above background. An upper limit of 4.7×10^{-12} photons cm^{-2} s^{-1} was calculated for 3C 120 at confidence level of 99% with a threshold energy of 0.29 TeV.

4.6 Conclusions

A study was carried out using archival H.E.S.S. data to determine whether there is any evidence for very high energy γ-ray emission from γ-ray-or X-ray-selected Seyfert galaxies. The results of the

Object	Mean ZA (∘)	Significance		Upper Limit	Threshold
		Ring Bkgrd	Reflected Bkgrd	(ph cm^{-2} s^{-1})	(TeV)
Mrk 50	30.6	0.35 σ	-0.12 σ	4.1×10^{-12}	0.29
3C273	30.2	0.98 σ	0.99 σ	4.5×10^{-12}	0.26
4U 1344-60	39.8	-0.11 σ	-0.01 σ	2.6×10^{-12}	0.51
Circinus Galaxy	44.4	0.08 σ	0.49 σ	2.1×10^{-11}	0.68
GRS 1734-292	21.0	-0.39 σ	-0.96 σ	1.42×10^{-12}	0.22
IGR J14471-6319	41.5	-0.19 σ	-1.1 σ	3.2×10^{-12}	0.46
IGR J17204-3554	18.6	0.49 σ	0.73 σ	5.5×10^{-13}	0.24
IGR J17488-2353	17.3	-0.43 σ	-1.2 σ	9.1×10^{-12}	0.24
IGR J22367-1231	15.3	-0.41 σ	-0.69 σ	5.8×10^{-12}	0.24
NGC 1068	26	1.2 σ	0.84 σ	5.1×10^{-12}	0.26
NGC 1365	19.5	-1.1 σ	-0.78 σ	2.8×10^{-12}	0.29
NGC 7469	33.5	-2.5 σ	-2.4 σ	1.8×10^{-12}	0.32
Mrk 1014	26.2	-1.4 σ	-1.2 σ	4.8×10^{-12}	0.26
Mrk 1501	26.2	-0.05 σ	0.2 σ	4.8×10^{-12}	0.26
Mrk 573	28.0	1.3 σ	-0.10 σ	6.4×10^{-12}	0.26
3C 120	31.9	-0.77 σ	-1.6 σ	4.7×10^{-12}	0.29

Table 4.2: List of significance above background returned by both analysis methods for all of the AGN studied, the mean zenith angle (ZA) of the observations and the upper limits calculated with the associated threshold energies.

study are reported in this chapter. Data were available for 14 Seyfert galaxies (9 Sy1s, 1 Sy1.5 and 4 Sy2s), 1 unclassified type 2 AGN, and a quasar which displays many of the properties of Seyfert galaxies, totalling $\approx$ 360 hours of usable data. No evidence was found for very high energy emission from any of the objects, although in a number of cases the amount of useful data available was relatively small (for example, the available livetime for the Circinus Galaxy was only 3.2 hours). Using the data available, flux upper limits were calculated for the objects and are displayed in Table 4.2.

Of the upper limits calculated the least constraining is that found for the Circinus galaxy of 2.1×10^{-11} ph cm^{-2} s^{-1} despite the relatively large amount of data available on the object However, this is due to the very high threshold energy of 0.68 TeV at the zenith angles for which the object could be observed. Despite a relatively high zenith angle, moderately constraining upper limits were found for 4U 1344-60 of 2.6×10^{-12} ph cm^{-2} s^{-1} above 0.51 TeV, possibly due to relatively low background in the region around the object. The most constraining upper limit is calculated for IGR J17204-354, which is probably because of the low zenith angles at which the object is observed.

Chapter 5

Modelling Very High Energy γ-ray Emission from Misaligned AGN

5.1 Introduction

Modelling the emission from AGN is important in furthering the understanding of the processes that take place in the extreme environments from which very high energy γ-rays originate. The rapid variability detected in blazars and in M87 helps to constrain the size of the region from which the TeV emission can originate, and this can be used to determine likely areas within the object where the required particle acceleration can occur. Due to the small inferred area of the emission region, most of the models proposed to describe very high energy emission from AGN focus on the area at the base of the jet or close to the central black hole. The detection of M87 at very high energies led to the development of a number of new models, as the characteristics of the emission were impossible to explain with then current models without invoking physically improbable bulk Lorentz factors and magnetic fields. These new models are interesting, because for AGN unification they must be able to model successfully both misaligned AGN and blazars. As further data are collected it should become possible to distinguish more easily between the new models. These models can lead to greater knowledge of the processes going on deep down at the base of the jets, in regions that, in blazars are masked by events further up the jet.

5.2 Modelling Blazar Emission

Blazars have high inferred bolometric luminosities and display rapid variability, while the jets show apparent superluminal motion; these factors provide strong evidence that the nonthermal

continuum emission detected must be produced within an emission region $\lesssim 1$ light day across. This emission region must be propagating relativistically with a velocity, β_Γ, along a jet directed at a small angle $\theta_{\rm obs}$ to the line of sight (Schlickeiser, 1996). Radiation originating from the emission region will be boosted to higher energies via Doppler boosting, determined by the Doppler factor, D, which is related to the bulk Lorentz factor (the Lorentz factor of the outflow), $\Gamma = (1-\beta_\Gamma^2)^{-\frac{1}{2}}$, by $D = (\Gamma[1-\beta_\Gamma \cos\theta_{\rm obs}])^{-1}$. The observed frequency $\nu_{\rm obs}$ is therefore related to the emitted frequency, ν', through $\nu_{obs} = D\nu'/(1+z)$, where z is the redshift of the source. The observed flux, $F_{\rm obs}$, is related to the intrinsic flux, $F_{\rm in}$, via $F_{\rm obs} = \delta^{3+\alpha} F_{\rm in}$, where α is the spectral index.

While the origin of low-energy emission from blazars is well established to be synchrotron radiation from a high-energy population of electrons, the origin of the high-energy emission is still widely debated. As discussed in Section 3.3 there are two main categories of blazar model, leptonic models and hadronic models. In leptonic models, high-energy emission originates from the upscattering of soft photons off the population of ultrarelativistic electrons producing the synchrotron emission. Hadronic models require that a significant fraction of the jet power is converted into the acceleration of relativistic protons in a very strong magnetic field. If protons are accelerated to the threshold for $p\gamma$ pion production, then high-energy emission will be dominated by $p\gamma$ pair and pion production, as well as synchrotron emission from protons, $\pi^\pm$ and $\mu^\pm$.

5.2.1 Leptonic Models

Leptonic models assume that the high-energy emission is produced via the interaction of soft photons with the population of ultrarelativistic electrons through Compton upscattering. The source of the target photons for Compton upscattering can be synchrotron photons produced within the jet, a process referred to as synchrotron self-Compton (SSC) emission (Bloom & Marscher, 1996), or from external photons, in which case the process is termed external-Compton (EC) emission. In the case of EC emission, the target photons can originate from a number of possible sources, including accretion-disc radiation (Dermer & Schlickeiser, 1993), reprocessed optical - ultraviolet radiation from circumnuclear material (Dermer, Sturner & Schlickeiser, 1997) or the dusty torus (Błażejowski et al., 2000), and synchrotron emission from populations of electrons within other parts of the jet (Ghisellini & Tavecchio, 2008).

In leptonic models, it is required that the object has a relatively low matter density in the emission region so that the $\gamma\gamma$ absorption opacity of this region is low over most of the high-energy spectrum, as a high opacity would lead to a large percentage of the high-energy emission being reprocessed to lower frequencies. The requirement of low opacity in the emission region can be fulfilled if there is strong Doppler boosting as a less dense population of electrons can produce

the observed fluxes (Böttcher, 2010); however, at the highest photon energies, the absorption opacity of the jet will still be high enough to result in a non-negligible contribution to the shape of the spectrum (Aharonian, Khangulyan & Costamante, 2008). Interactions between the jet and the surrounding medium result in deceleration of the jet, which can have a significant effect on the observable properties of blazar emission. This occurs due to radiative interaction between emission regions with different bulk velocities (Ghisellini, Tavecchio & Chiaberge, 2005) or through variations in the Doppler factor (Böttcher & Principe, 2009). Changes in the observed Doppler factor can also be the result of a slight change in jet orientation without the requirement for a change in speed, as observed in a helical-jet configuration (Villata & Raiteri, 1999). In the case of such ordered magnetic field structures, synchrotron polarisation signatures should be observed, such as the polarisation-angle swing detected during an optical and *Fermi*-LAT γ-ray flare in 3C279 (Abdo et al., 2010d).

It is possible to model blazar SEDs successfully by modelling the underlying lepton distribution as a simple, single or broken power law with low-and high-energy cut-offs, as in Ghisellini et al. (1998) for example. However, this approach lacks a self-consistent basis for the shape of the electron distribution More realistic models rely on using the self-consistent steady-state solution of the Fokker-Planck equation (Böttcher, 2010); this is then modified to include a physical mechanism for particle acceleration and all relevant radiative and adiabatic cooling mechanisms, such as in the model put forward by Acciari et al. (2009c) and used by Böttcher (2010) Further to producing broadband SEDs, it is also useful for a model to be able to reproduce successfully the observed variability. To do this requires that the time-dependent electron-dynamics and radiation-transfer problem is solved self-consistently. Such models have been developed by a number of authors, including Katoka et al. (2000) and Böttcher & Chiang (2002).

To date, leptonic models have proven very successful when used to model the SEDs and spectral variability of blazars. The radiative cooling timescales of synchrotron electrons in a typical $B \sim 1$ G magnetic field are of the order of several hours to ~ 1 day at optical frequencies and $\lesssim 1$ hr in X-rays, which is consistent with the observed intraday variability. However, the recent detection of very rapid variability from objects such as PKS 2155-304 (discussed in 3.3.1) on timescales of a few minutes poses problems for simple one-zone models even if large bulk Lorentz factors of ~ 50 are assumed, as causality requires that the emitting region must be smaller than the Schwarzschild radius of the central black hole of the AGN (Begelman, Fabian & Rees, 2008). A possible solution to this, presented by Tavecchio & Ghisellini (2008), suggests that the γ-ray emission region may be only a small spine of ultrarelativistic plasma within a larger, slower-moving jet. Such small spines could be powered by magnetic reconnection in a Poynting-flux-dominated jet, as proposed

by Giannios, Uzdensky & Begelman (2009).

5.2.2 Hadronic Models

Hadronic models require that a significant fraction of the jet power is available for the acceleration of ultrarelativistic protons to energies of $E_p^{\rm max} \gtrsim 10^{19}$ eV, reaching the threshold for pγ pion production in a strongly magnetized environment and resulting in the production of synchrotron-supported pair cascades (Mannheim, 1993). Despite the fact that the inverse-Compton scattering of protons is identical to that of electrons, the energy loss rate of protons is suppressed by a factor of $(m_e/m_p)^4 \approx 10^{-13}$ (where m_e is the electron mass and m_p is the proton mass); at energies above the threshold for pair production, this process is 4 orders of magnitude lower than for pair production (Kelner & Aharonian, 2008). To accelerate protons to these high energies requires extremely high magnetic fields (several tens of gauss) to constrain the Larmor radius to be smaller than the radius of the emission region inferred from the rapid observed variability of blazars, typically $R \lesssim 10^{16}$ cm. In the presence of such high magnetic fields, synchrotron emission from the primary protons (Aharonian, 2000) and from secondary muons and mesons (Mücke & Protheroe, 2000; Mücke et al., 2003) will provide a non-negligible contribution to the observed spectrum. Electromagnetic cascades within the object can originate due to a number of processes: π^0 cascades initiated by photons from π^0 decay; $\pi^\pm$ cascades caused by electrons from $\pi^\pm$ decay ($\pi^\pm \rightarrow \mu^\pm \rightarrow e^\pm$); proton-synchrotron photons; and synchrotron photons from $\mu^\pm$, $\pi^\pm$ and K particles, known as the $\mu^\pm$-synchrotron cascade (Böttcher, 2010). In the case of hadronic models, the largest contribution to the observed spectra of blazars at high energy are proton-synchrotron cascades and $\mu^\pm$ cascades, both of which produce two-component γ-ray spectra, while low-energy emission is dominated by synchrotron emission from primary e^- with some contribution from secondary e^-. The emission from π^0 and $\pi^\pm$ cascades from ultrahigh-energy protons generates featureless γ-ray spectra (Mücke & Protheroe, 2001; Mücke et al., 2000) and so is unlikely to be responsible for the bulk of the emission.

An issue of using hadronic models to model blazars is the difficulty such models have in reproducing the rapid variability observed in such objects. This is because it is very difficult to reconcile the very rapid high-energy variability with the radiative cooling timescales of protons (which is $\sim$ several days for magnetic fields of $\sim$ 10 G and typical Doppler factors) (Böttcher, 2010). One potential solution is to assume that the observed variability is caused by geometrical effects and, hence does not require rapid changes in proton energy. Modelling hadronic models in a time-dependent manner usually requires that extremely time-consuming Monte Carlo simulations are carried out. However, it is possible to utilise a simplified model as in Kelner & Aharonian

(2008). In this approach, analytic fit functions to results from the publicly available Monte Carlo code SOPHIA were produced. These described the spectra of the final decay products, but the model requires prior knowledge of the target photon field and the initial proton spectrum. Once the first generation products are taken into account, cascades must be considered as the synchrotron emission from most of the electrons and positrons produced and the γ-rays from π^0 decay are at energies $\gg 1$ TeV. A semi-analytical treatment of the cascades, taken from Böttcher (2010), is discussed below.

Böttcher (2010) begins by considering the injection rates of first-generation high-energy γ-rays, $\dot{N}_\epsilon^0$, with Lorentz factor γ and pairs, $Q_e(\gamma)$. $\dot{N}_\epsilon^0$ and $Q_e(\gamma)$ are taken from the analytical fit functions of Kelner & Aharonian (2008). Assuming that the cascades can be well-described linearly allows the optical depth for $\gamma\gamma$ absorption, $\tau_{\gamma\gamma}(\epsilon)$, to be precalculated from the low-energy radiation field. Under the conditions described, the spectrum of escaping photons, $\dot{N}_\epsilon^{\rm esc}$, can be calculated as follows:

$$\dot{N}_\epsilon^{\rm esc} = \dot{N}_\epsilon^{\rm em}\left(\frac{1-e^{-\tau_{\gamma\gamma}[\epsilon]}}{\tau_{\gamma\gamma}[\epsilon]}\right) \tag{5.1}$$

Where contributions to $\dot{N}_\epsilon^{\rm em}$ come from the initial high-energy photon spectrum and synchrotron emission from secondaries, $\dot{N}_\epsilon^{\rm em} = \dot{N}_\epsilon^0 + \dot{N}_\epsilon^{\rm syn}$. The synchrotron spectrum can be evaluated with an acceptable level of accuracy assuming a single-electron emissivity, j_ν, of the form $j_\nu \propto \nu^{1/3}e^{-\epsilon/\epsilon_0}$, where $\epsilon_0 = b\gamma^2$, $b = B/B_{\rm crit}$ and $B_{\rm crit} = 4.4\times10^{13}$ G, B is the magnetic field in the emission region. The electron distribution, $N_e(\gamma)$ (where γ is essentially being used to express energy through $E = \gamma m_0 c^2$), will be the solution to the isotropic Fokker-Planck equation in equilibrium:

$$\frac{\partial}{\partial\gamma}(\dot{\gamma}N_e[\gamma]) = Q_e(\gamma) + \dot{N}_e^{\gamma\gamma}(\gamma) + \dot{N}_e(\gamma)^{\rm esc} \tag{5.2}$$

where $\dot{N}_e^{\gamma\gamma}(\gamma)$ is the rate of particle injection due to $\gamma\gamma$ absorption, which must be evaluated self-consistently with the radiation field. For the high magnetic fields ($B \gtrsim 10$ G) at which hadronically produced γ-ray emission is expected to be dominant, electron cooling will be dominated by synchrotron losses. For the particles involved in γ-ray production (those emitting synchrotron radiation at X-ray or higher energies), the synchrotron cooling time will be much shorter than the escape timescale, allowing the escape term in Equation 5.2 to be neglected. To find an expression for $\dot{N}_e^{\gamma\gamma}(\gamma)$, the relation between the energies of the electron-positron pair produced must be found, also noting that Equation 5.1 implies that every photon that does not escape will produce an electron-positron pair. In the $\gamma\gamma$ absorption of a high energy photon of energy, ϵ, one of the

particles produced will receive the major fraction, f_γ, of the photon energy, $\gamma_1 = f_\gamma \epsilon$, while the other will receive $\gamma_2 = (1 - f_\gamma)\epsilon$. This leads to the pair-production rate shown below:

$$\dot{N}_e^{\gamma\gamma}(\gamma) = f_{\rm abs}(\epsilon_1)(\dot{N}_{\epsilon_1}^0 + \dot{N}_{\epsilon_1}^{\rm syn}) + f_{\rm abs}(\epsilon_2)(\dot{N}_{\epsilon_2}^0 + \dot{N}_{\epsilon_2}^{\rm syn}) \tag{5.3}$$

where $\epsilon_1 = \gamma/f_\gamma$, $\epsilon_2 = \gamma/(1 - f_\gamma)$ and $f_{\rm abs}(\epsilon) = 1 - (1 - e^{-\tau_{\gamma\gamma}[\epsilon]})/\tau_{\gamma\gamma}[\epsilon]$. This leads to an implicit solution to Equation 5.2:

$$N_e(\gamma) = \frac{1}{\nu_0 \gamma^2} \int_\gamma^\infty d\tilde{\gamma}\{Q_e(\tilde{\gamma}) + \dot{N}_e^{\gamma\gamma}(\tilde{\gamma})\} \tag{5.4}$$

In Equation 5.4, $\tilde{\gamma}$ is the Lorentz factor at which $\dot{N}_e^{\gamma\gamma}$ is currently being evaluated within the integral. The solution is implicit because the particle spectrum, $N_e(\gamma)$, occurs on both sides of Equation 5.4, as $\dot{N}_e^{\gamma\gamma}$ depends on synchrotron emissivity, which requires knowlege of $N_e(\tilde{\gamma})$. The majority of radiative output relevant to pair production at an energy γ for $N_e(\tilde{\gamma})$ is provided by electron-positron pairs at energies of $\tilde{\gamma}_1 = \sqrt{\gamma/(f_\gamma b)}$ and $\tilde{\gamma}_2 = \sqrt{\gamma/(1 - f_\gamma)b}$; however, for practical purposes, it is generally assumed that γ is much smaller than $\tilde{\gamma}_1$ and $\tilde{\gamma}_2$, which is fulfilled if there is no pion-induced pair injection at energies above $\gamma_{\rm crit} = 4.4 \times 10^{13}([1 - f_\gamma]B_G)^{-1}$ or $E_{e,{\rm crit}} = 2.3 \times 10^{19}([1 - f_\gamma]B_G)^{-1}$ eV. In most synchrotron proton models for blazars, no substantial pion-induced pair injection is expected above $E_{e,{\rm crit}}$, allowing Equation 5.4 to be evaluated progressively, starting at the highest pair energies for which $Q_0(\gamma) \neq 0$ or $\dot{N}_{\epsilon 1,2}^0 \neq 0$, and then solving for $N_e(\gamma)$ for progressively lower γs. Once the equilibrium pair distribution, $N_e(\gamma)$, is known, it can be used to evaluate the synchrotron emissivity and hence, using Equation 5.1, the photon spectrum expected.

5.3 A Simple SSC Model

Modelling of high-energy emission from AGN has primarily concentrated on leptonic models, in which the low-energy emission is interpreted as synchrotron emission from energetic leptons and the high-energy component is interpreted as radiation from target photons Compton-upscattered by relativistic jet leptons. These target photons can come from the synchrotron radiation or from external sources, such as the broad-line region, a dusty torus or the accretion disc. In standard, simple, time-dependent AGN models, such as the one put forward by Ghisellini & Madau (1996), the low-and high-energy components are fitted simultaneously by injecting nonthermal electrons and positrons into the jet and allowing the electrons to evolve through radiative and adiabatic cooling. Another modelling technique, proposed by Finke, Dermer & Böttcher (2008), fits the

optical/X-ray νF_ν spectrum and uses this to deduce the electron distribution in the jet, assuming that this emission is dominated by nonthermal lepton synchrotron radiation. The high-energy SSC component is then calculated using this inferred electron distribution and a small set of well-constrained observables.

The model proposed in Finke, Dermer & Böttcher (2008) considers a one-zone spherical blob of relativistic plasma moving with a Lorentz factor $\Gamma = (1-\beta^2)^{-1/2}$ within a relativistic jet. In the notation used, quantities are primed in the frame comoving with the jet while those in the observer's frame are unprimed, so the comoving volume of the emitting blob is $V'_b = 4\pi R'^3_b/3$, where R'_b is the comoving radius of the blob. The Doppler factor is given by $\delta_D = [\Gamma(1-\beta\mu)]^{-1}$, where μ is the cosine of the angle of inclination with respect to the line of sight θ: $\mu = \cos\theta$. In many blazars, rapid variability is observed; this implies that the emitting region in such sources is confined to a small volume with a comoving variability timescale, t'_v, limited by light travel time. For the observer, the variability timescale satisfies:

$$t_v \gtrsim t_{v,\min} = \frac{(1+z)R'_b}{\delta_D c} \tag{5.5}$$

where $t_{v,\min}$ is the minimum observed variability time across all wavelengths for nonthermal emission.

5.3.1 Synchrotron Modelling in Finke, Dermer & Böttcher (2008)

A derivation of the expression for the comoving synchrotron emissivity, $J'_{\rm syn}$, from isotropic electrons in a randomly oriented magnetic field can be found in Crusius & Schlickeiser (1986) with further details in Ghisellini, Guilbert & Svensson (1988). This gives:

$$\epsilon' J'_{\rm syn}(\epsilon') = \frac{\sqrt{3}\epsilon' e^3 B}{h} \int_1^\infty N'_e(\gamma') R(x) d\gamma' \tag{5.6}$$

where B is the magnetic field in the emission region, $N'_e(\gamma')$ is the emitting electron distribution, $\epsilon' = (1+z)\epsilon/\delta_D$ (the incident photon's dimensionless energy in the blob frame), γ' is the relativistic γ factor as seen comoving with the jet blob, and $R(x)$ is the function:

$$R(x) = \frac{x}{2} \int_0^\pi \sin\theta d\theta \int_{x/\sin\theta}^\infty K_{5/3}(t) dt \tag{5.7}$$

where x is given by:

$$x = \frac{4\pi\epsilon' m_e^2 c^3}{3eBh\gamma'^2} \tag{5.8}$$

and $K_{5/3}(t)$ is the modified Bessel function of the second kind of order 5/3. Following from this, the synchrotron flux is given by:

$$f_{\epsilon}^{\rm syn} = \frac{\delta_D^4 \epsilon' J'_{\rm syn}(\epsilon')}{4\pi d_L^2} = \frac{\sqrt{3}\delta_D^4 \epsilon'}{4\pi h d_L^2} \int_1^{\infty} d\gamma' N'_e(\gamma') R(x) \tag{5.9}$$

where d_L is the luminosity distance to the object.

5.3.2 SSC Emission Modelling in Finke, Dermer & Böttcher (2008)

The comoving SSC emissivity $J'_{\rm SSC}$, integrated over volume, for isotropic and homogeneous photon and electron distributions, is given by

$$\epsilon'_s J'_{\rm SSC}(\epsilon'_s) = \frac{3}{4} c\sigma_T \epsilon_s'^2 \int_0^{\infty} \frac{u'(\epsilon')}{\epsilon'^2} d\epsilon' \int_{\gamma'_{\rm min}}^{\gamma'_{\rm max}} \frac{N'_e(\gamma')}{\gamma'^2} F_C(q, \Gamma_e) d\gamma' \tag{5.10}$$

where $\epsilon'_s = (1+z)\epsilon_s/\delta_D$ (the scattered photon's dimensionless energy in the blob frame), and $F_C(q, \Gamma_e)$ is the Compton scattering kernel for isotropic photon and electron distributions, given by (Jones, 1968; Blumenthal & Gould, 1970):

$$F_C(q, \Gamma_e) = \left[2q \ln q + (1+2q)(1-q) + \frac{(\Gamma_e q)^2}{2(1+\Gamma_e q)}(1-q) \right] H\left(q; \frac{1}{4\gamma'^2}, 1\right) \tag{5.11}$$

In the above, $H\left(q; \frac{1}{4\gamma'^2}, 1\right)$ is a Heaviside step function that is equal to $\frac{1}{4\gamma'^2}$ for negative q and 1 for positive q , $\Gamma_e = 4\epsilon'\gamma'$ and

$$q = \frac{\epsilon'_s/\gamma'}{\Gamma_e(1-\epsilon'_s)} \tag{5.12}$$

In Equation 5.10 $u'(\epsilon')$ is the electron radiation energy density, calculated by Finke, Dermer & Böttcher (2008) using the δ-approximation (in which it is assumed that an electron of Lorentz factor γ radiates at a frequency $\nu = \gamma^2 \nu_g$ where ν_g is the nonrelativistic electron gyrofrequency) for the synchrotron flux (e.g., Dermer & Schlickeiser, 2002):

$$u'(\epsilon') = \frac{3 d_L^2 f_{\epsilon}^{\rm syn}}{c R_b'^2 \delta_D^4 \epsilon'} \tag{5.13}$$

Combining the electron radiation energy density, Equation 5.13, and the SSC emissivity, Equation 5.10, with the synchrotron flux, Equation 5.9, leads to:

$$\epsilon'_s J'_{\rm SSC}(\epsilon'_s) = \frac{9\sigma_T d_L^2 \epsilon_s'^2}{4\delta_D^4 R_b'^2} \int_0^{\infty} \frac{f_{\epsilon}^{\rm syn}}{\epsilon'^3} d\epsilon' \int_{\gamma'_{\rm min}}^{\gamma'_{\rm max}} \frac{N'_e(\gamma')}{\gamma'^2} F_C(q, \Gamma) d\gamma' \tag{5.14}$$

The νF_ν SSC spectrum is given by:

$$f_{\epsilon_s}^{\rm SSC} = \frac{\delta_D^4 \epsilon_s' J_{\rm SSC}'(\epsilon_s')}{4\pi d_L^2} \tag{5.15}$$

so the observed SSC flux can be expressed as:

$$f_{\epsilon_s}^{\rm SSC} = \frac{9(1+z)^2 \sigma_T \epsilon_s'^2}{16\pi \delta_D^2 c^2 t_{v,\rm min}^2} \int_0^\infty \frac{f_\epsilon^{\rm syn}}{\epsilon'^3} d\epsilon' \int_{\gamma_{\rm min}'}^{\gamma_{\rm max}'} \frac{N_e'(\gamma')}{\gamma'^2} F_C(q,\Gamma) d\gamma' \tag{5.16}$$

5.3.3 Internal $\gamma\gamma$ Photoabsorption in the Finke, Dermer & Böttcher (2008) Model

Interaction of the Compton-scattered photons with the internal synchrotron radiation field results in $\gamma\gamma$ photoabsorption, which can be described by the photoabsorption optical depth $\tau_{\gamma\gamma}$. Absorption modifies the high-energy SSC spectrum by the factor k_{SSC}:

$$k_{SSC} = \frac{1 - e^{-\tau_{\gamma\gamma}}}{\tau_{\gamma\gamma}} \tag{5.17}$$

The approach taken in Finke, Dermer & Böttcher (2008) uses the form given in Gould & Schréder (1967) for $\tau_{\gamma\gamma}$, where the photoabsorption optical depth for a γ-ray photon with energy ϵ_1 in a radiation field with spectral photon density $n(\epsilon', \mu'; r')$, where $\mu' = \cos\theta'$ and r') is the position in the comoving frame, is:

$$\tau_{\gamma\gamma}(\epsilon_1') = \int_{r_1'}^{r_2'} dr' \int_{-1}^{1} (1-\mu') d\mu' \int_{2/\epsilon_1'(1-\mu')}^{\infty} \sigma_{\gamma\gamma}[\epsilon' \epsilon_1'(1-\mu')] n'(\epsilon', \mu'; r') d\epsilon' \tag{5.18}$$

As in this treatment the radiation field is assumed to be uniform and isotropic, in the comoving frame, $n_{\rm rad}(\epsilon', \mu'; r') \approx n_{\rm rad}/2$. This leads to:

$$\tau_{\gamma\gamma}(\epsilon_1') \cong R_b' \int_{\frac{1}{\epsilon_1'}}^{\infty} \sigma_{\gamma\gamma}(\epsilon', \epsilon_1') n_{\rm rad}'(\epsilon') d\epsilon' \tag{5.19}$$

Inserting the absorption cross section gives:

$$\tau_{\gamma\gamma}(\epsilon_1') = \frac{R_b' \pi r_e^2}{\epsilon_1'^2} \int_{1/\epsilon_1'}^{\infty} d\epsilon' n_{\rm rad}'(\epsilon') \bar{\phi}(s_0) \epsilon'^2 \tag{5.20}$$

where $s_0 = \epsilon' \epsilon_1'$; ϵ', ϵ are related by $\epsilon' = (1+z)\epsilon/\delta_D$. $\bar{\phi}$ describes how the absorption cross section varies with energy and is given by:

$$\bar{\phi}(s_0) = \frac{1+\beta_0^2}{1-\beta_0^2} \ln w_0 - \beta_0^2 \ln w_0 - \frac{4\beta_0}{1-\beta_0^2} + 2\beta_0 + 4 \ln w_0 \ln(1+w_0) - 4L(w_0) \tag{5.21}$$

In Equation 5.21, $\beta_0^2 = 1 - 1/s_0$, $w_0 = (1+\beta_0)/(1-\beta_0)$, and

$$L(w_0) = \int_1^{w_0} \frac{1}{w} \ln(1+w) dw \tag{5.22}$$

Substituting for $n'_{\rm rad}(\epsilon')$, the synchrotron photon number density $n'_{\rm syn}$ given by:

$$n'_{\rm syn} \cong \frac{R'_{\rm syn}}{c} \dot{n}'_{\rm syn}(\epsilon') \cong \frac{3 d_L^2 f_\epsilon^{\rm syn}}{m_e c^3 R_b'^2 \delta_D^4 \epsilon_B^2 \gamma_s'^4} \tag{5.23}$$

leads to:

$$\tau_{\gamma\gamma}(\epsilon_1') = \frac{9 d_L^2 \sigma_T (1+z)}{8 m_e c^4 t_{v,\rm min} \delta_D^5 \epsilon_1'^2} \int_{1/\epsilon_1'}^{\infty} \frac{d\epsilon'}{\epsilon'^4} f_\epsilon^{\rm syn} \bar{\phi}(s_0) \tag{5.24}$$

5.4 The Difficulty of Modelling Misaligned AGN

Since the detection of M87 at very high energies, it has become apparent that single-zone SSC models, such as the one described in Section 5.3, have difficulty modelling the spectra of such objects. This is the case due to the relatively high viewing angle for radio galaxies ($\sim 20^\circ$ for M87) compared with blazars, as discussed earlier. For SSC models to describe accurately the very high energy emission and variability observed in blazars, they must take into account the very high Doppler factors of the jet, which, due to the relativistic motion of the material in the jet moving almost straight towards the observer, cause the observed photon energies to be higher than in the rest frame of the jet (Doppler boosting) (Buckley, 1998). In the case of radio galaxies and other misaligned AGN, however, assuming that the jets of such objects are comparable to those in blazars, the Doppler factor with respect to the observer is expected to be much more moderate. With more moderate Doppler factors, it is almost impossible to reproduce accurately the spectra of misaligned AGN at high energies using a single-zone SSC model (Tavecchio & Ghisellini, 2008).

For the specific case of M87, the synchrotron component of the spectrum peaks at $\sim 10^{14}$ Hz and extends into the X-ray band, while the TeV emission belongs to a second, inverse-Compton component. There is no evidence of an external source of soft photons in M87 to provide the photon field for external-Compton emission (Tavecchio & Ghisellini, 2008), suggesting that the high-energy emission is probably dominated by SSC emission. For a one-zone model, successfully reproducing the spectra requires assuming both a rather low magnetic field and a large Doppler factor; the latter is unlikely considering the angle to the line of sight for the jet (Tavecchio & Ghisellini, 2008). An example of the result of using a single-zone blob-in-jet model to attempt to reproduce the VHE γ-ray emission from M87 is shown in Figure 5.1. One potential solution

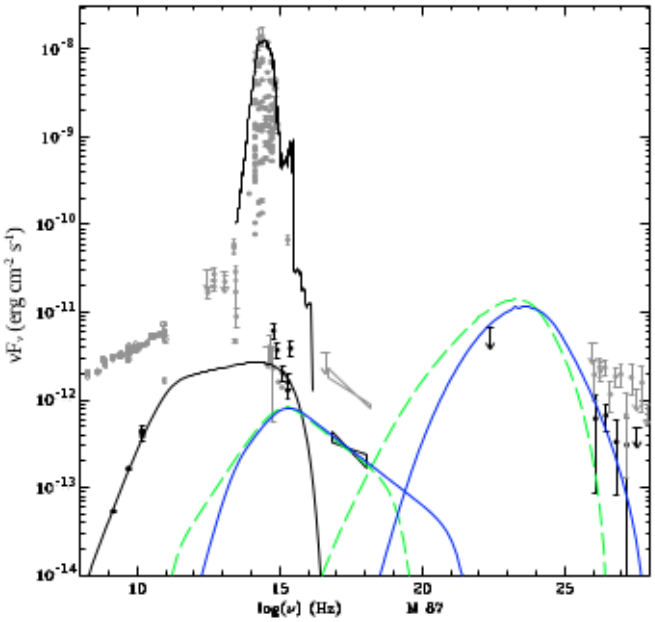

Figure 5.1: Single-zone modelling of the SED of M87, with $\delta_b = 3.07$, represented by the dashed green curve, assuming an inclination to the line of sight $\theta = 19°$. The data points that provide solid constraints on the models are shown in black while those providing looser constraints are shown in grey. The black curve at optical wavelengths is emission from the host galaxy computed using the PEGASE code (Fioc & Rocca-Volmerange, 1997). The empty grey circles correspond to radio data obtained from the NASA extragalactic database, with fluxes $\sim 10^{-12}$ erg cm^{-2} $textrms^{-1}$; this emission originates from the extended kpc jet and the radio lobes. The black curve at radio to ultraviolet/X-ray energies represents results from the single-zone model of Katarzyński, Sol & Kus (2001, 2003) for the inner jet, with corresponding radio data, at fluxes $\sim 10^{-13}$ erg cm^{-2} s^{-1} shown in black. The first bump peaks at $\sim 10^{15}$ Hz and is synchrotron emission, while the second bump is inverse Compton emission, peaking at $\sim 10^{23}$ Hz. The synchrotron emission and inverse-Compton emission both originate from the same zone as the VHE emission. The solid blue curve is the SED produced by a blob moving close to the direction of the line of sight at an angle of 1° with $\delta_b = 8$, which comes closest to successfully reproducing the VHE γ-ray data. Taken from Lenain et al. (2008).

might be that the jet is initially at a small angle to the line of sight (only deviating further out from the core) and that the high-energy emission originates there. If this is the case, then high Doppler factors would be considerably more likely; however, this leads to the prediction of steep energy spectra, contrary to the hard VHE γ-ray spectrum observed from the object (Neronov & Aharonian, 2007). It is more likely, then, that the VHE emission is due to the interplay between two (or more) regions in the jet, or that it is produced in the vicinity of the supermassive black hole of M87 independently of jet processes.

5.5 Inhomogeneous Jet Models

Inhomogeneous jet models were initially developed to model the complicated and often inconsistent variability observed in blazars; however, the detection of M87 in TeV γ-rays has led to greater interest in such models and to the development of more complicated multizone models, such as the spine-sheath model of Tavecchio & Ghisellini (2008) and the decelerating-jet model of Georganopoulos & Kazanas (2003). In such models differential relativistic motion between various emission zones leads to Doppler boosting of the emission from one zone in the rest frame of another zone. These models reduce the requirements that single-zone leptonic models have for extremely high bulk Lorentz and Doppler factors, and such models have been used successfully to model the SEDs of rapidly varying VHE γ-ray blazars such as Mrk 501 and PKS 2155-304 (Böttcher, 2010).

5.5.1 Shock-in-Jet Models

Shock-in-jet models are discussed here as one of the earlier classes of inhomogeneous jet models. They were initially developed to explain the radio spectra of blazars, as in Marscher & Gear (1985). Spada et al. (2001) proposed applying such models to high-energy emission from such objects. These models have had success in explaining SEDs and time-lag features in some blazars (Böttcher, 2010); however, to date there have been few, if any, attempts to use such models to describe emission from misaligned AGN. The models assume that the central engine intermittently ejects shells of relativistic plasma at varying speeds, which subsequently collide (Mimica et al., 2004). To apply an internal-shock model to radiation transfer within a blazar jet requires time-dependent evaluation of all parts of the shocked regions of the jet that are producing the radiation fields, resulting in a highly non-linear model. The non-linear nature of the models produced, means that they generally cannot be solved analytically, and so they must generally be solved numerically, as in Sokolov, Marscher & McHardy (2004), Mimica et al. (2004) and Graff et al. (2008). Currently, the use of detailed internal-shock models to evaluate the SED of an object are very time-consuming as the models require either full expressions or accurate approximations to the emissivities of both synchrotron and Compton emission. This makes it difficult to use such models to explore a large parameter space, and thus far they have generally been successful in modelling objects using very specific (but observationally poorly constrained) parameters.

Böttcher & Dermer (2010) propose a solution to the time-consuming aspects of many internal-shock models by developing a semi-analytical model. In this model, the temporally and spatially dependent electron spectra are calculated analytically, taking into account the effects of forward- and reverse-shock acceleration on the electron population and subsequent radiative cooling; the

observed synchrotron and external-Compton spectra are similarly calculated, taking into account light travel-time effects and using δ-function approximations for the emissivities. Using their model, Böttcher & Dermer (2010) were able to scan successfully a substantial region of parameter space to observe the dependence of the produced SEDs on the parameters used and investigate the effects of different parameters on crossband correlations and time lags. Interestingly, the authors found that only slight changes in the physical parameters can lead to substantial changes in the interband time lags, in some cases even resulting in a reversal in the sign of the lag. This approach therefore helps to explain some of the temporal inconsistency between different wavebands in flare events seen for many sources.

5.5.2 The Spine-Layer Model

Tavecchio & Ghisellini (2008) argue that the inner subparsec-scale jet of M87 is the most likely site of very high energy γ-ray emission and they note the problems a single-zone SSC model has reproducing the observed spectrum as discussed in Section 5.4. To overcome the problems inherent in a single-zone SSC model, Tavecchio & Ghisellini (2008) propose a multizone model in which the jet is made up of two components, an inner, fast-moving "spine" and an outer, slower "layer", as shown in Figure 5.2. In the model, the layer is approximated as a hollow cylinder with internal radius R, outer radius R_2, height H_l (as measured in the frame of the sheath), moving with a bulk Lorentz factor Γ_l. The central spine is modelled as a cylinder with height H_s (as measured in the frame of the spine) and radius R, moving with a bulk Lorentz factor Γ_s. The spine and layer are characterised by tangled magnetic fields of intensity B_s and B_l respectively. Each region contains relativistic electrons assumed to follow a smoothed broken power-law distribution extending from $\gamma_{\rm min}$ to $\gamma_{\rm cut}$, with indices n_1 and n_2 below and above the break at γ_b, respectively.

$$\begin{aligned} N(\gamma) &= K\gamma^{-n_1}\left[1+\left(\frac{\gamma}{\gamma_b}\right)^{n_1-n_2}\right]e^{\frac{-\gamma}{\gamma_{\rm cut}}} \quad && \gamma > \gamma_{\rm min} \\ N(\gamma) &= 0 && \gamma \leq \gamma_{\rm min} \end{aligned} \tag{5.25}$$

The normalisation constant, K, in Equation 5.25, is found by requiring that $N(\gamma)$ produce a given intrinsic synchrotron luminosity $L_{\rm syn}$ and is one of the input parameters required for the model. Both the spine and the layer emit through synchrotron and inverse-Compton processes; the radiation emitted by the spine is seen boosted by the layer, and vice versa, by a factor of $\sim (\Gamma')^2$, with Γ' given by:

$$\Gamma' = \Gamma_s\Gamma_l(1-\beta_s\beta_l) \tag{5.26}$$

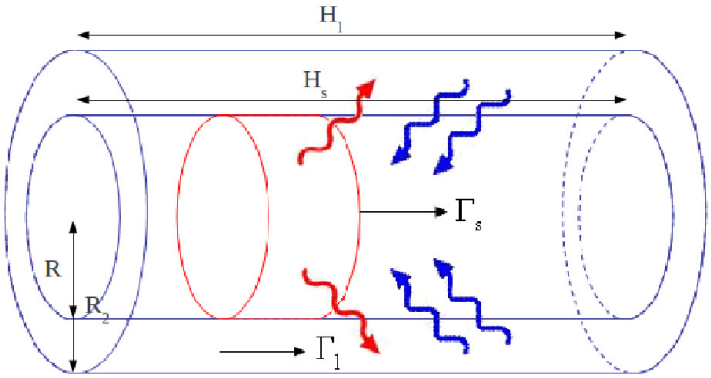

Figure 5.2: Schematic of the spine-layer model: the central cylinder represents the spine, of height H_s and radius R, moving with a Lorentz factor of Γ_s, and the volume between the spine and outer cylinder represents the layer, of height H_l and outer radius R_s, moving with a Lorentz factor Γ_l. Photons emitted by the spine are Doppler boosted as seen by the sheath, and vice versa. After Ghisellini, Tavecchio & Chiaberge (2005).

where $c\beta_s$ and $c\beta_l$ are the velocities of the spine and layer, respectively. It is assumed that $H_l > H_s$. The seed photons for inverse-Compton scattering originate not only locally in the region being considered (spine or layer) but are also produced in the other component (referred to henceforth as external-Compton), leading to strong feedback between the two. A consequence of the structure proposed is that the emission observed from the jet will depend strongly on the angle of the jet to the line of sight. At small angles, as in blazars, the emission is dominated by boosted spine emission, while at large viewing angles ($\theta > 45°$), as in many radio galaxies, emission from the spine is suppressed. In the case of large viewing angles, it becomes probable that the layer, characterised by a broader beaming cone, will contribute significantly to the overall emission, possibly dominating in some cases. At intermediate angles, both components can contribute significantly to the output, as illustrated in Figure 5.3.

In the comoving frame of one component, the photons produced in the other are not isotropic and are observed to be aberrated, requiring the different beaming patterns associated with the two regions to be taken into account. Most of the external-Compton photons come from a single direction (opposite to the relative velocity vector). It is important to note that this anisotropy only applies to the external-Compton radiation, while the synchrotron and SSC emission within the region are isotropic in the comoving frame. For the spine, the external-Compton radiation is more concentrated along the jet axis with respect to its synchrotron and SSC emission, while for the layer it is more concentrated in the direction of the black hole. To simplify the transformations, the authors assumed, as in Dermer (1995), that, due to the strong aberration in the rest frame of one component, all the photons from the other component come from a single direction opposite

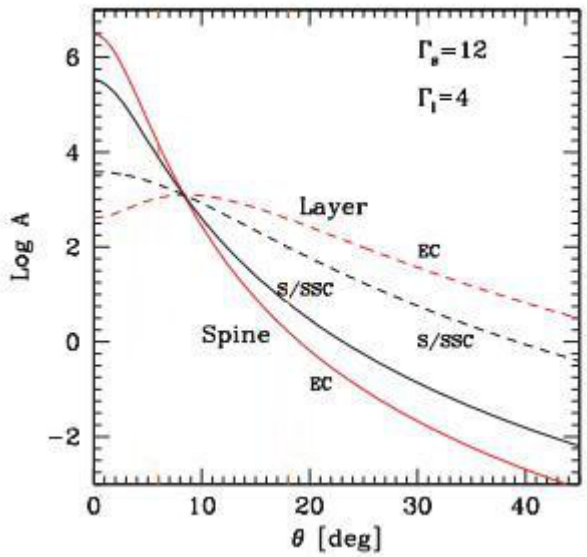

Figure 5.3: Amplification factors for the emission from the spine (solid lines) and layer (dashed lines) as a function of viewing angle, for $\Gamma_s = 12$, $\Gamma_l = 4$ and a spectral index, $\alpha = 1$, the values used when modelling M87 in Ghisellini & Tavecchio (2008). The black lines show the synchrotron to SSC factors and the red lines the external-Compton factors. Taken from Ghisellini & Tavecchio (2008).

to the jet axis. The net result of the transformations is that in the observer frame the external-Compton emission from the layer is less boosted than that from the spine (Ghisellini & Tavecchio, 2008).

By applying this model to M87, Ghisellini & Tavecchio (2008), were able to reproduce the spectrum of the object, and, using the parameters obtained, a theoretical spectrum for the case of a hypothetical M87-like object at a small angle to the line of sight was constructed. This blazar-like spectrum of M87 closely resembles that of LBLs, and the spine is characterised by physical parameters close to those usually inferred for such sources. In this model, the optical and X-ray emission are produced mainly in the spine, while TeV γ-rays would primarily originate in the layer, so a strict correlation between these bands is not directly required. Additionally, MeV-GeV emission from M87 would be produced primarily in the spine and so would not exactly follow the TeV component.

A major problem with this model is that it requires a large number of parameters to be determined, almost double the number for a single-zone model because two sets are required, one for the spine and another for the layer. This leads to a total of 18 free parameters that must be defined. Furthermore, the model has difficulty in reproducing the hard spectrum observed during the flaring of M87 in 2005, because the slope of the TeV spectrum found by the model is mainly dictated by the absorption of TeV photons in the dense optical radiation field rather than by the

intrinsic TeV spectrum, resulting in a predicted spectrum softer than that observed (Tavecchio & Ghisellini, 2008).

5.5.3 The Decelerating-Jet Model

Noting the weaknesses apparent in single-zone SSC models, Georganopoulos & Kazanas (2003) proposed that the high-energy emitting region of TeV BL Lacs is relativistic and decelerating, and in later work the model was applied to M87 (Georganpoulos, Perlman & Kazanas, 2005). The model proposes that a power-law electron distribution is injected at the base of a relativistic jet which decelerates as the distance from the initial injection site increases, while the electron distribution cools radiatively. A consequence of this is that the highest synchrotron frequencies originate at the base of the jet where the electrons are more energetic, while further along the jet the emitted synchrotron spectrum shifts to lower energies and the beaming pattern becomes wider. This means that the observed synchrotron spectrum is expected to vary depending on the angle at which the jet is observed. At small angles of inclination, the synchrotron spectrum is dominated by emission from the base of the jet, while at larger angles, as seen in M87, this emission from the inner, faster, part of the jet is beamed away from the observer and the major contribution to the spectrum is instead from the slower parts, leading to softer observed spectra.

As in simpler one-zone models, the synchrotron photons interact with the high-energy electrons in the jet resulting in inverse-Compton emission; however, in the case of a decelerating jet, the interactions are more complicated. Electrons will upscatter not only the synchrotron photons produced locally, but also those produced downstream in the jet. The synchrotron photons from the slower, downstream, region, with bulk Lorentz factor Γ_s, appear Doppler-boosted in the fast part of the jet, where the bulk Lorentz factor is Γ_f, by a factor $\sim \Gamma_{\rm rel}^2$, where $\Gamma_{\rm rel} \sim (\Gamma_f/\Gamma_s + \Gamma_s/\Gamma_f)/2$ is the relative Lorentz factor between the two regions (Ioka, 2003). As the maximum energy of the synchrotron photons further along the jet is lower, and their energy density is amplified by the effect of Doppler-boosting, they contribute more to the inverse-Compton emission at higher energies than would be expected in a uniform-velocity jet without needing such large Doppler factors. This is known as upstream Compton emission.

The model constructed by Georganpoulos & Kazanas assumes that a power-law electron distribution $n(\gamma) \propto \gamma^{-2}$ is injected at the base of a relativistic jet. The jet is assumed to have a velocity profile $\Gamma(z) = \Gamma_0(z/z_0)^{-2}$, and the electrons cool radiatively as they propagate downstream. The model shows stronger angular dependence for emission from the base of the flow than further along the jet, and the base can account for the highest frequencies in each spectral component; capable of accounting for high-energy emission with only modest Lorentz factors. As seen in Figure 5.4

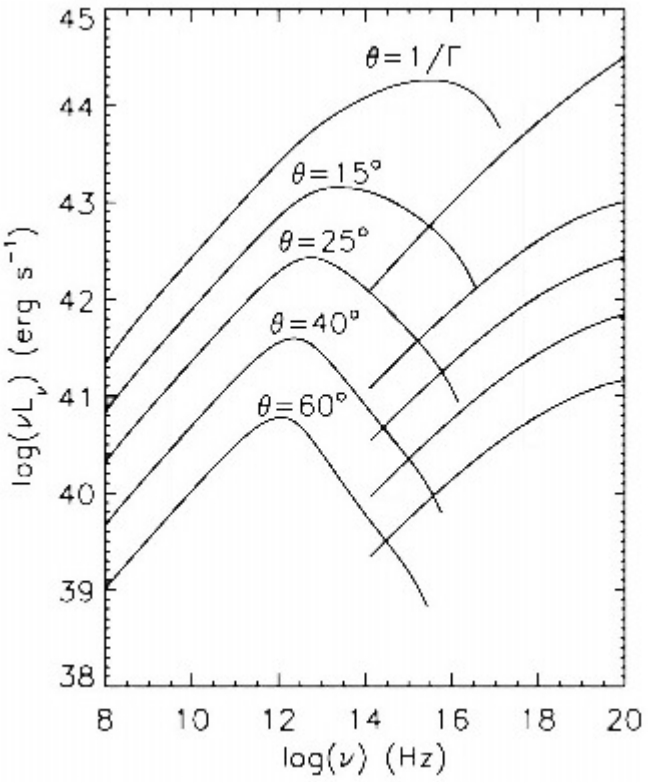

Figure 5.4: SEDs for a range of angles of a flow that decelerates from $\Gamma_1 = 15$ to $\Gamma_2 = 4$ within a length of 2×10^{16} cm. The radius of the cylindrical flow is set to 2×10^{16} cm and a power-law electron distribution, $n(\gamma) \propto \gamma^{-2}$, $\gamma \leq 2 \times 10^5$, is injected at the base of the jet, in the presence of a magnetic field $B = 0.1$ G. Taken from Georganopoulos & Kazanas (2003).

the model is able to reproduce VHE emission for objects with a wide range of angles to the line of sight, and the spectra produced are consistent with those seen in both BL Lac and FR1 objects, as required for AGN unification.

The later work by Georganpoulos, Perlman & Kazanas (2005) applies the model to M87. The authors assume that the inner jet decelerates from a bulk Lorentz factor of $\Gamma_0 = 20$ to $\Gamma = 5$ over a distance of 3×10^{17} cm, and that it is at $\theta = 13°$ to the line of sight. The results of the modelling for two different jet luminosities, $L_{\rm jet} = 2.2 \times 10^{44}$ ergs s^{-1} and $L_{\rm jet} = 1.6 \times 10^{44}$ ergs s^{-1}, can be seen in Figure 5.5. The model predicts that most of the jet power at lower energies originates in the slower, downstream, part of the flow (dotted lines in the figure), while the TeV flux is upstream Compton emission from the faster flow (dashed lines), close to the core of the object. In agreement with observations, a decrease in jet power leads to a steeper X-ray SED. The bulk Lorentz factors used to model M87 were also applied to a hypothetical object at an angle to the line of sight of $\theta = 1/\Gamma_0 = 2.9°$, resulting in a qualitatively similar spectrum to those seen from TeV BL Lacs and lending support to the validity of the model.

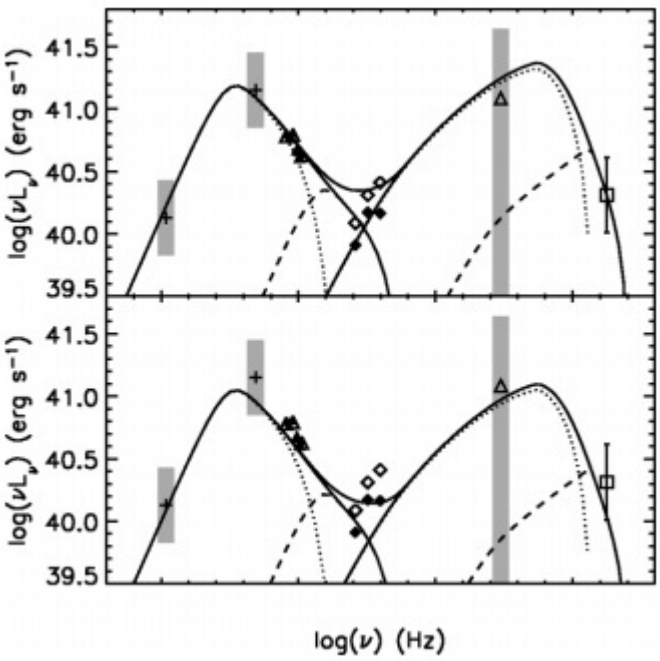

Figure 5.5: Decelerating-flow modelling for M87 at two different jet powers. The top SED is for a jet power of $L_{\rm jet} = 2.2 \times 10^{44}$ ergs s^{-1} and the bottom SED is for $L_{\rm jet} = 1.6 \times 10^{44}$ ergs s^{-1}. The injected electron distribution is a power law with slope $p = 2$, and the magnetic field is $B = 0.015$G. The solid lines represent the synchrotron, Compton and total luminosity, dashed lines the synchrotron and Compton luminosity of the fastest one-fifth of the flow, and the dotted lines that of the remaining four-fifths. Taken from Georganopoulos, Perlman & Kazanas (2005).

When the model of M87 was published, no other misaligned AGN had been detected at TeV energies, and it was suggested that the tighter beaming for very high energy emission implied by the model could explain this. This observation is called into question by the more recent detections of Centaurus A and NGC 1275 at TeV energies, discussed in Section 3.4. Although Abdo et al. (2010e) successfully reproduced the high-energy spectrum of Centaurus A detected with the *Fermi*-LAT using the model, it appears to have some difficulty explaining the TeV emission from this object, (see the blue line in Figure 5.6). It is important to note, however, that the very high energy data are not contemporaneous with the data collected with the *Fermi*-LAT, and it is possible that TeV emission is only observed when the object is in a different state. Another difficulty that the model faces is that, due to the length scales involved, it is difficult to formulate a scenario where variability on the scale of days could be easily reproduced (Rieger & Aharonian, 2008a). Furthermore, results at radio wavelengths suggest that the flow in M87 *accelerates* with increasing distance from the central black hole. Radio observations of the inner jet, out to 1.6 pc, show typical speeds of only a few percent of the speed of light, with no evidence of motions faster than $0.07c$ (Kovalev et al., 2007), and although a study carried out by Ly, Walker & Junor (2007) using the VLBI reported higher velocities ($0.3c$-$0.5c$) in this region, this is still far below the highest velocities (up to $2.5c$) of jet components detected at 15 GHz on larger (kpc) by Biretta, Zhou & Owen (1995).

5.5.4 The Multiblob Model

The model proposed by Lenain et al. (2008) is built on a blob-in-jet model similar to that presented in Section 5.3. It uses the basic scenario presented in Katarzyński, Sol & Kus (2001, 2003), which has been used to model successfully the high-energy emission of the blazars Mrk 421 and Mrk 501. The goal of the model presented by Lenain et al. (2008) is to reconcile beamed and unbeamed sources within the same framework of models, as it is likely that the physics behind generation of very high energy γ-rays in both categories of object is the same. The model presented by Katarzyński, Sol & Kus (2001, 2003) is similar to that presented by Finke, Dermer & Böttcher (2008); however, while it describes the high-energy emission as originating in the blob, it considers that the observed emission at radio through to ultraviolet wavelengths is contributed by radiation emitted directly from an inhomogeneous, conical, extended jet. In the Katarzyński, Sol & Kus, model the effect of the EBL is modelled using the estimations described by Stecker, Malkan & Scully (2006); however, the Lenain model initially disregards EBL modelling, as it is primarily used to describe nearby AGN where the effects of EBL absorption are minimal.

The electron distribution in the Lenain et al. (2008) model is described as a broken power-law:

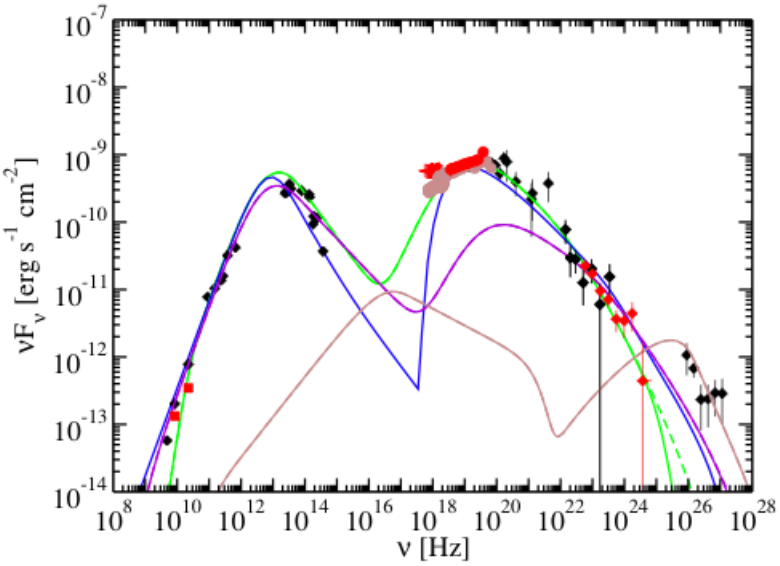

Figure 5.6: SED of the core of Cen A with models fitted by Abdo et al. (2010d) overlaid. Coloured symbols are contemporaneous observations with a number of instruments at the epoch of the LAT observations. From low to high frequency: TANAMI VLBI (red squares), *Swift*-XRT (red crosses), *Swift*-BAT (red circles) and *Fermi*-LAT (red diamonds). The black symbols are archival data (Marconi et al. 2000), including H.E.S.S. observations (Aharonian et al. 2009). The curves are multiple models fitted to the nuclear region of Cen A. The green curve is a synchrotron/SSC fit to the entire data set, the dashed green curve shows that model without $\gamma\gamma$ attenuation, the violet curve is a similar fit but designed to fit under the X-ray data, and the brown curve is a fit to the H.E.S.S. data, designed not to overproduce the rest of the observations. The blue curve is the decelerating-jet model fitted to the data; as can be seen, it appears to underproduce the TeV γ-ray emission. Taken from Abdo et al. (2010d).

$$N_e(\gamma) = \begin{cases} K_1\gamma^{-n_1} & \gamma_{\rm min} \leq \gamma \leq \gamma_{\rm br} \\ K_2\gamma^{-n_2} & \gamma_{\rm br} \leq \gamma \leq \gamma_c \end{cases} \quad {\rm cm}^{-3} \tag{5.27}$$

where $K_2 = K_1\gamma_{\rm br}^{n_2-n_1}$, $\gamma = E/m_ec^2$, $\gamma_{\rm br}$ is the Lorentz factor at which the break in the spectrum occurs, γ_c is the maximum Lorentz factor, and E is the electron energy. These electrons emit through synchrotron processes at energies up to the X-ray range, at which point they reinteract with the photons produced via the inverse-Compton process described earlier. The synchrotron emission is assumed to originate from a different population of electrons to the one producing the lower-energy emission in the extended jet.

The initial model has eight significant parameters on which limits must be placed. Three of these are related to the macrophysics of the object: the magnetic field B, the radius of the emitting blob r_b, and the Doppler factor $\delta_b = [\Gamma_b(1 - \beta_b \cos\theta)]^{-1}$, where β_b is the speed of the moving blob in units of c, $\Gamma_b = (1 - \beta_b^2)^{-\frac{1}{2}}$ is the blob Lorentz factor and θ is the viewing angle. The remaining five parameters are related to the description of the population of emitting particles and are taken from the initial electron distribution described in Equation 5.27: these are K_1, $\gamma_{\rm br}$, γ_c, n_1 and n_2. The value for $\gamma_{\rm min}$ is not crucial for interpreting the SED, and for objects with well-sampled spectra all of these parameters can be well constrained. Owing to limitations in the spectral coverage of M87, Lenain et al. (2008) used the observed very high energy variability to argue that the source of the emission is likely close to the central black hole, probably close to the broadening zone at the base of the jet as described in magnetohydrodynamic jet models such as that proposed by McKinney (2006), who found the Alfvén surface to be at $\sim 50r_s$. To allow for shocks and Fermi acceleration (acceleration of charged particles by a magnetic field) to occur, it is assumed that the emission zone is located slightly above this surface, at $\sim 100r_s$.

The model diverges from the standard blob-in-jet scenarios by proposing that it is statistically unlikely that there is only a single relativistic blob in a jet moving directly towards the observer and that the structure of the jet is likely to be more complicated. To model this, it is suggested that there are a large number of blobs of plasma moving within the jet, harbouring relativistic electrons and propagating in the widened jet-formation zone. The emission zone is modelled as a spherical cap centered on the supermassive black hole and at a distance of $R_{\rm cap}$ from it, filled with several similar homogeneous blobs. The value of $R_{\rm cap}$ is a new free parameter in the model, but it is constrained by magnetohydrodynamic jet models and is assumed to correspond to a position slightly above the Alfvén surface.

For simplicity, the Lenain et al. (2008) model considers a hexagonal pattern of seven blobs of equal radius r_b as shown in Figure 5.7, located at a distance of $100r_s$ from the black hole.

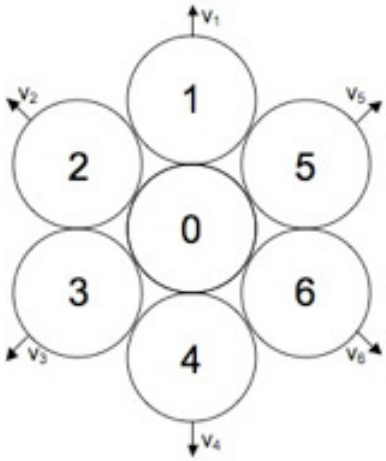

Figure 5.7: Forward view of the geometry of the multiple blobs just above the Alfvén surface as proposed by Lenain et al. The blobs are numbered from $i = 0$ to $i = 6$, as are the associated velocity vectors.

The macroscopic parameters are derived from McKinney (2006), while the choice of seven blobs is justified as the resulting diameter of the cap is of the same order of magnitude as the size of the emitting zone inferred from previous studies. The smaller the radius of each blob, the more the predictions of the model are in line with those of continuous-zone models. A direct consequence of the geometry is that there are two extreme situations depending on the position of the blobs with respect to the line of sight. In the first, the line of sight passes exactly through the gap between three blobs, termed the "inter-blob" case by the authors, while in the second, the line of sight is exactly aligned with the velocity vector of the central blob, termed the "on-blob" case. The emission detected from a single blob (blob i) is dependent on the Doppler factor for that blob, δ_b^i, given by:

$$\delta_b^i = \frac{1}{\Gamma_b(1 - \beta_b \cos(\alpha_i))} \tag{5.28}$$

where α_i is the angle between the velocity vector of blob i and the line of sight. For the inter-blob case, the three blobs closest to the line of sight will all contribute equal amounts to the total flux and will have the same Doppler factor, while the contribution of the remaining blobs decreases with increasing blob radius r_b. In the on-blob case, the central blob, $i = 0$, displays the highest Doppler factor, δ_b^0; however, the contribution to the total flux of the six other blobs is non-negligible, and they all have the same Doppler factor, which is lower than that observed from the central blob. If $r_b << r_s$, then the contributions from the surrounding blobs are more significant. Any transverse gradient in the velocity of the jet is ignored as it is usually small compared to the radial velocity profile, and so it is assumed that all of the blobs have the same Lorentz factor but

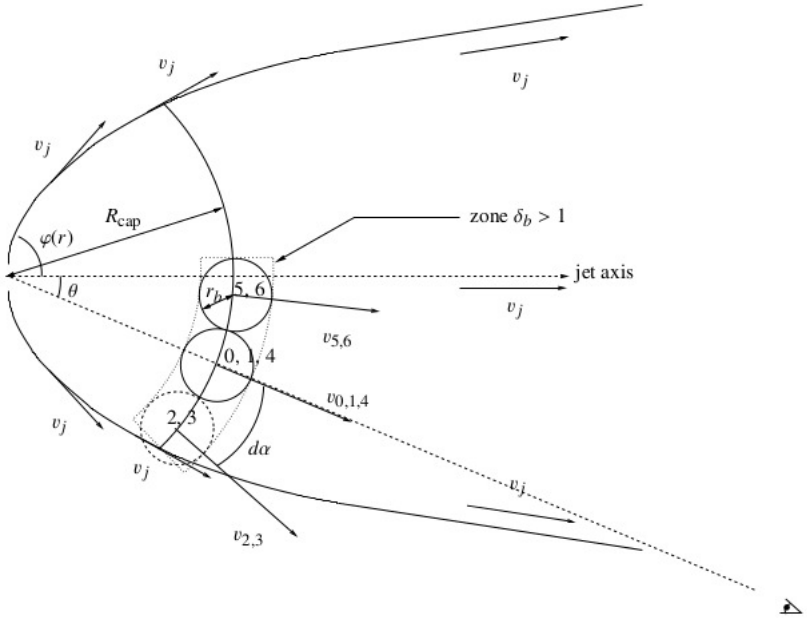

Figure 5.8: Geometric side view of the jet-formation zone in which line of sight passes directly through the central blob. The blobs are numbered 0-6, as shown in Figure 5.7, and their velocities are v_{0-6}, θ is the viewing angle with respect to the jet axis, $\phi(r)$ is the opening angle, r_b is the radius of an individual blob, $R_{\rm cap}$ is the distance of the blobs from the central black hole, v_j is the velocity of the jet and δ_b is the Doppler factor of the blob. In this sketch, blobs 2 and 3 lie outside the jet and their contributions would be ignored. Taken from Lenain et al. (2008).

are ejected at slightly different angles. The geometry of the on-blob case is shown in Figure 5.8, where the central blob is moving directly towards the observer and the velocity vector of each of the surrounding blobs is at an angle $d\alpha$ to the line of sight given by $d\alpha = 2\arcsin(r_b/R_{\rm cap})$.

To calculate the output SED, the radiative transfer of each blob in its own source frame and the flux emitted are calculated, after which the contributions of each blob are summed up. The seed photons for the inverse-Compton emission from a blob are those generated within it by synchrotron emission. Any blob with a Doppler factor $\delta_b^i < 1$ is neglected; this will occur for $\alpha_i > \arccos[(\Gamma_b - 1)/(\Gamma_b\beta_b)]$. Figure 5.9 shows the contribution to the SED of the central blob as compared to the other blobs for the on-blob case, the total SED for that case, and the total SED for the inter-blob case.

Application of the model to M87 by Lenain et al. (2008) results in SEDs which are consistent with currently available data on the object. Assuming a magnetic field of 0.5 G results in relatively small blob radii, smaller than r_s; this raises a potential issue, as very small blobs could disappear on timescales as short as ∼10 minutes due to adiabatic expansion and might not be large enough for particle acceleration to develop. It is argued, however, that this is not necessarily an argument against the model, as long, stable emission would still be possible if the emitting zone is located at

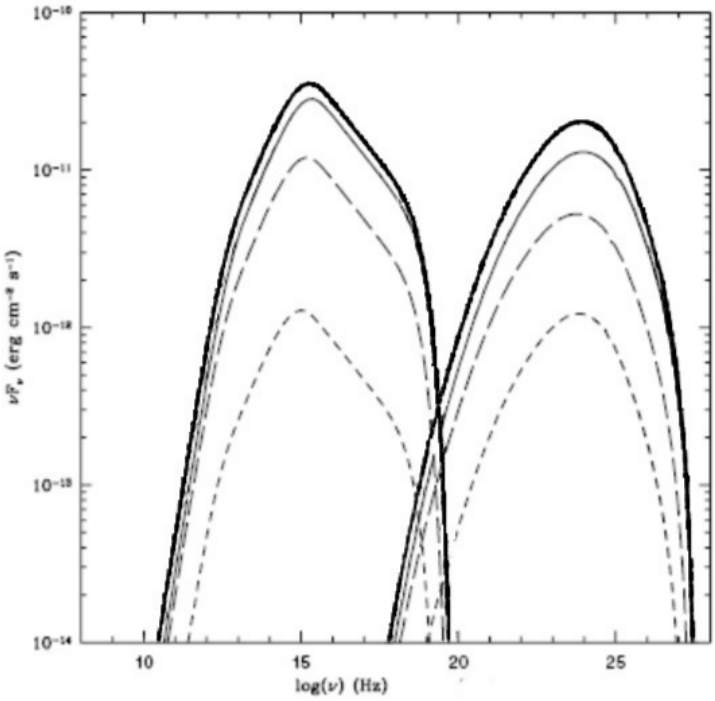

Figure 5.9: An example of the SEDs output by various components of the multiblob model and the total SEDs for both on-blob and inter-blob cases. The thin solid curve shows the contribution of the central blob, which is the most strongly beamed and accounts for most of the emission, while the curve with short dashes shows the total contribution of the six other blobs. The bold solid curve shows the sum of all contributions for the on-blob case, and the curve with longer dashes shows this for the inter-blob case. The closest blob to the line of sight strongly dominates the total emission for high values of r_b. Taken from Lenain et al. (2008).

a stable stationary shock front just above the Alfvén surface. In this scenario, the shock initiates the acceleration of particles in a large number of small blobs continuously crossing the shock; these particles radiate and then produce a quiescent background of VHE emission. The flares seen at TeV energies can then be explained as density fluctuations in the injection of material. If it is assumed that $r_b \gtrsim r_s$, then the SED of M87 can be successfully modelled assuming a lower magnetic field strength, which is at odds with the magnetic fields predicted by magnetohydrodynamc models, although if the emitting zone expands then a local decrease in the magnetic field can be achieved. The model can also reproduce the hard spectra seen by H.E.S.S. during the 2005 flare of M87. The model also predicts a radical change in the X-ray regime at that time but unfortunately there are no contemporaneous X-ray data with which to place constraints.

In addition to modelling M87, Lenain et al. (2008) also applied the model to Centaurus A and predicted detection of TeV γ-rays with the H.E.S.S. telescopes after $\sim$ 50 h of observation, assuming that the soft γ-ray peak detected is of synchrotron origin. If it was assumed to be of inverse-Compton origin, however, no detection was expected. Following the detection of Centaurus A at TeV energies, Lenain et al. (2009) modelled the emission detected by both H.E.S.S. and the *Fermi*-LAT. In that paper, the authors argue that the currently available data favour the suggestion in the previous paper that the soft γ-ray emission is most likely synchrotron in origin and that the model describes well the observed SED. A discrepancy in the flux normalisation between the H.E.S.S. and *Fermi*-LAT data is noted, but as the two data sets are not contemporaneous, this discrepancy could be due to flux variations within the object. The only major difference in the parameters required to reproduce the spectrum of the source when compared with the SSC results for blazars is a relatively high value for the magnetic field, $B = 10$G.

5.6 The Core-Emission Model

In addition to jet models, another potential region for TeV γ-ray emission in radio galaxies and other misaligned AGN is in the vicinity of the central black hole. Rieger & Aharonian (2008b) argue that the most likely site for very high energy γ-ray production in M87 is close to the event horizon of the central black hole at a radius $r \sim r_s$. If this is the case then modelling the emission in this manner can be used to show a link between accretion-disc physics and jet-formation theory, as the mechanism for particle acceleration described could provide the energetic seed particles required for efficient Fermi acceleration on larger scales.

Rieger and Aharonian's model relies on a rigidly rotating, dipolar magnetosphere in the vicinity of the black hole to accelerate particles to high energies. This magnetosphere is generated in a

magnetohydrodynamic jet-disc framework as magnetic flux is dragged inwards and amplified by dynamo action in the inner accretion disc. Efficient particle acceleration occurs close to the light surface, $r_L = c/\Omega \sim (5-10)r_s$ (where Ω = angular velocity, assumed to be constant), on radial scales that are small compared to the curvature of the magnetic field so that the magnetic field can be modelled as a simple monopole-like structure without too great a loss of accuracy. The AGN-black hole environment is plasma-rich and any electric field component parallel to the magnetic field is expected to be screened off at $r < r_L$, so efficient gap-type particle acceleration, as seen in pulsars, is unlikely and inertial effects become the main driving mechanism.

Using Hamiltonian mechanics, and assuming that the charged particle corotates with the field as in bead-on-wire motion, Rieger and Aharonian (2008b) find that as the radius of rotation of the particle approaches r_L, its Lorentz factor, γ, must increase dramatically. As the Lorentz factor of the particle increases, radiative energy losses also increase, the bead-on-wire approximation breaks down, and the field lines bend with increasing inertia so a maximum obtainable Lorentz factor will be reached. The maximum achievable Lorentz factor can be constrained by the validity of the bead-on-wire approximation, requiring that the characteristic acceleration timescale derived from the Hamiltonian must be greater than the relativistic gyrofrequency, leading to:

$$\gamma_{\rm max}^{\rm BB} \leq \frac{1}{\tilde{m}^{\frac{1}{6}}} \left(\frac{qBr_L}{2m_0c^2} \right)^{\frac{2}{3}} \tag{5.29}$$

where $\tilde{m} = 1/(\gamma_0^2[1 - r_0^2/r_L^2]^2)$ and hence is determined by the initial conditions of the particle. This is equivalent to the requirement that the Coriolis force must not exceed the Lorentz force. Using parameters consistent with observations of M87, $B(r_L) \sim 10$ G, $r_L \sim 5 \times 10^{15}$ cm, Rieger and Aharonian (2008b) found that $\gamma_{\rm max}^{\rm BB} \sim 5 \times 10^8$ for electrons, and because $\gamma_{\rm max}^{\rm BB} \propto m_0^{-2/3}$ (Equation 5.29), centrifugal acceleration is not an efficient mechanism for protons, indicating that interactions of accelerated proton with the ambient photon field are negligible. Radiative energy losses due to inverse-Compton interactions with the ambient photon field close to r_L (in relatively low luminosity sources) are not expected to play a large enough role to provide any stronger constraints and hence $\gamma_{\rm max}^{\rm BB}$ is likely to be a sensible estimate of the electron Lorentz factors present.

The TeV emission from a misaligned AGN in this model is thus assumed to arise via inverse-Compton scattering of photons from an advection-dominated accretion disc by the centrifugally accelerated electrons. At energies $<<$ 5 TeV, assuming a power-law electron distribution, the interaction between the highly energetic electrons from the acceleration process and a comptonised photon field originating from the accretion disc results in a power-law evolution for the inverse-Compton spectrum, independent of the incident photon spectrum. At TeV energies, however, the

inverse-Compton spectrum becomes sensitive to the seed-photon distribution from the accretion disc, where the comptonisation of soft cyclosynchrotron photons adds to the spectrum a power-law tail with spectral index $\alpha_c \sim 1.2$. This leads to the very high energy spectrum following a power law with spectral index $\alpha \approx \alpha_c$.

The model presented shows good agreement with the spectrum observed in M87 and is able to reproduce rapid variability as detected from the object. Rieger & Aharonian (2008b) argue that if the particle acceleration and TeV emission do indeed originate close to the central black hole in misaligned AGN, these effects would be difficult to discern in more luminous objects that are more closely aligned to the line of sight, as the emission would be swamped by relativistically beamed emission from the jet. A particularly interesting consequence of the model is that detection at TeV energies could be expected, even for very highly misaligned AGN, something that is extremely unlikely in the case of any of the jet models. Without the detection of such objects, however, it is difficult to distinguish between jet models and the core-emission model. Attempts to model the multiwavelength spectrum of M87 using a core-emission model have had difficulties reproducing flared emission from the object (Hilburn & Liang, 2012). Another potential issue is that the region closest to the black hole is expected to have a high photon density, effectively rendering it opaque to any TeV emission in the region as a result of photon-photon annihilation (Cheung, Harris & Stawarz, 2007); however this view is contested by Rieger and Aharonian (2008b), who argue that this region in M87 is transparent to 10 TeV photons on scales of $5r_s$ - $13r_s$, consistent with the scenario they present.

5.7 Conclusions

To explain the SED of blazars, relatively simple single-zone models, such as that discussed in Section 5.3, can be used; however, such models have great difficulty reproducing the very high energy spectra of AGN observed at greater angles. To explain the emission from such objects, more complicated scenarios such as those presented in this chapter must be envisaged. Three of these are inhomogeneous-jet SSC models and rely on either a structured jet or multiple smaller structures within the jet to reproduce the detected SED; the remaining model posits that TeV emission originates close to the central black hole and is an EC model in which the seed photons for the inverse-Compton emission originate in the accretion disc. Unfortunately, currently available data do not allow for unambiguous rejection of any of the models. Moreover, in all cases, there are issues that need to be resolved.

Of the jet models, possibly the simplest and most successful at reproducing all the observed

characteristics is the multiblob model proposed by Lenain et al. (2008). As it is merely an extension of previously presented blob-in-jet models, it requires few extra assumptions when compared to them. It posits that nonthermal emission from AGN originates in a number of relativistic blobs of plasma close to the Alfvén surface, moving at slightly different angles to the line of sight. The model has shown success in explaining the spectrum of M87 at very high energies, including data both from the low state of the object and from the flare detected in 2005.

The decelerating-jet model of Georganopoulos & Kazanas (2003) has been used to successfully explain the TeV emission from M87 during its low state; however, owing to the requirement of relatively large length scales, this model has great difficulty explaining the rapid variability observed during the flaring from the object in 2005. Additionally, the model appears to have difficulty reproducing the TeV spectrum observed from Centaurus A, leading to potential problems with AGN unification.

The spine-layer model presented in Tavecchio & Ghisellini (2008) proposes that the jets of AGN consist of a central fast-moving spine, surrounded by a slower-moving layer. Unfortunately, the model requires 18 free parameters to successfully describe the jet, making it difficult to derive meaningful constraints. Additionally, this model has great difficulty explaining the hard TeV spectrum observed during the flare of M87 in 2005.

The final model presented here is the core-emission model proposed by Rieger & Aharonian (2008b), in which the nonthermal emission from misaligned AGN originates close to the central black hole. In this model, the seed photons for inverse-Compton scattering are provided by the accretion disc, and the electrons are centrifugally accelerated in the vicinity of the black hole. A potential problem for the model is explaining how the TeV photons escape the intense photon field expected in the proposed emission region, although the authors claim that this would not be a problem for photons of energy 10 TeV. Additionally the authors themselves acknowledge that the model is relatively simplistic and that further work would be required to develop it fully.

Chapter 6

Modelling the Emission from *Fermi*-LAT Selected Misaligned AGN

6.1 Introduction

The detection of three misaligned AGN by current-generation IACTs has opened up a new class of TeV γ-ray source for study and over the coming years the construction of the Cherenkov Telescope Array (CTA), discussed in Section 6.4, will hopefully lead to the detection of more such objects. To identify likely targets, it is useful to model the SEDs of misaligned AGN detected at high energies, using currently available data to place constraints on the physical parameters. By considering projected CTA response curves and the SEDs generated, it should be possible to make reasonable predictions relating to the detection or non-detection of the objects modelled.

As discussed in the previous chapter, modelling the observed TeV emission of the currently detected misaligned AGN has required a shift away from relatively simple single-zone models towards more complicated multizone models. Of the models discussed, the most successful thus far has been the multiblob model of Lenain et al. (2008), which has been able to reproduce the TeV emission from both M87 (Lenain et al., 2008) and Centaurus A (Lenain et al., 2009). This model will be used in this chapter to produce the SEDs of *Fermi*-LAT-selected misaligned AGN.

Object	R.A. (J2000.0)	Dec. (J2000.0)	Redshift z	Class		Catalogue
				Radio	Optical	
3C 78/NGC 1218	03h 08m 26.2s	+04° 06' 39"	0.029	FRI	G	3CR
3C 84/NGC 1275	03h 19m 48.1s	+41° 30' 42"	0.018	FRI	G	3CR
3C 111	04h 18m 21.3s	+38° 01' 36"	0.049	FRII	BLRG	3CRR
3C 120	04h 33m 11.1s	+05° 21' 16"	0.033	FRI	BLRG	3CR
PKS 0625-354	06h 27m 06.7s	-35° 29' 15"	0.055	FRI[a]	G	MS4
3C 207	08h 40m 47.6s	+13° 12' 24"	0.681	FRII	SSRQ	3CRR
PKS 0943-76	09h 43m 23.9s	-76° 20' 11"	0.27	FRII	G	MS4
M87/3C 274	12h 30m 49.4s	+12° 23' 28"	0.004	FRI	G	3CRR
Cen A	13h 25m 27.6s	-43° 01' 09"	0.0009[b]	FRI	G	MS4
NGC 6251	16h 32m 32.0s	+82° 32' 16"	0.024	FRI	G	3CRR
3C 380	18h 29m 31.8s	+48° 44' 46"	0.692	FRII/CSS	SSRQ	3CRR

Table 6.1: *Fermi*-detected misaligned AGN. **Notes** [a] PKS 0625-354 shows some BL Lac object characteristics in the optical band (Wills et al., 2004); [b] Distance to Cen A is assumed to be 3.8 Mpc (Harris et al. 2010). Taken from Abdo et al. (2010c).

6.2 Fermi-LAT observations of Misaligned AGN

The launch of the *Fermi* satellite has opened up many new sources to investigation at γ-ray energies. Of the 709 AGN detected in the first 11 months of *Fermi* operation, 11 have been found with jets misaligned to the line of sight (Abdo et al., 2010f). These 11 sources were found through association of LAT detections with three main low-frequency surveys, the 3CR catalogue (Bennett, 1962; Spinrad et al., 1985), its revised version the 3CRR catalogue (Laing, Riley & Longair, 1983) and the Molonglo Southern 4 Jy Sample (MS4) (Burgess & Hunstead, 2006a, 2006b). The 11 sources included (Table 6.1) M87, Cen A and NGC 1275, all very high energy γ-ray AGN discussed in Chapter 3, 4 additional FRI galaxies, 2 FRII galaxies, and 2 steep-spectrum radio quasars (SSRQs) - objects showing steep radio spectra dominated by core and jet emission. More recently, another potential radio galaxy was detected, IC 310 (Neronov, Semikoz & Vovk, 2010); however, the observed high-energy photons could not originate in a jet but are likely produced at the bow shock formed by the motion of the jet through a dense intercluster medium, a scenario which cannot be modelled using the Lenain et al. (2008) model.

Of the sample of AGN, only three (Cen A, NGC 6251 and 3C 111) were *EGRET* candidate sources; the other eight objects represent new discoveries made with *Fermi*-LAT. The FRIIs detected show significantly lower γ-ray luminosities than, and comparable spectral indices to, their parent population of FSRQs, while the FRI radio galaxies are also less luminous at γ-ray wavelengths than their parent population of BL Lac objects, as expected from AGN unification. Interestingly, the two SSRQs appear very similar to γ-ray emitting FSRQs, suggesting that more powerful Doppler boosting is occurring within the jets than is seen in the other AGN. The average flux for the all of the misaligned AGN discussed here above 100 MeV is $F \sim 6 \times 10^{-8}$ photons cm^{-2}

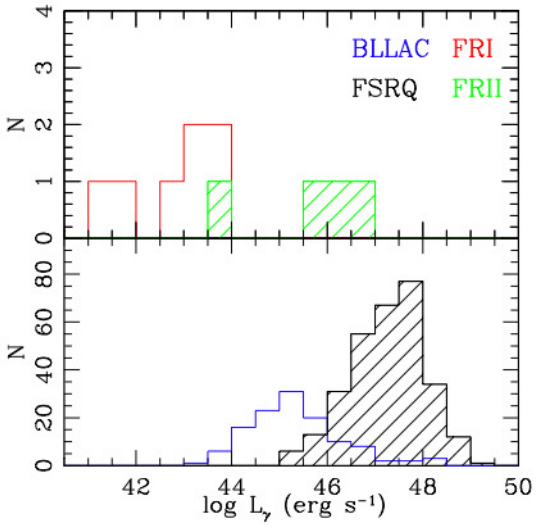

Figure 6.1: Histogram showing the luminosity of *Fermi*-LAT-detected misaligned AGN (upper panel, FRIs - red, FRIIs - green hatched) and blazars (lower panel, BL Lac objects - blue, FSRQs - black hatched). The FRI galaxies show significantly lower luminosities than their parent population of BL Lac objects, while 3C 111 is the only FRII outside the luminosity range of FSRQs. Taken from Abdo et al. (2010c).

s^{-1}, which is not particularly high, but all of the sources were detected with significance $\gtrsim 5\sigma$. The spectra of all of the objects can be described using simple power laws, except for NGC 1275, the brightest at *Fermi*-LAT energies in the sample, whose spectrum softens above ≈ 3 GeV. Additionally, NGC 1275 is the only object in the sample for which variability on timescales of months is observed, although comparison between *Fermi* and *EGRET* fluxes does indicate variability on timescales of years for two other objects, NGC 6251 and 3C 111. Despite the small number of FRIIs with *Fermi*-LAT associations, this does not necessarily suggest that they are less likely to emit at γ-ray wavelengths, as there are fewer nearby FRIIs than FRIs, and the statistics are low. The results of the *Fermi* analysis taken from Abdo et al. (2010c) are summarised in Table 6.2.

6.3 Modelling the Objects

The aim of this work is to investigate the likelihood of future detection at VHE of the *Fermi* misaligned AGN using the planned CTA, and to determine whether the multiblob model can successfully account for the detected γ-ray emission using sensible parameter values (of the order of the values used in the modelling in Lenain et al. (2008)). With this in mind, the spectra of the three misaligned AGN already detected at very high energies, M87, Cen A and NGC 1275 will not be modelled, leaving a total of eight objects to be considered. Starting from parameter values for each of the eight objects being considered inferred from the literature, and those for similar

Object	Γ	Flux (ph cm^{-2} s^{-1}) (>100 MeV)	logLum (erg s^{-1}) (0.1 − 10 GeV)
3C 78/NGC 1218	1.95 ± 0.14	4.7 ± 1.8	42.85
3C 84/NGC 1275	2.13 ± 0.02	222 ± 8	44.00
3C 111	2.54 ± 0.19	40 ± 8[a]	44.00
3C 120	2.71 ± 0.35	29 ± 17	43.43
PKS 0625-354[b]	2.06 ± 0.16	4.8 ± 1.1	43.43
3C 207	2.42 ± 0.10	24 ± 4	46.44
PKS 0943-76	2.83 ± 0.16	55 ± 12	45.71
M87/3C 274	2.21 ± 0.14	24 ± 6	41.67
Cen A	2.75 ± 0.04	214 ± 12	41.13
NGC 6251	2.52 ± 0.12	36 ± 8	43.30
3C 380	2.51 ± 0.30	31 ± 18	46.57

Table 6.2: Results of the *Fermi*-LAT analysis. **Notes** [a] Flux estimated keeping the spectral shape; [b] Likelihood analysis limited to the 300 MeV-100 GeV range, flux(> 300 MeV) and luminosity extrapolated down to 100 MeV. Taken from Abdo et al. (2010c).

objects from their parent population of blazars, it is possible to generate a number of SEDs for each AGN consistent with the data from the *Fermi*-LAT. For each object, parameter values are found that produce a spectrum for the on-blob case consistent with the *Fermi*-LAT spectrum. Using these SEDs, the situations in which a γ-ray detection would be expected with the next-generation IACT array, the Cherenkov telescope array (CTA) discussed in Section 6.4, can be determined. Future multiwavelength studies will hopefully help to narrow down the likely SEDs, enabling a more accurate determination of potential targets to be made.

6.3.1 Correcting for the EBL in Distant Objects

After publication of Lenain et al. (2008) the multiblob model was adapted to allow for modification of the SEDs produced to take account of absorption by the EBL using the corrections proposed in Kneiske, Mannheim & Hartmann (2002) and Kneiske et al. (2004). This addition to the model allows it to be used to model the two relatively distant AGN detected by the *Fermi*-LAT, 3C 207 at $z = 0.681$ and 3C 380 at $z = 0.692$.

The model for the EBL put forward in Kneiske, Mannheim & Hartmann (2002) uses the star-formation rates of the galaxies considered and the ultraviolet escape fraction (a description of the amount of ultraviolet radiation absorbed and re-emitted by the interstellar medium) as the dominant parameters. In the 2002 paper, using data from deep optical galaxy surveys as the primary observational input, the authors construct the model through semi-empirical means; however, this leads to a deficit in the predicted EBL at infrared wavelengths. To resolve this problem, data from luminous infrared galaxies (LIGs), which represent a population of galaxies with infrared luminosities $L_{\rm IR} > 10^{11}$ L$_\odot$ and high star-formation rates are included. These LIGs are not particularly numerous today, but a significant fraction of the infrared light could originate

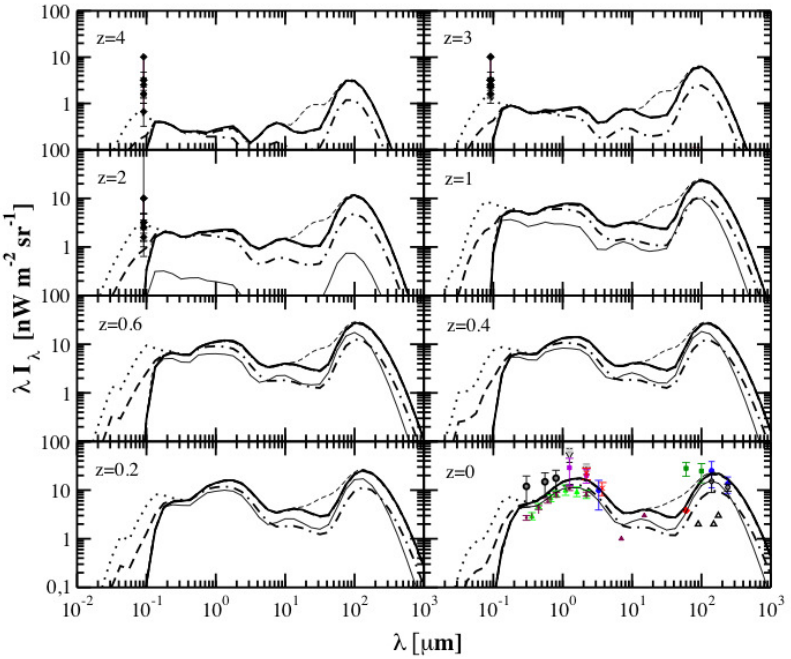

Figure 6.2: The evolving spectrum of the EBL as modelled by Kneiske et al. (2004) for the six different sets of parameters described in the paper. The "best-fit" model is represented by the thick solid line, "warm-dust model" by the thin dashed line, "low-infrared" model by the dot-dashed line, "low star-formation rate model" by the thin solid line, "stellar-ultraviolet" model by the dashed line and "high stellar-ultraviolet" model by the dotted line. The data at $z = 2$, 3 and 4 are taken from Scott et al. (2000). The sources for the datapoints at $z = 0$ are shown in Kneiske, Mannheim & Hartmann (2002).

from them. The resulting model constructed by the authors using the data is shown in Figure 6.2 for a series of different values for the initial parameters.

In the second paper (Kneiske et al., 2004), the effects of using different values for the initial parameters on the EBL model and on the absorption of γ-rays is investigated. By comparing the results from six different EBL models the authors determined that the optical depth from $0.2 < z < 1$ is relatively insensitive to the initial parameters selected, but that at lower redshifts the effects are significant. It is noted that there are a number of weaknesses to using faint-galaxy counts for constructing an accurate model of the EBL, in that these counts tend to be limited to relatively narrow wavelength ranges, thereby introducing strong selection effects. Additionally, galaxy counts are not sensitive to any truly diffuse component of the EBL.

6.3.2 3C 111

3C 111 is an FRII-type radio source, at a distance of $z = 0.0485$, that displays several small-scale features characteristic of a highly active nucleus (Sguera et al., 2005). The central core of the object is bright, and variable on timescales of a few months. The host galaxy is classified as a

Seyfert 1; however, the optical properties of the host galaxy are difficult to study as it is obscured by a region associated with the Galactic dark cloud complex Taurus B (Ungerer et al., 1985). It appears to be a small, elliptical-like galaxy strongly dominated by the bright nucleus. On kpc scales, the object displays a radio double lobe and a single jet that leads into one of the radio lobes. On parsec scales, the jet displays a number of interesting features, including superluminal behaviour (Preuss, Alef & Kellermann, 1988). Additionally, recollimation shocks and regions of interaction between the jet and the surrounding medium are also present. The jet is oriented at an angle of $\theta = 18.1^\circ \pm 5.0^\circ$ to the line of sight (Jorstad et al., 2005).

At X-ray energies, 3C 111 has been observed by every major instrument and shows long-term variations of at least a factor of 5 in the $2-10$ keV range (Reynolds et al., 1998), but no statistically significant variations on timescales less than an hour have been observed (Eracleous, Sambruna & Mushotzky, 2000). It has been suggested (Hartman et al. 1999) that 3C 111 is associated with the *EGRET* source, 3EG J0416+3650, although initially this association was relatively tentative as the optical position of the object is outside the 99% contour. However more recent work using multiwavelength data has strengthened the likelihood of this association (Sguera et al., 2005), and in 2008 it was shown that 3EG J0416 is most likely composed of three variable sources, one of which is positionally coincident with 3C 111 (Hartman, Kadler & Tueller, 2008). The *EGRET* source closest to 3C 111 was detected by *EGRET* only at energies above 100 MeV, and it is likely that the object has a low duty cycle for γ-ray emission as it was only occasionally detectable by *EGRET* (Hartman, Kadler & Tueller, 2008). Similarly, 3C 111 was not detected by the *Fermi*-LAT in every time interval and reached the minimum significance required for detection on only one occasion, with a bin-integration time of 3 months (Abdo et al., 2010c). The γ-ray flux from 3C 111 observed by the *Fermi*-LAT is ~ 20 times smaller than the maximum recorded by *EGRET*, suggesting significant variability in the decade between *EGRET* and *Fermi*-LAT observations; however, low statistics make it impossible to calculate the significance of such variability (Kataoka et al., 2011). Interestingly, a bright flare at 230 GHz was observed by the University of Michigan Radio Astronomy Observatory towards the end of 2008 (during the initial 6 months of *Fermi*-LAT observations), with a subsequent decline in flux over the next year and a half (Chatterjee, Marscher & Jorstad, 2011).

On consulting the literature, it became apparent that the physical parameters of 3C 111 have not been firmly constrained, and since 2000 a number of values have been proposed both for the mass of the central black hole and for the inclination angle of the jet. Marchesini, Celotti & Ferrarese (2004) estimated the central black hole mass to be 36×10^8 $M_\odot$, using a relation between $M_{\rm BH}$ and the magnitude of the bulge of the host galaxy derived from observations of nearby galactic

	$N_{\rm H}$ ($\rm cm^{-3}$)	n_1	n_2	$\gamma_{\rm min}$	$\gamma_{\rm c}$	$\gamma_{\rm br}$
A	1.0×10^6	1.5	3.5	1.0×10^2	1.3×10^5	0.9×10^3
B	1.0×10^6	1.5	3.5	1.0×10^2	1.3×10^5	0.9×10^3
C	1.0×10^6	1.5	3.5	1.0×10^2	1.3×10^5	0.9×10^3
D	1.0×10^6	1.5	3.5	1.0×10^2	1.3×10^5	0.9×10^3
E	1.0×10^6	1.5	3.5	1.0×10^2	1.3×10^5	0.9×10^3
F	1.0×10^6	1.5	3.5	1.0×10^2	1.3×10^5	0.9×10^3

Table 6.3: The electron distributions used in the multiblob modelling of 3C 111.

	$\Gamma_{\rm b}$	z	θ	$M_{\rm BH}$ ($\rm M_\odot$)	$R_{\rm cap}$ ($r_{\rm g}$)	$r_{\rm b}$ (cm)	B (G)
A	3.3	0.0491	19°		100	2.8×10^{14}	1.9
B	3.2	0.0491	10°	2.0×10^8	100	2.8×10^{14}	1.7
C	4.2	0.0491	24°		100	2.8×10^{14}	2.1
D	2.7	0.0491	19°		100	2.8×10^{14}	1.5
E	2.6	0.0491	10°	36×10^8	100	2.8×10^{14}	1.5
F	2.9	0.0491	24°		50	2.8×10^{14}	1.5

Table 6.4: The object parameter values used in the multiblob modelling of 3C 111. The initial black hole mass is within the range proposed in Chatterjee et al. (2011) and the 2nd, larger, black-hole mass is from Marchesini, Celotti, & Ferrarese (2004). The value of 19° for the inclination angle of the jet is calculated using radio observations in Kadler et al. (2008), while the other values used represent the extremes of the range inferred by Lewis et al. (2005), within the scope of the multiblob model.

bulges and dynamical modelling of the stars and gas within them. It is noted that the relation between $M_{\rm BH}$ and the magnitude of the bulge of the host galaxy displays considerable scatter, corresponding to an uncertainty in the measurement of $M_{\rm BH}$ of 42%. More recently, $M_{\rm BH}$ was estimated using the observed properties of the Hα line (taken from Eracleous & Halpern, 2003) in the object and a relation used in Decarli, Dotti & Treves (2011) to determine the mass of the central black holes in a sample of blazars, returning a value of $M_{\rm BH} = 2.4^{+0.6}_{-0.5} \times 10^8$ $\rm M_\odot$ (Chatterjee et al., 2011). The same authors then attempted to estimate $M_{\rm BH}$ using the relationship between it and the FWHM line width of the Hβ broad emission line presented in Vestergaard & Peterson (2006); however, no accurate measurement for the FWHM of the Hβ line for 3C 111 had been published, and so it was assumed that FWHM(Hβ) $\approx$ FWHM(Hα) = 4800 km $\rm s^{-1}$, leading to $M_{\rm BH} = 1.5^{+0.4}_{-0.3} \times 10^8$ $\rm M_\odot$. Further to this, the authors used the correlation between the widths of the Hα and Hβ lines from Greene & Ho (2005), to estimate that FWHM(Hβ) = 5400 $\pm$ 400 km $\rm s^{-1}$ and used this estimate to calculate that $M_{\rm BH} = 1.8^{+0.5}_{-0.4} \times 10^8$ $\rm M_\odot$. It is suggested that the discrepancy between the values found for $M_{\rm BH}$ by Chatterjee et al. (2011) and by Marchesini, Celotti & Ferrarese (2004) is due to a different extinction correction adopted by the later work, $\approx$ 3 magnitudes lower than in the earlier paper. If the same extinction correction is applied in both cases, similar values for the black hole mass are found. Without stronger evidence for or against either conclusion, it was decided, for completeness, that 3C 111 should be modelled for

both estimates of the black hole mass. In the case of the estimates taken from Chatterjee et al. (2011) a value of 2.0×10^8 $M_\odot$ was selected as it is relatively central compared to the extremes of the values calculated.

Using data from a 1996 radio outburst from 3C 111, during which a bright component was ejected in the jet, Kadler et al. (2008) calculated a value of 19° for the angle of inclination by assuming that a similarly bright component was also ejected into the counterjet; a jet speed of $\beta = 0.956$ was also derived. One weakness with the estimate of the inclination is that it assumes symmetry between the jet and counterjet, which need not be the case if the counterjet is covered by an obscuring torus, as implied by X-ray spectral observations (Lewis et al., 2005) indicating substantial amounts of obscuring material. Constraints on the inclination angle were also calculated in Lewis et al. (2005) by using the observed superluminal motion in the radio jet and the projected linear size of the radio lobes. It is found that the apparent velocity implies that either $\theta < 13°$ or $10° < \theta < 26°$. However, assuming that the radio lobes of 3C 111 are of a size comparable with the majority of powerful radio sources (defined as those with $\log_{10} P_{1215\mathrm{MHz}} > 25.0$), the authors argue that is likely that $\theta > 21.7°$ and that even if 3C 111 is a giant radio galaxy (with far larger radio lobes), $\theta > 10.6°$. This makes it unlikely that the upper limit of 13° is correct and supports the conclusion that $10° < \theta < 26°$. It was decided to model the object for the inclination angle found in Kadler et al. (2008) and the extremes of the range suggested in Lewis et al. (2005), as the conclusions drawn in both appear sound. Due to limitations in the model, attempts to model 3C 111 for angles $> 24°$ proved impossible because at such high angles of inclination all of the blobs are outside the jet, even assuming that the γ-ray emission region is relatively close to the central black hole ($r = 50r_g$). Therefore the maximum inclination angle used was $\theta = 24°$.

Modeling of 3C 111 using the multiblob model was successful for each of the six combinations of black hole masses and inclination angles, resulting in physically sensible values for the parameters describing the γ-ray emission region and reproducing the γ-ray spectrum detected by the *Fermi*-LAT; see Table **??** for the parameter values, Table **??** for the electron distributions, and Figures 6.3, 6.4 and 6.5 for the resulting SEDs. For each set of initial parameter values, a similar electron distribution was assumed, while the size of the blobs was kept constant throughout at $r_\mathrm{b} \approx 10r_\mathrm{g}$ for $M_\mathrm{BH} = 2.0 \times 10^8$ $M_\odot$ and $r_\mathrm{b} \approx 0.5r_\mathrm{g}$ for $M_\mathrm{BH} = 2.0 \times 10^8$. For $M_\mathrm{BH} = 36 \times 10^8$, the blobs are relatively small but not unreasonably so, as $r_\mathrm{b} \sim r_\mathrm{g}$, and this allows easier comparisons to be drawn between the models for both sizes of black hole. As would be expected, smaller angles require lower values of both Γ_b and B for both black hole masses; interestingly, however, the differences between the parameters for 19° and for 10° are relatively small, while the parameters required to model the *Fermi*-LAT data for 24° are more extreme though still physically plausible. Differences between

the parameters required to model the *Fermi*-LAT spectrum with a more massive black hole are smaller than those required with a less massive black hole, but in each case Γ_b and B can be significantly lower for a black hole ~ 10 times larger, no matter the angle of inclination. In the case of model E, the combination of a large black hole and an extreme angle of inclination requires that the formation region be closer to the black hole in terms of the gravitational radius, otherwise the Doppler factors of the blobs are too low to produce high-energy emission. Additionally, this relatively small distance from the black hole to the γ-ray emission region, combined with the relatively small size of the blobs results in the difference between the on-blob and inter-blob cases being very small, as can be seen in Figure 6.4. The *Fermi*-LAT spectrum for 3C 111, shown in Figure 6.5, is similar at lower γ-ray energies of $\sim 10^3$ MeV to that of M87 (Abdo et al., 2010c); however, it does appear to drop off slightly more rapidly at higher energy. Comparing the spectra produced by the multiblob model for 3C 111 with those produced for M87 in Lenain et al. (2008) the very high energy spectrum would appear far steeper; however, the spectra produced for 3C 111 do not rule out very high energy emission although it is likely to be significantly fainter than that seen from M87. Further discussion of potential future prospects for 3C 111 can be found in Section 6.5.

6.3.3 3C 120

3C 120 was one of the objects for which data were collected both intentionally and serendipitously while observing other objects by the H.E.S.S. telescopes. These data were analysed in Chapter 4 and it is discussed in detail in Section 4.5.16. There are two estimates for the black hole mass of this object in recent literature, 3.5×10^7 $M_\odot$ (León-Tavares et al., 2010) and 5.5×10^7 $M_\odot$ (Vestergaard & Peterson, 2006). The former estimate was calculated using the relation between black hole mass and stellar velocity dispersion within the galactic bulge of an object, proposed in Greene & Ho (2006) for AGN following on from work that showed a tight correlation between these parameters in inactive systems. The larger estimate of the black hole mass comes from work on determining the relationship between it and the luminosity and emission line-widths of the AGN (Vestergaard & Peterson, 2006); these authors calibrated the relationship using results for 32 AGN, leading to a relationship with relatively low scatter which enabled them to present fairly precise estimates for the black hole masses of these AGN, including 3C 120.

The inclination angle of 3C 120 was calculated using data collected with the VLBA at a wavelength of 7 mm between 1998 and 2001 (Jorstad et al., 2005). Using the radio data, seven components were identified by Jorstad et al. (2005) and the apparent velocity of each was measured over the period of observation. By measuring the variability timecale for each of the components,

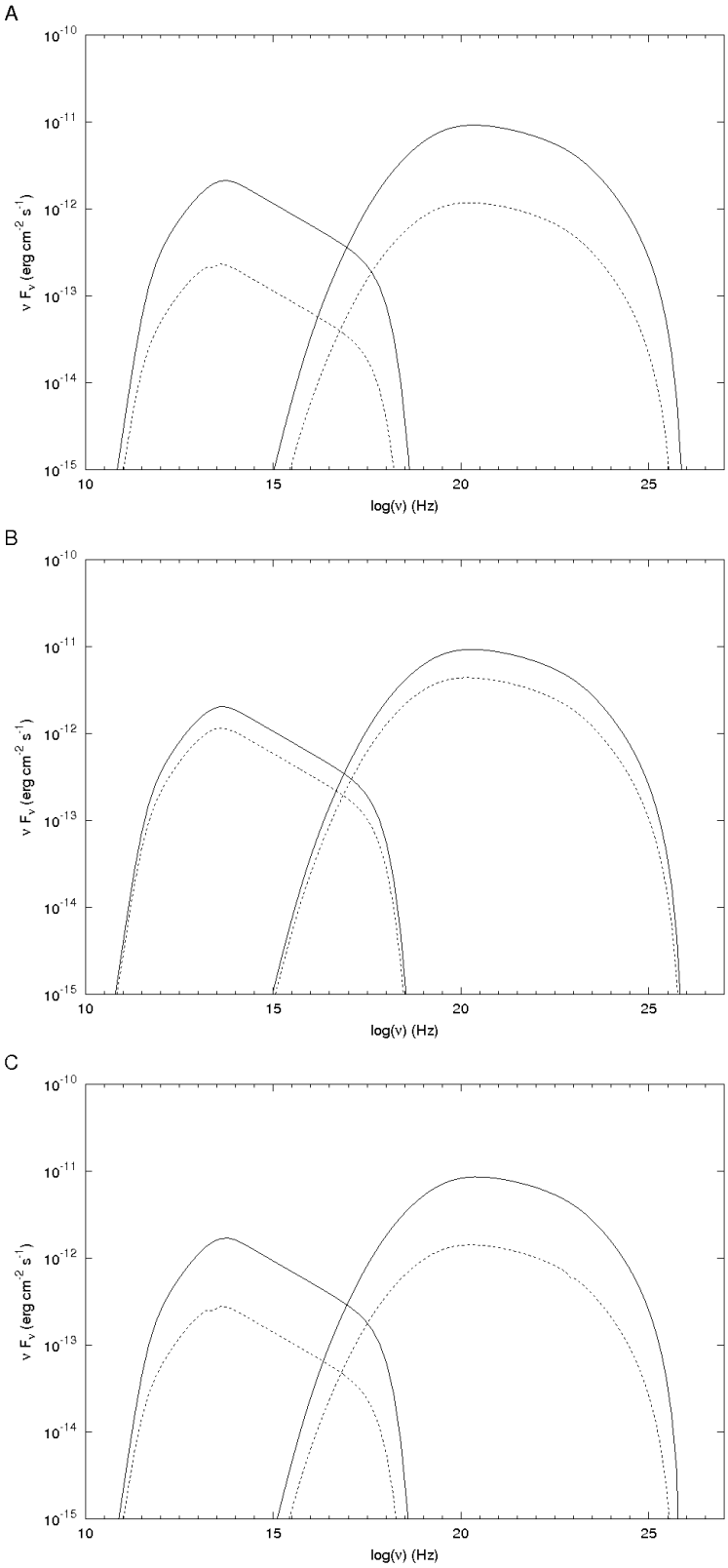

Figure 6.3: SEDs for 3C 111 produced with the parameter values shown in Table 6.4 and the electron distributions described in Table 6.3 using multiblob models A, B and C ($M_{\rm BH} = 2.0 \times 10^8$ $M_\odot$). The solid curves represent the on-blob case and the dashed curves the inter-blob case.

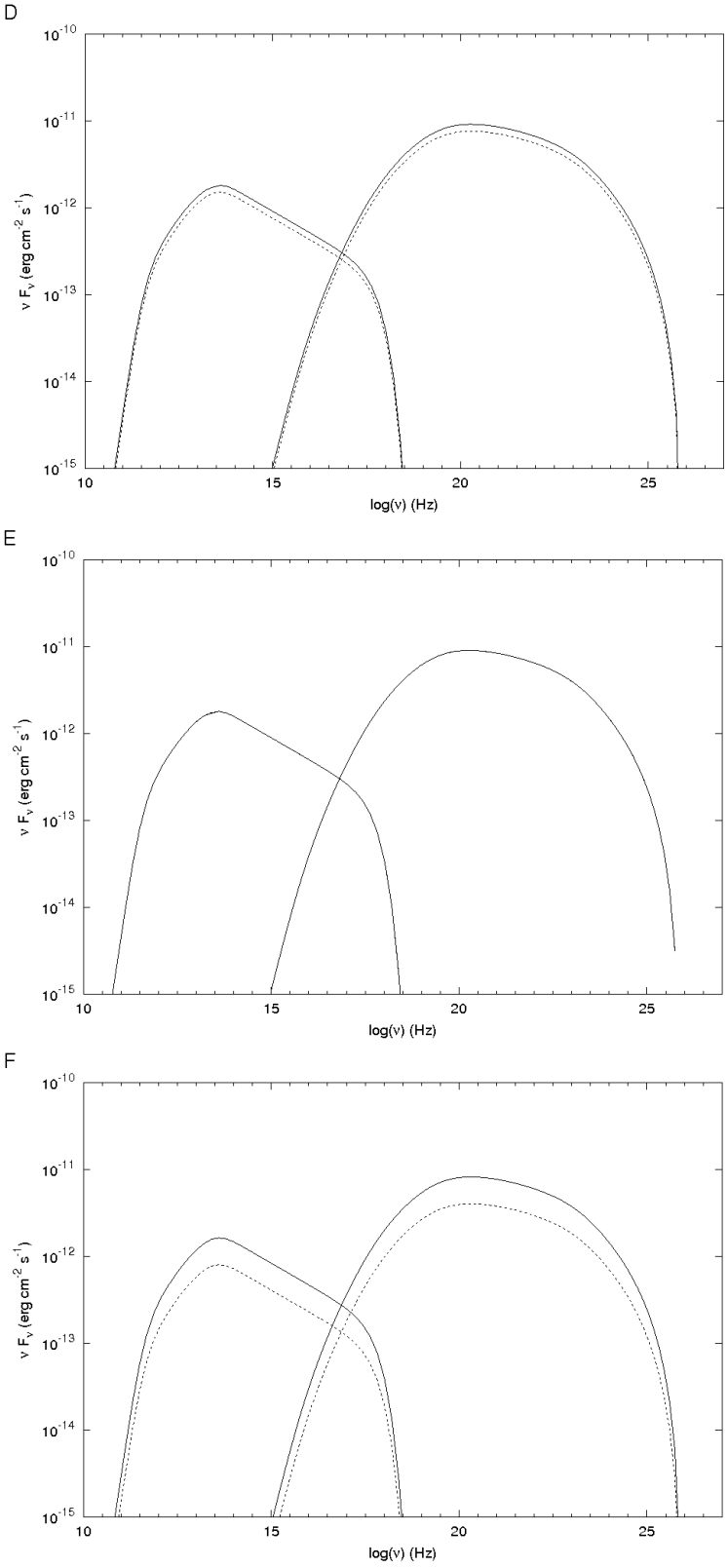

Figure 6.4: SEDs for 3C 111 produced with the parameter values shown in Table 6.4 and the electron distributions described in Table 6.3 using multiblob models D, E and F ($M_{\rm BH} = 36 \times 10^8$ $M_\odot$). The solid curves represent the on-blob case and the dashed curves the inter-blob case. In model E, the curves for the on-blob and inter-blob cases are indistinguishable due to the small relative distance of the γ-ray emission region from the black hole and the relative size of the blobs compared to the black hole's gravitational radius.

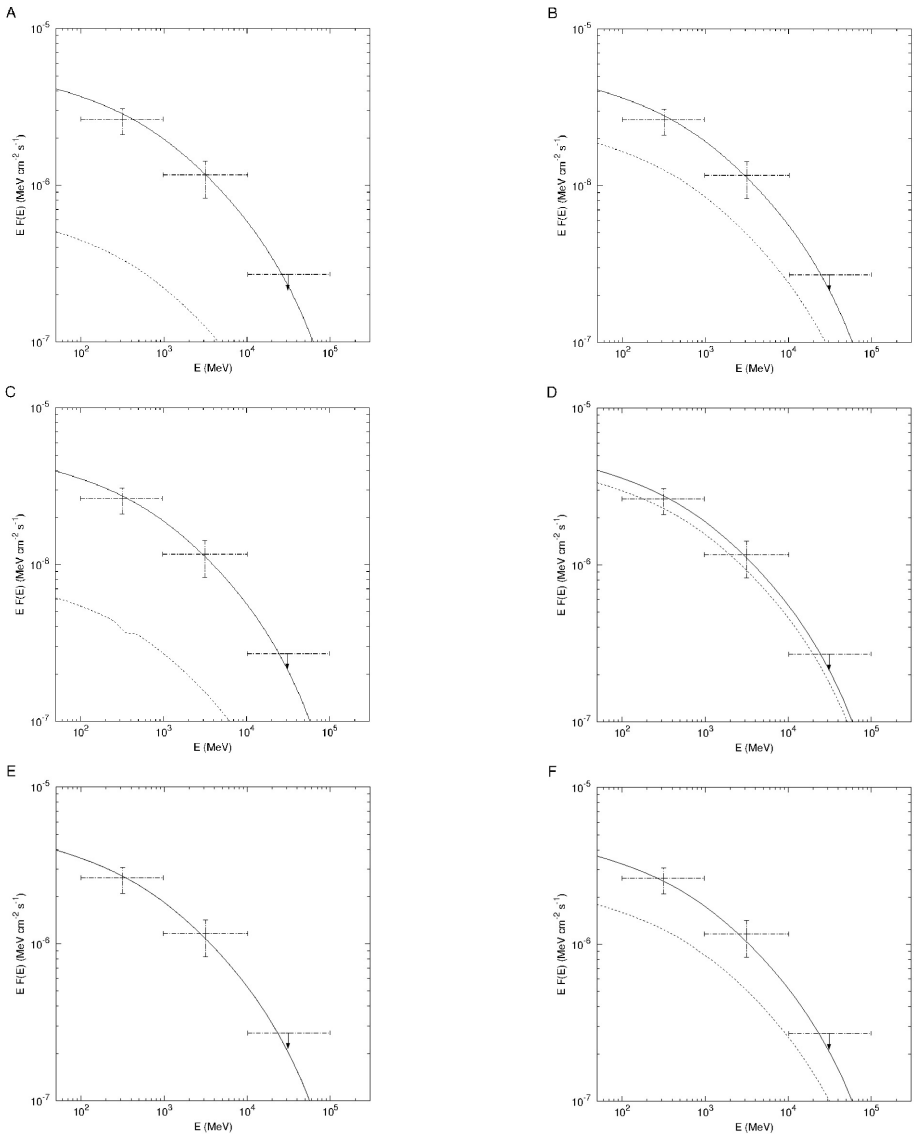

Figure 6.5: Close-up of the SEDs calculated for 3C 111 shown in Figures 6.3 and 6.4 in the energy regime observed by the *Fermi*-LAT, displayed together with the *Fermi*-LAT spectrum (the points) for the object (Abdo et al., 2010c). The SEDs on the left are for $M_{\mathrm{BH}} = 2.0 \times 10^8$ $\mathrm{M}_\odot$, while those on the right are for $M_{\mathrm{BH}} = 36 \times 10^8$ $\mathrm{M}_\odot$. The solid curves represent the on-blob case and the dashed curves the inter-blob case. In model E, the curves for the on-blob and inter-blob cases are indistinguishable due to the small relative distance of the γ-ray emission region from the black hole and the relative size of the blobs when compared to the black hole's gravitational radius.

	$N_{\rm H}$ ($\rm cm^{-3}$)	n_1	n_2	$\gamma_{\rm min}$	$\gamma_{\rm c}$	$\gamma_{\rm br}$
A	7.0×10^7	1.5	3.6	1.0×10^2	2.0×10^4	2.3×10^2

Table 6.5: The electron distribution used in the multiblob modelling of 3C 120.

	$\Gamma_{\rm b}$	z	θ	$M_{\rm BH}$ ($\rm M_\odot$)	$R_{\rm cap}$ ($r_{\rm g}$)	$r_{\rm b}$ (cm)	B (G)
A	6.2	0.033	20.5°	5.5×10^7	50	0.7×10^{14}	5.5

Table 6.6: The object parameter values used in the multiblob modelling of 3C 120. The black hole mass used in the modelling is estimated using optical and ultraviolet single-epoch spectroscopy in Vestergaard & Peterson (2006). A second, smaller, estimate of the black hole mass, 3.5×10^7 $\rm M_\odot$, is found in León-Tavares et al. (2010) using the black hole mass - stellar velocity dispersion of the galactic bulge relation proposed in Greene & Ho (2006); however, (as explained in the text) it proved impossible to replicate the *Fermi*-LAT data using this estimate. The angle of inclination for the jet is that estimated in Jorstad et al. (2005).

an estimate of the Doppler factor in each of the knots was calculated; this could then be used, along with the apparent velocity, to make an estimate of the inclination angle of the component being studied. To estimate the viewing angle of the jet, Jorstad et al. (2005) found a weighted average of the values for the viewing angles of each of the components with weights inversely proportional to the uncertainties in the apparent speed, obtaining a value for $\theta \approx 20.5°$.

The spectrum of 3C 120 constructed from the *Fermi*-LAT data is relatively steep and proved difficult to reproduce for $M_{\rm BH} = 5.5 \times 10^7$ $\rm M_\odot$. In the case of a smaller black hole mass, no solutions were found without resorting to physically improbable values for the parameters. The spectrum constructed successfully for the larger black hole mass uses the parameter values in Table 6.6 with the electron distribution described in Table 6.5, and is shown in Figure 6.6. Despite modelling the *Fermi*-LAT data with some success (Figure 6.7), the model has difficulty reproducing the steepness of the spectrum between 100 MeV and 1 GeV without resorting to physically improbable values for $\Gamma_{\rm b}$ and B. To approach the steepness, a relatively early break in the initial electron distribution must be assumed, $\gamma_{\rm br} \leq 2.3 \times 10^2$, which leads to the requirement that $\Gamma_{\rm b}$ and B must be relatively high to account for the *Fermi*-LAT observations; the earlier the assumed break in the spectrum, the higher these values must be. For $\gamma_{\rm br} = 2.3 \times 10^2$ the values of B and $\Gamma_{\rm b}$ needed to predict emission at *Fermi* energies are comparable to the values seen in other, similar objects and the spectrum can be reproduced relatively accurately. The blob size used in the model is $\sim 10 r_{\rm g}$, which is the cause of the relatively large discrepancy between the on-blob and inter-blob cases. As discussed, the spectrum of the object at *Fermi*-LAT energies is very steep, and the modelling suggests that there is likely to be very little, if any, emission at very high energies: this can clearly be seen in Figure 6.6.

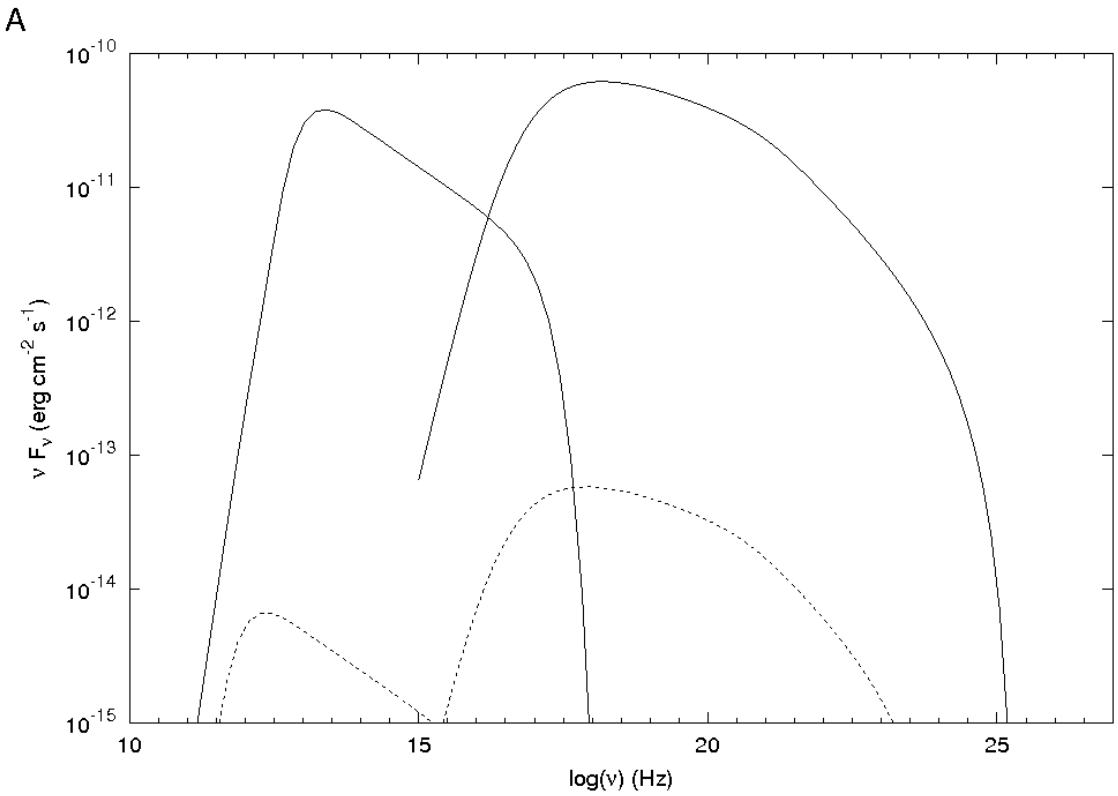

Figure 6.6: SED for 3C 120 produced with the parameter values shown in Table **??** and the electron distribution described in Table 6.5. The solid curve represents the on-blob case and the dashed curve the inter-blob case. The relatively high angle of inclination, high ratio between blob size and black hole gravitational radius, and relative closeness of the γ-ray emission region to the black hole lead to a large discrepancy between the on-blob and off-blob cases. The cut-off seen at the lowest inverse-Compton energies is an artifact of the model.

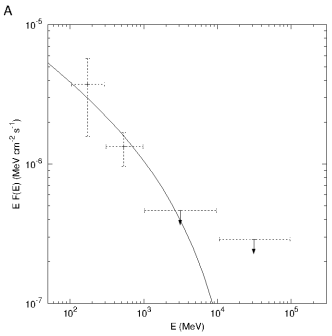

Figure 6.7: Close-up of the SED for 3C 120 shown in Figure 6.6 in the energy regime observed by the *Fermi*-LAT (right), displayed along with the *Fermi*-LAT spectrum for the object (the points) (Abdo et al., 2010c). The large difference between the on-blob and inter-blob cases means that the inter-blob case is not visible in the figure.

	$N_{\rm H}$ ($\rm cm^{-3}$)	n_1	n_2	$\gamma_{\rm min}$	$\gamma_{\rm c}$	$\gamma_{\rm br}$
A	1.3×10^6	1.5	3.6	1.0×10^2	1.1×10^5	2.0×10^3
B	4.5×10^6	1.5	3.5	1.0×10^2	1.1×10^5	2.0×10^3
C	1.3×10^6	1.5	3.5	1.0×10^2	1.1×10^5	2.0×10^3

Table 6.7: The electron distributions used in the multi-blob modelling of 3C 207.

6.3.4 3C 207

3C 207 is a powerful radio source associated with an SSRQ at a redshift of $z = 0.681$, hosted in an FRII galaxy (Abdo et al., 2010c). Radio imaging of the object shows extended radio emission with an extension of around 10 arcsec (Brunetti et al., 2002), as well as the presence of a relatively small, fairly symmetric triple source (Bogers et al., 1994) with a one-sided radio jet. At low radio frequencies, a symmetrical double-lobed structure can be observed. Reanalysis of available radio data by Brunetti et al. (2002), resolved the radio jet into three main components, an innermost knot $\sim 2''$ from the nucleus, a second knot $\sim 4''$ from the nucleus and a hotspot at the end of the jet. The angle of the jet with respect to the line of sight is unknown, but it displays strong curvature (Hough, Vermeulen & Readhead, 1998).

Observations of 3C 207 with *Chandra* in 2000 revealed a bright point-like source coincident with the radio nucleus, enhanced diffuse emission in the direction of the counter-lobe, and extended emission along the radio jet concentrated in two X-ray knots (Brunetti et al., 2002). These X-ray knots are coincident with the most distant radio knot in the jet and the radio hotspot at the end of the jet. The *Chandra* X-ray spectrum obtained for the nucleus is well fitted by a single absorbed power law, showing significant absorption above the Galactic value in the direction of 3C 207, and it is thought to be dominated by a nonthermal, beamed component (Brunetti et al., 2002). Additionally, evidence of highly ionised gas in the vicinity of the nucleus was detected. The non-nuclear X-ray components follow a relatively flat power law and do not show the absorption seen from the nucleus, suggesting that the knots are not affected by the dusty torus. The evidence suggests that the X-ray knots are sites of electron acceleration and SSC emission. Modelling the X-ray emission from the knots, it is argued that the angle of the jet to the line of sight at the position of the knots is $\sim \theta_{\rm bulk} \leq 10^\circ$, compatible with the angle for the innermost region of the radio jet. 3C 207 is associated with the *Fermi*-LAT source, 1FGL J0940.8+1310, with a probability of 99%; however two other AGN with lower association probabilities of 51% and 71% are also found within the LAT 95% error radius (Abdo et al., 2010c).

To date there are no estimates of the mass of the central black hole in 3C 207, so it was decided to model the object both for a fairly average black hole mass $M_{\rm BH} \sim 10^8$ $\rm M_\odot$ and for a larger black hole mass $M_{\rm BH} \sim 10^9$ $\rm M_\odot$, similar in mass to the one hosted in M87. The viewing angle

	Γ_b	z	θ	M_{BH} ($M_\odot$)	R_{cap} (r_g)	r_b (cm)	B (G)
A	7.0	0.681	15.0°	1.0×10^8	100	2.0×10^{14}	4.8
B	3.8	0.681	15.0°		100	2.0×10^{14}	2.6
C	4.2	0.681	15.0°	1.0×10^9	100	2.0×10^{14}	2.2

Table 6.8: The object parameter values used in the multiblob modelling of 3C 207. As there is little data on the mass of the black hole in 3C 207, the object was modelled for both s more massive, 1.0×10^9 $M_\odot$ black hole and a less massive, 1.0×10^8 $M_\odot$ black hole. The angle of $\theta = 15°$ is implied by observations of knots in the jet of 3C 207 described in Brunetti et al. (2002). Attempts were made to model the object with similar electron distributions for both black hole masses; however, the shape of the spectrum proved difficult to reproduce, leading to model B. Due to the large redshift of 3C 207 the results were corrected for the EBL, using the model of Kneiske, Mannheim & Hartmann (2002) and Kneiske et al. (2004).

of the jet is not strongly constrained. However, Brunetti et al. (2002) studied a number of X-ray features detected by the *Chandra* satellite within the lobes and jet of the object at both X-ray and radio wavelengths and used external inverse-Compton modelling to estimate the viewing angle of the knot detected in the jet, finding $\theta \leq 10°$. They argue that this is lower than would be expected for the initial inclination angle of an object such as 3C 207, but that, as the radio jet is relatively distorted, it is possible that the knot moves in a direction a few degrees closer to the line of sight than the innermost parts of the jet. If this line of reasoning is correct, then the jet may be at an inclination angle of $\theta \sim 15°$. Initially, the object was modelled for angles of $\theta \sim 15°$ and $\theta \sim 10°$; however, the differences between the parameter values required to reproduce the *Fermi*-LAT spectrum for the two angles were minimal and only the results for $\theta = 15°$ are presented here. The redshift of 3C 207 is relatively large ($z = 0.681$) so the EBL correction of Kneiske, Mannheim & Hartmann (2002) and Kneiske et al. (2004) was included in the modelling.

As shown in Figure 6.8, the object was modelled twice with black hole mass $M_{BH} = 10^8$ $M_\odot$ and once with $M_{BH} = 10^9$ $M_\odot$. This was an attempt to see if the *Fermi*-LAT spectrum could be reproduced using similar initial electron densities for both black hole masses, and the approach was successful (Figure 6.9). The parameter values used to successfully model the object are shown in Table 6.8 and the electron distributions are given in Table 6.7. For the models of the object using $M_{BH} = 10^8$ $M_\odot$, the blobs have $r_b \approx 13.5 r_g$, similar in relative size to those used to model Centaurus A in Lenain et al. (2008); however, the relatively large size leads to discrepancies between the on-blob and inter-blob SEDs, so much so that the inter-blob SEDs are not visible in Figure 6.9. The blobs used to model 3C 207 for $M_{BH} = 10^9$ $M_\odot$ are the same size as those used for the lower-mass black hole with $r_b \approx 1.35 r_g$. Although $r_b > r_g$, r_b is still close enough to r_g to mean that the difference in SED output between the on-blob and inter-blob cases is minimal.

If a similar electron density is assumed for both values of black hole mass there is a very large difference in the Γ_b and B values required to reproduce the *Fermi*-LAT spectrum, as would be

expected. In fact, if it is assumed that $M_{\rm BH} = 10^8$ $M_\odot$ and $N_{\rm H} = 1.3 \times 10^6$ cm^{-3}, then the values for $\Gamma_{\rm b}$ and B required to reproduce the *Fermi*-LAT spectrum are fairly large, $\Gamma_{\rm b} = 7.6$ and $B = 4.8$ G, compared to the more modest $\Gamma_{\rm b} = 4.5$ and $B = 2.2$ G for $M_{\rm BH} = 1.0 \times 10^9$ $M_\odot$. If the initial electron density is increased by a factor of ~ 3.5 to $N_{\rm H} = 4.5 \times 10^6$ cm^{-3} for $M_{\rm BH} = 10^8$ $M_\odot$, still well within physically sensible limits, the values of $\Gamma_{\rm b}$ and B required to model the spectrum at *Fermi*-LAT energies ($\Gamma_{\rm b} = 4.2$ and $B = 2.6$ G) approach those found for the larger assumed black hole mass. In all cases, the values for $\Gamma_{\rm b}$ and B used to reproduce the *Fermi*-LAT spectrum are larger than those required to model the spectra from the other objects investigated, but they are still physically reasonable. The synchrotron spectra generated for models B and C are significantly lower relative to the inverse-Compton spectrum when compared to model A due to the smaller values for $\Gamma_{\rm b}$ and B. Another consequence of the smaller $\Gamma_{\rm b}$ and B in models A and C is that the slope of the SEDs at high energy is slightly lower, although, the difference is not highly significant. In all cases, the VHE spectrum predicted for 3C 207 is very steep, far steeper than has been detected from M87 but similar to that predicted for PKS 0521-36, and it has been argued that PKS 0521-36 may be detectable with future instruments (Lenain et al., 2008).

6.3.5 NGC 6251

NGC 6251 is an FRI galaxy at a redshift of $z = 0.0244$ (Evans et al., 2005). It is classified as an FRI radio galaxy based on the morphology of the jet and its luminosity at 178 MHz; however, the overall structure observed at these wavelengths resembles that seen in FRIIs or intermediate FRI/FRII sources (Takeuchi et al., 2012). Close to the nucleus, the object hosts a radio jet 130 kpc in length (Evans et al. 2005) and believed to be at an angle of inclination $\theta \lesssim 40^\circ$ that appears to be relativistic up to large distances from the core (Takeuchi et al., 2012). Fitting of the jet with SSC models has led to a more constraining upper limit of $\theta_i \lesssim 18^\circ$ (Chiaberge et al., 2003), and an inclination angle of $\theta_i \lesssim 12^\circ$ has been suggested in Evans et al. (2005). The angle of the jet with respect to the line of sight is observed to change with distance from the core, from 33° at 50 arcsec from the core to 45° at 200 arcsec (Migliori et al., 2011). It has been argued that there is a counterjet (Sudou et al., 2000), although this has been disputed (Jones & Wehrle, 2002). NGC 6251 displays radio lobes with a linear extension of ≈ 2.1 Mpc, larger than those of Centaurus A (Takeuchi et al. 2012).

The central core of the NGC 6251 displays both thermal and nonthermal emission. At infrared ($\approx$ 15 to 30 μm) wavelengths, the SED appears to be dominated by thermal dust emission, with nonthermal synchrotron emission only contributing $\sim$ 30% of the flux (Leipski et al., 2009). It is likely that synchrotron emission accounts for most of the optical to ultraviolet flux from the

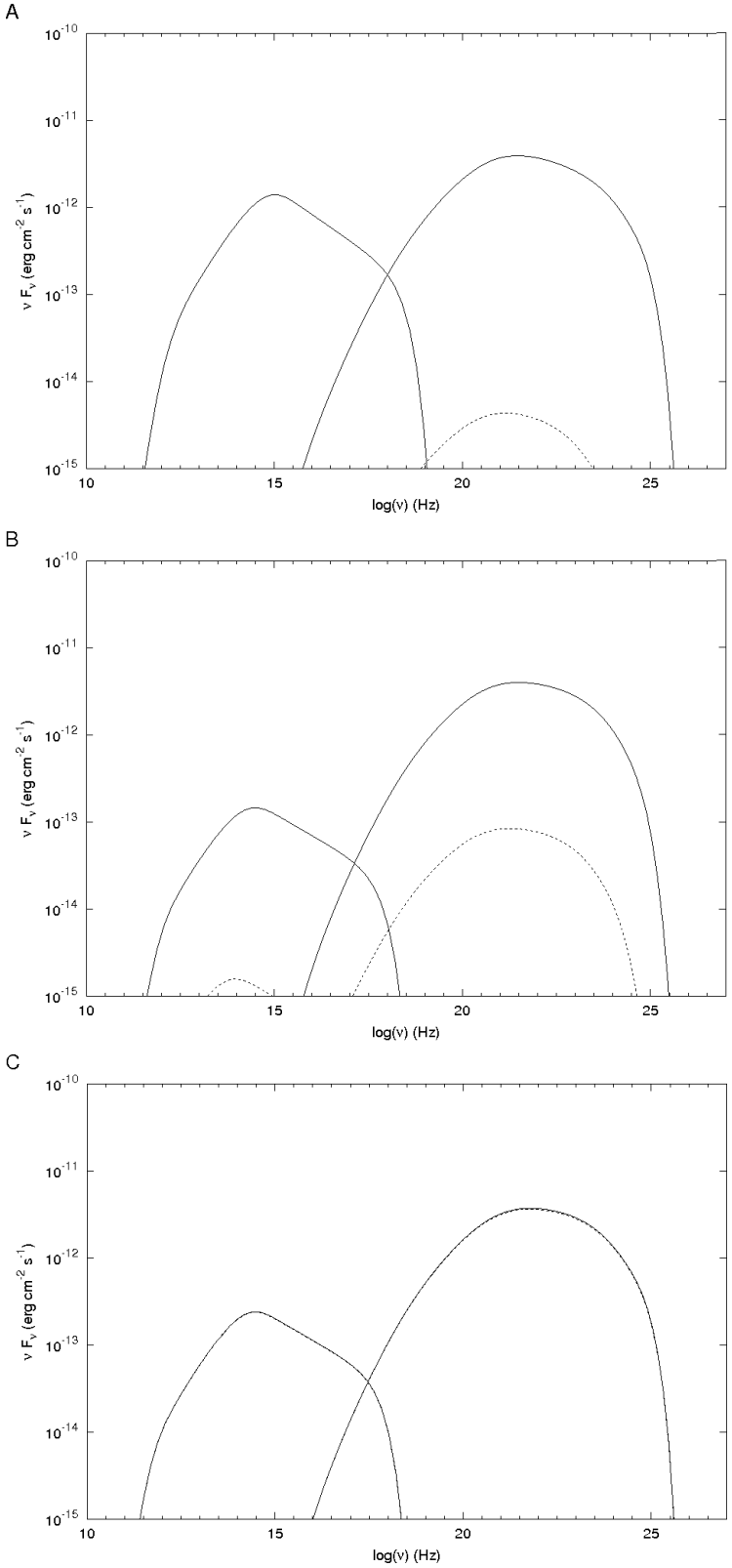

Figure 6.8: SEDs for 3C 207 produced using the multiblob model with the parameter values shown in Table 6.8 and the electron distributions in Table 6.7. The solid curves represents the on-blob case and the dashed curves the inter-blob case. In model C, the on-blob and inter-blob cases are indistinguishable due to the relatively small size of the blobs when compared with the assumed black hole mass.

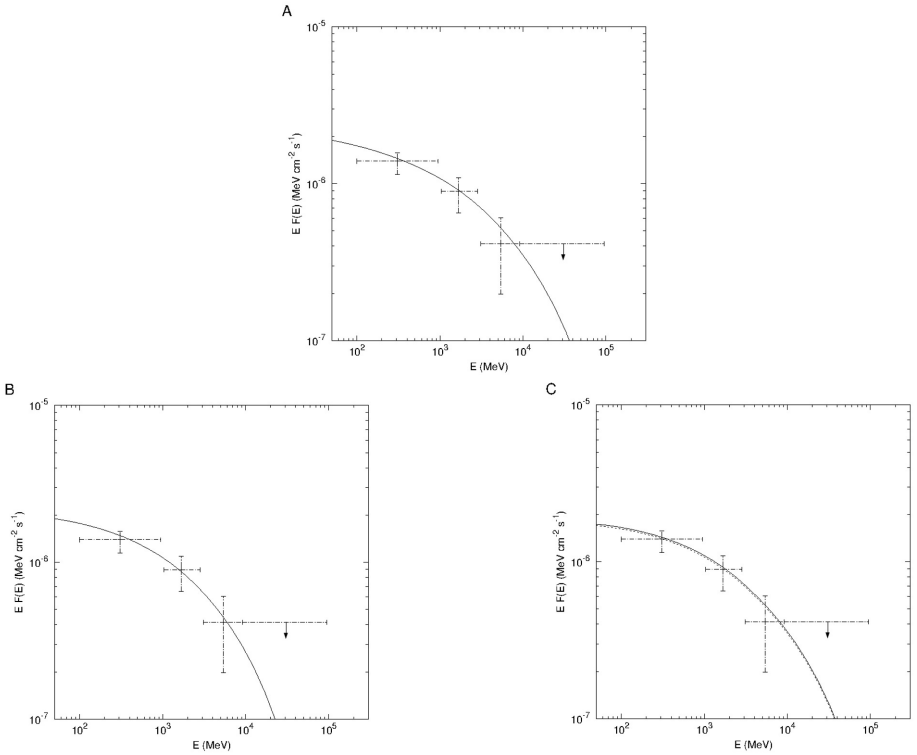

Figure 6.9: Close-up in the energy regime observed by the *Fermi*-LAT of the SEDs shown for 3C 207 in Figure 6.8, displayed together with the *Fermi*-LAT spectrum (the points) for the object (Abdo et al., 2010c). The solid curves represents the on-blob case and the dashed curves the inter-blob case. A number of factors lead to a minimal difference between the on-blob and inter-blob cases in model C. In models A and B, the difference between the on-blob and inter-blob cases is so large that the inter-blob SED is not visible in the figure.

	$N_{\rm H}$ ($\rm cm^{-3}$)	n_1	n_2	$\gamma_{\rm min}$	$\gamma_{\rm c}$	$\gamma_{\rm br}$
A	4.0×10^6	1.5	3.6	1.0×10^2	0.9×10^5	0.7×10^3
B	4.0×10^6	1.5	3.6	1.0×10^2	0.9×10^5	0.7×10^3

Table 6.9: The electron distributions used in the multiblob modelling of NGC 6251.

	$\Gamma_{\rm b}$	z	θ	$M_{\rm BH}$ ($\rm M_\odot$)	$R_{\rm cap}$ ($r_{\rm g}$)	$r_{\rm b}$ (cm)	B (G)
A	4.2	0.0244	18.0°	6.0×10^8	100	5.0×10^{13}	3.2
B	4.3	0.0244	12.0°		100	1.4×10^{14}	3.1

Table 6.10: The object parameters used in the multiblob modelling of NGC 6251. The value of $\rm M_{BH} = 6.0 \times 10^8\ M_\odot$ is consistent with the range reported in Ferrarese & Ford (1999) calculated using data collected with the *Hubble Space Telescope*. The smaller value for the angle of inclination, $\theta = 12°$ is taken from Evans et al. (2005) calculated by modelling X-ray data, while $\theta = 18°$ is taken from the upper limit reported in Chiaberge et al. (2003), calculated using data from radio through to *EGRET* wavelengths.

core of the object (Chiaberge et al., 2003). Surrounding the nucleus is a warped dusty disc that unevenly reflects ultraviolet emission from the core (Ferrarese & Ford, 1999). The dominant source of X-ray emission from NGC 6251 is the unresolved nucleus; however, observations with *Chandra* have revealed three distinct regions of the jet that are also X-ray emitters. A thermal X-ray halo extends out to $\sim$ 100 kpc around the object, and there is a drop in the surface brightness in positional agreement with one of the radio lobes, suggesting that the lobe has evacuated a cavity in the surrounding gas (Migliori et al., 2011). The object has been detected at higher energies with *INTEGRAL* (Foschini et al., 2005) and *Beppo-SAX* (Guainazzi et al., 2003), and it has also been proposed as the counterpart to the *EGRET* source 3EG J1621+8203 (Mukherjee et al., 2002). The nuclear SED of the object displays the typical structure seen in blazars, and it has been suggested that the observed nuclear emission is likely dominated by emission from a relativistic jet (Migliori et a., 2011). The initial *Fermi*-LAT detection of NGC 6251 suggested an association between the *Fermi*-LAT source and the nucleus of the object, but later observations have led to the suggestion that an association with the northwest radio lobe may be more likely. This possible association with the northwest radio lobe led to observations of the region with *Suzaku*, which revealed nonthermal diffuse X-ray emission associated with the lobe (Takeuchi et al., 2012).

The mass of the central black hole in NGC 6251 is currently estimated to be in the range $M_{\rm BH} = (4 - 8) \times 10^8\ \rm M_\odot$ (Ferrarese & Ford, 1999). The authors used *Hubble Space Telescope* observations of the gas orbiting the centre of NGC 6251 to determine the radial velocity of this gas. Further to this, they constructed two different analytical representations of the stellar brightness profile to estimate the effect of the stellar potential on the motion of the gas. This led them to conclude that the gas is in motion around a central body of mass $M_{\rm BH} = (4 - 8) \times 10^8\ \rm M_\odot$. For

the present study, it was decided to model NGC 6251 for $M_{\rm BH} = 6.0 \times 10^8 {\rm M}_\odot$, in the centre of the estimated range. The inclination angle of the jet used in model A is the upper limit, $\theta \lesssim 18°$, proposed in Chiaberge et al. (2003). This estimate was determined through SSC modelling of the emission observed from radio through to *EGRET* energies. Despite the simplicity of the model used, the upper limit reported appears relatively conservative considering the data, and so it was used for this work. It is noted by the authors that the inclination angle reported is lower than that those found for the orientation of the external dusty disc ($\theta \sim 76°$) and the inner gas disc ($\theta \sim 36°$) from Ferrarese & Ford (1999), but that the structure is warped and tilted, with the axis of the inner disc significantly twisted with respect to the outer dusty disc. Previous attempts to constrain the inclination angle using VLBI observations of the jet-counterjet ratio found $\theta < 47°$ (Jones & Wehrle, 2002), compatible with the value reported by Chiaberge et al. (2003). Another possible value for the inclination angle, $\theta = 12°$, was put forward in Evans et al. (2005), based on an inverse-Compton model that could reproduce the X-ray emission seen from the object further down the jet. Despite the different assumptions made by the authors in finding the inclination angle, it was decided to investigate NGC 6251 with $\theta = 12°$, as it is within the range previously suggested by Chiaberge et al. (2003). Additionally, Evans et al. (2005) modelled NGC 6251 with $\theta = 40°$, which was able to reproduce the sidedness observed in the jet and counterjet of the object; however, this angle is far beyond that suggested by Chiaberge et al. (2003) and beyond the scope of the multiblob model.

Attempts were made to use parameters for the initial electron distribution similar to those suggested in Evans et al. (2005); however, it proved impossible to replicate the γ-ray spectrum using these parameters with the multiblob model, as even with high values of $\Gamma_{\rm b} \sim 10$ and $B \sim 10$ G the SED produced at *Fermi*-LAT energies is more than an order of magnitude below that observed. By assuming an initial electron distribution with similar parameter values to those used for the other objects in this study, it proved possible to reproduce the general *Fermi*-LAT spectrum for NGC 6257 with the multiblob model for both inclination angles, although in both cases the error bars on the second point from the left lie above the predicted spectrum. The parameter values used are shown in Table 6.10, with the electron distributions shown in Table 6.9, and the SEDs produced are shown in Figure 6.10. As can be seen in Figure 6.11 the fifth point from the left in the *Fermi*-LAT spectrum is far above the predicted SED, but the extremely large errors on the value mean that both models are still valid. To successfully model the spectrum for $\theta = 18°$, the radius of the blob had to be slightly smaller in order for the blobs to remain in the jet; the result of this is that the blobs are relatively small compared to the gravitational radius of the black hole, with $r_{\rm b} = 0.56 r_{\rm g}$, but not unreasonably so. For $\theta = 12°$, the blobs can be larger than those for

$\theta = 18°$, and in this case $r_{\rm b} = 1.57 r_{\rm g}$. In both cases, the blobs are small enough that the differences between the on-blob and inter-blob cases are minimal, as seen in Figures 6.10 and 6.11. At very high energies, the predicted spectra are less steep than seen in some of the other objects studied but are about an order of magnitude below the spectrum predicted for 3C 273 in Lenain et al. (2008). Since it was argued that 3C 273 would at best be a marginal detection with H.E.S.S., NGC 6251 is not a promising target for current-generation telescopes. However, detection with CTA in the future cannot be ruled out and prospects for this will be discussed in Section 6.5.

6.3.6 3C 380

3C 380 is one of the brightest and most luminous extragalactic radio sources, displaying a luminosity at 178 MHz of $\sim 10^{28}$ W Hz^{-1} sr^{-1}. It is at a redshift of $z = 0.692$ (Wilkinson et al., 1991). At radio wavelengths, the object displays a complex structure on arcsecond and subarcsecond scales, which has led to some difficulty in classifying it. Unlike most FRII sources, which have a relatively weak core, the emission from the core of 3C 380 is quite strong, dominating the emission above ~ 20 GHz. The core is surrounded by a halo with a far less clear structure than the lobes present in most such objects (Wilkinson et al. 1984), leading to it being initially categorized as a compact steep-spectrum source. A one-sided radio jet is also detected. Work carried out by Wilkinson et al. (1991) detected the presence of superluminal motion in the jet out to ~ 100 pc from the core, with $\beta_{\rm app} = 10.7 \pm 2.7$. Detection of the radio halo was reported, and it is suggested that it could be a pair of overlapping radio lobes, while knots similar to those seen in FRII lobes are also observed. The detection of these features suggests that 3C 380 may be a FRII galaxy viewed from a relatively small angle to the line of sight ($\theta \sim 10°$); however, the core is neither as strong nor as variable at optical and radio wavelengths as would be expected if this were the case (Wilkinson et al., 1991). Later work has supported this conclusion, with evidence suggesting that the relative weakness of the core's radio emission and its apparent lack of variability are due to dilution by the emission from the halo at these wavelengths, while observations at wavelengths of 6 cm have shown the nuclear jet to be highly variable (Polatidis & Wilkinson, 1998).

At optical wavelengths, 3C 380 displays low polarisation, which is not consistent with data from other FRIIs at low angles to the line of sight. A possible explanation is that the region of the jet responsible for optical synchrotron emission, the ~ 1 pc closest to the core, is at a greater angle to the line of sight than the rest of the jet. It has been argued that a substantial contribution to the infrared emission from 3C 380 is likely nonthermal in origin (Shi et al., 2005). Work carried out using data from the *Hubble Space Telescope* discovered a close correspondence between optical and radio hotspots in the jet (O'Dea et al., 1999). Despite the relatively intense radio and optical

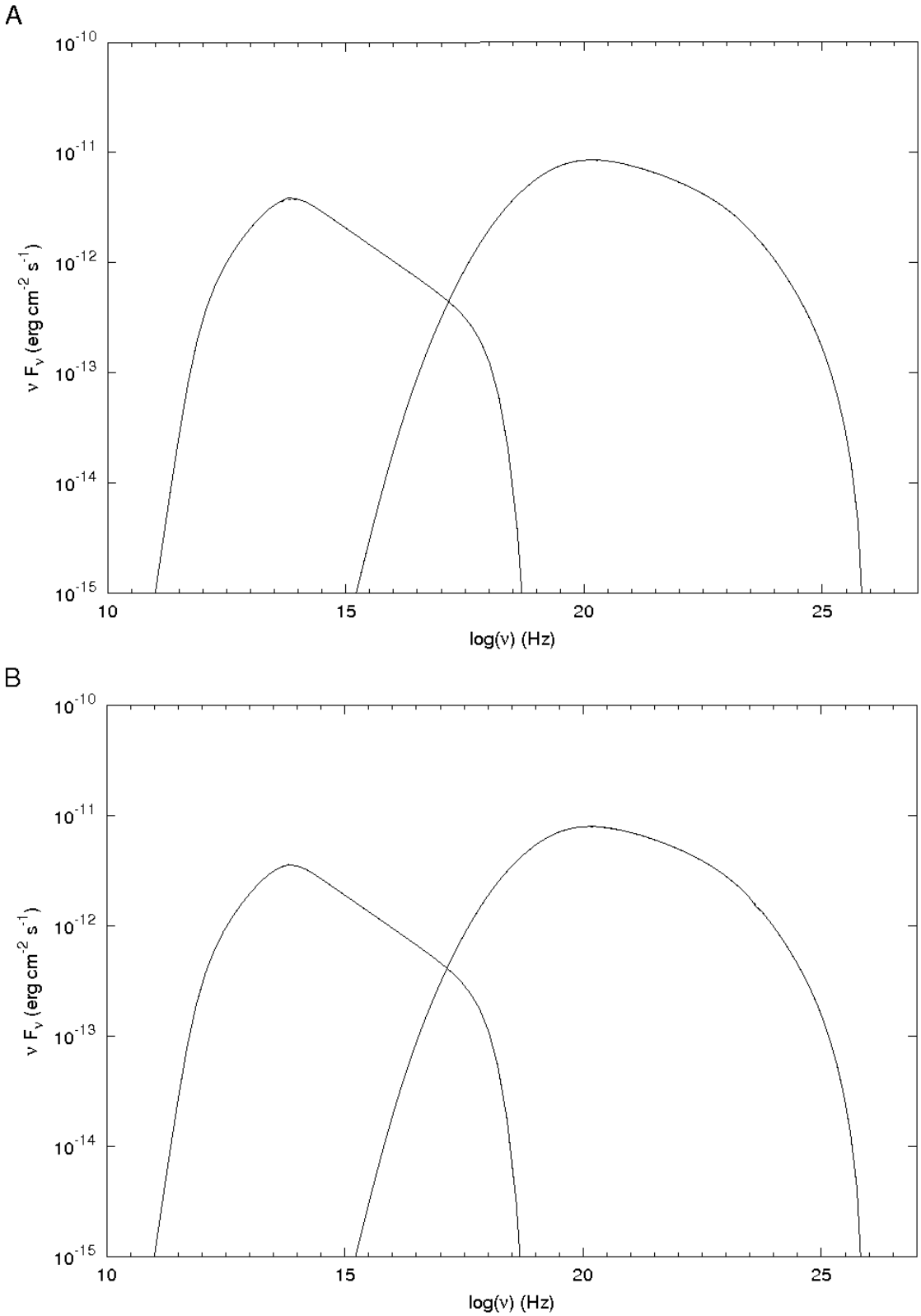

Figure 6.10: SEDs for NGC 6251, produced with the parameter values shown in Table 6.10 and the electron distributions shown in Table 6.9. The solid curve represents the on-blob case and the dashed line the inter-blob case. Due to the relatively small size of the gravitational radius of the black hole compared to the size of the blobs the difference between the on-blob and inter-blob cases is too small to be seen on the plots.

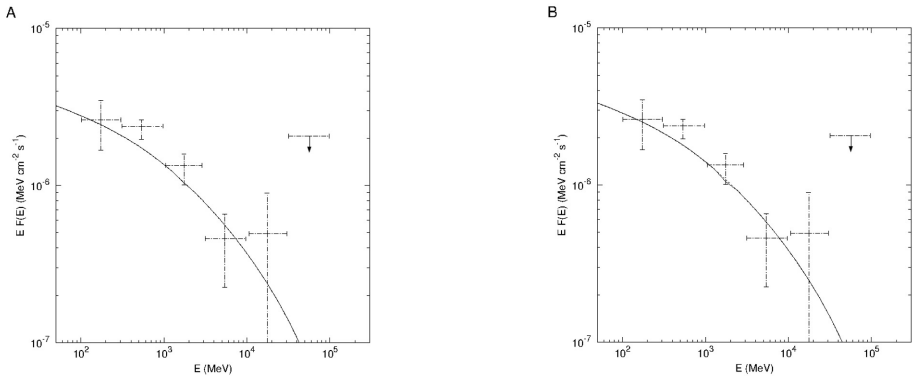

Figure 6.11: Close-up (in the energy regime observed by the *Fermi*-LAT) of the SEDs for NGC 6251 shown in Figure 6.10, displayed together with the *Fermi*-LAT spectrum (the points)(Abdo et al., 2010c). The solid curve represents the "on-blob" case and the dashed curve the inter-blob case. Due to the relatively small size of the gravitational radius of the black hole compared to the size of the blobs the difference between the on-blob and inter-blob cases is too small to be seen on the plots.

	$N_{\rm H}$ ($\rm cm^{-3}$)	n_1	n_2	$\gamma_{\rm min}$	$\gamma_{\rm c}$	$\gamma_{\rm br}$
A	2.1×10^7	1.4	3.6	1.0×10^2	1.1×10^5	0.9×10^3
B	2.1×10^7	1.4	3.6	1.0×10^2	1.1×10^5	0.9×10^3
C	1.2×10^7	1.4	3.5	1.0×10^2	1.1×10^5	0.9×10^3
D	2.1×10^7	1.4	3.5	1.0×10^2	1.3×10^5	0.9×10^3

Table 6.11: The electron distributions used in the multiblob modelling of 3C 380.

campaigns carried out on 3C 380, very little had been written about the object at X-ray energies or above until its detection by the *Fermi*-LAT.

As with 3C 207, the other more distant object studied (Section 6.3.4), the mass of the central black hole in 3C 380 is currently not constrained. It was decided to model the object for both an average mass black hole $M_{\rm BH} = 10^8$ $\rm M_\odot$ and a higher mass black hole $M_{\rm BH} = 10^9$ $\rm M_\odot$. The value of $\theta = 10.3°$ for the inclination angle comes from an upper limit calculated in Kameno et al. (2000), based on VLBI Space Observatory Programme (*VSOP*) observations of a number of components within the jet of the object. The authors used observations of superluminal motion in two components in the parsec-scale jet to estimate the viewing angle of these structures. Comparing the position vectors of the two components, the authors suggest that it is likely that they have been ejected ballistically, and that if this is the case then the angle of the jet to the line of sight must be less than the the viewing angle of the closest component to the core, hence $\theta \leq 10.3°$. A somewhat more controversial value for the inclination angle, $\theta = 0.7°$, is calculated in Polatidis & Wilkinson (1998) using VLBI observations with the VLBA and VLA . Assuming that the jet bends either away from or towards an angle of $\theta = 9.5°$ and has a constant minimum Lorentz factor of $\gamma_{\rm min} = 6.1$, the authors find that with the measured apparent velocity near the core, either $\theta = 0.7°$

	Γ_b	z	θ	M_{BH} ($M_\odot$)	R_{cap} (r_g)	r_b (cm)	B (G)
A	3.5	0.692	10.3°	1.0×10^8	100	1.2×10^{14}	3.2
B	3.1	0.692	0.7°		100	1.4×10^{14}	3.0
C	2.7	0.692	10.3°	1.0×10^9	100	1.4×10^{14}	2.6
D	2.8	0.692	0.7°		100	1.4×10^{14}	2.0

Table 6.12: The object parameters used in the multiblob modelling of 3C 380. As there is little data on the size of the black hole in 3C 380, the object was modelled for both a high mass black hole, 1.0×10^9 $M_\odot$ and lower mass black hole, 1.0×10^8 $M_\odot$. The inclination angle of 10.3° is implied by the motion of knots moving ballistically in the parsec-scale jet, as discussed in Kameno et al. (2000), while the much smaller angle of 0.7° comes from observations at radio wavelengths implying acceleration within the jet (Polatidis & Wilkinson, 1998). Due to the large redshift of the object, the results were corrected for EBL absorption using the model of Kneiske, Mannheim & Hartmann (2002) and Kneiske et al. (2004).

or $\theta > 72°$. It is argued that, because of the broad correlation between the brightness of the radio jet and the implied change in the size of θ required in the alternative geometry, that it is unlikely that the jet starts out at a large viewing angle and then bends to point close to the line of sight. The value $\theta = 0.7°$ is preferable. The value of $\theta = 0.7°$ is controversial, as it is difficult to explain the lack of blazar-like activity from the object if the jet begins so close to the line of sight.

The redshift of 3C 380 is relatively high, $z = 0.692$, requiring that the EBL correction of Kneiske et al. (2004), as applied in the case of 3C 207, be applied also to the models generated for 3C 380. The electron distributions and object parameter values used to successfully reproduce the *Fermi*-LAT spectrum for 3C 380 are shown in Tables 6.11 and 6.12, respectively, and the SEDs generated are displayed in Figures 6.12 and 6.13. It should be noted that in the case of $\theta = 0.7°$, the multiblob model performs similarly to a simple single-zone model. As shown in Figure 6.14, the multiblob model can successfully reproduce the *Fermi*-LAT spectrum for the values of M_{BH} and θ, used with physically sensible values for Γ_b and B in the modelling. In all cases the model spectrum drops off quite sharply at energies $> 10^4$ MeV. The blobs used in model A have radius $r_b = 8.08 r_g$ and those in model B have $r_b = 9.42 r_g$, which leads to a relatively small discrepancy between the on-blob and inter-blob cases as can be seen in the figures. For the larger black hole mass, the blobs have $r_b = 0.94 r_g$, the same size as those used in model B and similar to those used in model A, but due to the larger black hole mass the difference between the on-blob and inter-blob cases is minimal. As would be expected, the values for Γ_b and B required to reproduce the *Fermi*-LAT spectrum are lower in the case of greater M_{BH} and smaller θ; however, the difference in the values for these parameters between $\theta = 10.3°$ and $\theta = 0.7°$ is relatively small. All of the models show very steep spectra at high energies, which would suggest that 3C 380 is unlikely to be detected as a source of very high energy emission.

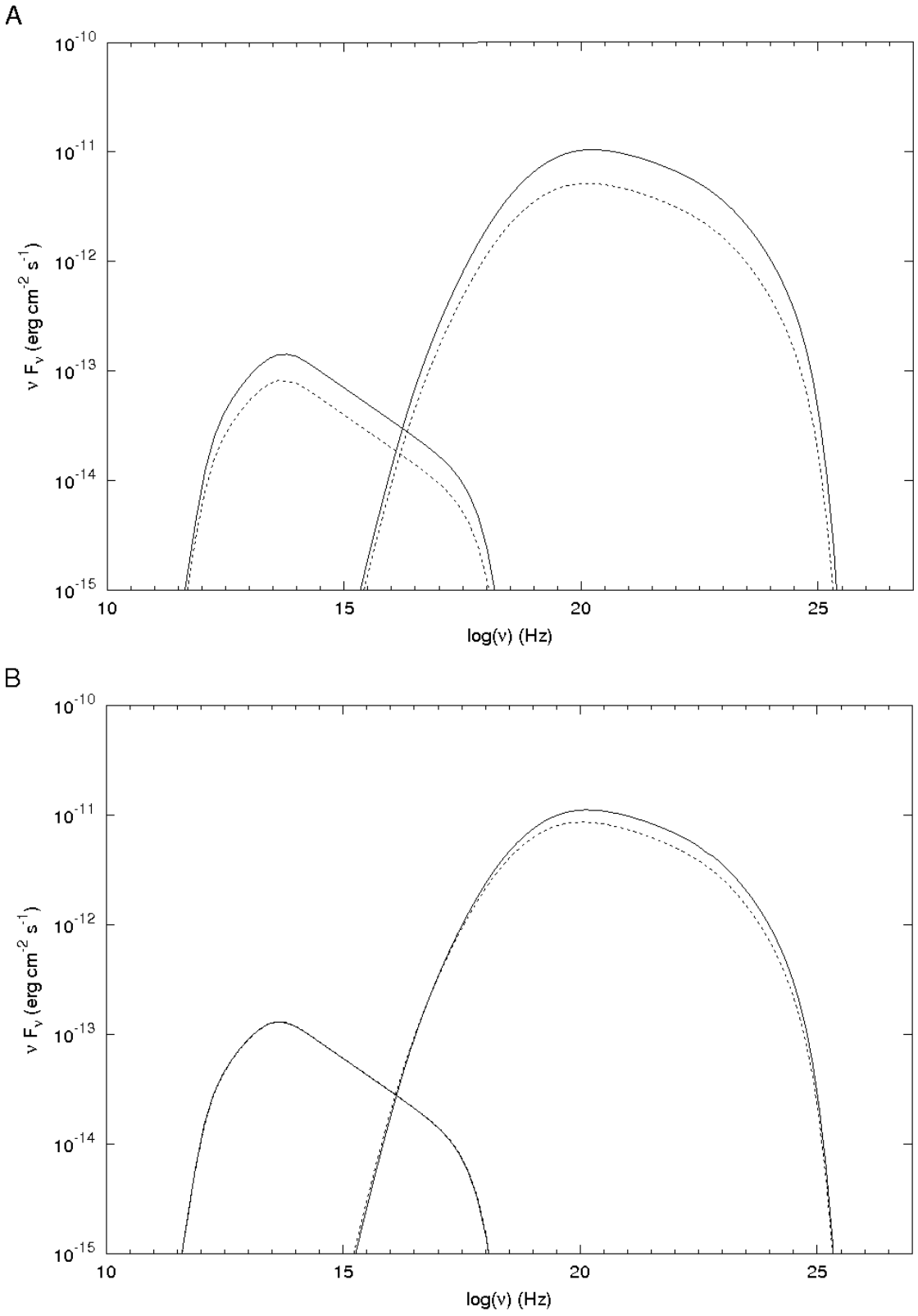

Figure 6.12: SEDs for 3C 380 produced using multiblob models A and B ($M_{\rm BH} = 1.0 \times 10^8$ M$_\odot$) with the parameter values shown in Table 6.12 and the electron distributions shown in 6.11. The solid curves represents the on-blob case and the dashed curves the inter-blob case.

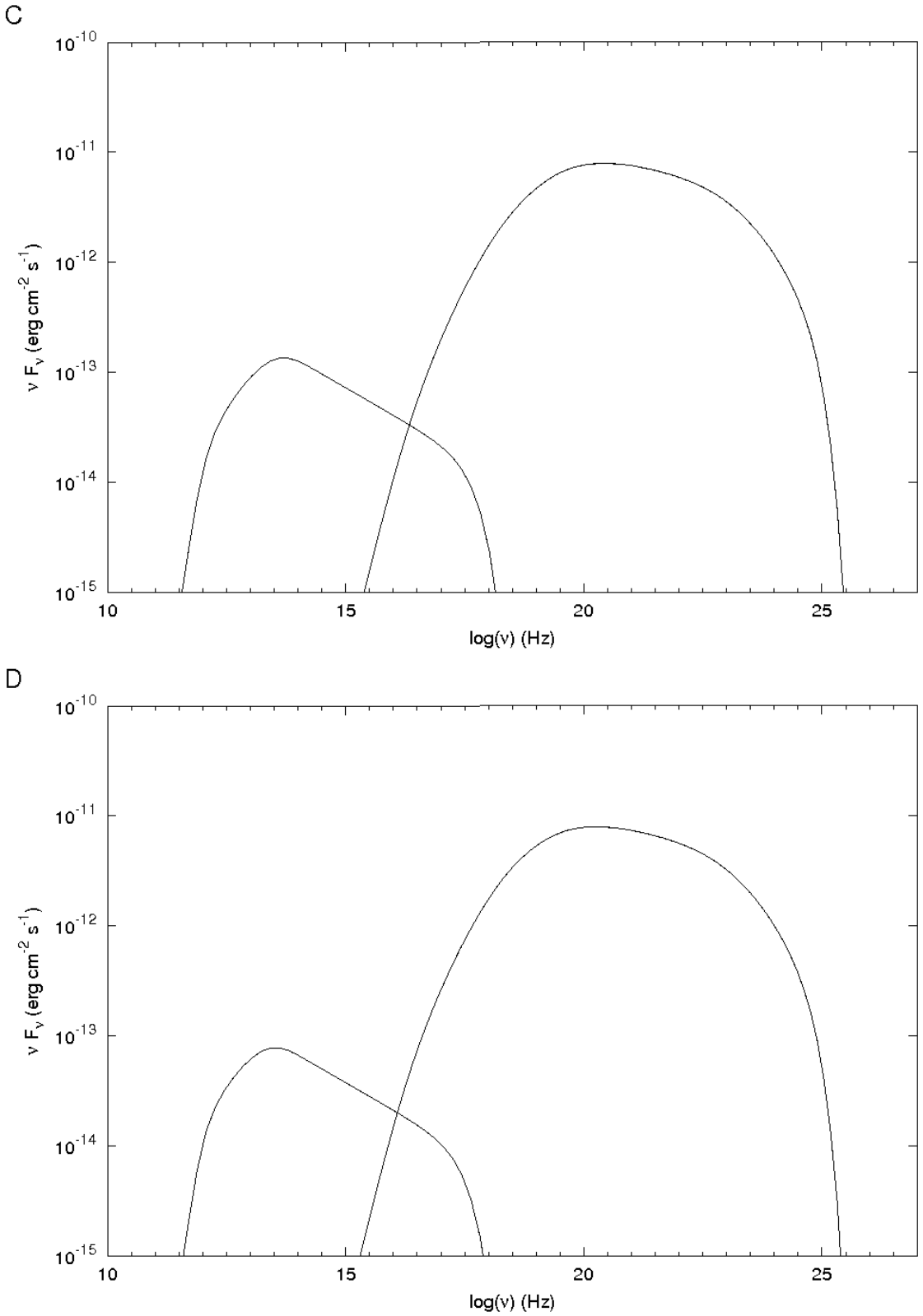

Figure 6.13: SEDs for 3C 380 produced using multiblob models C and D ($M_{\rm BH} = 1.0 \times 10^9$ $M_\odot$) with the parameter values shown in Table 6.12 and the electron distributions shown in 6.11. The solid curves represent the on-blob case and the dashed line the inter-blob case. Due to a combination of factors the difference between the on-blob and inter-blob cases is too small to be seen in the plots.

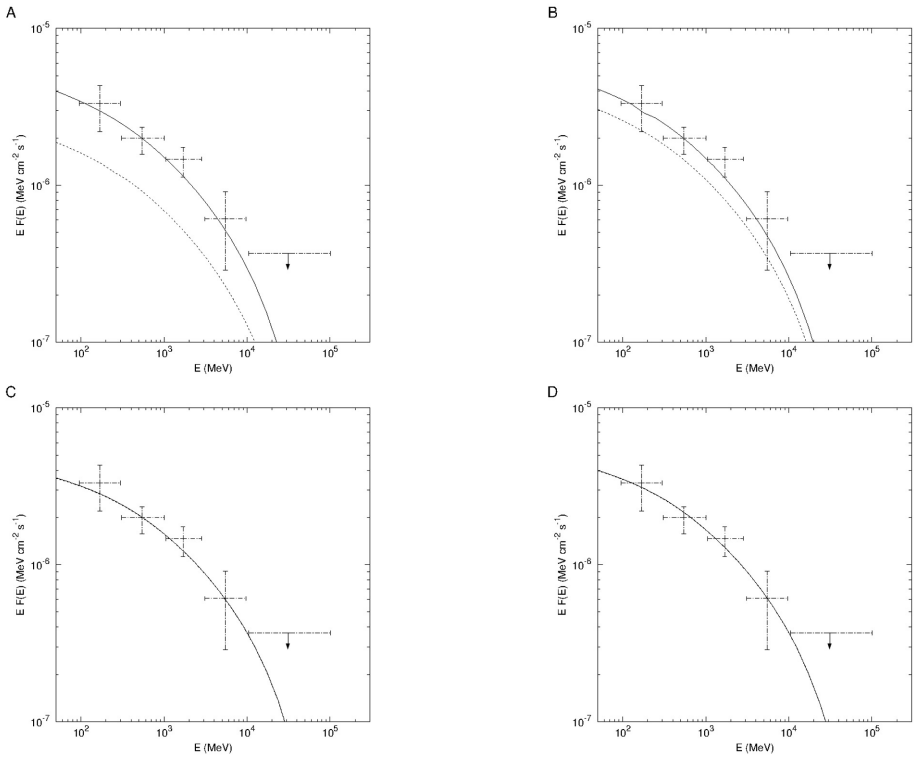

Figure 6.14: Close-up (in the energy regime observed by the *Fermi*-LAT) of the SEDs for 3C 380 shown in Figures 6.12 and 6.13 displayed together with the *Fermi*-LAT spectrum (the points)(Abdo et al., 2010c). The solid curves represent the on-blob case and the dashed curves the inter-blob case. In models C and D, the difference between the on-blob and inter-blob cases is too small to be visible, due to a number of factors discussed in the text.

6.3.7 Objects without *Fermi*-LAT Spectra

Three of the misaligned AGN detected with the *Fermi*-LAT were too faint for high-energy spectra to be calculated (Abdo et al. 2010c). These objects were not modelled, but are discussed here for completeness.

3C 78/NGC 1218

The radio source 3C 78 was initially identified with the S0a galaxy NGC 1218 by Mills (1960), before being confirmed by the work of Maltby, Matthews & Moffet (1963). The object is at a redshift of $z = 0.0289$ (Schmidt, 1965). Work carried out early in the 1970s hinted at the presence of extended radio emission associated with the nucleus (Fomalont, 1971), and data collected with the Multi-Element Radio Linked Interferometer Network (MERLIN) later confirmed the existence of a one-sided radio jet with an extent of ~ 1 kpc (Unger, Booler & Pedlar, 1984). Using the *Hubble Space Telescope*, an optical synchrotron jet, almost coincident with the radio jet, was discovered emanating from the nucleus of the object, similar to those in AGN such as M87, but with shorter apparent length (Sparks et al., 1995).

X-ray observations carried out with the *BeppoSAX* satellite in 1997 revealed an X-ray source with an extension of $\approx 4'$ (Trussoni et al., 1999a). The data collected were not consistent with pure thermal or nonthermal emission, suggesting the presence of both a hot corona with $T \sim 1$ keV and a nonthermal, basically unabsorbed source with a soft spectrum. The lack of absorption of the X-ray source is consistent with the previous detection of the optical jet, if the optical synchrotron emission is interpreted as due to limited Doppler boosting at an angle of $30° - 40°$ to the line of sight, as no interaction with a dusty torus than would be expected. The overall X-ray spectrum observed is similar to that seen in other FRI radio galaxies. The successful detection of γ-rays with the *Fermi*-LAT further strengthens the evidence for high-energy nonthermal emission from the object. 3C 78 is one of the weakest sources in the sample detected with the *Fermi*-LAT and is not detected at energies $\lesssim 100$ MeV.

PKS 0625-354

The AGN PKS 0625-354 is hosted in a cD elliptical galaxy, which is a member of the poor cluster (a galaxy cluster containing ¡ 1000 galaxies, most of which are spirals) A 3392 (Trussoni et al., 1999b), at a redshift of $z = 0.0525$ (Willis et al., 2004). The object is classified as an FRI, and there is evidence for the presence of an optical point source at the nucleus (Govoni ei al., 2000). At radio wavelengths, the emission is dominated by the core, with a one-sided radio jet at an inclination angle implied by the limited X-ray absorption to be $< 60°$ to the line of sight (Trussoni et al.,

1999a) and optical (Chiaberge, Capetti & Celotti, 1999) wavelengths. A low-brightness, extended radio halo, with a total extent of ~ 340 kpc, has been observed (Ekers et al., 1989). Initial X-ray observations showed apparently extended X-ray emission (Siebert et al., 1996); however, later work suggested the presence of a central component with a luminosity of $\sim 10^{43}$ erg s^{-1} (Trussoni et al., 1999a). It has been shown that the X-ray emission from the object is most likely composed of both a thermal and nonthermal component, the latter following a power-law spectrum. There is some suggestion, based on a study of the object's spectra, that PKS 0625-354 might be a BL Lac type object (Wills et al., 2004) and it does appear to be close to the transition between FRI radio galaxies and LBLs (Trussoni et al., 1999a). PKS 0625-354 was not detected by the *Fermi*-LAT at energies $\lesssim 300$ MeV (Abdo et al., 2010c) and the flux in the range 300 MeV - 100 GeV was relatively low. PKS 0625-354 was not detected by the *Fermi*-LAT at energies $\lesssim 300$ MeV and the spectrum was relatively noisy (Abdo et al., 2010c). Due to the relatively weak flux of the object, its spectral parameters could only be constrained using data from 300 MeV to 100 GeV and the low quality of the data meant that no *Fermi*-LAT spectrum could be be produced.

PKS 0943-76

Unfortunately no in-depth studies of PKS 0943-76, $z = 0.27$, have been carried out and so information on this object is relatively limited. The AGN is hosted in what appears to be a cD giant elliptical galaxy (Burgess & Hunstead, 2006) and is classified as an FRII (Abdo et al., 2010c). Initial optical observations did detect a faint envelope extending 15-20 arcseconds leading to suspicion of a spiral structure (Hunstead, 1971). At radio wavelengths (5 GHz), the object appears to display a double structure (Gaensler & Hunstead, 2000) and the AGN has been detected in X-rays with the *ROSAT* satellite (Brinkmann, Siebert & Boller, 1994). PKS 0943-76 is within the 95% error radius of the *Fermi*-LAT source 1FGLJ09040.2-7605, leading to a less secure association between the two objects than is seen for the other *Fermi*-LAT detected misaligned AGN that are with the 99% error radius of the *Fermi-LAT*; however, it is still a plausible candidate for the γ-ray emission (Abdo et al., 2010c). As the object is relatively faint, an SED could not be constructed using the *Fermi*-LAT data, and so modelling was not attempted.

6.4 The Cherenkov Telescope Array (CTA)

CTA is the proposed successor to the three currently operational arrays of IACTs discussed in Section 1.5. CTA will consist of two arrays, each consisting of many Cherenkov telescopes of various sizes with one array situated in the Northern hemisphere and one in the Southern hemisphere to

ensure full sky coverage at TeV energies (Actis et al., 2011). CTA will have a sensitivity an order of magnitude higher at TeV energies than current arrays and an increased energy range, extending from $\sim$ 10 GeV to beyond 100 TeV. The increased collection area planned for the array should significantly increase the detection rates of transient phenomena, and the large number of IACTs will allow for enhanced sky-survey capabilities. For studying extended sources, CTA will have an angular resolution of $\sim$ 0.2 arcmin, a factor of 5 better than that achievable with current instruments.

Designs for the IACTs that will be used in the construction of the array are based on understanding that has been collected during the construction and operation of the current generation of telescopes. Structurally, the CTA IACTs will resemble those currently in operation and the cameras used will probably consist of conventional photomultiplier tubes, although advanced photon detectors currently under development are also being considered. The overall structure of the array is currently being investigated, and a number of potential layouts are discussed in Section 6.5, as this will affect the capabilities of CTA in different energy ranges and hence the likelihood of VHE detection of the *Fermi*-LAT detected misaligned AGN. The array will contain three different sizes of telescopes to maximise the capability of the array across the desired energy range. At lower energies, $\lesssim$ 100 GeV, it is envisaged that a small number of large telescopes with dish diameter $\sim$ 23 m will provide the greatest coverage, as they will be able to collect enough photons to trigger from the fainter air-showers. Between 100 GeV and 1 TeV, shower detection and reconstruction is currently well understood, and it is assumed that this energy region will be well served by a grid of medium-sized telescopes of diameter $\sim$ 12 m, spaced $\sim$ 100 m apart. The increased number of medium-sized telescopes compared to current arrays will result in better shower reconstruction than is currently possible as more telescopes will image the Cherenkov light pool, while the increased area will give improved sensitivity. At very high energies, $>$ 10 TeV, the main limitation is the extremely low flux and so a large effective area is required, while the high energy of the photon primary ensures that the shower can be detected well beyond the 150 m radius typical of Cherenkov light pools. The high Cherenkov light yield of these photons means that they can be detected by relatively small individual IACTs, with diameter $\sim$ 6 m, and a spacing between the telescopes of 100 m $-$ 200 m should ensure that the parameters of the Cherenkov light pools can be accurately determined.

Subarray	LSTs	MSTs	SSTs
E	4	23	32
I	3	18	56
J	3	46	0
K	5	0	71
B	5	37	0

Table 6.13: The various configurations currently being considered for CTA. LSTs are large IACTs ($\sim$ 23 m in diameter), MSTs are smaller ($\sim$ 12 *textrmm* in diameter) and SSTs are the smallest (diameter $\sim$ 6m). Information taken from Rulten (2012).

6.5 Future Prospects for CTA

To determine the likelihood of any of the objects in the present study being detected with CTA, an assumed sensitivity curve must be compared with the emission predicted by the model. Recent work by Rulten (2012) studied the sensitivity for a number of potential arrangements for CTA, using Monte Carlo simulations to model air showers and potential CTA response. Initially 14 potential arrangements for CTA were considered, although only four of these (subarrays labelled E, I, J and K) have the potential to meet the sensitivity goals of the system. Each array is made up of a number of telescopes of various sizes: large-sized telescopes (LSTs) $\sim$23 m in diameter, medium-sized telescopes (MSTs) $\sim$12 m in diameter, and small-sized telescopes (SSTs) $\sim$6 m in diameter. Currently, the four subarray arrangements E, I, J and K are expected to be able to fulfil all of the design goals for CTA within a reasonable budget. The composition of these subarrays is shown in Table 6.13, and their potential layouts can be seen in Rulten (2012). An additional design, subarray-B, has also been proposed; although unable to achieve the sensitivity goals across the full CTA sensitivity range compared to the other four this subarray is expected to perform extremely well in energy range below 100 GeV. Judging from the SEDs generated for each of the objects investigated in Section 6.3, this arrangement would probably have a greater chance of successfully detecting such sources.

The sensitivity of CTA is defined as the γ-ray flux which can be detected significantly above background in a given observation time. In VHE γ-ray astronomy, a detection is considered significant if the signal is at least 5σ above the background, and sensitivity curves are typically constructed in the context of reaching this significance level in 50 hours of observations. The sensitivity curves constructed by Rulten (2012) for the five potential subarray arrangements, assuming data analysis is performed with the method used at Durham, described in Chapter 2, and the parameter space for background cuts are determined using a multi-layer perception (MLP) neural network (software simulating biological architecture, which can be "trained", described in detail in Rulten, 2012), are shown in Figure 6.15.

Using the SEDs produced in Section 6.3 with the senistivity curves in Figure 6.15 it is possible

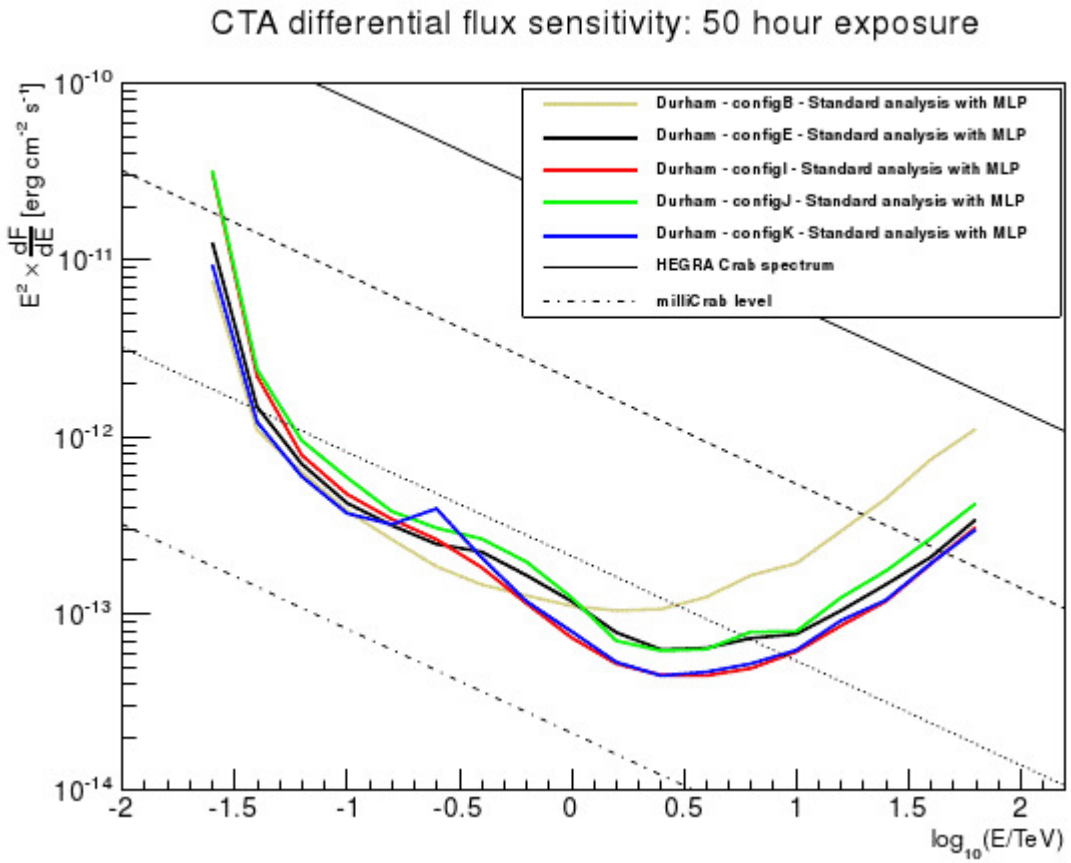

Figure 6.15: Predicted sensitivity curves for each of the subarrays currently being considered for the design of CTA. The bump at approximately 250GeV in the sensitivity curve for subarray-K occurs as the design has no medium sized telescopes leading to a discontinuity in performance in this energy regime. The dot-dashed line represents 0.1% of the HEGRA Crab Nebula spectrum, the dotted line represents 1% of the HEGRA Crab Nebula spectrum, the dashed line represents 10% of the Crab Nebula spectrum and the solid straight line represents 100% of the Crab Nebula spectrum. Taken from Rulten (2012).

to predict whether the objects investigated could be detected with CTA. If the SED lies above the sensitivity curve, then the probability of a detection after 50 hours of observations is relatively high. Using the Durham method, it would appear unlikely that any of the objects will be detectable with the proposed subarrays, although three of the models for 3C 111 (A, C (Figure 6.3) and D (Figure 6.4)) predict fluxes around 60 GeV close to the level necessary for detection by configurations K and B (see Figure 6.16).

However, as can be seen from Figure 6.17, the sensitivity that can be achieved by CTA is strongly dependent on the analysis method used. In the figure, all except for the Paris method of the analysis methods shown use standard Hillas-style reconstruction similar to the seen described in Section 2.2 and the difference in sensitivity is due to different methods used for background rejection and determination of the parameter space for background cuts. In addition to the MLP method, Rulten (2012) also modelled the sensitivity of CTA for two analysis methods using the boosted decision tree (BDT) method for determining the parameter space for background cuts (described in Ohm, van Eldik & Egberts, 2009), which combines the information carried in several parameters into a single classification parameter which is then used to carry out the background cuts. The method used by the MAGIC telescopes, shown in the figure as the red curve, uses the "Random Forest" approach to background rejection described in Albert et al. (2008), where acceptance or rejection of an event is determined using multiple binary decision trees constructed using Monte Carlo simulations and data from hadronic showers. The Paris analysis (described in Lemoine-Goumard, Degrange & Tluczykon, 2006 and shown on the figure as a fuchsia curve) calculates third order moments for detected Cherenkov light pools (such as the average lateral spread of Cherenkov photon origins) as opposed to the second order moments used by the standard analysis described in Section 2.2 and then combines these moments into a single dimensionless parameter which uses the BDT method to determine if the event passes the selection cuts. This requires an increase in the amount of available processing time but leads to a significant improvement in sensitivity at energies $<\sim$ 2.5 TeV for CTA. Using the Paris analysis method, it appears that it should be possible for CTA to achieve flux sensitivity right down to the milliCrab level.

Comparing the SEDs generated from the modelling with the sensitivity predicted for subarray-E using the Paris analysis method suggests that 3C 111 is likely very close to the threshold required for a detection at energies of $\sim$ 40 GeV; this is the case for all of the models, although models A and D appear the most promising (with $\theta = 19°$). Additionally, NGC 6251 shows some potential, as the predictions for model A are relatively close to the flux sensitivity expected for subarray-E at $\sim$ 40 GeV. It should be noted that the likelihood of detection of 3C 111 or NGC 6251 is greater in the case of subarray-K using the Paris analysis, as this configuration shows greater sensitivity

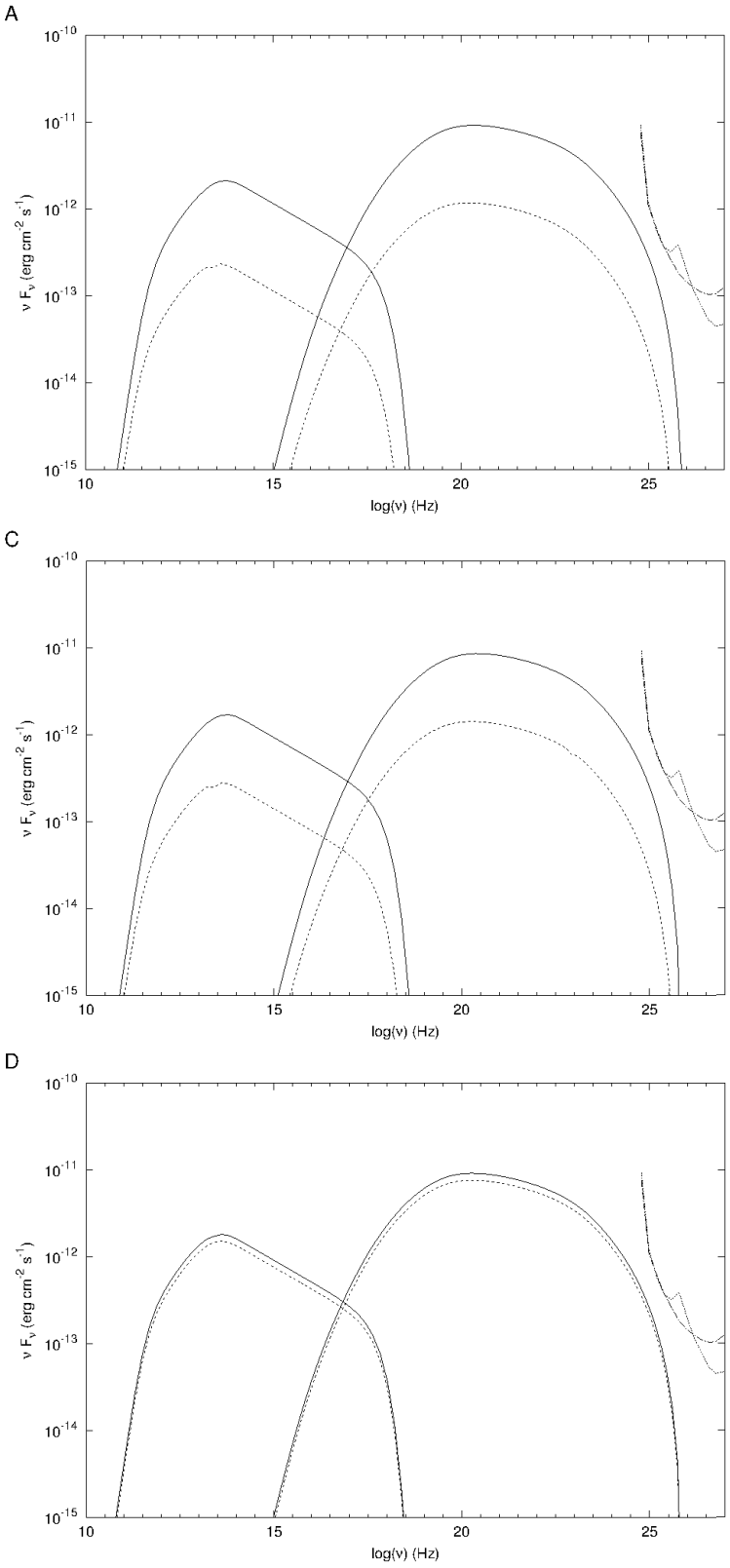

Figure 6.16: The predicted SEDs for models A, C and D of 3C 111 compared with the predicted sensitivity of CTA configurations K and B. The solid lines are the "on-blob" case, the dashed lines the "inter-blob" case, the dotted lines represent the sensitivity curve for configuration B and the dot-dashed line is the sensitivity curve for configuration K. The dot-dashed line represents 0.1% of the HEGRA Crab Nebula spectrum, the dotted line represents 1% of the HEGRA Crab Nebula spectrum, the dashed line represents 10% of the Crab Nebula spectrum and the solid straight line represents 100% of the Crab Nebula spectrum. Taken from Rulten (2012).

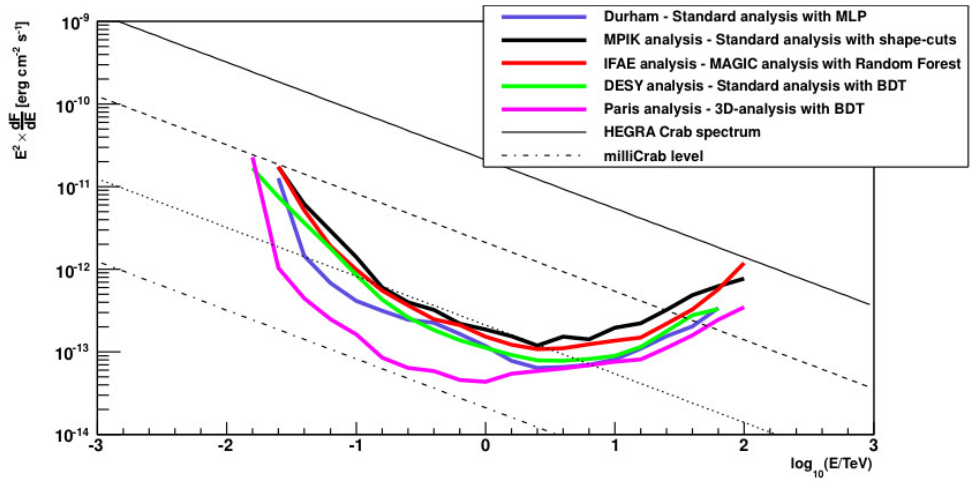

Figure 6.17: Predicted sensitivity of subarray-E using various analysis methods. Taken from Rulten (2012).

than subarray-E in the region around ~ 40 GeV. The raw data used in the construction of Figure 6.17 were not available at the time of writing, precluding display of the sensitivity curve alongside the constructed SEDs for the objects in question. During a high-energy flare, the SEDs of any of the objects may change significantly in the VHE γ-ray region, making them interesting as targets of opportunity in the case that such an event is detected by an instrument monitoring them at lower energies.

6.6 Conclusions

Using the multiblob model of Lenain (2008), the γ-ray spectra of five misaligned AGN detected with the *Fermi*-LAT and reported in Abdo et al (2010c) were successfully modelled using sensible values for the initial electron distribution and other physical parameters, although some difficulty was found in reproducing the *Fermi*-LAT spectrum from NGC 6251. The inclination angles and black hole masses assumed for the objects studied were taken from the literature; however, in two cases, 3C 207 and 3C 380, no estimates of the central black hole mass were available. It was decided that for these two objects central black hole masses of $M_{\mathrm{BH}} = 1 \times 10^8$ M$_\odot$ and $M_{\mathrm{BH}} = 1 \times 10^9$ M$_\odot$ would be used in the modelling, as black holes with similar masses are observed in many AGN. Additionally, these two objects are at redshifts $z > 0.6$, meaning that to accurately model their spectra the effects of the EBL must be taken into account. The effect of the EBL on the spectra of these two objects was accounted for by using the EBL corrections proposed in Kneiske, Mannheim & Hartmann (2002) and Kneiske et al. (2004). For most of the objects studied, the black hole masses and inclination angles from the literature led to predictions consistent with the spectra

observed with the *Fermi*-LAT. However, it proved impossible to reproduce the γ-ray spectrum of 3C 120 using the black hole mass of 3.5×10^7 $M_\odot$ proposed by León-Tavares et al. (2010) without resorting to extreme values of Γ_b and B.

The SEDs generated for 3C 111, 3C 120, 3C 207, 3C 380 and NGC 6251 were then compared to the predicted sensitivity curves for the next-generation IACT system, CTA, from Rulten (2012), to determine the likelihood of detection of these misaligned AGN. These sensitivity curves have been constructed for five potential arrangements, and it was found that the subarrays with the highest sensitivities at energies ~ 30 GeV show the most potential for detecting the objects studied; nevertheless with the standard analysis methods used in Durham, none of the objects are likely to be detected within 50 hours of observations. Further to the work with the Durham analysis methods, Rulten (2012) also simulated the sensitivity of one of the subarrays, subarray-E, using a number of other approaches to the analysis. One of these approaches, the analysis method used in Paris, leads to a significant increase in sensitivity, particularly at lower energies, where the misaligned AGN are closest to the sensitivity curves. The most likely object to be detected with CTA is 3C 111, whose SED approaches close to the sensitivity curve for subarray-E using the Paris analysis methods. Detection of the other objects investigated here appears unlikely. Nonetheless, it should be noted that AGN are intrinsically variable, and a flare event from one of the objects studied may enable its detection with CTA. In particular, in the case that a high energy flare from 3C 120 or NGC 6251 (both at redshifts $z < 0.1$) is detected by another instrument, it would potentially be worth observing with CTA, as the fluxes predicted by the multiblob model at CTA energies are not too far from the predicted sensitivity of the array. The two more-distant objects, 3C 207 and 3C 380, are unlikely to be detected by CTA even in the case of a flare; however, they would still be worth observing should they flare at high-energies because such observations could be used to help to improve the limits placed on the energy density of the EBL.

Chapter 7

Conclusions and Future Prospects

7.1 Introduction

The detection of M87 at very high energies by Aharonian et al. (2006d) showed that the relativistic jets in AGN need not be aligned directly with the line of sight for VHE emission to be observed from such objects. This detection, coupled with the later detections of Centaurus A (Aharonian et al., 2009b) and NGC 1275 (Aleksić et al., 2012c) at very high energies, provided the primary stimulus behind the investigation discussed in this work. Initially, the potential for emission from Seyfert galaxies at very high energies was studied using data collected with the H.E.S.S. array; the results of this study are discussed in detail in Chapter 4. An important question raised by the detection of GeV-TeV emission from misaligned AGN is how to successfully reproduce it in models, as simple single-zone models have great difficulty in predicting such high energy emission from sources with relatively high inclination angles without resorting to physically improbable scenarios. To answer this, a number of more complicated models have been proposed and some of the more successful approaches are discussed in Chapter 5. Using one of these models, the multiblob model proposed in Lenain et al. (2008), the GeV emission from a number of misaligned AGN detected with the *Fermi*-LAT (Abdo et al., 2010c) was modelled, both to determine whether the emission could be accounted for using this approach and whether any TeV emission might be expected from these objects. Chapter 6 contains a full discussion of the results of this study. The early chapters of this work, Chapters 1-3, focus on providing the background necessary to understand both the context of these studies and the underlying theory.

A summary of this work is provided in this chapter, as well as discussion of the potential for further investigation into the areas studied.

7.2 Current Status of TeV AGN Observations

As previously stated in Chapter 3 AGN are extremely luminous objects hosted at the centre of some galaxies. These objects are believed to harbour supermassive black holes consuming gas and dust from their local environment. Despite the broad range of properties observed, it is currently argued that they are likely all manifestations of the same phenomenon viewed from different angles, and that the differing properties are a result of the anisotropic nature of these sources. AGN have been detected over a broad range of energies, from radio waves all the way through to VHE γ-rays, and since the construction of the current generation of IACTs the number known to emit at TeV energies has grown dramatically, as has our understanding of their properties in this extreme energy band.

To date, more than 40 AGN have been detected at TeV energies; the vast majority of these are blazars, AGN oriented such that the jet points at a small angle to the line of sight. In blazars, the radiation emitted by particles within the jet is likely to be due to synchrotron self-Compton emission shifted to higher energies by relativistic Doppler boosting to give the VHE emission detected. The emission from AGN has been observed to be highly variable across all wavelengths; such variability has been detected even at TeV energies, with PKS 2155-304 displaying variability on timescales of $\sim$ 3 minutes, the fastest known at any wavelength. In addition to the blazars detected, three AGN with higher inclination angles have also been observed at TeV energies, M87, Centaurus A and NGC 1275. All of the AGN detected so far are at relatively small redshifts, with the furthest at a redshift of $\sim$ 0.5. This is at least in part because TeV photons undergo pair production with photons from the background infrared radiation field known as the EBL.

7.3 Seyfert Galaxies

Seyfert nuclei are the most numerous AGN and the brightest observed in the local Universe. Despite this, they are significantly less luminous than quasars and, unlike quasars and radio galaxies, they appear to be hosted primarily in spiral galaxies. Prominent emission lines in the optical and ultraviolet parts of the spectrum are seen in all Seyfert nuclei, and like other AGN they emit nonthermally across the entire electromagnetic spectrum, although they tend to be weaker at radio wavelengths. They are classified as either Seyfert 1 (Sy1) or Seyfert 2 (Sy 2), depending on the observed spectrum. Sy1s show broad permitted emission lines with FWHM > 1000 km s^{-1}, believed to originate from rapidly moving gas near the central black hole, and narrow emission lines from permitted and forbidden transitions with FWHM $\lesssim 500$ km s^{-1}, believed to originate from slower-moving gas further away from the black hole. Sy2s on the other hand only display

the narrow emission lines, implying that they are objects viewed at a higher angle to the line of sight so that the broad-line region is obscured. Sy1s are further categorised from 1.2 to 1.9 depending on the ratio of the luminosity of the broad-line to narrow-line components, with lower ratios corresponding to numerically higher categorisations.

7.3.1 Seyfert Galaxies in the GeV Regime

The first detection of a Seyfert galaxy with the *Fermi*-LAT was that of PMN J0948+0022, reported in Abdo et al. (2009b), although prior to this hints of blazar-like activity had been observed from a number of such objects. PMN J0948+0022 is a relatively distant Sy1 galaxy at $z = 0.585$; owing to absorption by the EBL, this makes it unlikely to be a source of TeV γ-rays. However, since its detection, three other such objects have also been reported as GeV γ-ray emitters. All four Sy1s detected at these energies display narrow permitted lines, spectra similar to blazars and luminosities typical of or higher than those of many BL Lac objects. Two of the Sy1s detected by the *Fermi*-LAT are at much lower redshifts than PMN J0948+0022, z = 0.061 and z = 0.24, and are potentially of more interest for VHE γ-ray astronomy.

Further to the detection of these Sy1s at GeV energies, detection of the Sy2 galaxy NGC 4945 was reported in the 11-month *Fermi*-LAT catalogue (Abdo et al., 2010a). Additionally another *Fermi*-LAT source was found in the region of NGC 1068 (another Sy2) and the*Fermi*-LAT source has since been associated with this object. Both of these Sy2s display both AGN and starburst activity in their central regions, either of which could be responsible for the observed GeV emission. Further work analysing the γ-ray emission from these objects by Lenain et al. (2010) suggests that the emission from NGC 1068 likely originates from the central AGN, while the emission from NGC 4945 is probably connected with starburst activity. It is argued that unlike the GeV emission from the Sy1s, which is likely due to similar processes to those seen in blazars, the emission from the AGN in NGC 1068 is more likely to be external inverse-Compton emission.

7.3.2 The Search for TeV Emission from Seyfert Galaxies

The detection of M87 at very high energies showed that the jets of AGN need not be aligned with the line of sight for TeV emission to be observed. Taken together with the blazar-like properties observed from some Seyfert galaxies, this suggested that there may be potential for TeV emission from such objects, and it was decided to analyse data collected serendipitously with the H.E.S.S. array in regions near high-energy Seyferts. The study was carried out initially between 2008 and 2009, before the launch of the *Fermi* satellite, so the *INTEGRAL*-IBIS catalogue of lower-energy γ-ray sources was used to select the objects for study. The resulting list was then expanded to

include a number of X-ray-emitting Seyfert nuclei detected by *XMM-Newton*.

The list constructed from the catalogues was then sorted so that only those objects within the field of view of the H.E.S.S. array were selected; any Seyfert galaxies at redshifts $z > 0.3$ were removed, as any very high energy emission would likely be heavily attenuated by the EBL. The positions of the remaining objects were then compared to the list of H.E.S.S. observing runs to determine those for which data unaffected by hardware faults or adverse weather conditions had been previously collected. After selection, 16 objects were determined to be of interest: 9 Sy1s, 1 Sy 1.5, 3 Sy2s, a quasar and a type 2 AGN displaying Seyfert-like properties. The amount of data available for each object varied considerably.

The data from each of the objects were analysed using the standard H.E.S.S. analysis as discussed in Chapter 2; two different background models were used (reflected-region and ring background). No evidence for very high energy emission was found for any of the objects studied, although in some cases the very limited amount of data makes it impossible to draw any strong conclusions. Flux upper limits for each of the objects were calculated assuming similar spectral shapes to M87; in most cases these limits are not very constraining.

7.4 Misaligned AGN at High energies

Currently,all the misaligned AGN detected at TeV energies have been FRI radio galaxies, although NGC 1275 is also classified as a Seyfert 1.5 and Centaurus A displays an extremely complex morphology. Due to the relatively large point-spread functions of current IACTs, it is not possible to directly resolve the source of the emission in these objects; however, variability studies allow an upper limit to be placed on the size of the emission region, thereby constraining likely sites of the VHE γ-ray production. Thus far, all of the misaligned TeV AGN have also been detected at GeV energies by the *Fermi* satellite.

M87 was the first of the misaligned AGN to be detected at TeV energies and was initially reported by the H.E.S.S. Collaboration. It is a giant elliptical galaxy with a redshift of $z = 0.004233$, hosting a very high mass ($> 10^9$ $M_\odot$) supermassive black hole at its nucleus and displaying a radio jet, with superluminal features, at an angle of $\approx 20^\circ$ to the line of sight. At TeV energies, the M87 displays variability on timescales of $\sim$ 1 day, faster than has been detected at other wavelengths and providing strong constraints on the size of the emission region. These constraints imply that the TeV photons probably originate close to the central black hole, although there is still a possibility that HST-1 (a knot in the jet) may be the source of the very high energy activity.

Centaurus A was eventually detected after a very large number of hours of observation with

the H.E.S.S. telescopes. The object displays a complex morphology, a radio jet with an angle of inclination $\sim 50°$, and two radio lobes. The nucleus hosts a supermassive black hole with a mass $\sim 10^8$ $M_\odot$. Unfortunately, Centaurus A is relatively weak at TeV energies; this has made it impossible to carry out any variability analysis and so the source of the emission is currently unknown. Interestingly, there is some evidence that Centaurus A may be the source of four of the UHECR protons detected above 57 EeV, although the statistics are clearly very low.

NGC 1275 is the misaligned AGN most recently detected at very high energies; it was initially detected at GeV energies with the *Fermi*-LAT prior to its detection with the MAGIC telescopes. The object is a very bright radio source, with an extended jet at an angle of inclination that increases from $10° - 20°$ on milliarcsecond scales up to $40° - 60°$ on arcsecond scales. It is situated relatively nearby at a redshift $z = 0.0179$. Comparing the spectrum of the source at TeV energies to the spectrum at *Fermi*-LAT energies suggests a break or cut-off at energies of some tens of GeV.

In 2010, the detection of 11 misaligned AGN, using data collected with the *Fermi*-LAT, was reported. These detections offer potentially interesting objects for study at very high energies, particularly for the planned Cherenkov Telescope Array (CTA). *Fermi*-LAT detection of NGC 1275 has already led to the detection of this object with the MAGIC telescopes as previously discussed. It was decided that it would be interesting to estimate the potential for very high energy emission from these objects and use these estimates to determine the likelihood of detecting them at TeV energies. To do this, four of the models that have been proposed to account for the TeV emission of the currently detected misaligned AGN were investigated. These models are discussed below.

7.4.1 Modelling Emission from TeV Misaligned AGN

The detection of misaligned AGN at TeV energies has raised a number of interesting questions about the mechanisms responsible for high-energy emission in such objects, as they cannot be adequately modelled using the simple one-zone SSC models that are generally used to reproduce the spectra of blazars. This is because the simple models used rely on Doppler boosting to increase the energies of the photons emitted by particles in the jets of blazars. This requires that the jet is at a small angle to the line of sight, which is clearly not the case in misaligned AGN. To explain the emission from misaligned AGN, a number of different models have been put forward; for this work, three inhomogeneous jet approaches and one approach focusing on emission from the core were considered and are discussed in detail in Sections 5.5 and 5.6. A brief description of each of these models is included below.

It has been proposed by Tavecchio & Ghisellini (2008) that the high-energy emission from M87 can be explained if the jet is structured in such a manner as to have a fast-moving inner spine,

surrounded by a slower moving sheath. The TeV emission then originates from inverse-Compton scattering in one region of photons produced in the other, which are seen in the local frame as boosted in energy due to relativistic effects. One issue with the model is that by introducing two physically distinct regions, there are 18 free parameters to be constrained. Additionally, the model has difficulty reproducing the hard very high energy spectrum observed from M87 during the flare in 2005, because the slope of the TeV spectrum in the model depends primarily on absorption of the TeV photons by the dense optical radiation field rather than the intrinsic spectrum.

The decelerating-jet model proposed by Georganopoulos & Kazanas (2003) similarly relies on synchrotron photons being upscattered through inverse-Compton processes by electrons in a region of the jet with different physical parameters to the initial emission region. In this model, it is assumed that a power-law electron distribution is injected at the base of the jet, which then decelerates as the distance from the initial injection site increases, and the electrons cool radiatively. The increase in detected energies comes about as synchrotron photons from downstream in the jet appear strongly boosted in the upstream part of the jet so that they contribute to the inverse-Compton emission at higher energies than would otherwise be expected. Although the model can successfully reproduce the TeV spectrum of M87, it is difficult to formulate a scenario where the observed short-term variability could be generated. The model also has difficulty reproducing the very high energy spectrum of Centaurus A, although it can successfully model the object at *Fermi*-LAT energies.

The final jet model considered was that proposed by Lenain et al. (2008) which expands on the simple blob-in-jet models used previously. Instead of modelling the emission as originating from a single, homogeneous blob of plasma, seven such blobs are modelled, moving along the jet and situated on (or near) the Alfvén surface, $\sim 50 - 100 r_s$ from the central black hole. This is likely a more accurate description of the plasma in the jet than single-blob models, although it is still a simplification of the actual scenario. Due to the proximity to the central black hole, the blobs are still within the collimation region, and it is assumed that they are situated on a spherical "cap"; this means that the angle to the line of sight for a given blob depends on its position in the jet. In this scenario, each of the blobs contributes to the emission detected from an object by an amount dependent on its Doppler factor. The geometry of the model leads to two extremes, the "on-blob" case, in which the line of sight passes directly through a blob, leading to the maximum predicted emission for given parameter values, and the "inter-blob" case, where the line of sight passes between three blobs, resulting in a minimum. The model has proven relatively robust and has been used successfully to model both the TeV emission from M87, including the emission observed during the 2005 flare, and that from Centaurus A.

In addition to jet models, the core emission model of Rieger & Aharonian (2008b) was also considered, in which it is suggested that the emission originates primarily from a region very close to the event horizon of the central black hole. In this model, electrons are accelerated to high energies by a rigidly rotating dipolar magnetosphere, generated as magnetic flux is dragged inward and amplified by dynamo action in the inner accretion disc. The TeV emission in such a model is assumed to arise via inverse-Compton scattering of photons from an advection-dominated accretion disc by this population of accelerated electrons. The model shows good agreement with the TeV spectrum observed from M87 and can reproduce the observed variability; however, the region close to the central black hole is expected to have a high photon density which may render the region effectively opaque to TeV γ-rays.

7.4.2 Multiblob Modelling of GeV Selected Misaligned AGN

Of the models investigated, it was decided to use the multiblob model of Lenain et al. (2008), as it makes relatively few assumptions compared to the other models and has been successfully used to account for the very high energy emission of both M87 and Centaurus A. After selecting the multiblob model, it was decided that, in addition to determining whether the misaligned AGN detected with the *Fermi*-LAT could be potential targets for CTA, it would also be useful to determine the capacity of the model to successfully reproduce the high-energy emission from these objects using physically sensible parameters. The model has been adapted to take account of the absorption of VHE γ-rays by the EBL, using the prescription described in Kneiske, Manheim & Hartmann (2002) and Kneiske et al. (2004). This proved important when considering the spectra of the two most distant misaligned AGN detected by *Fermi*-LAT, 3C 207 at $z = 0.681$ and 3C 380 at $z = 0.692$.

M87, Centaurus A and NGC 1275 were all excluded from the modelling, as previous work has already been done in this area and the objects have already been detected with current instruments. This left eight sources of high-energy emission detected with the *Fermi*-LAT to be studied; however, due to paucity of data, the *Fermi*-LAT spectra for three of these objects have not currently been determined and so only the remaining five were modelled. Before modelling each object, the literature was consulted to determine, where available, the currently accepted values for the mass of the central black hole and the angle of inclination with respect to the line of sight. The modelling of the AGN was done such that parameters were found that produced spectra for the on-blob case which were consistent with the spectra derived from the *Fermi*-LAT data.

The multiblob model proved successful in reproducing the spectra for the misaligned AGN considered using physically sensible values for the parameters in each case, although some difficulty

was noted in reproducing the *Fermi*-LAT spectrum of NGC 6251. The predicted spectra for each of the objects at very high energies are very steep, and in most cases very low fluxes are predicted, although the predicted spectrum for 3C 111 at TeV energies is brighter than those of the other objects. Interestingly, the model had great difficulty reproducing the spectrum of 3C 120 using the black hole mass of 3.5×10^7 $M_\odot$ put forward by León-Tavares et al. (2010) without resorting to physically improbably values of Γ_b and B, so a value of 5.5×10^7 $M_\odot$ (Vestergaard & Peterson, 2006) is preferred. By comparing the spectra produced using the multiblob model for each of these objects with the projected sensitivity curves for CTA from Rulten (2012), it was found that none of the objects are likely to be detected by any of the proposed array configurations within 50 hours of observations using the standard analysis methods used in Durham. However, if the more-sensitive Paris analysis is used, then the sensitivity of the array should be close to that required to detect 3C 111, assuming it is in a similar state to that during the *Fermi*-LAT observations. It is important to note that the fluxes generated using the multiblob model for each object are not necessarily very far from the predicted sensitivity of the potential CTA arrays, and that during flares at GeV energies the possibility of TeV detection will probably be significantly higher.

7.5 Future Prospects for the Study of Misaligned AGN at TeV Energies

Despite the lack of detection of Seyfert galaxies using data collected by the H.E.S.S. array, the relatively few objects for which significant data were available limits the ability to draw any strong conclusions about these objects, and in most cases the upper limits calculated are not particularly constraining. The detection of a number of Sy1s and a Sy2 at high energies with the *Fermi*-LAT suggests some potential for TeV emission from these types of object, but the spectra predicted suggest that detection with current IACTs is perhaps unlikely. Further to the work described here, it would potentially be of great interest to model the spectra of the GeV Seyfert galaxies at TeV energies and compare the spectra generated to projected sensitivity curves for CTA to determine the likelihood of detection with the planned array. Modelling these objects is likely to be more complicated than modelling the misaligned AGN discussed in Chapter 6, as it is probable that there is a significant contribution to the seed photon field for inverse-Compton scattering from external sources such as the accretion disc. To help constrain the parameters required for such models, it is important to obtain well-sampled, contemporaneous SEDs of the objects through multiwavelength campaigns. Additionally, the radio galaxy NGC 1275 detected by the MAGIC telescopes displays similar spectral properties to Sy 1.5 galaxies, suggesting that detailed study of

this object may help to constrain potential sources of TeV emission in true Seyfert galaxies.

The modelling of the five misaligned AGN detected with the *Fermi*-LAT for which high-energy spectra are available using the multiblob model proved successful, allowing potential SEDs to be generated in each case. In spite of this, the SEDs produced are not heavily constrained, with multiple alternative solutions existing in each case. To further constrain the parameters used in these models, multiwavelength studies for each of the objects, covering the peaks of the synchrotron and inverse-Compton emission as well as the spectrum at *Fermi*-LAT energies, would be extremely useful. If such data were available that for those objects for which multiple potential values for the angle of inclination and black hole mass exist, then it might be possible to provide some support for more specific values for these parameters using the multiblob model. Further *Fermi*-LAT observations of all of the misaligned AGN would be of great interest to determine the high-energy spectra for those objects for which a spectrum is currently unavailable, while also allowing variability studies of the objects to be carried out. Any variability at high energies is of particular interest when considered alongside the results of the modelling. The modelling suggests that it is unlikely that CTA will be able to detect most of the modelled objects within 50 hours of observations; however, the predicted TeV spectra are bright enough that it is probable that detection will be possible during a flare, particularly for the less distant AGN.

The construction of CTA will hopefully lead to the detection at TeV energies of a number of misaligned AGN, including 3C 111 modelled here. However, even without new detections, CTA observations will allow the physical processes behind emission from M87, Centaurus A and NGC 1275 to be studied in greater detail. In spite of the current work going into modelling the very high energy emission of these objects, the mechanisms and regions responsible for this emission remain relatively unconstrained. It is to be expected that the increased resolution and energy range of CTA will help provide evidence supporting or refuting these models and significantly increasing our understanding of emission from misaligned AGN. Observations of the more distant misaligned AGN 3C 207 and 3C 380, particularly during GeV flares, could be of great importance in placing limits on the EBL, as the expected spectra are steeper than those seen from blazars. The construction of water-based Cherenkov telescopes such as the High Altitude Water Cherenkov Observatory (HAWC) is unlikely to contribute greatly to our understanding of misaligned AGN as such telescopes have high threshold energies ($\sim 1-\sim 100$ TeV) beyond the energy range at which significant emission from misaligned AGN is expected.

Bibliography

Abdo A. et al. 2008, Science 322, 1218, *The Fermi Gamma-Ray Space Telescope Discovers the Pulsar in the Young Galactic Supernova Remnant CTA 1.*

Abdo A. et al. 2009a, Science 323, 1688, *Fermi Observations of High-Energy Gamma-Ray Emission from GRB 080916C.*

Abdo A. et al. 2009b, ApJ 699, 976, *Fermi/Large Area Telescope Discovery of Gamma-Ray Emission from a Relativistic Jet in the Narrow-Line Quasar PMN J0948+0022.*

Abdo A. A. et al. 2009c, ApJ 707, L142, *Radio-Loud Narrow-Line Seyfert 1 as a New Class of Gamma-Ray Active Galactic Nuclei.*

Abdo A. A. et al. 2010a, ApJS 188, 405, *Fermi Large Area Telescope First Source Catalog.*

Abdo A. A. et al. 2010b, ApJ 709, L152, *Detection of Gamma-Ray Emission from the Starburst Galaxies M82 and NGC 253 with the Large Area Telescope on Fermi.*

Abdo A. A. et al. 2010c, ApJ 720, 912, *Fermi Large Area Telescope Observations of Misaligned Active Galactic Nuclei.*

Abdo A. A. et al. 2010d, Nature 463, 919, *A change in the optical polarization associated with a -ray flare in the blazar 3C279.*

Abdo A. A. et al. 2010e, ApJ 719, 1433, *Fermi Large Area Telescope View of the Core of the Radio Galaxy Centaurus A.*

Abdo A. A. et al. 2010f, ApJ 715, 429, *The First Catalog of Active Galactic Nuclei Detected by the Fermi Large Area Telescope.*

Abraham J. et al. 2008, APh 29, 188, *Correlation of the highest-energy cosmic rays with the positions of nearby active galactic nuclei.*

Abramowski A. et al. 2011, ApJ 746, 141, *The 2010 Very High Energy γ-Ray Flare and 10 Years of Multi-wavelength Observatios of M87.*

Abramowski A. et al. 2012a, A&A 545, L2, *Discovery of gamma-ray emission from the extragalactic pulsar wind nebula N 157B with H.E.S.S..*

Abramowski A. et al. 2012b, A&A 537, 114, *Discovery of extended VHE γ-ray emission*

from the vicinity of the young stellar cluster Westerlund 1.

Abramowski A. et al. 2012c, ApJ 746, 151, *The 2010 Very High Energy γ-Ray Flare and 10 Years of Multi-Wavelength Observations of M87.*

Acciari V. A. et al. 2008, ApJ 679, 1427, *VERITAS Observations of the γ-Ray Binary LS I +61 303.*

Acciari V. A. et al. 2009a, ApJ 693, L104, *Veritas Observations of a Very High Energy γ-Ray Flare From the Blazar 3C 66A.*

Acciari V. A. et al. 2009b, Nature 462, 770, *A connection between star formation activity and cosmic rays in the starburst galaxy M82.*

Acciari V. A. et al. 2009c, ApJ 707, 612, *Multiwavelength Observations of a TeV-Flare from W Comae.*

Acero F. et al. 2009, Science 326, 1080, *Detection of Gamma Rays from a Starburst Galaxy.*

Actis M. et al. 2011, Exp. Astron. 32, 193, *Design concepts for the Cherenkov Telescope Array CTA: an advanced facility for ground-based high-energy gamma-ray astronomy.*

Adams T. F. 1977, ApJs 33, 19, *A Survey of the Seyfert Galaxies Based on Large-Scale Image-Tube Plates.*

Aharonian F. et al. 1999, A&A 349, 11, *The time averaged TeV energy spectrum of Mkn 501 of the extraordinary outburst as measured with the stereoscopic Cherenkov telescope system of HEGRA.*

Aharonian F. A. 2000, New Astron. 5, 377, *TeV gamma rays from BL Lac objects due to synchrotron radiation of extremely high energy protons.*

Aharonian F. et al. 2001, A&A 370, 112, *Evidence for TeV gamma ray emission from Cassiopeia A.*

Aharonian F. et al. 2003, A&A 403, L1, *Is the giant radio galaxy M 87 a TeV gamma-ray emitter?*

Aharonian F. et al. 2005a, A&A 430, 865, *H.E.S.S. observations of PKS 2155-304.*

Aharonian F. et al. 2005b, A&A 441, 465, *Observations of selected AGN with HESS.*

Aharonian F. et al. 2006a A&A 457, 899, *Observations of the Crab nebula with HESS.*

Aharonian F. et al. 2006b, A&A 460, 365, *Energy dependent γ-ray morphology in the pulsar wind nebula HESS J1825-137.*

Aharonian F. et al. 2006c, A&A 460, 743, *3.9 day orbital modulation in the TeV -ray flux and spectrum from the X-ray binary LS 5039.*

Aharonian F. et al. 2006d, Science 314, 1424, *Fast Variability of Tera-Electron Volt Rays from the Radio Galaxy M87.*

Aharonian F. et al. 2007, ApJ 664 L71, *An Exceptional Very High Energy Gamma-Ray Flare of PKS 2155-304.*

Aharonian F. et al. 2008, APh 29, 55, *Observations of the Sagittarius dwarf galaxy by the HESS experiment and search for a dark matter signal.*

Aharonian. F. A., Khangulyan D. & Costamante L. 2008, MNRAS 387, 1206, *Formation of hard very high energy gamma-ray spectra of blazars due to internal photon-photon absorption.*

Aharonian F. et al. 2009a, Science 326, 1080 *Detection of Gamma Rays from a Starburst Galaxy.*

Aharonian F. et al. 2009b, ApJ 695, L40, *Discovery of Very High Energy γ-Ray Emission from Centaurus A with H.E.S.S..*

Aharonian F. et al. 2009c, A&A 502, 749, *Simultaneous multiwavelength observations of the second exceptional γ-ray flare of PKS 2155-304 in July 2006.*

Aharonian F. et al. 2009d, ApJ 692, 1500, *Discovery of Gamma-Ray Emission From the Shell-Type Supernova Remnant RCW 86 With Hess.*

Albert J. et al. 2006, Science 312, 1771, *Variable Very-High-Energy Gamma-Ray Emission from the Microquasar LS I +61 303.*

Albert J. et al. 2007a, ApJ 664, 87, *Discovery of Very High Energy Gamma Radiation from IC 443 with the MAGIC Telescope.*

Albert J. et al. 2007b, ApJ 665, L51, *Very High Energy Gamma-Ray Radiation from the Stellar Mass Black Hole Binary Cygnus X-1.*

Albert J. et al. 2007c, ApJ 669, 862, *Variable Very High Energy γ-Ray Emission from Markarian 501.*

Albert J. et al. 2009, Nucl. Instrum. Methods Phys. Res. A 588, 424, *Implementation of the Random Forest method for the Imaging Atmospheric Cherenkov Telescope MAGIC.*

Aleksić J. et al. 2010, ApJ 723, 207, *Detection of Very High Energy γ-ray Emission from the Perseus Cluster Head-Tail Galaxy IC 310 by the MAGIC Telescopes.*

Aleksić J. et al. 2012a, APh 35, 435, *Performance of the MAGIC stereo system obtained with Crab Nebula data.*

Aleksić J. et al. 2012b, A&A 540, 69, *Phase-resolved energy spectra of the Crab pulsar in the energy range of 50-400 GeV measured with the MAGIC telescopes.*

Aleksić J. et al. 2012c, A&A 539, L2, *Detection of very-high energy -ray emission from NGC 1275 by the MAGIC telescopes.*

Aliu E. et al. 2009, ApJ 692, L29, *Discovery of a Very High Energy Gamma-Ray Signal*

from the 3C 66A/B Region.

Aliu E. et al. 2012, ApJ 759, 102, *VERITAS Observations of Six Bright, Hard-spectrum Fermi-LAT Blazars.*

Aliu E. et al. 2012, ApJ 746, 141, *Veritas Observations of Day-Scale Flaring of M87 in 2010 April.*

Antón S., Browne, I. W. A. & Marchã, M. J. 2008, A&A 490, 583, *VERITAS Observations of Six Bright, Hard-spectrum Fermi-LAT Blazars.*

Antonucci R. R. J. & Miller J. S. 1985, ApJ 297, 621.

Antonucci, R. 1993, ARA&A 31, 473, *Unified models for active galactic nuclei and quasars.*

Arp H. 1968, ApJ 152, 1101, *A Compact Galaxy (iii ZW 2) and a Compact Radio Galaxy (3C 120) with Seyfert-Type Spectra.*

Artamonov B. P. et al. 2010, Astron. Rep. 54, 767, *Nuclear activity of the Seyfert galaxy NGC 7469 in 1990-2006: Observations from the Mt. Maidanak Observatory.*

Atwood W. B. et al. 2009, ApJ 697, 1071, *The Large Area Telescope on the Fermi Gamma-Ray Space Telescope Mission.*

Becker R. H., White R. L., & Edwards A. L. 1991, ApJS 75, 1, *A new Catalog of 53,522 4.85 GHz sources.*

Bélanger G. et al. 2006, ApJ 636, 275, *A Persistent High-Energy Flux from the Heart of the Milky Way: INTEGRAL's View of the Galactic Center.*

Benbow W. et al. 2005, Technical Report for the H.E.S.S. Collaboration, Max Planck Institut für Kernphysik, Postfach 103980, D-69029, Germany, *The H.E.S.S. Standard Analysis Technique.*

Bennett C. L., Lawrence C. R., Burke B. F., Hewitt J. N. & Mahoney, J. 1986, ApJS, 61, 1, *The MIT-Green Bank (MG) 5 GHz survey.*

Baade W. & Minkowski R. 1954, ApJ 119, 206B, *Identification of the Radio Sources in Cassiopeia, Cygnus A, and Puppis A.*

Ballantyne D. R., Fabian A. C. & Iwasawa K. 2004, MNRAS 354, 839, *The XMM-Newton view of the broad-line radio galaxy 3C 120.*

Band D. L. and Grindlay J. E. 1986, ApJ 311, 595, *Synchrotron and inverse Compton emission from expanding sources in jets - Application to SS 433.*

Barger A. J. et al. 2005, AJ 129, 578, *The Cosmic Evolution of Hard X-Ray-selected Active Galactic Nuclei.*

Bassani L. et al. 2005, ApJ 634, L21, *Is the INTEGRAL IBIS Source IGR J17204-3554 a Gamma-Ray-emitting Galaxy Hidden behind the Molecular Cloud NGC 6334?*

Batcheldor D. et al. 2010, ApJ 717, L6, *A Displaced Supermassive Black Hole in M87.*

Beckmann V., Engels D., Bade N. & Wucknitz O. 2003, A&A 401, 927, emphThe HRX-BL Lac sample - Evolution of BL Lac objects.

Beckmann V. et al. 2009, A&A 505, 417, *The second INTEGRAL AGN catalogue.*

Bednarek W. & Idec W. 2011, MNRAS 414, 2229, *On the variability of the GeV and multi-TeV gamma-ray emission from the Crab nebula.* Begelman M. & Sikora M. 1987, ApJ 322, 650, *Inverse Compton scattering of ambient radiation by a cold relativistic jet - A source of beamed, polarized continuum in blazars?*

Begelman M. C., Fabian A. C. & Rees M. J. et al. 2008, MNRAS 384, L19, *Implications of very rapid TeV variability in blazars.*

Beilicke M. 2009, AIP Conf. Proc. 1112, 33, *VERITAS-Status and Results (2007/08 Season).*

Bennert N., Jungwiert B., Komossa S., Haas M. & Chini R. 2006, A&A 459, 55 *Size and properties of the narrow-line region in Seyfert-1 galaxies from spatially-resolved optical spectroscopy.*

Bennett A. S. 1962, MNRAS 125, 75, *The preparation of the revised 3C catalogue of radio sources.*

Bergström L. 1999, AIP Conf. Proc. 478, 352, *Indirect detection of neutralino dark matter.*

Bernlöhr et al. 2003, APh 20, 111, *The optical system of the H.E.S.S. imaging atmospheric Cherenkov telescopes. Part I: layout and components of the system.*

Bernstein R. A., Freedman W. L. & Madore B. F. 2002, ApJ 571, 56, *The First Detection of the Extragalactic Background Light at 3000, 5500, and 8000 Å. I. Results.*

Bianchi S. et al. 2002, A&A 396, 793, *Flux and spectral variations in the Circinus Galaxy.*

Bianchi S. et al. 2010, MNRAS 405, 553, *High-resolution X-ray spectroscopy and imaging of Mrk 573.*

Bicknell G. V. & Begelman M. C. 1996, ApJ 467, 597, *Understanding the Kiloparsec-Scale Structure of M87.*

Bignami G. et al. 1981, A&A 93, 71, *3C273 Revisited - Confirmation by Cos-B of High Energy Gamma-Ray Emission.*

Bird A. J. et al. 2006, ApJ 636, 765, *The Second IBIS/ISGRI Soft Gamma-Ray Survey Catalog.*

Biretta J. A., Owen F. N. & Cornwell T. J. 1989, ApJ 342, 128, *A search for motion and flux variations in the M87 jet.*

Biretta J. A. & Junor W. 1995, Proc. Natl Acad. Sci. 92, 11364, *The Parsec-Scale Jet in M87.*

Biretta J. A., Zhou F. & Owen F. N. 1995, ApJ 447, 582, *Detection of Proper Motions in the M87 Jet.*

Biretta J. A., Sparks W. B. & Macchetto F. 1999, ApJ 520, 621, *Hubble Space Telescope Observations of Superluminal Motion in the M87 Jet.*

Bissaldi E. 2011, AIP Conf. Proc. 1358, 13, *The 52 Brightest and Hardest GRBs Detected with the Gamma-ray Burst Monitor on Fermi.*

Błażejowski M. et al. 2000, ApJ 545, 107, *Comptonization of Infrared Radiation from Hot Dust by Relativistic Jets in Quasars.*

Błażejowski M. et al. 2005, ApJ 630, 130, *A Multiwavelength View of the TeV Blazar Markarian 421: Correlated Variability, Flaring, and Spectral Evolution.*

Bloom S. D. & Marscher A. P. 1996, ApJ 461, 657, *An Analysis of the Synchrotron Self-Compton Model for the Multi–Wave Band Spectra of Blazars.*

Blumenthal G. R. & Gould R. J. 1970, Rev. Mod. Phys. 42, 237, *Bremsstrahlung, Synchrotron Radiation, and Compton Scattering of High-Energy Electrons Traversing Dilute Gases.*

Bogers W. J., Hes R., Barthel P. D. & Zensus J. A. 1994, A&AS 105, 91, *High resolution radio observations of intermediate redshift quasars and radio galaxies.*

Boldt E. & Loewenstein M. 2000, MNRAS 316, 29, *Cosmic ray generation by quasar remnants: constraints and implications.*

Boller Th., Gallo L. C., Lutz D. & Sturm E. 2002, MNRAS 336, 1146, *Mrk 1014: an AGN-dominated ultraluminous infrared galaxy.*

Boroson T. A. & Green R. F. 1992, ApJS 80, 109, *The emission-line properties of low-redshift quasi-stellar objects.*

Boroson T. A. 2002, ApJ 565, 78, *Black Hole Mass and Eddington Ratio as Drivers for the Observable Properties of Radio-loud and Radio-quiet QSOs.*

Böttcher M. & Chang J. 2002, ApJ 581, 127, *X-Ray Spectral Variability Signatures of Flares in BL Lacertae Objects.*

Böttcher M. & Reimer A. 2004, ApJ 609, 576 *Modeling the Multiwavelength Spectra and Variability of BL Lacertae in 2000.*

Böttcher M. 2007, Ap&SS 309, 95, *Modeling the emission processes in blazars.*

Böttcher M. & Principe D. 2009, ApJ 692, 1374, *Optical Variability of the Quasar 3C 279: The Signature of a Decelerating Jet?*

Böttcher M. & Dermer C. D. 2010, ApJ 711, 445, *Timing Signatures of the Internal-Shock Model for Blazars.*

Böttcher, M. 2010, *Fermi* meets Jansky - AGN at Radio and Gamma rays 41; arXiv:1006.5048, *Models for the Spectral Energy Distributions and Variability of Blazars.*

Brinkmann W., Siebert J. & Boller Th. 1994, A&A 281, 355.

Brown A. M. & Adams J. 2011, MNRAS 413, 2785, *The X-ray AGN content of the Molonglo 408 MHz Survey: Bulk properties of previously optically identified sources.*

Brunetti G., Bondi M., Comastri A. & Setti G. 2002, A&A 381, 795, *Chandra discovery of extended non-thermal emission in 3C 207 and the spectrum of the relativistic electrons.*

Brunthaler A. et al. 2000, A&A 357, L45, *III Zw 2, the first superluminal jet in a Seyfert galaxy.*

Brunthaler A. et al. 2005, A&A 435, 497, *The extreme flare in III Zw 2:. Evolution of a radio jet in a Seyfert galaxy.*

Buckley J. H. 1998, Science 279, 676, *ASTROPHYSICS: What the Wild Things Are.*

Burgess A. M. & Hunstead R. W. 2006a, AJ 131, 100, *The Molonglo Southern 4 Jy Sample (MS4). I. Definition.*

Burgess A. M. & Hunstead R. W. 2006b, AJ 131, 114, *The Molonglo Southern 4 Jy Sample (MS4). II. ATCA Imaging and Optical Identification.*

Buttiglione S. et al. 2010, A&A 509, 6,*An optical spectroscopic survey of the 3CR sample of radio galaxies with z ¡ 0.3 . II. Spectroscopic classes and accretion modes in radio-loud AGN.*

Bykov A. A. et al. 2006, A&A 449, 917, *INTEGRAL detection of hard X-rays from NGC 6334: nonthermal emission from colliding winds or an AGN?*

Cambrésy L., Reach W. T., Beichman C. A. & Jarrett, T. H. 2001, ApJ 555, 563, *The Cosmic Infrared Background at 1.25 and 2.2 Microns Using DIRBE and 2MASS: A Contribution Not Due to Galaxies?*

Caproni A. et al. 2006, ApJ 638, 120, *Bardeen-Petterson Effect and the Disk Structure of the Seyfert Galaxy NGC 1068.*

Caraveo P. A. 2012, Mem. S.A.It. Suppl. 19, 19, *The Fermi Gamma-Ray Sky.*

Celotti A. and Ghisellini G. 2008, MNRAS 385, 283, *The power of blazar jets.*

Chadwick P. M. et al. 1999a, ApJ 513, 161, *Very High Energy Gamma Rays from PKS 2155-304.*

Chadwick P. M. et al. 1999b, Proc. of the 26th ICRC 3, 338, *VHE gamma rays from PKS 2155-304.*

Chang C. S., Ros E., Kovalev Y. Y. & Lister, M. L. 2010, A&A 515, 38, *VLBI detection of the HST-1 feature in the M 87 jet at 2 cm.*

Chapman G. N. F., Geller M. J., Huchra J. P. 1985, ApJ 297, 151, *The ultraviolet variability of Seyfert 1 galaxies.*

Chatterjee R. et al. 2011, ApJ 734, 43, *Connection Between the Accretion Disk and Jet in the Radio Galaxy 3C 111.*

Chaves R. C. G. 2009, Proc. 31st ICRC; arxiv:0907.0768, *Extending the H.E.S.S. Galactic Plane Survey.*

Cheung C. C., Harris D. E. & Stawarz Ł. 2007, ApJ 663, L65, *Superluminal Radio Features in the M87 Jet and the Site of Flaring TeV Gamma-Ray Emission.*

Chiaberge M., Capetti A. & Celotti A. 2001, MNRAS, 324, L33, *The Nuclear Spectral Energy Distribution of NGC 6251: A BL Lacertae Object in the Center of an FR I Radio Galaxy.*

Chiaberge M., Gilli R., Capetti A. & Macchetto F. D. 2003, ApJ 597, 166.

Chiaberge, M.; Capetti, A.; Celotti, A 1999, A&A 349, 77, *The HST view of FR I radio galaxies: evidence for non-thermal nuclear sources.*

Condon J. J., Helou G., Sanders D. B. & Soifer B. T. 1996, ApJS, 103, 81, *A 1.425 GHz Atlas of the IRAS Bright Galaxy Sample, Part II.*

Cortina J. 2011, Proc. 32nd ICRC; arXiv:1110.4747, *Highlights of the MAGIC Telescopes.*

Croston J. H. et al. 2009, MNRAS 395, 1999, *High-energy particle acceleration at the radio-lobe shock of Centaurus A.*

Crusius A. & Schlickeiser R. 1986, A&A, 164, L16, *Synchrotron radiation in random magnetic fields.*

Cui Y.-D., Yuan Y.-F., Li Y.-R. & Wang J.-M. 2012, ApJ 746, 177, *A General Relativistic External Compton-Scattering Model for TeV Emission from M87.*

Curtis H. D. 1918, Pub Lick Obs. 13, L31, *Descriptions of 762 Nebulae and Clusters Photographed with the Crossley Reflector.*

Cutri, R. M., et al. 2003, *The IRSA 2MASS All-Sky Point Source Catalog*, NASA/IPAC Infrared Science Archive.

Czerny B. & Lehto H. J. 1997, MNRAS 285 365, *Testing the X-ray variability of active galactic nuclei with the non-linear prediction method.*

Daniel M. K. et al. 2005, ApJ 621, 181, *Spectrum of Very High Energy Gamma-Rays from the blazar 1ES 1959+650 during Flaring Activity in 2002.*

Davies J. M. & Cotton E. S. 1957, Journ. of Solar Energy 1, 16, *Design of the quartermaster solar furnace.*

de Vaucouleurs G. et al. 1991, *Third Reference Catalogue of Bright Galaxies*, Springer-Verlag,

New York.

Decarli R., Dotti M. & Treves A. 2011, MNRAS 413, 39, *Geometry and inclination of the broad-line region in blazars.*

Del Monte E. et al. 2008, A&A 478, 5, *GRB 070724B: the first gamma ray burst localized by SuperAGILE and its Swift X-ray afterglow.*

Deo R. P., Crenshaw D. M. &Kraemer S. B. 2006, AJ 132, 321, *The Host Galaxies of Narrow-Line Seyfert 1 Galaxies: Nuclear Dust Morphology and Starburst Rings.*

Dermer C. D. & Schlickeiser R. 1993, ApJ 416, 458, *Model for the High-Energy Emission from Blazars.*

Dermer C. D. 1995, ApJ 446, L63, *On the Beaming Statistics of Gamma-Ray Sources.*

Dermer C. D., Sturner S. J. & Schlickeiser R. 1997, ApJS 109, 103 *Nonthermal Compton and Synchrotron Processes in the Jets of Active Galactic Nuclei.*

Dermer C. D. & Schlickeiser R. 2002, ApJ 575, 667, *Transformation Properties of External Radiation Fields, Energy-Loss Rates and Scattered Spectra, and a Model for Blazar Variability.*

Doi A. et al. 2006, PASJ 58, 829, *VLBI Observations of the Most Radio-Loud, Narrow-Line Quasar SDSS J094857.3+002225.*

Doi A. et al. 2007, PASJ 59, 703 *Japanese VLBI Network Observations of Radio-Loud Narrow-Line Seyfert 1 Galaxies.*

Dole H. et al. 2006, A&A 451, 517.

Doroshenko V. T., Sergeev S. G., Efimov Yu. S., Klimanov S. A. & Nazarov S. V., 2009, Astron. Lett. 2009, 35, 361, *Comparison of the X-ray and optical variabilities in the Seyfert galaxy 3C 120.*

Duric N. 2004, *Advanced Astrophysics*, Cambridge University Press.

Dwek E. & Arendt R. G. 1998, ApJ 508, L9, *A Tentative Detection of the Cosmic Infrared Background at 3.5μm from COBE/DIRBE Observations.*

Dwek E. & Krennrich F. 2012, APh 43, 112, *The extragalactic background light and the gamma-ray opacity of the universe.*

Ekers R. D. et al. 1989, MNRAS 236, 737, *A complete sample of radio galaxies. I - The radio data.*

Elitzur M. 2011, Proceedings of AGN Physics in the CTA Era (AGN 2011), 30, *Unification and Evolution of AGN.*

Eracleous M., Sambruna R. & Mushotzky R. F. 2000, ApJ 537, 654.

Eracleous M. & Halpern J. P. 2003, ApJ 599, 886, *Completion of a Survey and Detailed*

Study of Double-peaked Emission Lines in Radio-loud Active Galactic Nuclei.

Evans R. D. 1955, *The Atomic Nucleus*, McGraw-Hill.

Evans D. A. et al. 2004, ApJ 612, 786, *Chandra and XMM-Newton Observations of the Nucleus of Centaurus A.*

Evans D. A., Hardcastle M. J., Croston J. H., Worrall D. M. & Birkinshaw 2005, MNRAS 359, 363, *Chandra and XMM-Newton observations of NGC 6251.*

Falcke H., Wilson A. S. & Simpson C. 1998, ApJ 502, 199, *Hubble Space Telescope and VLA Observations of Seyfert 2 Galaxies: the Relationship Between Radio Ejecta and the Narrow-Line Region.*

Fanidakis N. et al. 2012, MNRAS 419, 2797, *The evolution of active galactic nuclei across cosmic time: what is downsizing?*

Fazio G. G. et al. 2004, ApJ 154, 39, *Number Counts at* $3\ \mu m < \lambda < 10\ \mu m$ *from the Spitzer Space Telescope.*

Fegan D. J. 1997, J. Phys. G. Nucl. Part. Phys. 23, 1013, *Topical Review:* γ*/hadron separation at TeV energies.*

Feldman & Cousins 1998, Phys. Rev. D 57, 3873, *A Unified Approach to the Classical Statistical Analysis of Small Signals.*

Fernow R. C. 1989, *Introduction to Experimental Particle Physics*, Cambridge University Press.

Ferrarese L. & Ford H. C. 1999, ApJ 515, 583, *Nuclear Disks of Gas and Dust in Early-Type Galaxies and the Hunt for Massive Black Holes: Hubble Space Telescope Observations of NGC 6251.*

Finke J. D., Dermer C. D. & Böttcher M. 2008, ApJ 686, 181, *Synchrotron Self-Compton Analysis of TeV X-Ray-Selected BL Lacertae Objects.*

Finke J. D. & Razzaque S. 2009, ApJ 698, 1761, *Constraints on the Extragalactic Background Light from very High Energy Gamma-Ray Observations of Blazars.*

Finke J.D., Razzaque S. & Dermer D. 2010, ApJ 712, 238, *Modeling the Extragalactic Background Light from Stars and Dust.*

Fioc M. & Rocca-Volmerange B. 1997, A&A 326, 950, *PEGASE: a UV to NIR spectral evolution model of galaxies. Application to the calibration of bright galaxy counts.*

Fixsen D. J., Dwek E., Mather J. C., Bennett C. L. & Shafer R. A. 1998, ApJ 508, 123, *The Spectrum of the Extragalactic Far-Infrared Background from the COBE FIRAS Observations.*

Fomalont E. B. 1971, ApJ. 76, 513, *Two-dimensional structures of 76 extragalactic radio*

sources at 1425 MHz.

Ford H. C. et al. 1994, ApJ 435, L27, *Narrowband HST images of M87: Evidence for a disk of ionized gas around a massive black hole.*

Forman W. et al. 1978, ApJS 38, 357, *The fourth Uhuru catalog of X-ray sources.*

Foschini L. et al. 2005, A&A 433, 515, *Investigating the EGRET-radio galaxies link with INTEGRAL: The case of 3EG J1621+8203 and NGC 6251.*

Foschini L. et al. 2010, ASPC 427, 243, *Fermi/LAT Discovery of Gamma-Ray Emission from a Relativistic Jet in the Narrow-Line Seyfert 1 Quasar PMN J0948+0022.*

Fossati G., Maraschi L., Celotti A., Comastri A. & Ghisellini G. 1998, MNRAS 299, 433, *A unifying view of the spectral energy distributions of blazars.*

Frank I. M. & Tamm I. E. 1937, Proc. USSR Acadamy of Sciences, 14, 109, *Coherent Visible Radiation of Fast Electrons Passing Through Matter.* Fu H. & Stockton A. 2009, ApJ 690, 953, *Extended Emission-Line Regions: Remnants of Quasar Superwinds?*

Gaensler B. M. & Hunstead R. W. 2000, Publ. Astron. Soc. Aust. 17, 72, *Long-term monitoring of Molonglo calibrators.*

Gaidos J. A. et al. 1996, Nature 383, 319, *Extremely rapid bursts of TeV photons from the active galaxy Markarian 421.*

Gallimore J. F., Baum S. A. & O'Dea C. P. 2004, ApJ 613, 794, *The Parsec-Scale Radio Structure of NGC 1068 and the Nature of the Nuclear Radio Source.*

Georganopoulos M. & Kazanas D. 2003, ApJ 594, L27, *Decelerating Flows in TeV Blazars: A Resolution to the BL Lacertae-FR I Unification Problem.*

Georganopoulos M., Perlman E. S. & Kazanas D. 2005, ApJ 634, L33, *Is the Core of M87 the Source of Its TeV Emission? Implications for Unified Schemes.*

Ghisellini G., Guilbert P. W. & Svensson R. 1988, ApJ 334, L5, *The synchrotron boiler.*

Ghisellini G. & Madau P. 1996, MNRAS 280, 67, *On the origin of the gamma-ray emission in blazars.*

Ghisellini G. et al. 1998, MNRAS 301, 451, *A theoretical unifying scheme for gamma-ray bright blazars.*

Ghisellini G. 2004, Nuclear Physics B 132, 76, *The high energy view of blazars.*

Ghisellini G., Tavecchio F. & Chiaberge M. 2005, A&A 432, 401, *Structured jets in TeV BL Lac objects and radiogalaxies. Implications for the observed properties.*

Ghisellini G. & Tavecchio F. 2008, MNRAS 386, L28, *Rapid variability in TeV blazars: the case of PKS2155-304.*

Ghisellini G. and Tavecchio 2009, MNRAS 397, 985, *Canonical high-power blazars.*

Ghisellini G. et al. 2010, MNRAS 402, 497, *General physical properties of bright Fermi blazars.*

Giannios D., Uzdensky D. A. & Begelman M. C. 2009, MNRAS 395, L29, *Fast TeV variability in blazars: jets in a jet.*

Gilmore R. C., Madau P., Primack J. R., Somerville R. S. & Haardt F. 2009, MNRAS 399, 1694 *GeV gamma-ray attenuation and the high-redshift UV background.*

Giuliani et al. 2008, A&A 491, L25, *AGILE detection of delayed gamma-ray emission from GRB 080514B.*

Gondek D. et al. 1996, MNRAS 282, 646, *The average X-ray/gamma-ray spectrum of radio-quiet Seyfert 1s.*

Goodrich R. W. 1989, ApJ 342, 224, *Spectropolarimetry of 'narrow-line' Seyfert 1 galaxies.*

Goodrich R. W. 1995, ApJ 440, 141, *Dust in the broad-line regions of Seyfert galaxies.*

Gorjian V., Wright E. L. & Chary R. R. 2000, ApJ 536, 550, *Tentative Detection of the Cosmic Infrared Background at 2.2 and 3.5 Microns Using Ground-based and Space-based Observations.*

Gould R. J. & Schréder G. P. 1967, Phys. Rev. 155, 1404, *Opacity of the Universe to High-Energy Photons.*

Govoni F., Falomo R., Fasano G. & Scarpa R. 2000, A&A 353, 507, *The optical properties of low redshift radio galaxies.*

Gracia J., Tsinganos K. & Bogovalov S. V. 2005, A&A 442 L7, *Magnetic collimation of the relativistic jet in M 87.*

Graff P. B., Georganopoulos M., Perlman E. S. & Kazanas D. 2008, ApJ 689, 68, *A Multizone Model for Simulating the High-Energy Variability of TeV Blazars.*

Greene J. E. & Ho L. C. 2005, ApJ 630, 122, *Estimating Black Hole Masses in Active Galaxies Using the Hα Emission Line.*

Greene J. E. & Ho L. C. 2006, ApJ 641, L21, *The $M_{BH} - \sigma_*$ Relation in Local Active Galaxies.*

Greenstein J. 1963, Nature 197, 1041 *Red-Shift of the Unusual Radio Source: 3C 48.*

Gregory P. C., & Condon J. J. 1991, ApJS, 75, 1011, *The 87GB Catalog of radio sources covering delta between O and + 75 deg at 4.85 GHz.*

Griffith M. R., Wright A. E., Burke B. F., & Ekers R. D. 1995, ApJS, 97, 347, *The Parkes-MIT-NRAO (PMN) surveys. 6: Source Catalog for the equatorial survey (-9.5 deg less than delta less than +10.0 deg).*

Griffiths R.E., Briel U., Chaisson L. & Tapia S. 1979, ApJ 234, 810, *Optical and X-ray*

properties of the newly discovered BL Lacertae object PKS 2155-304 (= H2155-304).

Griffiths D. 1987, *Introduction to Elementary Particles*, Wiley.

Grindlay J. E., Helmken H. F., Brown R. H., Davies J. & Allen L. R. 1975, ApJ 197, L9, *Evidence for the detection of gamma rays from Centaurus A at gamma-ray energies above 300 GeV.*

Guainazzi M., Grandi P., Comastri A. & Matt G. 2003, A&A 410, 131, *The hard X-ray view of the low-luminosity blazar in the radio galaxy NGC 6251.*

Haardt F. & Maraschi L. 1993, ApJ 413, 507, *X-ray spectra from two-phase accretion disks.*

Haardt F. et al. 1994, ApJ 432, L95, *A model for the X-ray and ultraviolet emission from Seyfert galaxies and galactic black holes.*

Hardcastle M. J. et al. 2003, ApJ 593, 169, *Radio and X-Ray Observations of the Jet in Centaurus A.*

Hardcastle M. J., Cheung C. C., Feain I. J. & Stawarz, Ł. 2009, MNRAS 393, 1041, *High-energy particle acceleration and production of ultra-high-energy cosmic rays in the giant lobes of Centaurus A.*

Häring-Neumayer N. et al. 2006, ApJ 643, 226, *VLT Diffraction-limited Imaging and Spectroscopy in the NIR: Weighing the Black Hole in Centaurus A with NACO.*

Harms R. J. et al. 1994, ApJ 435, L35, *HST FOS spectroscopy of M87: Evidence for a disk of ionized gas around a massive black hole.*

Harris D. E. et al. 2003, ApJ 586, L41 *Flaring X-Ray Emission from HST-1, a Knot in the M87 Jet.*

Harris D. E. et al. 2006, ApJ 640, 211, *The Outburst of HST-1 in the M87 Jet.*

Harris G. L. H., Rejkuba M., Harris W. E. 2010, PASA 27, 457, *The Distance to NGC 5128 (Centaurus A).*

Hartman R. C. et al. 1999, ApJS 123, 79, *The Third EGRET Catalog of High-Energy Gamma-Ray Sources.*

Hartman R. C., Kadler M. & Tueller J. 2008, ApJ 688, 852, *Gamma-Ray Emission from the Broad-Line Radio Galaxy 3C 111.*

Hasinger G., Miyaji T. & Schmidt M. 2005, A&A 441, 417, *Luminosity-dependent evolution of soft X-ray selected AGN. New Chandra and XMM-Newton surveys.*

Hauser, M. G., et al. 1998, ApJ 508, 25, *The COBE Diffuse Infrared Background Experiment Search for the Cosmic Infrared Background. I. Limits and Detections.*

Hazard C. & Mitton S. 1979, *Active Galactic Nuclei*, Cambridge University Press.

Hilburn G. & Liang E. P. 2012, ApJ 746, 87, *Numerical Modeling of Multi-wavelength*

Spectra of M87 Core Emission.

Hillas A. 1985, Proc. of the 19th ICRC 3, 445, *Electromagnetic and muonic structure of showers initiated by gamma-rays and by hadrons.*

Hinton J. 2009, New J. Phys. 11, 055005, *Ground-based gamma-ray astronomy with Cherenkov telescopes.*

Hjelm M. & Lindblad P. O. 1996, A&A 305, 727, *The nuclear high excitation outflow cone in NGC 1365. A kinematic model.*

Hönig S. F., Prieto M. A. & Beckert T. 2008, A&A 485, 33, *High-spatial resolution SED of NGC 1068 from near-IR to radio. Disentangling the thermal and non-thermal contributions.*

Hopkins P. F. et al. 2005, ApJ 630, 716, *Luminosity-dependent Quasar Lifetimes: A New Interpretation of the Quasar Luminosity Function.*

Horiuchi S., Meier D. L., Preston R. A. & Tingay S. J. 2006, PASJ 58, 211, *Ten Milliparsec-Scale Structure of the Nucleus Region in Centaurus A.*

Hough D. H., Vermeulen R. C. & Readhead A. C. S. 1998, IAU Colloquium 164: Radio Emission from Galactic and Extragalactic Compact Sources, ASPC 144, *First VLBA Images of the Nuclei in 3CR Lobe-dominated Quasars.*

Hughes P. A. 1991, *Beams and Jets in Astrophysics*, Cambridge University Press.

Ioka K. 2003, ApJ 583, 819, *Ultrafast Self-Compton Cooling.*

Israel F. P. 1998, A&A Rev 8, 237, *Centaurus A - NGC 5128.*

Itoh T. et al. 2008, PASJ 60, 251, *Suzaku Wide-Band X-Ray Spectroscopy of the Seyfert2 AGN in NGC 4945.*

Ivezić Ž et al. 2002, AJ 124, 2364, *Optical and Radio Properties of Extragalactic Sources Observed by the FIRST Survey and the Sloan Digital Sky Survey.*

Iwasawa K. et al. 1993, ApJ 409, 155, *X-ray evidence for Seyfert activity buried in the infrared galaxy NGC 4945.*

Jaffe A. et al. 2004, Nature 429, 47, *The central dusty torus in the active nucleus of NGC 1068.*

Jansen F. & Parmer A. N. 2001, ASPC 251, 10, *Status of the XMM-Newton Mission (Invited).*

Jelley J. V. 1958, *Čerenkov Radiation and its Applications*, Pergamon Press.

Jelley J. V. 1987, Very high energy gamma-ray astronomy; Proceedings of the NATO Advanced Research Workshop, 27, *In days of yore.*

Jones F. C. 1968, Phys. Rev. 167, 1159, *Calculated Spectrum of Inverse-Compton-Scattered Photons.*

Jones D. L. et al. 1996, ApJ 466, L63, *Discovery of a Sub-Parsec Radio Counterjet in the Nucleus of Centaurus A.*

Jones D. L. & Wehlre A. E. 2002, ApJ 580, 114, *What Happened to the NGC 6251 Counterjet?*

Jorstad S. G. et al. 2005, AJ 130, 1418, *Polarimetric Observations of 15 Active Galactic Nuclei at High Frequencies: Jet Kinematics from Bimonthly Monitoring with the Very Long Baseline Array.*

Jourdain E. et al. 1993, ApJ 412, 586, *On the hard X-ray variability of Centaurus A.*

Junor W., Biretta J. A. & Livio M. 1999, Nature 401, 891, *Formation of the radio jet in M87 at 100 Schwarzschild radii from the central black hole.*

Kabuki S. et al. 2007, ApJ 668, 968, *CANGAROO III Search for Gamma Rays from Centaurus A and the Centauri Region.*

Kadler M. et al. 2008, ApJ 680, 867, *The Trails of Superluminal Jet Components in 3C 111.*

Kadler et al. 2012, A&A 538, 1, *The blazar-like radio structure of the TeV source IC 310.*

Kameno S., Inoue M., Fujisawa K., Shen Z-Q & Wajima K. 2000, PASJ 52, 1045, *First-Epoch VSOP Observation of 3C 380: Kinematics of the Parsec-Scale Jet.*

Kataoka J. et al. 2000, ApJ 528, 243, *Variability Pattern and the Spectral Evolution of the BL Lacertae Object PKS 2155-304.*

Kataoka J. et al. 2011, ApJ 740, 29, *Broad-line Radio Galaxies Observed with Fermi-LAT: The Origin of the GeV γ-Ray Emission.*

Katarzyński K., Sol H. & Kus A. 2001, A&A 367, 809, *The multifrequency emission of Mrk 501. From radio to TeV gamma-rays.*

Katarzyński K., Sol H. & Kus A. 2003, A&A 410, 101, *The multifrequency variability of Mrk 421.*

Keel W. C. 1996, AJ 111, 696, *Seyfert Galaxies With Companions: Orbital and Kinematic Clues to AGN Triggering.*

Kellerman K. I. et al. 1989, AJ 98, 1195, *VLA observations of objects in the Palomar Bright Quasar Survey.*

Khachikian E. Y. & Weedman D. W. 1974, ApJ 192, 581, *An atlas of Seyfert galaxies.*

Kinkhabwala A. et al. 2002, ApJ 575, 732.

Knödlseder J. et al. 2005, A&A 441, 513, *The all-sky distribution of 511 keV electron-positron annihilation emission.*

Kneiske T. M., Mannheim K. & Hartmann D.H. 2002, A&A 386, 1, *Implications of cosmological gamma-ray absorption. I. Evolution of the metagalactic radiation field.*

Kneiske T. M., Bretz T., Mannheim K. & Hartmann D. H. 2004, A&A 413, 807, *Implications of cosmological gamma-ray absorption. II. Modification of gamma-ray spectra.*

Komissarov S. S., Falle S. A. E. G. 1997, MNRAS 288, 833, *Simulations of Superluminal Radio Sources.*

Komossa S. & Schulz H. 1998, A&A 339, 345, *The ROSAT view of NGC 1365 and the luminous highly variable off-nuclear X-ray source NGC 1365-X1.*

Komossa S. et al. 2006, AJ 132, 531, *Radio-loud Narrow-Line Type 1 Quasars.*

Kovalev Y. Y., Lister M. L., Homan D. C. & Kellermann, K. 2007, ApJ 668, L27, *The Inner Jet of the Radio Galaxy M87.*

Kraft R. P. et al. 2001, ApJ 560, 675, *Chandra Observations of the X-Ray Point Source Population in Centaurus A.*

Krawczynski H. et al. 2001, ApJ 559, 187, *Simultaneous X-Ray and TeV Gamma-Ray Observation of the TeV Blazar Markarian 421 during 2000 February and May.*

Krawczynski H. et al. 2004, ApJ 601, 151, *Multiwavelength Observations of Strong Flares from the TeV Blazar 1ES 1959+650.*

Kristen H. et al. 1997, A&A 328, 483, *Imaging the nuclear environment of NGC 1365 with the Hubble Space Telescope.*

Krivonos R. et al. 2007, A&A 475, 775, *INTEGRAL/IBIS all-sky survey in hard X-rays.*

Kukula M. J. et al. 1999, ApJ 518, 117, *Parsec-Scale Radio Structures in the Nuclei of Four Seyfert Galaxies.*

Laing R. A. & Bridle A. H. 2002, MNRAS 336, L328, *Relativistic models and the jet velocity field in the radio galaxy 3C 31.*

Laing R. A., Riley J. M. & Longair M. S. 1983, MNRAS 204, 151, *Bright radio sources at 178 MHz - Flux densities, optical identifications and the cosmological evolution of powerful radio galaxies.*

Lal D. V., Shastri P. & Gabuzda D. C. 2004, A&A 425, 99, *Milliarcsec-scale radio structure of a matched sample of Seyfert 1 and Seyfert 2 galaxies.*

Laor A. 2000, ApJ 543, L111, *On Black Hole Masses and Radio Loudness in Active Galactic Nuclei.*

Lawson A. J., McHardy I. M. and Newsam A. M. 1999, Nuclear Physics B, 69, 439, *RXTE monitoring of the blazars 3C 279 and 3C 273.*

Le Bohec S. et al. 2004, ApJ 610, L156, *Observation of M87 at 400 GeV with the Whipple 10 Meter Telescope.*

León-Tavares J. et al. 2010, ApJ 715, 355, *Relativistic Plasma as the Dominant Source of*

the Optical Continuum Emission in the Broad-Line Radio Galaxy 3C 120.

Lebofsky M. J. & Rieke G. H. 1980, Nature 284, 410, *Variations in the thermal emission of Seyfert galaxies.*

Leighly K. M. 1999, ApJS, 125, 297, *A Comprehensive Spectral and Variability Study of Narrow-Line Seyfert 1 Galaxies Observed by ASCA. I. Observations and Time Series Analysis.*

Leipski C. & Bennert N. 2006, A&A 448, 165, *[O III] profile substructure in radio-quiet quasars.*

Leipski C., Antonucci R., Ogle P. & Whysong D. 2009, ApJ 701, 891, *The Spitzer View of FR I Radio Galaxies: On the Origin of the Nuclear Mid-Infrared Continuum.*

Lemoine-Goumard M., Degrange B. & Tluczykont M. 2006, APh 25, 195L, *Selection and 3D-reconstruction of gamma-ray-induced air showers with a stereoscopic system of atmospheric Cherenkov telescopes.*

Lenain J.-P., Boisson C. & Sol H. 2008, IJMPD 17, 1577, *SSC Scenario for Tev Emission from Non-Blazar AGNs.*

Lenain J.-P., Boisson C., Sol H. & Katarzyński K. 2008 A&A 478, 111, *A synchrotron self-Compton scenario for the very high energy γ-ray emission of the radiogalaxy M 87: Unifying the TeV emission of blazars and other AGNs?*

Lenain J.-P., Medina M. C., Boisson C., Romero G. E., Sol H. & Zech A. 2009, Proc. 31st ICRC; arXiv:0907.2258, *A synchrotron self-Compton model for the VHE gamma-ray emission from Cen A.*

Lenain J. P., Ricci C., Türler M., Dorner D. & Walter R. 2010, A&A 524, L72, *Seyfert 2 galaxies in the GeV band: jets and starburst.*

Lester D. F. et al. 1987, ApJ 321, 755, *Far-infrared continuum emission from the nucleus, starburst, and extended spiral arms of NGC 1068.*

Levinson A. 2000, Phys. Rev. Lett. 85, 912, *Particle Acceleration and Curvature TeV Emission by Rotating, Supermassive Black Holes.*

Levenson L. R., Wright E. L. & Johnson B. D. 2007, ApJ 666, 34.

Levenson L. R. & Wright E. L. 2008, ApJ 683, 585, *DIRBE Minus 2MASS: Confirming the CIRB in 40 New Regions at 2.2 and 3.5 μm.*

Lewis K. T., Eracleous M., Gliozzi M., Sambruna R. M. & Mushotzky R. F. 2005, ApJ 622, 816, *A Simultaneous RXTE and XMM-Newton Observation of the Broad-Line Radio Galaxy 3C 111.*

Li T.-P. & Ma Y.-Q. 1983, ApJ 272, 317, *Analysis methods for results in gamma-ray*

astronomy.

Li L. & Paczyński B. 2000, ApJ 534, L197, *Extracting Energy from Accretion into a Kerr Black Hole.*

Lister M. L. et al. 2009, AJ 137, 3718, *MOJAVE: Monitoring of Jets in Active Galactic Nuclei with VLBA Experiments. V. Multi-Epoch VLBA Images.*

Lloyd C. 1984, MNRAS 209, 697, *Optical monitoring of radio sources.*

Longair M. S. 1981, *High Energy Astrophysics: Volume 1 - Particles, photons and their detection*, Cambridge University Press.

Ly C., Walker R. & Wrobel J. M. 2004, AJ 127, 119, *An Attempt to Probe the Radio Jet Collimation Regions in NGC 4278, NGC 4374 (M84), and NGC 6166.*

Ly C., Walker R. & Junor W. 2007, ApJ 660, 200, *High-Frequency VLBI Imaging of the Jet Base of M87.*

Mészáros P. 1992, *High Energy Radiation from Magnetized Neutron Stars*, The University of Chicago Press.

Monet, D. G., et al. 2003, AJ, 125, 984, *The USNO-B Catalog*

Mücke A. et al. 2000, Comp. Phys. Comm. 124, 290, *Monte Carlo simulations of photo-hadronic processes in astrophysics.*

Mücke A. & Protheroe R. J. 2000, AIP Conf. Proc. 515, 149, *Modeling the April 1997 flare of Mkn 501.*

Mücke A. & Protheroe R. J. 2001, Aph 15, 121, *A proton synchrotron blazar model for flaring in Markarian 501.*

Mücke A. et al. 2003, Astropart. Phys. 18, 593, *BL Lac objects in the synchrotron proton blazar model.*

Macchetto F. et al. 1997, ApJ 489, 579, *The Supermassive Black Hole of M87 and the Kinematics of Its Associated Gaseous Disk.*

Madau P. et al. 1994, MNRAS 270, L17, *The Unified Seyfert Scheme and the Origin of the Cosmic X-Ray Background.*

Madau P. & Pozzetti L. 2000, MNRAS 312, L9, *Deep galaxy counts, extragalactic background light and the stellar baryon budget.*

Majumdar P. 2011, Proc. 32nd ICRC; arXiv:1109.6000, *Observation of selected IBLs and LBLs with VERITAS.*

Malizia A. et al. 2007, ApJ 668, 81, *Swift XRT Observation of 34 New INTEGRAL IBIS AGNs: Discovery of Compton-Thick and Other Peculiar Sources.*

Maltby P., Matthews T. A. & Moffet A. T. 1963, ApJ 137, 153, *Brightness Distribution in*

Discrete Radio Sources.IV. a Discussion of 24 Identified Sources.

Mannheim K. 1993, A&A 269, 67, *The proton blazar.*

Marchesini D., Celotti A. & Ferrarese L. 2004, MNRAS 351, 733, *[*A transition in the accretion properties of radio-loud active nuclei].

Marconi A. et al. 2000, ApJ 665, 209.

Marconi A. et al. 2001, ApJ, 549, 915, *Peering through the Dust: Evidence for a Supermassive Black Hole at the Nucleus of Centaurus A from VLT Infrared Spectroscopy.*

Marconi A. et al. 2006, A&A 528, 276, *Unveiling the Active Nucleus of Centaurus A.*

Marisaldi M. et al. 2008, A&A 490, 1151, *Gamma-ray burst detection with the AGILE mini-calorimeter.*

Markarian B. E., Lipovetskij V. A. & Stepanian J. A. 1977, Astrofizika, 13, 116, *Galaxies with ultraviolet continuum. X.*

Marscher A. P. & Gear W. K. 1985, ApJ 298, 114, *Models for high-frequency radio outbursts in extragalactic sources, with application to the early 1983 millimeter-to-infrared flare of 3C 273.*

Marscher A. P. et al. 2002, Nature 417, 625, *Observational evidence for the accretion-disk origin for a radio jet in an active galaxy.*

Marsden G. et al. 2009, ApJ 707, 1729, *BLAST: Resolving the Cosmic Submillimeter Background.*

Martí J., Mirabel I. F., Chaty S. & Rodriguez L. F. 1998, A&A 330, 72, *The hard X-ray source GRS 1734-292: a Seyfert 1 galaxy behind the Galactic Center.*

Masetti N. et al. 2006a, A&A 449a, 1139, *Unveiling the nature of INTEGRAL objects through optical spectroscopy. III. Observations of seven southern sources.*

Masetti N. et al. 2006b, A&A 459, 21, *Unveiling the nature of INTEGRAL objects through optical spectroscopy. V. Identification and properties of 21 southern hard X-ray sources.*

Mazin D. & Raue M. 2007, A&A 471, 439, *New limits on the density of the extragalactic background light in the optical to the far infrared from the spectra of all known TeV blazars.*

McKinney J. C. 2006, MNRAS 368, 1561, *General relativistic magnetohydrodynamic simulations of the jet formation and large-scale propagation from black hole accretion systems.*

Meegan C. et al. 2009, ApJ 702, 791, *The Fermi Gamma-Ray Burst Monitor.*

Meisenheimer K. et al. 2007, A&A 471, 453, *Resolving the innermost parsec of Centaurus A at mid-infrared wavelengths.*

Metcalf R. B. & Magliocchetti M. 2006, MNRAS 365, 101, *The role of black hole mass in quasar radio activity.*

Metcalfe L., et al. 2003, A&A 407, 791, *An ISOCAM survey through gravitationally lensing galaxy clusters. I. Source lists and source counts for A370, A2218 and A2390.*

Middelberg E. et al. 2004, A&A 417, 925, *Motion and properties of nuclear radio components in Seyfert galaxies seen with VLBI.*

Migliori G. et al. 2011, A&A 533 A72, *Implications for the structure of the relativistic jet from multiwavelength observations of NGC 6251.*

Miller J. S. & Antonucci R. R. J. 1983, ApJ 271, L7, *Evidence for a highly polarized continuum in the nucleus of NGC 1068.*

Mills B. 1960, Australian J. Phys. 13, 550, *On the Identification of Extragalactic Radio Sources.*

Mimica P., Aloy M. A., Müller E. & Brinkmann W. 2004, A&A 418, 947, *Synthetic X-ray light curves of BL Lacs from relativistic hydrodynamic simulations.*

Miyoshi S. et al. 1988, PASJ, 40, 127, *X-ray observations of IC 4329.*

Moiseev A. 2011, Nucl. Instrum. Meth. Phys. A 630, 1, *Possible interpretations of the high energy cosmic ray electron spectrum measured with the Fermi space telescope.*

Molendi S., Bianchi S. & Matt G. et al. 2003, MNRAS 343, L1, *Iron and nickel line properties in the X-ray-reflecting region of the Circinus galaxy.*

Momjian E. et al. 2003, ApJ 597, 809, *Sensitive VLBI Continuum and H I Absorption Observations of NGC 7674: First Scientific Observations with the Combined Array VLBA, VLA, and Arecibo.*

Moran J. M. et al. 1990, ApJ 348, 147, *The large scattering disk of NGC 6334B.*

Morganti R. et al. 1999, A&AS 137, 457, *Radio continuum morphology of southern Seyfert galaxies.*

Moudden Y. et al. 2011, APh 34, 568, *The topological second-level trigger of the HESS phase 2 telescope.*

Mukherjee R., Halpern J., Mirabel N. & Gotthelf E. V. 2002, ApJ 574, 693, *Is the EGRET Source 3EG J1621+8203 the Radio Galaxy NGC 6251?*

Muraishi H. et al. 2000, A&A 354, 57, *Evidence for TeV gamma-ray emission from the shell type SNR RX J1713.7-3946.*

Nagar N. M. et al. 2001, ApJ 559, 87, *Evidence for Jet Domination of the Nuclear Radio Emission in Low-Luminosity Active Galactic Nuclei.*

Nakase T. et al. 2003, Proc. of the 28th ICRC 2587, *TeV Gamma-Ray Observations of Southern Hemisphere BL Lacertae Objects with CANGAROO-II/III Telescope.*

Nandra K. et al. 1998, ApJ 505, 594, *New Constraints on the Continuum Emission*

Mechanism of Active Galactic Nuclei: Intensive Monitoring of NGC 7469 in the X-Ray and Ultraviolet.

Nandra K. et al. 2000, ApJ 544, 734, *The Origin of the X-Ray and Ultraviolet Emission in NGC 7469.*

Neronov A. & Aharonian F. A. 2007, ApJ 671, 85, *Production of TeV Gamma Radiation in the Vicinity of the Supermassive Black Hole in the Giant Radio Galaxy M87.*

Neronov A., Semikoz D. & Vovk Ie. 2010, A&A 519, L6, *Very high-energy -ray emission from IC 310.*

Netzer H. & Laor A. 1993, ApJ 404, L51, *Dust in the narrow-line region of active galactic nuclei.*

Nishijima K. et al. 2001, Proc. of the 27th ICRC 2626, *Very High Energy Gamma-Ray Observation of Southern AGNs with CANRAGOO-II Telescope.*

Nolan P. L. et al. 2012, ApJS 199, 31, *Fermi Large Area Telescope Second Source Catalog.*

Nolan S. J., Pühlhofer G. & Rulten C. B. 2010, APh 34, 304, *Detailed studies of atmospheric calibration in imaging Cherenkov astronomy.*

Ogle P. M. et al. 2003, A&A 402, 849, *Testing the Seyfert unification theory: Chandra HETGS observations of NGC 1068.*

Ogle P. M. et al. 2005, ApJ 618, 139, *Testing the Seyfert unification theory: Chandra HETGS observations of NGC 1068.*

Ohm S., van Eldik C. & Egberts K 2009, Astropart. Phys. 31, 383, *γ/hadron separation in Very-High-Energy γ-ray astronomy using a multivariate analysis method.*

Orienti M. & Prieto M. A. 2010, MNRAS 401, 2599, *Radio structures of the nuclei of nearby Seyfert galaxies and the nature of the missing diffuse emission.*

Osterbrock D. E. 1977, ApJ 215, 733, *Spectrophotometry of Seyfert 1 galaxies.*

Osterbrock D. E. 1978, PNAS 75, 540, *Observational Model of the Ionized Gas in Seyfert and Radio-Galaxy Nuclei.*

Osterbrock D. E. 1981, ApJ 249, 462, *Seyfert galaxies with weak broad H alpha emission lines.*

Osterbrock D. E. & Pogge R. W. 1985, ApJ 297, 166, *The spectra of narrow-line Seyfert 1 galaxies.*

Osterbrock D. E. & Ferland G. J. 2006, *Astrophysics of Gaseous Nebulae and Active Galactic Nuclei*, University Science Books.

Owen F. N., Eilek J. A. & Kassim N. E. 2000, ApJ 543, 611, *M87 at 90 Centimeters: A Different Picture.*

Pacciani L. et al. 2009, A&A 494, 49, *AGILE observation of a gamma-ray flare from the blazar 3C 279.*

Padmanabhan T. 2000, *Theoretical Astrophysics: Volume 1 - Astrophysical Processes*, Cambridge University Press.

Papovich C. et al. 2004, ApJS 154, 70, *The 24 Micron Source Counts in Deep Spitzer Space Telescope Surveys.*

Paturel G. et al. 2002, LEDA, 0, *Comparison LEDA/SIMBAD octobre 2002. Catalogue to be published in 2003..*

Pavlinsky M. N., Grebenev S. A. & Sunyaev R. A. 1992, SvA 18, 88, *The new X-ray sources GRS1734 - 292, GRS1736 - 297, and GRS1747 - 312, discovered with the ART-P telescope onboard the GRANAT Observatory in the region of the Galactic center.*

Pellizzoni A. et al. 2009, ApJ 695, 115, *Discovery of New Gamma-Ray Pulsars with AGILE.*

Pellizzoni A. et al. 2010, Science 327, 663, *Detection of Gamma-Ray Emission from the Vela Pulsar Wind Nebula with AGILE.*

Perley R. A., Dreher J. W. & Cowan J. J. 1984, ApJ 285, L35, *The jet and filaments in Cygnus A.*

Perlman E. S. & Wilson A. S. 2005, ApJ 627, 140, *The X-Ray Emissions from the M87 Jet: Diagnostics and Physical Interpretation.*

Peterson B. M. 1997, *An Introduction to Active Galactic Nuclei*, Cambridge University Press.

Peterson B. M. 2006, Physics of Active Galactic Nuclei at all Scales: Lecture Notes in Physics 693, 77, *The Broad-Line Region in Active Galactic Nuclei.*

Petry D. et al. 2009, A&A 507, 549, *Soft gamma-ray sources detected by INTEGRAL.*

Phillips S. 2005, *The Structure & Evolution of Galaxies*, Wiley.

Piccinotti G. et al. 1982, ApJ 253, 485, *A complete X-ray sample of the high-latitude ($|b| > 20°$) sky from HEAO 1 A-2 - $\log N - \log S$ and luminosity functions.*

Piconcelli E. et al. 2006, A&A 453, 839, *4U 1344-60: a bright intermediate Seyfert galaxy at $z = 0.012$ with a relativistic Fe Kα emission line.*

Pittori C. 2012, Mem. S.A.It. 83, 186, *AGILE highlights.*

Polatidis A. G. & Wilkinson P. N. 1998, MNRAS 294, 327, *Superluminal motion in the parsec-scale jet in 3C 380.*

Preuss E., Alef W. & Kellermann K. I. 1988, Proceedings of the 129th IAU Symp. Cambridge, MA, May 10-15, 1987 (Kluwer Academic Publishers), 105, *The Impact of VLBI on Astrophysics and Geophysics.*

Punch M. et al. 1992, Nature 358, 477, *Detection of TeV photons from the active galaxy Markarian 421.*

Razzaque, S., Dermer, C. D. & Finke, J. D. 2009, ApJ 697, 483, *The Stellar Contribution to the Extragalactic Background Light and Absorption of High-Energy Gamma Rays.*

Reid M. J. et al. 1989, ApJ 336, 112, *Subluminal motion and limb brightening in the nuclear jet of M87.*

Reimer A., Protheroe R. J. & Donea A.-C. 2004, A&A 419, 89, *M 87 as a misaligned synchrotron-proton blazar.*

Reimer A., Pohl M. & Reimer O. 2006, ApJ 644 1118, *Nonthermal High-Energy Emission from Colliding Winds of Massive Stars.*

Reynolds C. S. et al. 1996, MNRAS 283, L111, *The 'quiescent' black hole in M87.*

Reynolds C. S., Iwasawa K., Crawford C. S. & Fabian A. C. 1998, MNRAS 299, 410, *X-ray spectroscopy of the broad-line radio galaxy 3C 111.*

Rieger F. M. & Duffy P. 2004, ApJ 617, 155, *Shear Acceleration in Relativistic Astrophysical Jets.*

Rieger F. M. & Aharonian F. A. 2008a, AIP Conf. Proc. 1085, 640, *On the Origin of VHE Gamma-Ray Emission in M87.*

Rieger F. M. & Aharonian F. A. 2008b, Int. J. Mod. Phys. D 17, 1569, *Particle Acceleration Close to the Supermassive Black Hole Horizon:. the Case of M87.*

Rieger F. M. & Aharonian F. A. 2009, A&A 506, L41, *Centaurus A as TeV γ-ray and possible UHE cosmic-ray source.*

Risaliti G. et al. 2007, ApJ 659, L111, *Occultation Measurement of the Size of the X-Ray-emitting Region in the Active Galactic Nucleus of NGC 1365.*

Risaliti G. et al. 2009, MNRAS 393, L1, *The XMM-Newton long look of NGC 1365: uncovering of the obscured X-ray source.*

Roberts M. D. et al. 1999, A&A 343, 691, *TeV gamma-ray observations of three X-ray selected BL Lacs.*

Romano P. 2012, Mem. S. A. It. Suppl. 19, 306, *Swift: The science across the rainbow. Mission Overview and Highlights of Results.*

Romero G. E., Benaglia P. & Combi J. A. 1997, A&AS 124, 307, *Variability observations of selected southern extragalactic radio sources.*

Rowell G. P. et al. 1999, Aph 11, 217, *TeV observations of Centaurus A.*

Rulten C. 2012, *Performance studies for the Cherenkov Telescope Array (CTA) with prospects for detecting pulsed gamma-ray emission*, Ph. D. Thesis. University of Durham:

UK;(http://etheses.dur.ac.uk/2047/).

Rybicki G. B. and Lightman, A.P. 1979, *Radiative Processes in Astrophysics*, Wiley-VCH.

Sadler E. M. et al. 1995, MNRAS 276, 1373, *Parsec-scale radio cores in spiral galaxies.*

Sahu S., Zhang B., & Fraija N. 2012, Phys. Rev. D 85, 043012, *Hadronic-origin TeV γ-rays and ultrahigh energy cosmic rays from Centaurus A.*

Salvi N. J. et al. 2002, MNRAS 335, 177.

Sambruna R. M. 1997, ApJ 487, 536, *Soft X-ray Properties of Flat-Spectrum Radio Quasars.*

Sanders R. H. 1983, ApJ 266, 73, *The reconfinement of jets.*

Sandqvist A., Joersaeter S. & Lindblad P. O. 1995, A&A 295, 585, *The central region of NGC 1365. VLA and SEST observations of the radio continuum and CO.*

Sazonov S. Yu. et al. 2004, A&A 421, L21, *Broadband X-ray spectrum of GRS 1734-292, a luminous Seyfert 1 galaxy behind the Galactic Center.*

Schiminovich D., van Gorkom J. H., van der Hulst J. M. & Kasow S. 1994, ApJ 423, L101, *Discovery of Neutral Hydrogen Associated with the Diffuse Shells of NGC 5128 (Centaurus A).*

Schlickeiser R. 1996, A&AS 120, 481, *Models of high-energy emission from active galactic nuclei.*

Schmidt M. 1963, Nature 197, 1040, *3C 273: A Star-Like Object with Large Red-Shift.*

Schmidt M. 1965, ApJ. 141, 1, *Optical Spectra and Redshifts of 31 Radio Galaxies.*

Schmidt M. & Green R. F. 1983, ApJ 269, 352, *Quasar evolution derived from the Palomar bright quasar survey and other complete quasar surveys.*

Schnopper H. W. et al. 1978, ApJ 222, L91, *X-ray and radio emission from the compact galaxy III ZW 2.*

Schulz H. et al. 1999, A&A 346, 764, *Clues on the obscured active nucleus of NGC 1365.*

Scott J. et al. 2000, ApJS 130, 67, *A Uniform Analysis of the Lyα Forest at z = 0-5. II. Measuring the Mean Intensity of the Extragalactic Ionizing Background Using the Proximity Effect.*

Setti G. & Woltjer L. 1989, A&A 224, L21, *Active Galactic Nuclei and the spectrum of the X-ray background.*

Seyfert C. K. 1943, ApJ 97, 28, *Nuclear Emission in Spiral Nebulae.*

Sguera V. et al. 2005, A&A 430, 107, *Is 3C 111, an apparently normal radio galaxy, the counterpart of 3EG J0416+3650?*

Shi Y. et al. 2005, ApJ 629, 88, *Far-Infrared Observations of Radio Quasars and FR II Radio Galaxies.*

Shu F. H. 1991, *The Physics of Astrophysics: Volume 1 - Radiation*, University Science Books

Siebert J. et al. 1996, MNRAS 279, 1331, *The soft X-ray properties of a complete sample of radio sources.*

Sikora M., Begelman M. C., Madejski G. M. & Lasota J.-P. 2005, ApJ 625, 72, *Are Quasar Jets Dominated by Poynting Flux?*

Sitarek J. & Bednarek W. 2012, Phys. Rev. D 86, 063011, *GeV-TeV gamma rays and neutrinos from the Nova V407 Cygni.*

Sokolov A., Marscher A. P. & McHardy I. A. 2004, ApJ 613, 725, *Synchrotron Self-Compton Model for Rapid Nonthermal Flares in Blazars with Frequency-dependent Time Lags.*

Spada M., Ghisellini G., Lazzati D. & Celotti A. 2001, MNRAS 325, 1559, *Internal shocks in the jets of radio-loud quasars.*

Sparke L. S. & Gallagher J. S. 2000, *Galaxies in the Universe: An Introduction*, Cambridge University Press.

Sparks W. B., Fraix-Burnet D., Macchetto F. & Owen F. N. 1992, Nature 355, 804, *A counterjet in the elliptical galaxy M87.*

Sparks W. B. et al. 1995, ApJ 450, L55, *Discovery of an Optical Synchrotron Jet in 3C 78.*

Spinrad H., Marr J., Aguilar L. & Djorgovski S. 1985, PASP 97, 932, *A third update of the status of the 3CR sources - Further new redshifts and new identifications of distant galaxies.*

Sreekumar P., Bertsch D. L., Hartman R. C., Nolan P. L. & Thompson D. J. 1999, APh 11, 221, *GeV emission from the nearby radio galaxy Centaurus A.*

Stawarz Ł. et al. 2006a, MNRAS 370, 981, *Dynamics and high-energy emission of the flaring HST-1 knot in the M 87 jet.*

Stawarz Ł., Aharonian F., Wagner S. & Ostrowski M 2006b, MNRAS 371, 1705, *Absorption of nuclear γ-rays on the starlight radiation in FR I sources: the case of Centaurus A.*

Stecker F. W., Malkan M. A. & Scully S. T. 2006, ApJ 648, 774, *Intergalactic Photon Spectra from the Far-IR to the UV Lyman Limit for $0 < z < 6$ and the Optical Depth of the Universe to High-Energy Gamma Rays.*

Steinle H. et al. 1998, A&A 330, 97, *COMPTEL observations of Centaurus A at MeV energies in the years 1991 to 1995.*

Stephen J. B. et al. 2005, A&A 432, l49, *Using the ROSAT Bright Source Catalogue to find counterparts for IBIS/ISGRI survey sources.*

Stiavelli M., Biretta J., Møller P. & Zeilinger W. W. 1992, Nature 355, 802, *Optical counterpart of the east radio lobe of M87.*

Striani E. et al. 2010, ApJ 718, 455, *The Extraordinary Gamma-ray Flare of the Blazar 3C 454.3.*

Sudou H. et al. 2000, PASJ 52, 989, *Sub-Parsec-Scale Acceleration of the Radio Jet in the Powerful Radio Galaxy NGC 6251.*

Svensson R. 1996, A&AS 120 475, *Models of X-ray and -ray emission from Seyfert galaxies.*

Swanenburg B. N. et al. 1978, Nature 275, 298, *COS B observation of high-energy gamma radiation from 3C273.*

Takeuchi Y. et al. 2012, ApJ 749, 66, *Suzaku X-Ray Imaging of the Extended Lobe in the Giant Radio Galaxy NGC 6251 Associated with the Fermi-LAT Source 2FGL J1629.4+8236*

.

Tavani M. et al. 2009a, A&A 502, 995, *The AGILE Mission.*

Tavani M. et al. 2009b, ApJ 698, L142, *Detection of Gamma-Ray Emission from the Eta-Carinae Region.*

Tavani M. et al. 2009c, Nature 462, 620, *Extreme particle acceleration in the microquasar CygnusX-3.*

Tavani M. et al. 2011, Science 331, 736, *Discovery of Powerful Gamma-Ray Flares from the Crab Nebula*

Tavecchio F. & Ghisellini G. 2008, MNRAS 385, L98, *Spine-sheath layer radiative interplay in subparsec-scale jets and the TeV emission from M87.*

Tavecchio F. & Ghisellini G. 2009, MNRAS 394, L131, *3C 66B as a TeV radio galaxy.*

Thean A. et al. 2000, MNRAS 314, 573, *High-resolution radio observations of Seyfert galaxies in the extended 12-μm sample - I. The observations.*

Thronson H. et al. 1989, ApJ 343, 158, *Near-infrared image of NGC 1068 - Bar-driven star formation and the circumnuclear composition.*

Tibolla O. et al. 2009, Fermi Symposium (Washington D. C.), eConf Proceedings C091122; arxiv:0912.3811.

Tibolla O. 2012, Proc. 13th ICATPP; arXiv:1201.2295, *New unidentified Galactic H.E.S.S. sources.*

Tingay S. J. et al. 1998, AJ 115, 960, *The Subparsec-Scale Structure and Evolution of Centaurus A: The Nearest Active Radio Galaxy.*

Tingay S. J. & Murphy D. W. 2001, ApJ 546, 210, *Estimates of the Free-Free Optical Depth toward the Subparsec-Scale Radio Source in Centaurus A.*

Tingay S. J., Preston R. A. & Jauncey D. L. 2001, AJ 122, 1697, *The Subparsec-Scale Structure and Evolution of Centaurus A. II. Continued Very Long Baseline Array Monitoring.*

Trippe M. L. et al. 2010, ApJ 725, 1749, *A Multi-wavelength Study of the Nature of Type 1.8/1.9 Seyfert Galaxies.*

Trussoni E. et al. 1999a, Mem. S.A.It. 70, 141, *X-ray observation of the FR-I radiogalaxy 3C 78.*

Trussoni E. et al. 1999b, A&A 348, 437, *X-ray observations of low-power FR I radio galaxies.*

Turner T., Urry C. M. & Mushotzky R. F. 1993, ApJ 418, 653, *Position Sensitive Proportional Counter Soft X-Ray Observations of Seyfert 2 Galaxies.*

Ulvestad J. S. & Wilson A. S. 1984a, ApJ 285, 439, *Radio structures of Seyfert galaxies. VI - VLA observations of a nearby sample.*

Ulvestad J. S. & Wilson A. S. 1984b, ApJ 278, 544, *Radio structures of Seyfert galaxies. V - A flux-limited sample of Markarian galaxies.*

Ulvestad J. S. et al. 1987, AJ 93, 22, *Radio structure in the inner 1 arcsecond of NGC 1068.*

Ulvestad J. S. et al. 1998, ApJ 496, 196, *A Subparsec Radio Jet or Disk in NGC 4151.*

Ungerer V., Nguyen-Quang-Rieu, Mauron N. & Brillet J. 1985, A&A 146, 123, *The Taurus dark cloud around the position of 3C 111 - an optical and C-18O line study.*

Urry C. M. 1995, PASP 107, 803, *Unified Schemes for Radio-Loud Active Galactic Nuclei.*

Vaks V. G. & Ioffe B.L. 1958, Il Nuovo Cimento 10, 342, *On* $\pi \rightarrow e + \nu + \gamma$ *Decay.* Valtaoja E. & Teräsranta 1995, A & A 297, L13, *Gamma radiation from radio shocks in AGN jets.*

van Gorkom J. H., van der Hulst J. M., Haschick A. D. & Tubbs A. D. 1990, AJ 99, 1781, *Gamma radiation from radio shocks in AGN jets.*

Vassiliev V. V. 2000, Aph 12, 217, *Extragalactic background light absorption signal in the TeV gamma-ray spectra of blazars.*

Veilleux S. et al. 2003, AJ 126, 2185, *A Search for Very Extended Ionized Gas in Nearby Starburst and Active Galaxies.*

Véron-Cetty M. -P. & Véron P. 2000, A Catalogue of Quasars and Active Galactic Nuclei (9th ed.; Garching: ESO).

Veron-Cetty M.-P. & Veron P. 1998, Scientific Report of ESO, No. 18, *Quasars and Active Galactic Nuclei (8th Ed.).*

Vestergaard M. & Peterson B. M. 2006, ApJ 641, 689, *Determining Central Black Hole Masses in Distant Active Galaxies and Quasars. II. Improved Optical and UV Scaling Relationships.*

Vestrand W. T., Stacy J. G. & Sreekumar P. 1995, ApJ 454, L93, *High-Energy Gamma Rays from the BL Lacertae Object PKS 2155-304.*

Villata M. & Raiteri C. 1999, A&A 347, 30, *Helical jets in blazars. I. The case of MKN 501.*

Voges W. 1992, Proc. of the ISY Conference, Space Sciences, ESA-3, ESA Publications, 9, *The ROSAT all-sky X ray survey.*

von Montigny C. et al. 1997, ApJ 483, 161, *Multiwavelength Observations of 3C 273 in 1993-1995.*

Wagner R. M. 2008, MNRAS 385, 119, *Synoptic studies of 17 blazars detected in very high-energy γ-rays.*

Wagner R. M. et al. 2009, Proc. 31st ICRC, arXiv:0907.1465, *A first joint M87 campaign in 2008 from radio to TeV gamma-rays.*

Walker R. C., Ly C., Junor W. & Hardee P. J. 2008, J. Phys. Conf. Ser. 131, 012053, *A VLBA movie of the jet launch region in M87.*

Wandel A. & Urry C. M. 1991, ApJ 367, 78, *Accretion disk emission from a BL Lacertae object.*

Wang T., Brinkmann W. & Bergeron, J. 1996, A&A 309, 81, *X-ray properties of active galactic nuclei with optical FeII emission.*

Wang J. et al. 2009, ApJ 694, 718, *Imaging the Circumnuclear Region of NGC 1365 with Chandra.*

Warwick R. S. et al. 1988, MNRAS 232, 551, *A survey of the galactic plane with EXOSAT.*

Weekes T. C. 2003, *Very High Energy Gamma-Ray Astronomy*, CRC Press.

Weinstein A. 2011, Proc. 32nd ICRC; arXiv:1111.2093 *Recent Observations of Supernova Remnants with VERITAS.*

White R. L., & Becker R. H. 1992, ApJS, 79, 331, *A new Catalog of 30,239 1.4 GHz sources.*

Wilkinson P.N., Booth R. S., Cornwell T. J. & Clarke R. R. 1984, Nature 308, 619, *Peculiar radio structure in the quasar 3C380.*

Wilkinson P. N., Akujor E. C., Cornwell T. J. & Saikia D. J. 1991, MNRAS 248, 86, *3C380 - A powerful radio source seen end-on?*

Wills K. A., Morganti R., Tadhunter C. N., Robinson T. G. & Villar-Martín M. 2004, MNRAS 347, 771, *Emission lines and optical continuum in low-luminosity radio galaxies.*

Wilson M. J. & Falle S. A. E. G. 1985, MNRAS 216, 971, *Steady jets.*

Winkler P. F. Jr. & White A. E. 1975, ApJ 199, L139, *A sudden increase in the X-ray flux from Centaurus A.*

Winkler C. 2007, Proc. of the VI INTEGRAL Workshop 2006 (Moscow) 622, 3, *INTEGRAL - Overview and Current Status*

Winkler C. 2011, Proc. of The Extreme and Variable High Energy Sky, arxiv:1110.6094 *INTEGRAL status of the mission.*

Wright E. L. & Reese E. D. 2000, ApJ 545, 43, *Detection of the Cosmic Infrared Background at 2.2 and 3.5 Microns Using DIRBE Observations.*

Wrobel J. M. 1984, ApJ 284, 531, *Radio continuum activity in the elliptical galaxy NGC 1052.*

Yang, Y. et al. 2009, ApJ 691, 131, *Suzaku Observations of the Circinus Galaxy.*

Young A. J., Wilson A. S. & Shopbell, P. L. 2001, ApJ 556, 6, *A Chandra X-Ray Study of NGC 1068. I. Observations of Extended Emission.*

Yuan W. et al. 2008, ApJ 685, 801, *A Population of Radio-Loud Narrow-Line Seyfert 1 Galaxies with Blazar-Like Properties?*

Yun M. S., Reddy N. A. & Condon J. J. 2001, ApJ 554, 803, *Radio Properties of Infrared-selected Galaxies in the IRAS 2 Jy Sample.*

Yun-Yong T., Zu-Cheng D. & Li Z. 2010, RAA 10, 415, *Multifrequency emission analysis of TeV blazars H 2356309 and 1ES 1218+304.*

Zdziarski A. A. et al. 1990, ApJ 363 L1, *Electron-positron pairs, Compton reflection, and the X-ray spectra of active galactic nuclei.*

Zdziarski A. A. et al. 1994, MNRAS 269, L55, *Physical Processes in the X-Ray/Gamma-Ray Source of IC4329A.*

Zdziarski A. A. 1999, ASP Conference Series Vol. 161, 16, *X-rays and Soft Gamma-rays from Seyferts, Radio Galaxies, and Black-Hole Binaries.*

Zdziarski A. A. et al. 2000, ApJ 542, 703, *Observations of Seyfert Galaxies by OSSE and Parameters of their X-Ray/Gamma-Ray Sources.*

Zhang Y. H. 2002, MNRAS 337, 609, *Cross-spectral analysis of the X-ray variability of Markarian 421.*

Zhou H. et al. 2006, ApJS 166, 128, *A Comprehensive Study of 2000 Narrow Line Seyfert 1 Galaxies from the Sloan Digital Sky Survey. I. The Sample.*

Zhou H. et al. 2007, ApJ, 658, L13, *A Narrow-Line Seyfert 1Blazar Composite Nucleus in 2MASX J0324 3410.*

Appendix A

Analysis Dataset Details

Tables containing the details of the data used in the analysis of the Seyfert galaxies discussed in Chapter 4 are found in this appendix. For each observation, the run number, its target, the position, offset from the analysis position, the date of observation and the duration of the observation are given. In this thesis only data where all four H.E.S.S. telescopes were operational and without technical problems and during periods of good weather were used. The target of each observation is the object for which the runs were initially taken to study.

A.1 MRK50

Run Number	Target	Pointing Direction J2000.0		Offset	Date	Duration
		R.A. (deg)	Dec. (deg)	(deg)	yyyy-mm-dd	(s)
20250	3C 273	187.28	2.55	1.4	2004-04-13	1682
20251	3C 273	187.28	1.55	1.8	2004-04-13	1683
20252	3C 273	187.28	2.55	1.4	2004-04-13	1683
20274	3C 273	187.28	1.55	1.8	2004-04-14	1682
20275	3C 273	187.28	2.55	1.4	2004-04-14	1683
20912	3C 273	187.28	1.55	1.8	2004-05-22	1682
20915	3C 273	186.78	2.05	1.1	2004-05-22	1680
20916	3C 273	187.78	2.05	2.0	2004-05-22	1683
20937	3C 273	187.28	1.55	1.8	2004-05-23	1684
24101	3C 273	187.28	2.55	1.4	2005-02-10	1687

Run Number	Target	Pointing Direction J2000.0		Offset	Date	Duration
		R.A. (deg)	Dec. (deg)	(deg)	yyyy-mm-dd	(s)
24102	3C 273	187.28	1.55	1.8	2005-02-10	1687
24103	3C 273	187.78	2.05	2.0	2005-02-10	1687
25324	3C 273	186.78	2.05	1.1	2005-05-03	1678
25345	3C 273	187.28	2.55	1.4	2005-05-04	1678
25346	3C 273	187.28	1.55	1.8	2005-05-04	1677
25391	3C 273	187.78	2.05	2.0	2005-05-06	1681
25392	3C 273	186.78	2.05	1.1	2005-05-06	1679
25443	3C 273	187.28	2.55	1.4	2005-05-08	1677
25444	3C 273	187.28	1.55	1.8	2005-05-08	1677
25510	3C 273	186.78	2.05	1.1	2005-05-11	1677
25511	3C 273	187.78	2.05	2.0	2005-05-11	1677
25542	3C 273	187.28	1.55	1.8	2005-05-14	1678
25544	3C 273	187.28	2.55	1.4	2005-05-14	1678
37192	3C 273	187.28	1.55	1.8	2007-02-15	1688
37193	3C 273	187.78	2.05	2.0	2007-02-15	1688
37194	3C 273	186.78	2.05	1.1	2007-02-15	1689
37218	3C 273	187.28	2.55	1.4	2007-02-16	1688
37221	3C 273	187.28	1.55	1.8	2007-02-16	1688
37222	3C 273	187.78	2.05	2.0	2007-02-16	1691
37223	3C 273	186.78	2.05	1.1	2007-02-16	1689
37249	3C 273	187.28	2.55	1.4	2007-02-17	1688
37250	3C 273	187.28	1.55	1.8	2007-02-17	1688
37251	3C 273	187.78	2.05	2.0	2007-02-17	1688
37252	3C 273	186.78	2.05	1.1	2007-02-17	1688
37283	3C 273	187.28	2.55	1.4	2007-02-18	1688
37284	3C 273	187.28	1.55	1.8	2007-02-18	1688
37285	3C 273	187.78	2.05	2.0	2007-02-18	1689
37354	3C 273	187.28	2.55	1.4	2007-02-22	1688
38650	3C 273	187.28	1.55	1.8	2007-05-07	1688
38651	3C 273	187.28	2.05	1.5	2007-05-07	1688

Run Number	Target	Pointing Direction J2000.0		Offset	Date	Duration
		R.A. (deg)	Dec. (deg)	(deg)	yyyy-mm-dd	(s)
38677	3C 273	187.28	2.55	1.4	2007-05-08	1687
38678	3C 273	186.78	2.05	1.1	2007-05-08	1688
38702	3C 273	187.78	2.05	2.0	2007-05-09	1687
38703	3C 273	187.28	1.55	1.8	2007-05-09	1688
38739	3C 273	187.28	2.55	1.4	2007-05-10	1688
38740	3C 273	186.78	2.05	1.1	2007-05-10	1689

A.2 3C 273

Run Number	Target	Pointing Direction J2000.0		Offset	Date	Duration
		R.A. (deg)	Dec. (deg)	(deg)	yyyy-mm-dd	(s)
20250	3C 273	187.28	2.55	0.7	2004-04-13	1682
20251	3C 273	187.28	1.55	0.7	2004-04-13	1683
20252	3C 273	187.28	2.55	0.7	2004-04-13	1683
20274	3C 273	187.28	1.55	0.7	2004-04-14	1682
20275	3C 273	187.28	2.55	0.7	2004-04-14	1683
20912	3C 273	187.28	1.55	0.7	2004-05-22	1682
20915	3C 273	186.78	2.05	1.0	2004-05-22	1680
20916	3C 273	187.78	2.05	0.0	2004-05-22	1683
20937	3C 273	187.28	1.55	0.7	2004-05-23	1684
24101	3C 273	187.28	2.55	0.7	2005-02-10	1687
24102	3C 273	187.28	1.55	0.7	2005-02-10	1687
24103	3C 273	187.78	2.05	0.0	2005-02-10	1687
25324	3C 273	186.78	2.05	1.0	2005-05-03	1678
25345	3C 273	187.28	2.55	0.7	2005-05-04	1678
25346	3C 273	187.28	1.55	0.7	2005-05-04	1677
25391	3C 273	187.78	2.05	0.0	2005-05-06	1681
25392	3C 273	186.78	2.05	1.0	2005-05-06	1679

Run Number	Target	Pointing Direction J2000.0		Offset	Date	Duration
		R.A. (deg)	Dec. (deg)	(deg)	yyyy-mm-dd	(s)
25443	3C 273	187.28	2.55	0.7	2005-05-08	1677
25444	3C 273	187.28	1.55	0.7	2005-05-08	1677
25510	3C 273	186.78	2.05	1.0	2005-05-11	1677
25511	3C 273	187.78	2.05	0.0	2005-05-11	1677
25542	3C 273	187.28	1.55	0.7	2005-05-14	1678
25544	3C 273	187.28	2.55	0.7	2005-05-14	1678
37192	3C 273	187.28	1.55	0.7	2007-02-15	1688
37193	3C 273	187.78	2.05	0.0	2007-02-15	1688
37194	3C 273	186.78	2.05	1.0	2007-02-15	1689
37218	3C 273	187.28	2.55	0.7	2007-02-16	1688
37221	3C 273	187.28	1.55	0.7	2007-02-16	1688
37222	3C 273	187.78	2.05	0.0	2007-02-16	1691
37223	3C 273	186.78	2.05	1.0	2007-02-16	1689
37249	3C 273	187.28	2.55	0.7	2007-02-17	1688
37250	3C 273	187.28	1.55	0.7	2007-02-17	1688
37251	3C 273	187.78	2.05	0.0	2007-02-17	1688
37252	3C 273	186.78	2.05	1.0	2007-02-17	1688
37283	3C 273	187.28	2.55	0.7	2007-02-18	1688
37284	3C 273	187.28	1.55	0.7	2007-02-18	1688
37285	3C 273	187.78	2.05	0.0	2007-02-18	1689
37354	3C 273	187.28	2.55	0.7	2007-02-22	1688
38650	3C 273	187.28	1.55	0.7	2007-05-07	1688
38651	3C 273	187.28	2.05	0.5	2007-05-07	1688
38677	3C 273	187.28	2.55	0.7	2007-05-08	1687
38678	3C 273	186.78	2.05	1.0	2007-05-08	1688
38702	3C 273	187.78	2.05	0.0	2007-05-09	1687
38703	3C 273	187.28	1.55	0.7	2007-05-09	1688
38739	3C 273	187.28	2.55	0.7	2007-05-10	1688
38740	3C 273	186.78	2.05	1.0	2007-05-10	1689

A.3 4U 1344-60

Run Number	Target	Pointing Direction J2000.0		Offset	Date	Duration
		R.A. (deg)	Dec. (deg)	(deg)	yyyy-mm-dd	(s)
25007	G307.6+0.7	202.78	-61.81	2.4	2005-04-11	1677
25009	G308.2+0.7	204.03	-61.71	1.8	2005-04-11	1678
25011	G308.8+0.7	205.27	-61.60	1.3	2005-04-11	1677
25013	G309.1-0.7	206.51	-62.92	2.3	2005-04-12	1677
25027	G309.4+0.7	206.51	-61.48	0.9	2005-04-12	1138
25030	G309.7-0.7	207.79	-62.78	2.2	2005-04-12	1678
25031	G310.0+0.7	207.73	-61.35	0.9	2005-04-12	1677
25032	G310.3-0.7	209.06	-62.64	2.3	2005-04-12	1677
25046	G310.6+0.7	208.94	-61.21	1.2	2005-04-13	1680
25069	G311.2+0.7	210.14	-61.06	1.7	2005-04-15	1678
25370	G311.8+0.7	211.33	-60.89	2.2	2005-05-05	1677
25842	G309.4+0.7	206.51	-61.48	0.9	2005-05-30	1691
25933	G310.6+0.7	208.94	-61.21	1.2	2005-06-01	1691
26023	G311.2+0.7	210.14	-61.06	1.7	2005-06-03	1693
26074	G311.8+0.7	211.33	-60.89	2.2	2005-06-04	1692
26840	G311.2+0.7	210.14	-61.06	1.7	2005-06-30	1694
51408	G308.5+00.0	204.93	-62.35	2.0	2009-05-19	1688
51453	G311.0+01.0	209.59	-60.82	1.3	2009-05-21	1689
56495	G308.5+00.0	204.93	-62.35	2.0	2010-03-15	1688
56564	G308.0+01.0	203.51	-61.45	1.9	2010-03-17	1689
56565	G310.0+01.0	207.59	-61.06	0.6	2010-03-17	1688
56786	G311.0+01.0	209.59	-60.82	1.3	2010-03-23	1473
56803	G309.5+00.0	207.03	-62.15	1.5	2010-03-24	1698
56804	G309.0+01.0	205.56	-61.27	0.9	2010-03-24	1695
56805	G310.5+00.0	209.10	-61.91	1.7	2010-03-24	1697
57620	G308.0+01.0	203.51	-61.45	1.9	2010-05-09	1688
57800	G310.0+01.0	207.59	-61.06	0.6	2010-05-18	1688

A.4 The Circinus Galaxy

Run Number	Target	Pointing Direction J2000.0		Offset	Date	Duration
		R.A. (deg)	Dec. (deg)	(deg)	yyyy-mm-dd	(s)
32077	PSR J1357-6429	210.89	-64.49	1.3	2006-05-15	1363
32374	PSR J1357-6429	209.26	-65.19	1.7	2006-05-25	1689
32431	PSR J1357-6429	210.89	-64.49	1.3	2006-05-27	1688
32434	PSR J1357-6429	209.26	-65.19	1.7	2006-05-27	1689
32435	PSR J1357-6429	209.26	-63.79	2.3	2006-05-27	1689
32436	PSR J1357-6429	210.89	-64.49	1.3	2006-05-27	1688
32457	PSR J1357-6429	209.26	-63.79	2.3	2006-05-28	1690
32545	PSR J1357-6429	209.26	-65.19	1.7	2006-05-31	1688
32546	PSR J1357-6429	210.89	-64.49	1.3	2006-05-31	1688
37751	HESS J1356-645	209.02	-63.84	2.3	2007-03-23	1688
37798	HESS J1356-645	210.64	-64.54	1.4	2007-03-24	1687
37890	HESS J1356-645	209.02	-63.84	2.3	2007-03-28	1688

A.5 GRS 1734-292

Run Number	Target	Pointing Direction J2000.0		Offset	Date	Duration
		R.A. (deg)	Dec. (deg)	(deg)	yyyy-mm-dd	(s)
20191	Sgr A	266.30	-28.30	1.9	2004-03-29	1682
20192	Sgr A	266.30	-29.30	1.7	2004-03-29	1683
20193	Sgr A	266.30	-28.30	1.9	2004-03-30	1682
20194	Sgr A	266.30	-29.30	1.7	2004-03-30	1682
20195	Sgr A	266.30	-28.30	1.9	2004-03-30	1682
20198	Sgr A	266.30	-29.30	1.7	2004-03-30	1682
20199	Sgr A	266.30	-28.30	1.9	2004-03-30	1433
20549	Sgr A*	266.42	-28.51	1.9	2004-04-26	1683
20550	Sgr A*	266.42	-29.51	1.8	2004-04-26	1683

Run Number	Target	Pointing Direction J2000.0		Offset	Date	Duration
		R.A. (deg)	Dec. (deg)	(deg)	yyyy-mm-dd	(s)
20551	Sgr A*	266.42	-28.51	1.9	2004-04-26	1683
20552	Sgr A*	266.42	-29.51	1.8	2004-04-26	1683
20553	Sgr A*	266.42	-28.51	1.9	2004-04-26	1682
20554	Sgr A*	266.42	-29.51	1.8	2004-04-26	1682
20567	Sgr A*	266.42	-28.51	1.9	2004-04-27	1683
20568	Sgr A*	266.42	-29.51	1.8	2004-04-27	1683
20572	Sgr A*	266.42	-28.51	1.9	2004-04-27	1683
20573	Sgr A*	266.42	-29.51	1.8	2004-04-27	1682
20580	Sgr A*	266.42	-28.31	2.0	2004-04-27	1679
20581	Sgr A*	266.42	-29.71	1.9	2004-04-27	1682
20582	Sgr A*	265.62	-29.01	1.1	2004-04-28	1683
20583	Sgr A*	267.22	-29.01	2.5	2004-04-28	1682
20584	Sgr A*	266.42	-28.31	2.0	2004-04-28	1683
20596	Sgr A*	266.42	-29.71	1.9	2004-04-29	1682
20597	Sgr A*	267.22	-29.01	2.5	2004-04-29	1682
20598	Sgr A*	265.62	-29.01	1.1	2004-04-29	1682
20608	Sgr A*	266.42	-28.31	2.0	2004-04-30	1683
20609	Sgr A*	266.42	-29.71	1.9	2004-04-30	1682
20765	G357.3+0.0	264.76	-31.23	2.1	2004-05-15	1683
20922	Sgr A*	266.42	-29.71	1.9	2004-05-22	1683
20923	Sgr A*	266.42	-28.31	2.0	2004-05-23	1682
20924	Sgr A*	265.62	-29.01	1.1	2004-05-23	1682
20925	Sgr A*	267.22	-29.01	2.5	2004-05-23	1683
20929	Sgr A*	265.62	-29.01	1.1	2004-05-23	1125
20930	Sgr A*	267.22	-29.01	2.5	2004-05-23	1126
20968	Sgr A*	266.42	-28.31	2.0	2004-05-25	1683
20978	G358.0+0.0	265.19	-30.64	1.7	2004-05-25	1682
20979	G000.8+0.0	266.88	-28.25	2.4	2004-05-26	1683
20989	G358.7+0.0	265.62	-30.04	1.4	2004-05-26	1682
20990	G359.4+0.0	266.05	-29.45	1.5	2004-05-26	1683

Run Number	Target	Pointing Direction J2000.0		Offset	Date	Duration
		R.A. (deg)	Dec. (deg)	(deg)	yyyy-mm-dd	(s)
20991	G000.1+0.0	266.46	-28.85	1.9	2004-05-26	1682
20998	Sgr A*	265.62	-29.01	1.1	2004-05-27	1682
20999	Sgr A*	267.22	-29.01	2.5	2004-05-27	1683
21006	Sgr A*	266.42	-28.31	2.0	2004-05-28	1683
21007	Sgr A*	266.42	-29.71	1.9	2004-05-28	1683
21016	Sgr A*	265.62	-29.01	1.1	2004-05-29	1683
21017	Sgr A*	267.22	-29.01	2.5	2004-05-29	1683
21027	Sgr A*	266.42	-28.31	2.0	2004-05-30	1684
21028	Sgr A*	266.42	-29.71	1.9	2004-05-30	1683
21146	Sgr A*	266.42	-28.31	2.0	2004-06-12	1682
21147	Sgr A*	266.42	-29.71	1.9	2004-06-12	1682
21148	Sgr A*	267.22	-29.01	2.5	2004-06-12	1683
21149	Sgr A*	265.62	-29.01	1.1	2004-06-13	1683
21152	G359.4-1.0	267.03	-29.97	2.5	2004-06-13	902
21165	Sgr A*	265.62	-29.01	1.1	2004-06-13	1683
21166	Sgr A*	267.22	-29.01	2.5	2004-06-13	1682
21167	Sgr A*	266.42	-29.71	1.9	2004-06-13	1682
21168	Sgr A*	266.42	-28.31	2.0	2004-06-14	1682
21169	G358.7-1.0	266.61	-30.57	2.4	2004-06-14	1683
21238	G000.1+1.0	265.49	-28.33	1.3	2004-06-16	1684
21245	Sgr A*	267.22	-29.01	2.5	2004-06-17	1683
21270	G359.4+1.0	265.07	-28.92	0.7	2004-06-17	1683
21272	G358.7+1.0	264.65	-29.51	0.4	2004-06-17	1682
21274	G358.0+1.0	264.21	-30.10	1.0	2004-06-18	1683
21275	Sgr A*	266.42	-29.71	1.9	2004-06-18	1682
21276	Sgr A*	266.42	-28.31	2.0	2004-06-18	1683
21298	G357.3+1.0	263.78	-30.69	1.6	2004-06-18	1682
21300	G356.6+1.0	263.33	-31.28	2.3	2004-06-19	1294
21323	G000.8+1.0	265.91	-27.73	1.9	2004-06-19	1683
21347	Sgr A*	267.22	-29.01	2.5	2004-06-20	1683

Run Number	Target	Pointing Direction J2000.0		Offset	Date	Duration
		R.A. (deg)	Dec. (deg)	(deg)	yyyy-mm-dd	(s)
21348	Sgr A*	265.62	-29.01	1.1	2004-06-21	1682
21349	Sgr A*	266.42	-28.31	2.0	2004-06-21	1682
21350	Sgr A*	266.42	-29.71	1.9	2004-06-21	1683
21372	Sgr A*	265.62	-29.01	1.1	2004-06-21	1682
21373	Sgr A*	267.22	-29.01	2.5	2004-06-21	1683
21376	Sgr A*	266.42	-29.71	1.9	2004-06-22	1683
21377	Sgr A*	266.42	-28.31	2.0	2004-06-22	1683
21389	Sgr A*	267.22	-29.01	2.5	2004-06-22	1683
21390	Sgr A*	265.62	-29.01	1.1	2004-06-22	1682
21420	G356.6+1.0	263.33	-31.28	2.3	2004-06-24	1682
21452	Sgr A*	266.42	-28.31	2.0	2004-06-27	1683
21453	Sgr A*	266.42	-29.71	1.9	2004-06-27	1682
21463	Sgr A*	265.62	-29.01	1.1	2004-06-28	1682
21464	Sgr A*	267.22	-29.01	2.5	2004-06-28	1682
21486	Sgr A*	267.22	-29.01	2.5	2004-07-04	1496
21491	Sgr A*	266.42	-28.51	1.9	2004-07-05	1684
21492	Sgr A*	266.42	-29.51	1.8	2004-07-05	1683
21493	Sgr A*	265.62	-29.01	1.1	2004-07-05	1687
21494	Sgr A*	265.62	-29.01	1.1	2004-07-05	926
21496	Sgr A*	266.42	-28.51	1.9	2004-07-06	1683
21497	Sgr A*	266.42	-29.51	1.8	2004-07-06	1133
21508	Sgr A*	267.22	-29.01	2.5	2004-07-08	1682
21894	Sgr A*	266.42	-28.31	2.0	2004-08-06	1683
21895	Sgr A*	266.42	-29.71	1.9	2004-08-06	1682
21896	Sgr A*	267.22	-29.01	2.5	2004-08-06	1323
21897	Sgr A*	265.62	-29.01	1.1	2004-08-06	1323
21909	Sgr A*	266.42	-28.31	2.0	2004-08-07	1683
21910	Sgr A*	266.42	-29.71	1.9	2004-08-07	1683
22258	Sgr A*	266.42	-28.51	1.9	2004-08-31	804
22270	G0.87+0.07	266.37	-27.90	2.1	2004-09-02	1681

Run Number	Target	Pointing Direction J2000.0		Offset	Date	Duration
		R.A. (deg)	Dec. (deg)	(deg)	yyyy-mm-dd	(s)
22272	G0.87+0.07	266.37	-27.90	2.1	2004-09-02	1682
22278	G0.87+0.07	266.37	-27.90	2.1	2004-09-03	1683
22280	G0.87+0.07	266.37	-27.90	2.1	2004-09-03	1682
22290	G0.87+0.07	266.37	-27.90	2.1	2004-09-04	1682
22292	G0.87+0.07	266.37	-27.90	2.1	2004-09-04	1683
22293	G0.87+0.07	266.37	-27.90	2.1	2004-09-04	1682
22322	G0.87+0.07	266.37	-27.90	2.1	2004-09-06	1682
22384	G0.87+0.07	266.37	-27.90	2.1	2004-09-10	1682
25330	Sgr A*	265.62	-29.01	1.1	2005-05-04	1523
25331	Sgr A*	267.22	-29.01	2.5	2005-05-04	658
25349	Sgr A*	266.42	-28.31	2.0	2005-05-05	1678
25353	Sgr A*	265.62	-29.01	1.1	2005-05-05	1533
25379	Sgr A*	265.62	-29.01	1.1	2005-05-06	1678
25380	Sgr A*	267.22	-29.01	2.5	2005-05-06	1678
25402	Sgr A*	266.42	-28.31	2.0	2005-05-07	1689
25403	Sgr A*	266.42	-28.31	2.0	2005-05-07	1677
25404	Sgr A*	266.42	-29.71	1.9	2005-05-07	1679
25405	Sgr A*	267.22	-29.01	2.5	2005-05-07	1559
25709	Sgr A*	265.62	-29.01	1.1	2005-05-20	1263
26078	Sgr A*	266.42	-28.31	2.0	2005-06-04	1691
26079	Sgr A*	266.42	-29.71	1.9	2005-06-04	1691
26080	Sgr A*	267.22	-29.01	2.5	2005-06-04	1701
26081	Sgr A*	265.62	-29.01	1.1	2005-06-04	1700
26082	Sgr A*	266.42	-28.31	2.0	2005-06-04	1701
26083	Sgr A*	266.42	-29.71	1.9	2005-06-04	1701
26084	Sgr A*	267.22	-29.01	2.5	2005-06-04	1702
26085	Sgr A*	265.62	-29.01	1.1	2005-06-04	1701
26086	Sgr A*	266.42	-28.31	2.0	2005-06-05	1700
26087	Sgr A*	266.42	-29.71	1.9	2005-06-05	1700
26088	Sgr A*	267.22	-29.01	2.5	2005-06-05	1700

Run Number	Target	Pointing Direction J2000.0		Offset	Date	Duration
		R.A. (deg)	Dec. (deg)	(deg)	yyyy-mm-dd	(s)
26089	Sgr A*	265.62	-29.01	1.1	2005-06-05	1369
26090	Sgr A*	266.42	-28.31	2.0	2005-06-05	2420
26091	Sgr A*	266.42	-29.71	1.9	2005-06-05	2421
26092	Sgr A*	265.62	-29.01	1.1	2005-06-05	1469
26104	Sgr A*	267.22	-29.01	2.5	2005-06-05	1701
26105	Sgr A*	265.62	-29.01	1.1	2005-06-05	1700
26106	Sgr A*	266.42	-28.31	2.0	2005-06-05	1700
26107	Sgr A*	266.42	-29.71	1.9	2005-06-05	1700
26108	Sgr A*	267.22	-29.01	2.5	2005-06-05	1700
26109	Sgr A*	265.62	-29.01	1.1	2005-06-05	1700
26110	Sgr A*	266.42	-28.31	2.0	2005-06-05	1700
26111	Sgr A*	266.42	-29.71	1.9	2005-06-06	1703
26112	Sgr A*	267.22	-29.01	2.5	2005-06-06	1700
26113	Sgr A*	265.62	-29.01	1.1	2005-06-06	1414
26114	Sgr A*	266.42	-28.31	2.0	2005-06-06	1703
26115	Sgr A*	266.42	-29.71	1.9	2005-06-06	1700
26116	Sgr A*	267.22	-29.01	2.5	2005-06-06	1700
26128	HESS J1745-303	265.45	-30.37	1.5	2005-06-06	1691
26154	HESS J1745-303	265.45	-30.37	1.5	2005-06-07	1694
26177	HESS J1745-303	265.45	-30.37	1.5	2005-06-08	1691
26201	HESS J1745-303	265.45	-30.37	1.5	2005-06-09	1690
26233	HESS J1745-303	265.45	-30.37	1.5	2005-06-10	1691
26789	Sgr A*	266.42	-28.31	2.0	2005-06-27	1691
26790	Sgr A*	267.22	-29.01	2.5	2005-06-27	1690
26810	Sgr A*	265.62	-29.01	1.1	2005-06-28	1690
26811	Sgr A*	267.22	-29.01	2.5	2005-06-28	1690
26812	Sgr A*	266.42	-29.71	1.9	2005-06-28	1693
26813	Sgr A*	266.42	-28.31	2.0	2005-06-28	1690
26844	HESS J1745-303	265.45	-30.37	1.5	2005-06-30	1690
26875	HESS J1745-303	265.45	-30.37	1.5	2005-07-01	1691

Run Number	Target	Pointing Direction J2000.0		Offset	Date	Duration
		R.A. (deg)	Dec. (deg)	(deg)	yyyy-mm-dd	(s)
26931	HESS J1745-303	265.45	-30.37	1.5	2005-07-03	1691
27376	Sgr A*	266.42	-28.31	2.0	2005-07-24	1690
27377	Sgr A*	265.62	-29.01	1.1	2005-07-24	932
27378	Sgr A*	267.22	-29.01	2.5	2005-07-24	769
27498	Sgr A*	267.22	-29.01	2.5	2005-07-27	1690
27499	Sgr A*	265.62	-29.01	1.1	2005-07-27	1691
27500	Sgr A*	266.42	-28.31	2.0	2005-07-27	1693
27501	Sgr A*	266.42	-29.71	1.9	2005-07-27	1691
27502	Sgr A*	267.22	-29.01	2.5	2005-07-27	1691
27503	Sgr A*	265.62	-29.01	1.1	2005-07-27	1693
27504	Sgr A*	266.42	-28.31	2.0	2005-07-27	1692
27505	Sgr A*	266.42	-29.71	1.9	2005-07-27	1695
27506	Sgr A*	267.22	-29.01	2.5	2005-07-27	1694
27507	Sgr A*	265.62	-29.01	1.1	2005-07-27	1690
27535	Sgr A*	266.42	-29.71	1.9	2005-07-28	1691
27536	Sgr A*	266.42	-28.31	2.0	2005-07-28	1691
27537	Sgr A*	265.62	-29.01	1.1	2005-07-28	1690
27539	Sgr A*	266.42	-29.71	1.9	2005-07-28	1691
27540	Sgr A*	266.42	-28.31	2.0	2005-07-28	1694
27541	Sgr A*	265.62	-29.01	1.1	2005-07-28	1694
27542	Sgr A*	267.22	-29.01	2.5	2005-07-28	1691
27543	Sgr A*	266.42	-29.71	1.9	2005-07-28	1694
27544	Sgr A*	266.42	-28.31	2.0	2005-07-28	1691
27545	Sgr A*	265.62	-29.01	1.1	2005-07-28	1690
27546	Sgr A*	267.22	-29.01	2.5	2005-07-28	1690
27566	Sgr A*	266.42	-28.31	2.0	2005-07-29	1690
27567	Sgr A*	266.42	-29.71	1.9	2005-07-29	1690
27568	Sgr A*	267.22	-29.01	2.5	2005-07-29	1690
27569	Sgr A*	265.62	-29.01	1.1	2005-07-29	1693
27570	Sgr A*	266.42	-28.31	2.0	2005-07-29	1689

Run Number	Target	Pointing Direction J2000.0		Offset	Date	Duration
		R.A. (deg)	Dec. (deg)	(deg)	yyyy-mm-dd	(s)
27571	Sgr A*	266.42	-29.71	1.9	2005-07-29	1694
27572	Sgr A*	267.22	-29.01	2.5	2005-07-29	1691
27573	Sgr A*	265.62	-29.01	1.1	2005-07-29	1693
27574	Sgr A*	266.42	-28.31	2.0	2005-07-29	1690
27575	Sgr A*	266.42	-29.71	1.9	2005-07-29	1694
27576	Sgr A*	267.22	-29.01	2.5	2005-07-29	1690
27577	Sgr A*	266.42	-28.31	2.0	2005-07-29	1522
27592	Sgr A*	265.62	-29.01	1.1	2005-07-30	1693
27593	Sgr A*	267.22	-29.01	2.5	2005-07-30	1690
27594	Sgr A*	266.42	-29.71	1.9	2005-07-30	1691
27595	Sgr A*	266.42	-28.31	2.0	2005-07-30	1693
27599	Sgr A*	265.62	-29.01	1.1	2005-07-30	864
27600	Sgr A*	267.22	-29.01	2.5	2005-07-30	1691
27601	Sgr A*	266.42	-29.71	1.9	2005-07-30	1693
27602	Sgr A*	266.42	-28.31	2.0	2005-07-30	1690
27603	Sgr A*	265.62	-29.01	1.1	2005-07-30	1690
27604	Sgr A*	267.22	-29.01	2.5	2005-07-30	1691
27605	Sgr A*	266.42	-29.71	1.9	2005-07-30	805
27606	Sgr A*	266.42	-29.71	1.9	2005-07-31	1691
27625	Sgr A*	267.22	-29.01	2.5	2005-07-31	1695
27626	Sgr A*	265.62	-29.01	1.1	2005-07-31	1691
27627	Sgr A*	266.42	-28.31	2.0	2005-07-31	1701
27628	Sgr A*	266.42	-29.71	1.9	2005-07-31	1694
27629	Sgr A*	267.22	-29.01	2.5	2005-07-31	1703
27630	Sgr A*	265.62	-29.01	1.1	2005-07-31	1689
27631	Sgr A*	266.42	-28.31	2.0	2005-07-31	1690
27632	Sgr A*	266.42	-29.71	1.9	2005-07-31	1694
27633	Sgr A*	267.22	-29.01	2.5	2005-07-31	1691
27634	Sgr A*	265.62	-29.01	1.1	2005-07-31	1690
27635	Sgr A*	266.42	-28.31	2.0	2005-07-31	1690

Run Number	Target	Pointing Direction J2000.0		Offset	Date	Duration
		R.A. (deg)	Dec. (deg)	(deg)	yyyy-mm-dd	(s)
27636	Sgr A*	266.42	-29.71	1.9	2005-07-31	1690
27637	Sgr A*	267.22	-29.01	2.5	2005-08-01	1690
27662	Sgr A*	266.42	-29.71	1.9	2005-08-01	1690
27663	Sgr A*	266.42	-28.31	2.0	2005-08-01	1690
27664	Sgr A*	265.62	-29.01	1.1	2005-08-01	1691
27665	Sgr A*	267.22	-29.01	2.5	2005-08-01	1690
27666	Sgr A*	266.42	-29.71	1.9	2005-08-01	1690
27667	Sgr A*	266.42	-28.31	2.0	2005-08-01	1689
27668	Sgr A*	265.62	-29.01	1.1	2005-08-01	1694
27669	Sgr A*	267.22	-29.01	2.5	2005-08-01	1691
27670	Sgr A*	266.42	-29.71	1.9	2005-08-01	1699
27671	Sgr A*	266.42	-28.31	2.0	2005-08-01	1690
28127	Sgr A*	266.42	-28.31	2.0	2005-08-22	1691
28128	Sgr A*	266.42	-29.71	1.9	2005-08-22	1692
28129	Sgr A*	267.22	-29.01	2.5	2005-08-22	1695
28130	Sgr A*	265.62	-29.01	1.1	2005-08-22	900
28167	Sgr A*	266.42	-28.31	2.0	2005-08-23	1694
28168	Sgr A*	265.62	-29.01	1.1	2005-08-23	1694
28169	Sgr A*	267.22	-29.01	2.5	2005-08-23	1691
31579	G1.0+0.7	266.32	-27.72	2.2	2006-04-30	1689
31594	G0.6+0.7	266.08	-28.06	1.8	2006-05-01	1688
33159	Sgr A*	266.42	-28.31	2.0	2006-06-27	1690
33160	Sgr A*	266.42	-29.71	1.9	2006-06-27	1689
33161	Sgr A*	267.22	-29.01	2.5	2006-06-27	1693
33162	Sgr A*	265.62	-29.01	1.1	2006-06-27	1688
33207	Sgr A*	267.22	-29.01	2.5	2006-06-29	1688
33208	Sgr A*	265.62	-29.01	1.1	2006-06-29	1688
33458	Sgr A*	267.22	-29.01	2.5	2006-07-14	696
33467	Sgr A*	266.42	-29.71	1.9	2006-07-15	1688
33468	Sgr A*	266.42	-28.31	2.0	2006-07-15	1689

Run Number	Target	Pointing Direction J2000.0		Offset	Date	Duration
		R.A. (deg)	Dec. (deg)	(deg)	yyyy-mm-dd	(s)
33469	Sgr A*	265.62	-29.01	1.1	2006-07-15	1088
33482	Sgr A*	267.22	-29.01	2.5	2006-07-16	1688
33483	Sgr A*	266.42	-29.71	1.9	2006-07-16	1688
33484	Sgr A*	265.62	-29.01	1.1	2006-07-16	1689
33485	Sgr A*	267.22	-29.01	2.5	2006-07-16	1689
33499	Sgr A*	266.42	-28.31	2.0	2006-07-17	1689
33500	Sgr A*	266.42	-29.71	1.9	2006-07-17	1689
33501	Sgr A*	265.62	-29.01	1.1	2006-07-17	1689
33502	Sgr A*	267.22	-29.01	2.5	2006-07-17	1689
34148	Sgr A*	266.00	-29.60	1.5	2006-08-18	1689
34187	Sgr A*	266.83	-28.41	2.3	2006-08-19	1689
34188	Sgr A*	266.00	-29.60	1.5	2006-08-19	1690
34209	Sgr A*	267.10	-29.37	2.4	2006-08-20	1689
34310	Sgr A*	266.83	-28.41	2.3	2006-08-23	1689
34313	Sgr A*	266.00	-29.60	1.5	2006-08-23	1689
34314	Sgr A*	265.74	-28.64	1.3	2006-08-23	1689
34949	Sgr A*	266.42	-28.51	1.9	2006-09-22	1688
34950	Sgr A*	266.42	-29.51	1.8	2006-09-22	1688
34951	Sgr A*	266.99	-29.01	2.3	2006-09-22	1689
34952	Sgr A*	265.84	-29.01	1.3	2006-09-22	1689
34953	Sgr A*	266.42	-28.51	1.9	2006-09-22	1689
34976	Sgr A*	266.42	-29.51	1.8	2006-09-23	1692
34977	Sgr A*	266.99	-29.01	2.3	2006-09-23	1689
34978	Sgr A*	265.84	-29.01	1.3	2006-09-23	1689
34979	Sgr A*	266.42	-28.51	1.9	2006-09-23	1689
35001	Sgr A*	266.42	-29.51	1.8	2006-09-24	1689
38832	Sgr A*	265.62	-29.01	1.1	2007-05-13	1687
38833	Sgr A*	267.22	-29.01	2.5	2007-05-14	1688
38834	Sgr A*	266.42	-29.71	1.9	2007-05-14	1688
38835	Sgr A*	266.42	-28.31	2.0	2007-05-14	1688

Run Number	Target	Pointing Direction J2000.0		Offset	Date	Duration
		R.A. (deg)	Dec. (deg)	(deg)	yyyy-mm-dd	(s)
38862	Sgr A*	266.42	-29.71	1.9	2007-05-14	1688
38863	Sgr A*	267.22	-29.01	2.5	2007-05-15	1688
38865	Sgr A*	265.62	-29.01	1.1	2007-05-15	1682
38895	Sgr A*	266.42	-29.71	1.9	2007-05-15	1688
38896	Sgr A*	266.42	-28.31	2.0	2007-05-16	1688
38897	Sgr A*	265.62	-29.01	1.1	2007-05-16	1689
38898	Sgr A*	266.42	-29.71	1.9	2007-05-16	1688
38930	Sgr A*	266.42	-28.31	2.0	2007-05-16	1687
38931	Sgr A*	267.22	-29.01	2.5	2007-05-17	1688
38932	Sgr A*	265.62	-29.01	1.1	2007-05-17	1689
38959	Sgr A*	266.42	-29.71	1.9	2007-05-17	1688
38960	Sgr A*	266.42	-28.31	2.0	2007-05-17	1687
38961	Sgr A*	267.22	-29.01	2.5	2007-05-18	1687
38962	Sgr A*	265.62	-29.01	1.1	2007-05-18	1689
40801	G357.6+0.7	264.26	-30.60	1.5	2007-08-06	1689
40826	G357.2+0.8	263.91	-30.89	1.8	2007-08-07	1060
40827	G357.2+0.8	263.91	-30.89	1.8	2007-08-07	1689
40851	G357.6+0.7	264.26	-30.60	1.5	2007-08-08	1688
40852	G356.8+0.8	263.66	-31.22	2.2	2007-08-08	1689
40881	G357.6+0.7	264.26	-30.60	1.5	2007-08-09	1689
40940	G358.0+0.7	264.51	-30.27	1.1	2007-08-11	1688
40942	G357.4-0.6	265.42	-31.46	2.5	2007-08-11	1687
40972	G357.2+0.8	263.91	-30.89	1.8	2007-08-12	1689
41036	G358.2-0.7	266.01	-30.84	2.2	2007-08-14	1688
45378	Sgr A*	265.62	-29.01	1.1	2008-05-07	1689
45445	Sgr A*	266.42	-29.71	1.9	2008-05-11	1689
45446	Sgr A*	267.22	-29.01	2.5	2008-05-11	1689
45447	Sgr A*	265.62	-29.01	1.1	2008-05-11	1689
45448	Sgr A*	266.42	-28.31	2.0	2008-05-11	1689
45449	Sgr A*	266.42	-29.71	1.9	2008-05-11	1689

Run Number	Target	Pointing Direction J2000.0		Offset	Date	Duration
		R.A. (deg)	Dec. (deg)	(deg)	yyyy-mm-dd	(s)
45466	Sgr A*	267.22	-29.01	2.5	2008-05-11	1688
45467	Sgr A*	265.62	-29.01	1.1	2008-05-12	1689
45468	Sgr A*	266.42	-28.31	2.0	2008-05-12	1689
45469	Sgr A*	266.42	-29.71	1.9	2008-05-12	1689
45470	Sgr A*	267.22	-29.01	2.5	2008-05-12	1689
45471	Sgr A*	265.62	-29.01	1.1	2008-05-12	1687
45472	Sgr A*	266.42	-28.31	2.0	2008-05-12	1688
45487	Sgr A*	266.42	-29.71	1.9	2008-05-12	1688
45488	Sgr A*	267.22	-29.01	2.5	2008-05-13	1687
45489	Sgr A*	265.62	-29.01	1.1	2008-05-13	1687
45490	Sgr A*	266.42	-28.31	2.0	2008-05-13	1687
45491	Sgr A*	266.42	-29.71	1.9	2008-05-13	1689
45492	Sgr A*	267.22	-29.01	2.5	2008-05-13	1689
45493	Sgr A*	265.62	-29.01	1.1	2008-05-13	1687
47027	Sgr A*	265.62	-29.01	1.1	2008-07-26	1688
47028	Sgr A*	267.22	-29.01	2.5	2008-07-26	1687
47029	Sgr A*	266.42	-29.71	1.9	2008-07-26	1688
47030	Sgr A*	266.42	-28.31	2.0	2008-07-26	1688
47031	Sgr A*	265.62	-29.01	1.1	2008-07-26	1687
47032	Sgr A*	267.22	-29.01	2.5	2008-07-26	1688
47033	Sgr A*	266.42	-29.71	1.9	2008-07-26	1689
47034	Sgr A*	266.42	-28.31	2.0	2008-07-26	1688
47064	Sgr A*	265.62	-29.01	1.1	2008-07-27	1689
47065	Sgr A*	267.22	-29.01	2.5	2008-07-27	1687
47066	Sgr A*	266.42	-29.71	1.9	2008-07-27	1688
47067	Sgr A*	266.42	-28.31	2.0	2008-07-27	916
50653	Sgr A*	266.91	-29.27	2.2	2009-04-03	1688
50654	Sgr A*	265.93	-28.75	1.4	2009-04-03	1688
50679	Sgr A*	266.12	-29.43	1.6	2009-04-05	1687
50680	Sgr A*	266.71	-28.58	2.1	2009-04-05	1688

Run Number	Target	Pointing Direction J2000.0		Offset	Date	Duration
		R.A. (deg)	Dec. (deg)	(deg)	yyyy-mm-dd	(s)
50681	Sgr A*	266.91	-29.27	2.2	2009-04-05	1688
50682	Sgr A*	265.93	-28.75	1.4	2009-04-05	1688
50683	Sgr A*	266.12	-29.43	1.6	2009-04-05	1301
50930	G358.6+03.5	262.19	-28.24	2.1	2009-04-23	1688
58911	Sgr A*	267.22	-29.01	2.5	2010-07-13	1688
58912	Sgr A*	265.62	-29.01	1.1	2010-07-13	1689
58913	Sgr A*	266.42	-28.31	2.0	2010-07-13	1688
58933	Sgr A*	267.22	-29.01	2.5	2010-07-14	1689
58934	Sgr A*	265.62	-29.01	1.1	2010-07-14	1687
58935	Sgr A*	266.42	-28.31	2.0	2010-07-14	1689
58936	Sgr A*	266.42	-29.71	1.9	2010-07-14	1689
63713	Sgr A*	265.64	-28.59	1.2	2011-05-06	1687
63745	Sgr A*	265.64	-28.59	1.2	2011-05-07	1027
63755	Sgr A*	265.64	-28.59	1.2	2011-05-08	1676
63780	Sgr A*	267.20	-29.42	2.5	2011-05-08	1687
63781	Sgr A*	265.64	-28.59	1.2	2011-05-08	1687
63805	Sgr A*	265.64	-28.59	1.2	2011-05-09	1695
66784	Sgr A*	265.64	-28.59	1.2	2011-08-31	1689
66785	Sgr A*	265.64	-28.59	1.2	2011-08-31	1687
66786	Sgr A*	267.20	-29.42	2.5	2011-08-31	1687
66803	Sgr A*	267.20	-29.42	2.5	2011-09-01	1669
67094	Sgr A*	265.64	-28.59	1.2	2011-09-18	1669
67095	Sgr A*	267.20	-29.42	2.5	2011-09-18	1687
67113	Sgr A*	267.20	-29.42	2.5	2011-09-19	1687
67114	Sgr A*	265.64	-28.59	1.2	2011-09-19	1687
67161	Sgr A*	267.20	-29.42	2.5	2011-09-21	1687
67162	Sgr A*	265.64	-28.59	1.2	2011-09-21	1687
67189	Sgr A*	265.64	-28.59	1.2	2011-09-22	1687
67190	Sgr A*	267.20	-29.42	2.5	2011-09-22	1687
67215	Sgr A*	267.20	-29.42	2.5	2011-09-23	1687

A.6 IGR J14471-6319

Run Number	Target	Pointing Direction J2000.0		Offset	Date	Duration
		R.A. (deg)	Dec. (deg)	(deg)	yyyy-mm-dd	(s)
21169	G358.7-1.0	266.61	-30.57	2.4	2004-06-14	1683
21170	G358.0-1.0	266.18	-31.16	2.0	2004-06-14	1682
21215	G357.3-1.0	265.75	-31.76	1.7	2004-06-15	1682
21216	G356.6-1.0	265.32	-32.35	1.7	2004-06-15	1683
21217	G355.9-1.0	264.88	-32.95	2.0	2004-06-16	1683
21218	G355.2-1.0	264.43	-33.54	2.4	2004-06-16	1682
34216	V4134 Sgr	268.82	-33.81	1.6	2006-08-20	1689
34244	V4134 Sgr	269.67	-33.11	2.1	2006-08-21	1688
34287	V4134 Sgr	268.82	-33.81	1.6	2006-08-22	1689
34366	V4134 Sgr	269.67	-33.11	2.1	2006-08-25	1688
40802	G356.2-0.5	264.57	-32.43	2.3	2007-08-06	1689
40803	G356.2-0.5	264.57	-32.43	2.3	2007-08-06	1689
40825	G357.0-0.6	265.17	-31.80	2.0	2007-08-07	1688
40850	G356.6-0.6	264.92	-32.14	2.1	2007-08-08	1687
40880	G357.0-0.6	265.17	-31.80	2.0	2007-08-09	1688
40942	G357.4-0.6	265.42	-31.46	2.1	2007-08-11	1687
41036	G358.2-0.7	266.01	-30.84	2.3	2007-08-14	1688
51617	G355.1-03.5	266.94	-34.94	2.0	2009-05-29	1687
65169	G356.7-01.0	265.38	-32.27	1.7	2011-06-30	1688

A.7 IGR J17204-3554

Run Number	Target	Pointing Direction J2000.0		Offset	Date	Duration
		R.A. (deg)	Dec. (deg)	(deg)	yyyy-mm-dd	(s)
20920	G349.6+0.0	259.58	-37.64	1.8	2004-05-22	1687
20921	G350.3+0.0	260.09	-37.07	1.2	2004-05-22	1683

Run Number	Target	Pointing Direction J2000.0		Offset	Date	Duration
		R.A. (deg)	Dec. (deg)	(deg)	yyyy-mm-dd	(s)
20940	G351.0+0.0	260.59	-36.49	0.7	2004-05-23	1683
20941	G351.7+0.0	261.08	-35.92	0.8	2004-05-23	1683
20957	G352.4+0.0	261.56	-35.34	1.3	2004-05-24	1683
20960	G353.1+0.0	262.04	-34.76	1.9	2004-05-24	1682
21241	G353.1-1.0	263.05	-35.31	2.5	2004-06-17	1683
21243	G352.4-1.0	262.58	-35.89	2.0	2004-06-17	1682
21269	G351.0-1.0	261.62	-37.06	1.7	2004-06-17	1682
21271	G351.7-1.0	262.10	-36.47	1.7	2004-06-17	1683
21273	G350.3-1.0	261.12	-37.64	1.9	2004-06-18	1683
21393	G353.1+1.0	261.03	-34.20	1.9	2004-06-22	1682
21406	G352.4+1.0	260.55	-34.77	1.2	2004-06-23	1683
21409	G351.7+1.0	260.06	-35.35	0.6	2004-06-23	1682
21410	G351.0+1.0	259.57	-35.92	0.4	2004-06-23	1682
21437	G349.6+1.0	258.56	-37.06	1.7	2004-06-25	1682
21438	G348.9+1.0	258.04	-37.63	2.4	2004-06-25	1682
25090	J1731-348	261.99	-34.84	1.9	2005-04-17	1122
25099	J1731-348	262.84	-35.54	2.3	2005-04-18	1677
25108	J1731-348	261.99	-34.84	1.9	2005-04-19	1678
25215	J1731-348	262.84	-35.54	2.3	2005-04-20	1677
25217	J1731-348	261.99	-34.84	1.9	2005-04-20	1078
25584	J1731-348	262.84	-35.54	2.3	2005-05-17	745
25992	J1731-348	262.84	-35.54	2.3	2005-06-03	1118
33108	HESS J1731-348	263.06	-35.46	2.4	2006-06-25	1689
33112	HESS J1731-348	262.21	-34.76	2.1	2006-06-26	1688
33158	HESS J1731-348	262.21	-34.76	2.1	2006-06-27	1690
33164	HESS J1731-348	263.06	-35.46	2.4	2006-06-27	1688
33166	HESS J1731-348	262.21	-34.76	2.1	2006-06-28	1688
33228	HESS J1731-348	263.06	-35.46	2.4	2006-06-30	1689
40078	J1731-348 P1	262.54	-35.38	2.1	2007-07-05	1688
40079	J1731-348 P1	262.54	-35.38	2.1	2007-07-05	1688

Run Number	Target	Pointing Direction J2000.0		Offset	Date	Duration
		R.A. (deg)	Dec. (deg)	(deg)	yyyy-mm-dd	(s)
40094	J1731-348 P1	262.54	-35.38	2.1	2007-07-06	1689
40095	J1731-348 P1	262.54	-35.38	2.1	2007-07-06	1688
40136	J1731-348 P1	262.54	-35.38	2.1	2007-07-08	1689
40180	J1731-348 P1	262.54	-35.38	2.1	2007-07-10	1689
40181	J1731-348 P1	262.54	-35.38	2.1	2007-07-10	1688
40257	J1731-348 P1	262.54	-35.38	2.1	2007-07-12	1688
40258	J1731-348 P1	262.54	-35.38	2.1	2007-07-12	1689
40261	J1731-348 P1	262.54	-35.38	2.1	2007-07-12	1688
40320	J1731-348 P3	261.73	-34.62	1.8	2007-07-14	1687
40321	J1731-348 P3	261.73	-34.62	1.8	2007-07-14	1689
40354	J1731-348 P3	261.73	-34.62	1.8	2007-07-15	1690
40355	J1731-348 P3	261.73	-34.62	1.8	2007-07-15	1688
40379	J1731-348 P3	261.73	-34.62	1.8	2007-07-16	1689
40440	J1731-348 P3	261.73	-34.62	1.8	2007-07-18	1689
40441	J1731-348 P1	262.54	-35.38	2.1	2007-07-18	1688
45751	G349.4+0.9	258.51	-37.28	1.9	2008-05-30	1688
45776	G349.4+0.9	258.51	-37.28	1.9	2008-05-31	1689
45835	G349.7-0.7	260.38	-37.96	2.1	2008-06-02	1688
45836	G349.7-0.7	260.38	-37.96	2.1	2008-06-02	1688
45839	G350.7+1.0	259.35	-36.17	0.7	2008-06-03	1690
45862	G349.4+0.9	258.51	-37.28	1.9	2008-06-03	1688
45864	G349.7-0.7	260.38	-37.96	2.1	2008-06-03	1688
45893	G349.7-0.7	260.38	-37.96	2.1	2008-06-04	1689
45894	G349.7-0.7	260.38	-37.96	2.1	2008-06-04	1688
45949	G350.5+0.2	260.03	-36.79	0.9	2008-06-06	1688
45950	G350.5+0.2	260.03	-36.79	0.9	2008-06-06	1688
45971	G349.4+0.9	258.51	-37.28	1.9	2008-06-07	1688
45972	G349.4+0.9	258.51	-37.28	1.9	2008-06-07	988
45973	G350.7+1.0	259.35	-36.17	0.7	2008-06-07	1688
45974	G350.5+0.2	260.03	-36.79	0.9	2008-06-07	1687

Run Number	Target	Pointing Direction J2000.0		Offset	Date	Duration
		R.A. (deg)	Dec. (deg)	(deg)	yyyy-mm-dd	(s)
45992	G349.4+0.9	258.51	-37.28	1.9	2008-06-08	1689
45993	G350.2+0.8	259.20	-36.69	1.1	2008-06-08	1020
45994	G350.5+0.2	260.03	-36.79	0.9	2008-06-08	1688
45995	G350.5+0.2	260.03	-36.79	0.9	2008-06-08	1687
46013	G350.2+0.8	259.20	-36.69	1.1	2008-06-09	791
52030	HESS J1731-347	262.98	-35.41	2.4	2009-06-22	1688
52150	HESS J1731-347	262.13	-34.71	2.0	2009-06-27	1689
52152	HESS J1731-347	262.98	-35.41	2.4	2009-06-27	1689
52373	HESS J1731-347	262.98	-35.41	2.4	2009-07-13	1689
52375	HESS J1731-347	262.13	-34.71	2.0	2009-07-13	1693
52390	HESS J1731-347	262.98	-35.41	2.4	2009-07-14	1693
52410	HESS J1731-347	262.13	-34.71	2.0	2009-07-15	1688
52469	HESS J1731-347	262.98	-35.41	2.4	2009-07-17	1689
52523	HESS J1731-347	262.98	-35.41	2.4	2009-07-19	1689
52547	HESS J1731-347	262.98	-35.41	2.4	2009-07-20	1688
52549	HESS J1731-347	262.13	-34.71	2.0	2009-07-20	1688
52596	HESS J1731-347	262.13	-34.71	2.0	2009-07-22	1689
52624	HESS J1731-347	262.13	-34.71	2.0	2009-07-23	1688
52649	HESS J1731-347	262.98	-35.41	2.4	2009-07-24	1688
53006	HESS J1731-347	262.13	-34.71	2.0	2009-08-13	1689
53024	HESS J1731-347	262.13	-34.71	2.0	2009-08-14	1689
53143	HESS J1731-347	262.13	-34.71	2.0	2009-08-19	1689
53173	HESS J1731-347	262.13	-34.71	2.0	2009-08-20	1688
59714	G349.7+00.2	259.50	-36.73	1.0	2010-08-26	994
59728	G349.7+00.2	260.13	-37.43	1.5	2010-08-27	1689
59796	G349.7+00.2	258.87	-37.43	1.8	2010-08-29	1689
59797	G349.7+00.2	259.50	-36.93	1.1	2010-08-29	1689
59812	G349.7+00.2	260.13	-37.43	1.5	2010-08-30	1689
59813	G349.7+00.2	258.87	-37.43	1.8	2010-08-30	1637
59871	G349.7+00.2	259.50	-36.93	1.1	2010-09-02	1688

Run Number	Target	Pointing Direction J2000.0		Offset	Date	Duration
		R.A. (deg)	Dec. (deg)	(deg)	yyyy-mm-dd	(s)
59872	G349.7+00.2	259.50	-37.93	2.1	2010-09-02	1688
59928	G349.7+00.2	259.50	-37.93	2.1	2010-09-04	1688
59963	G349.7+00.2	260.13	-37.43	1.5	2010-09-05	1688
59964	G349.7+00.2	258.87	-37.43	1.8	2010-09-05	1688
60204	G349.7+00.2	260.13	-37.43	1.5	2010-09-09	1688

A.8 IGR J17488-3253

Run Number	Target	Pointing Direction J2000.0		Offset	Date	Duration
		R.A. (deg)	Dec. (deg)	(deg)	yyyy-mm-dd	(s)
21169	G358.7-1.0	266.61	-30.57	2.4	2004-06-14	1683
21170	G358.0-1.0	266.18	-31.16	2.0	2004-06-14	1682
21215	G357.3-1.0	265.75	-31.76	1.7	2004-06-15	1682
21216	G356.6-1.0	265.32	-32.35	1.7	2004-06-15	1683
21217	G355.9-1.0	264.88	-32.95	2.0	2004-06-16	1683
21218	G355.2-1.0	264.43	-33.54	2.4	2004-06-16	1682
34216	V4134 Sgr	268.82	-33.81	1.6	2006-08-20	1689
34244	V4134 Sgr	269.67	-33.11	2.1	2006-08-21	1688
34287	V4134 Sgr	268.82	-33.81	1.6	2006-08-22	1689
34366	V4134 Sgr	269.67	-33.11	2.1	2006-08-25	1688
40802	G356.2-0.5	264.57	-32.43	2.3	2007-08-06	1689
40803	G356.2-0.5	264.57	-32.43	2.3	2007-08-06	1689
40825	G357.0-0.6	265.17	-31.80	2.0	2007-08-07	1688
40850	G356.6-0.6	264.92	-32.14	2.1	2007-08-08	1687
40880	G357.0-0.6	265.17	-31.80	2.0	2007-08-09	1688
40942	G357.4-0.6	265.42	-31.46	2.1	2007-08-11	1687
41036	G358.2-0.7	266.01	-30.84	2.3	2007-08-14	1688
51617	G355.1-03.5	266.94	-34.94	2.0	2009-05-29	1687

Run Number	Target	Pointing Direction J2000.0		Offset	Date	Duration
		R.A. (deg)	Dec. (deg)	(deg)	yyyy-mm-dd	(s)
65169	G356.7-01.0	265.38	-32.27	1.7	2011-06-30	1688

A.9 IGR J22367-1231

Run Number	Target	Pointing Direction J2000.0		Offset	Date	Duration
		R.A. (deg)	Dec. (deg)	(deg)	yyyy-mm-dd	(s)
21750	RBS 1888	340.93	-12.02	1.8	2004-07-21	1682
21751	RBS 1888	340.93	-13.02	1.8	2004-07-21	1685
21771	RBS 1888	340.93	-13.02	1.8	2004-07-22	1683
21772	RBS 1888	340.93	-12.02	1.8	2004-07-22	1682
21805	RBS 1888	340.93	-13.02	1.8	2004-07-23	1682
21806	RBS 1888	340.93	-12.02	1.8	2004-07-24	1683
33170	RBS 1888	340.41	-12.52	1.2	2006-06-28	1688
33171	RBS 1888	341.44	-12.52	2.2	2006-06-28	1688
33172	RBS 1888	340.93	-13.02	1.8	2006-06-28	777
33220	RBS 1888	340.93	-13.02	1.8	2006-06-30	1078
33239	RBS 1888	340.93	-12.02	1.8	2006-07-01	1688
33240	RBS 1888	341.44	-12.52	2.2	2006-07-01	727
33265	RBS 1888	341.44	-12.52	2.2	2006-07-02	1688
33266	RBS 1888	340.93	-13.02	1.8	2006-07-02	988

A.10 NGC 1068

Run Number	Target	Pointing Direction J2000.0		Offset	Date	Duration
		R.A.	Dec.			
		(deg)	(deg)	(deg)	yyyy-mm-dd	(s)
22958	NGC 1068	40.67	0.49	0.5	2004-10-09	1684
22959	NGC 1068	40.67	0.49	0.5	2004-10-09	1684
22960	NGC 1068	40.67	-0.51	0.5	2004-10-10	1684
22997	NGC 1068	40.17	-0.01	0.5	2004-10-11	1687
22998	NGC 1068	41.17	-0.01	0.5	2004-10-12	1686
23035	NGC 1068	41.17	-0.01	0.5	2004-10-13	1567
23036	NGC 1068	40.17	-0.01	0.5	2004-10-13	1567
23060	NGC 1068	40.67	0.49	0.5	2004-10-14	1687
23061	NGC 1068	40.67	-0.51	0.5	2004-10-14	1687
23077	NGC 1068	40.17	-0.01	0.5	2004-10-15	1686
23078	NGC 1068	41.17	-0.01	0.5	2004-10-15	1686
23123	NGC 1068	40.67	-0.51	0.5	2004-10-17	1686
23124	NGC 1068	40.67	0.49	0.5	2004-10-17	1686
35398	NGC 1068	40.17	-0.01	0.5	2006-10-13	1688
35434	NGC 1068	40.67	-0.51	0.5	2006-10-15	1689
35549	NGC 1068	40.67	0.49	0.5	2006-10-23	1690
35550	NGC 1068	40.17	-0.01	0.5	2006-10-23	1689
47815	NGC 1068	40.17	-0.01	0.5	2008-08-28	1687
47816	NGC 1068	41.17	-0.01	0.5	2008-08-28	1208
47840	NGC 1068	40.67	-0.51	0.5	2008-08-29	1688
47841	NGC 1068	40.67	0.49	0.5	2008-08-29	1688
47842	NGC 1068	41.17	-0.01	0.5	2008-08-29	848
47869	NGC 1068	40.17	-0.01	0.5	2008-08-30	1688
47870	NGC 1068	40.67	0.49	0.5	2008-08-30	1688
47871	NGC 1068	41.17	-0.01	0.5	2008-08-30	1124
47898	NGC 1068	41.17	-0.01	0.5	2008-08-31	1688
47899	NGC 1068	40.67	-0.51	0.5	2008-08-31	1688
47900	NGC 1068	40.67	0.49	0.5	2008-08-31	1687

Run Number	Target	Pointing Direction J2000.0		Offset	Date	Duration
		R.A.	Dec.			
		(deg)	(deg)	(deg)	yyyy-mm-dd	(s)
47922	NGC 1068	40.17	-0.01	0.5	2008-09-01	1689
47923	NGC 1068	41.17	-0.01	0.5	2008-09-01	1688
47924	NGC 1068	40.67	-0.51	0.5	2008-09-01	1688
47956	NGC 1068	40.67	0.49	0.5	2008-09-02	1688
47982	NGC 1068	40.17	-0.01	0.5	2008-09-03	1688
47983	NGC 1068	41.17	-0.01	0.5	2008-09-03	1687
47984	NGC 1068	40.67	-0.51	0.5	2008-09-03	1687
48035	NGC 1068	40.67	-0.51	0.5	2008-09-05	1688
48036	NGC 1068	40.67	0.49	0.5	2008-09-05	1687
48037	NGC 1068	40.17	-0.01	0.5	2008-09-05	1688
48038	NGC 1068	41.17	-0.01	0.5	2008-09-05	1688
48060	NGC 1068	40.67	-0.51	0.5	2008-09-06	1688
66682	NGC 1068	40.67	-0.71	0.7	2011-08-27	1669
66683	NGC 1068	40.67	0.69	0.7	2011-08-27	1177
66684	NGC 1068	39.97	-0.01	0.7	2011-08-27	1111
66706	NGC 1068	41.37	-0.01	0.7	2011-08-28	854
66730	NGC 1068	41.37	-0.01	0.7	2011-08-29	1687
66731	NGC 1068	39.97	-0.01	0.7	2011-08-29	1687
66755	NGC 1068	40.67	-0.71	0.7	2011-08-30	727
66799	NGC 1068	39.97	-0.01	0.7	2011-09-01	1687
66813	NGC 1068	40.67	-0.71	0.7	2011-09-02	1659
66814	NGC 1068	40.67	0.69	0.7	2011-09-02	1687
66815	NGC 1068	41.37	-0.01	0.7	2011-09-02	1687
66835	NGC 1068	39.97	-0.01	0.7	2011-09-03	1687
66854	NGC 1068	40.67	-0.71	0.7	2011-09-04	1669
66855	NGC 1068	40.67	0.69	0.7	2011-09-04	1687
66856	NGC 1068	41.37	-0.01	0.7	2011-09-04	1687
66889	NGC 1068	39.97	-0.01	0.7	2011-09-05	1669
66891	NGC 1068	40.67	-0.71	0.7	2011-09-05	1687
66892	NGC 1068	40.67	0.69	0.7	2011-09-05	1684

Run Number	Target	Pointing Direction J2000.0		Offset	Date	Duration
		R.A. (deg)	Dec. (deg)	(deg)	yyyy-mm-dd	(s)
66907	NGC 1068	41.37	-0.01	0.7	2011-09-06	1669
66908	NGC 1068	39.97	-0.01	0.7	2011-09-06	1687
66909	NGC 1068	40.67	-0.71	0.7	2011-09-06	1687
66910	NGC 1068	40.67	0.69	0.7	2011-09-06	1687
66925	NGC 1068	41.37	-0.01	0.7	2011-09-07	1687
66928	NGC 1068	39.97	-0.01	0.7	2011-09-07	1687
66929	NGC 1068	40.67	-0.71	0.7	2011-09-07	1056
66938	NGC 1068	40.67	-0.71	0.7	2011-09-08	1687
66939	NGC 1068	41.37	-0.01	0.7	2011-09-08	1687
66940	NGC 1068	39.97	-0.01	0.7	2011-09-08	1687
66950	NGC 1068	40.67	0.69	0.7	2011-09-09	1687
66951	NGC 1068	40.67	-0.71	0.7	2011-09-09	1235
67203	NGC 1068	41.37	-0.01	0.7	2011-09-23	1659
67204	NGC 1068	40.67	-0.71	0.7	2011-09-23	1258
67228	NGC 1068	40.67	0.69	0.7	2011-09-24	1669
67229	NGC 1068	39.97	-0.01	0.7	2011-09-24	1207
67317	NGC 1068	39.97	-0.01	0.7	2011-09-30	1587
67410	NGC 1068	40.67	-0.71	0.7	2011-10-02	1547
67411	NGC 1068	40.67	0.69	0.7	2011-10-02	1687
67412	NGC 1068	41.37	-0.01	0.7	2011-10-02	1687
67428	NGC 1068	39.97	-0.01	0.7	2011-10-02	1565
67429	NGC 1068	40.67	-0.71	0.7	2011-10-03	1687
67430	NGC 1068	40.67	0.69	0.7	2011-10-03	1687
67451	NGC 1068	41.37	-0.01	0.7	2011-10-03	1581
67452	NGC 1068	39.97	-0.01	0.7	2011-10-04	1687
67453	NGC 1068	40.67	-0.71	0.7	2011-10-04	1687
67490	NGC 1068	41.37	-0.01	0.7	2011-10-06	1687
68797	NGC 1068	41.37	-0.01	0.7	2011-12-15	1661
68811	NGC 1068	39.97	-0.01	0.7	2011-12-16	1661

A.11 NGC 1365

Run Number	Target	Pointing Direction J2000.0		Offset	Date	Duration
		R.A. (deg)	Dec. (deg)	(deg)	yyyy-mm-dd	(s)
27943	NGC 1399	55.48	-35.45	1.8	2005-08-12	1693
27987	NGC 1399	54.63	-34.75	1.7	2005-08-13	1690
28095	NGC 1399	54.63	-36.15	1.0	2005-08-15	1695
28096	NGC 1399	53.77	-35.45	0.8	2005-08-15	964
28111	NGC 1399	53.77	-35.45	0.8	2005-08-16	1631
28583	NGC 1399	54.63	-36.15	1.0	2005-09-12	1693
28584	NGC 1399	55.48	-35.45	1.8	2005-09-12	1692
28585	NGC 1399	53.77	-35.45	0.8	2005-09-12	1690
28586	NGC 1399	54.63	-34.75	1.7	2005-09-12	1690
28587	NGC 1399	54.63	-36.15	1.0	2005-09-12	1629
28630	NGC 1399	55.48	-35.45	1.8	2005-09-13	1573
28631	NGC 1399	53.77	-35.45	0.8	2005-09-13	1694
28663	NGC 1399	54.63	-36.15	1.0	2005-09-14	1691
28830	NGC 1399	55.48	-35.45	1.8	2005-09-25	1693
28831	NGC 1399	54.63	-36.15	1.0	2005-09-25	1694
28870	NGC 1399	54.63	-34.75	1.7	2005-09-26	1689
28873	NGC 1399	54.63	-36.15	1.0	2005-09-27	925
28895	NGC 1399	54.63	-36.15	1.0	2005-09-28	1689
28896	NGC 1399	54.63	-34.75	1.7	2005-09-28	1693
28897	NGC 1399	55.48	-35.45	1.8	2005-09-28	1221
28918	NGC 1399	53.77	-35.45	0.8	2005-09-28	1691
28919	NGC 1399	54.63	-36.15	1.0	2005-09-29	1690
28920	NGC 1399	54.63	-34.75	1.7	2005-09-29	1690
28921	NGC 1399	55.48	-35.45	1.8	2005-09-29	1690
28922	NGC 1399	53.77	-35.45	0.8	2005-09-29	1695
28923	NGC 1399	54.63	-36.15	1.0	2005-09-29	1139
28978	NGC 1399	54.63	-36.15	1.0	2005-09-30	1694
28979	NGC 1399	54.63	-34.75	1.7	2005-10-01	1690

Run Number	Target	Pointing Direction J2000.0		Offset	Date	Duration
		R.A. (deg)	Dec. (deg)	(deg)	yyyy-mm-dd	(s)
42135	1RXS J033311.8-361942	53.92	-36.33	0.4	2007-10-06	1687
42159	1RXS J033311.8-361942	53.30	-36.83	0.7	2007-10-07	1689
42222	1RXS J033311.8-361942	52.68	-36.33	0.6	2007-10-09	1688
42249	1RXS J033311.8-361942	53.92	-36.33	0.4	2007-10-10	1687
42283	1RXS J033311.8-361942	53.30	-36.83	0.7	2007-10-11	1688
42284	1RXS J033311.8-361942	53.30	-35.83	0.4	2007-10-11	1688
42312	1RXS J033311.8-361942	52.68	-36.33	0.6	2007-10-12	1688
42313	1RXS J033311.8-361942	53.92	-36.33	0.4	2007-10-12	1687

A.12 NGC 7469

Run Number	Target	Pointing Direction J2000.0		Offset	Date	Duration
		R.A. (deg)	Dec. (deg)	(deg)	yyyy-mm-dd	(s)
21633	NGC 7469	345.82	8.37	0.5	2004-07-16	1682
21725	NGC 7469	345.82	8.37	0.5	2004-07-20	1682
21726	NGC 7469	345.82	9.37	0.5	2004-07-20	1683
21820	NGC 7469	345.82	9.37	0.5	2004-07-25	1682
21822	NGC 7469	345.82	9.37	0.5	2004-07-25	1682
21823	NGC 7469	345.82	8.37	0.5	2004-07-25	1683
21831	NGC 7469	345.82	8.37	0.5	2004-07-26	1682
21832	NGC 7469	345.82	9.37	0.5	2004-07-26	1682
21833	NGC 7469	345.82	8.37	0.5	2004-07-26	1682
21834	NGC 7469	345.82	9.37	0.5	2004-07-26	1683
35379	NGC 7469	345.82	8.37	0.5	2006-10-11	1689
35383	NGC 7469	345.82	9.37	0.5	2006-10-12	1688
35384	NGC 7469	345.31	8.87	0.5	2006-10-12	1119
35408	NGC 7469	345.82	8.37	0.5	2006-10-14	1689
35429	NGC 7469	346.32	8.87	0.5	2006-10-15	1689

Run Number	Target	Pointing Direction J2000.0		Offset	Date	Duration
		R.A. (deg)	Dec. (deg)	(deg)	yyyy-mm-dd	(s)
35430	NGC 7469	345.82	9.37	0.5	2006-10-15	1689
35431	NGC 7469	346.32	8.87	0.5	2006-10-15	1689
35546	NGC 7469	346.32	8.87	0.5	2006-10-23	1688

A.13 Mrk 1014

Run Number	Target	Pointing Direction J2000.0		Offset	Date	Duration
		R.A. (deg)	Dec. (deg)	(deg)	yyyy-mm-dd	(s)
42693	RGB J0152+017	28.17	1.29	2.5	2007-11-02	1689
42744	RGB J0152+017	28.17	1.29	2.5	2007-11-04	1689
42808	RGB J0152+017	28.17	1.29	2.5	2007-11-07	1688
42840	RGB J0152+017	28.17	1.29	2.5	2007-11-08	1689
42864	RGB J0152+017	28.17	1.29	2.5	2007-11-09	1687
42908	RGB J0152+017	28.17	1.29	2.5	2007-11-11	1689
42955	RGB J0152+017	28.17	1.29	2.5	2007-11-13	1408
43263	RGB J0152+017	28.17	1.29	2.5	2007-11-30	1688
43322	RGB J0152+017	28.17	1.29	2.5	2007-12-03	1689
43417	RGB J0152+017	28.17	1.29	2.5	2007-12-07	1687
43439	RGB J0152+017	28.17	1.29	2.5	2007-12-08	1688
43464	RGB J0152+017	28.17	1.29	2.5	2007-12-09	1688
43545	RGB J0152+017	28.17	1.29	2.5	2007-12-13	1687
47550	RGB J0152+017	28.17	1.29	2.5	2008-08-10	1690
47575	RGB J0152+017	28.17	1.29	2.5	2008-08-12	1687
47582	RGB J0152+017	28.17	1.29	2.5	2008-08-13	1688
48897	RGB J0152+017	28.17	1.29	2.5	2008-10-22	1688
49025	RGB J0152+017	28.17	1.29	2.5	2008-11-01	1687

A.14 Mrk 1501

Run Number	Target	Pointing Direction J2000.0		Offset	Date	Duration
		R.A. (deg)	Dec. (deg)	(deg)	yyyy-mm-dd	(s)
33749	III Zw 2	2.63	11.47	0.5	2006-07-28	1689
33750	III Zw 2	2.63	10.47	0.5	2006-07-28	1689
33751	III Zw 2	3.14	10.97	0.5	2006-07-28	1689
34006	III Zw 2	2.63	10.47	0.5	2006-08-06	1287
39727	III Zw 2	3.14	10.97	0.5	2007-06-16	1086
39812	III Zw 2	2.12	10.97	0.5	2007-06-19	818
39856	III Zw 2	2.12	10.97	0.5	2007-06-21	1688
39889	III Zw 2	2.63	11.47	0.5	2007-06-23	1689
39890	III Zw 2	2.63	10.47	0.5	2007-06-23	1283
39915	III Zw 2	3.14	10.97	0.5	2007-06-24	1689
39916	III Zw 2	2.12	10.97	0.5	2007-06-24	1492
39957	III Zw 2	2.63	10.47	0.5	2007-06-25	828
39984	III Zw 2	2.63	11.47	0.5	2007-06-28	1172
40835	III Zw 2	2.63	10.47	0.5	2007-08-08	1688
40836	III Zw 2	2.63	11.47	0.5	2007-08-08	1688
40917	III Zw 2	2.63	10.47	0.5	2007-08-11	1688
40918	III Zw 2	2.63	11.47	0.5	2007-08-11	1689
40950	III Zw 2	2.12	10.97	0.5	2007-08-12	1688
40951	III Zw 2	3.14	10.97	0.5	2007-08-12	1688
40981	III Zw 2	2.63	10.47	0.5	2007-08-13	1687
41017	III Zw 2	2.63	11.47	0.5	2007-08-14	1689
41018	III Zw 2	2.12	10.97	0.5	2007-08-14	1688
41167	III Zw 2	2.12	10.97	0.5	2007-08-20	1688
41190	III Zw 2	3.14	10.97	0.5	2007-08-20	1688

A.15 Mrk 573

Run Number	Target	Pointing Direction J2000.0		Offset	Date	Duration
		R.A. (deg)	Dec. (deg)	(deg)	yyyy-mm-dd	(s)
42673	RGB J0152+017	27.67	1.79	1.8	2007-11-01	1688
42693	RGB J0152+017	28.17	1.29	2.4	2007-11-02	1689
42744	RGB J0152+017	28.17	1.29	2.4	2007-11-04	1689
42745	RGB J0152+017	28.17	2.29	2.2	2007-11-04	1688
42808	RGB J0152+017	28.17	1.29	2.4	2007-11-07	1688
42809	RGB J0152+017	28.17	2.29	2.2	2007-11-07	1687
42838	RGB J0152+017	27.67	1.79	1.8	2007-11-08	1689
42840	RGB J0152+017	28.17	1.29	2.4	2007-11-08	1689
42861	RGB J0152+017	28.17	2.29	2.2	2007-11-09	1688
42862	RGB J0152+017	27.67	1.79	1.8	2007-11-09	1689
42864	RGB J0152+017	28.17	1.29	2.4	2007-11-09	1687
42883	RGB J0152+017	28.17	2.29	2.2	2007-11-10	1687
42884	RGB J0152+017	27.67	1.79	1.8	2007-11-10	1687
42908	RGB J0152+017	28.17	1.29	2.4	2007-11-11	1689
42910	RGB J0152+017	28.17	2.29	2.2	2007-11-11	1689
42912	RGB J0152+017	27.67	1.79	1.8	2007-11-11	1689
42931	RGB J0152+017	28.17	2.29	2.2	2007-11-12	1689
42932	RGB J0152+017	27.67	1.79	1.8	2007-11-12	638
42933	RGB J0152+017	27.67	1.79	1.8	2007-11-12	1689
42955	RGB J0152+017	28.17	1.29	2.4	2007-11-13	1408
43211	RGB J0152+017	27.67	1.79	1.8	2007-11-27	1693
43263	RGB J0152+017	28.17	1.29	2.4	2007-11-30	1688
43307	RGB J0152+017	28.17	2.29	2.2	2007-12-02	1687
43309	RGB J0152+017	27.67	1.79	1.8	2007-12-02	1688
43322	RGB J0152+017	28.17	1.29	2.4	2007-12-03	1689
43323	RGB J0152+017	28.17	2.29	2.2	2007-12-03	1687
43415	RGB J0152+017	27.67	1.79	1.8	2007-12-07	1688
43417	RGB J0152+017	28.17	1.29	2.4	2007-12-07	1687

Run Number	Target	Pointing Direction J2000.0		Offset	Date	Duration
		R.A. (deg)	Dec. (deg)	(deg)	yyyy-mm-dd	(s)
43418	RGB J0152+017	28.17	2.29	2.2	2007-12-07	1688
43437	RGB J0152+017	27.67	1.79	1.8	2007-12-08	1688
43439	RGB J0152+017	28.17	1.29	2.4	2007-12-08	1688
43440	RGB J0152+017	28.17	2.29	2.2	2007-12-08	1687
43462	RGB J0152+017	27.67	1.79	1.8	2007-12-09	1688
43464	RGB J0152+017	28.17	1.29	2.4	2007-12-09	1688
43481	RGB J0152+017	28.17	2.29	2.2	2007-12-10	1688
43482	RGB J0152+017	27.67	1.79	1.8	2007-12-10	1688
43483	RGB J0152+017	28.17	2.29	2.2	2007-12-10	1688
43545	RGB J0152+017	28.17	1.29	2.4	2007-12-13	1687
47550	RGB J0152+017	28.17	1.29	2.4	2008-08-10	1690
47563	RGB J0152+017	28.17	2.29	2.2	2008-08-11	1689
47564	RGB J0152+017	27.67	1.79	1.8	2008-08-11	1688
47575	RGB J0152+017	28.17	1.29	2.4	2008-08-12	1687
47577	RGB J0152+017	27.67	1.79	1.8	2008-08-12	1309
47581	RGB J0152+017	28.17	2.29	2.2	2008-08-13	1688
47582	RGB J0152+017	28.17	1.29	2.4	2008-08-13	1688
48877	RGB J0152+017	28.17	2.29	2.2	2008-10-21	1688
48897	RGB J0152+017	28.17	1.29	2.4	2008-10-22	1688
48899	RGB J0152+017	27.67	1.79	1.8	2008-10-22	1688
49004	RGB J0152+017	28.17	2.29	2.2	2008-10-31	1688
49025	RGB J0152+017	28.17	1.29	2.4	2008-11-01	1687
53656	RGB J0152+017	27.67	1.79	1.8	2009-09-17	1689
53657	RGB J0152+017	28.17	2.29	2.2	2009-09-17	1688
54180	RGB J0152+017	27.67	1.79	1.8	2009-10-17	1689
54493	RGB J0152+017	27.67	1.79	1.8	2009-11-07	1693

A.16 3C 120

Run Number	Target	Pointing Direction J2000.0		Offset	Date	Duration
		R.A. (deg)	Dec. (deg)	(deg)	yyyy-mm-dd	(s)
23233	3C 120	68.30	4.85	0.5	2004-11-06	1686
23243	3C 120	68.30	5.85	0.5	2004-11-07	1687
23246	3C 120	67.79	5.35	0.5	2004-11-07	1686
23264	3C 120	68.80	5.35	0.5	2004-11-08	1687
23279	3C 120	67.79	5.35	0.5	2004-11-09	1686
23635	3C 120	68.30	5.85	0.5	2004-12-13	1686
23636	3C 120	68.30	4.85	0.5	2004-12-13	1686
23647	3C 120	67.79	5.35	0.5	2004-12-14	1687
23648	3C 120	68.80	5.35	0.5	2004-12-14	1686
23651	3C 120	68.30	4.85	0.5	2004-12-14	1689
23660	3C 120	68.80	5.35	0.5	2004-12-15	1686
23661	3C 120	67.79	5.35	0.5	2004-12-15	1686
67325	3C 120	67.79	5.35	0.5	2011-09-30	1689
67326	3C 120	68.30	5.85	0.5	2011-09-30	946
67415	3C 120	68.80	5.35	0.5	2011-10-02	1629
67433	3C 120	67.79	5.35	0.5	2011-10-03	1629
67434	3C 120	68.30	5.85	0.5	2011-10-03	877
67456	3C 120	68.30	4.85	0.5	2011-10-04	1637
67474	3C 120	68.80	5.35	0.5	2011-10-05	1645
67493	3C 120	68.30	5.85	0.5	2011-10-06	1651
67494	3C 120	68.30	4.85	0.5	2011-10-06	1247
67506	3C 120	68.80	5.35	0.5	2011-10-07	1645
67507	3C 120	67.79	5.35	0.5	2011-10-07	1687

Appendix B

List of Abbreviations

A list of abbreviations used in this thesis is found below.

Abbreviation	Meaning
ACD	Anticoincidence detector
AGN	Active galactic nucleus
ASI	Italian space agency
BDT	Boosted decision tree
BLR	Broad-line region
CDM	Cold dark matter
Dec	Declination
EBL	Extragalactic background light
EC	External Comptonisation
EIC	External inverse-Compton
ESA	European Space Agency
FRI	Fanaroff-Riley class 1
FRII	Fanaroff-Riley class 2
FSRQ	Flat-spectrum radio quasar
FWHM	Full width at half maximum
HBL	High-frequency BL Lacs
IACT	Imaging atmospheric Cherenkov telescope
IBL	Intermediate-frequency BL Lacs
LBL	Low-frequency BL Lacs
LIG	Luminous infrared galaxy

Abbreviation	Meaning
LMC	Large Magellanic Cloud
LST	Large-sized telescope
MLP	Multi-layered perception
MRSL	Mean reduced scaled length
MRSW	Mean reduced scaled width
MST	Medium-sized telescope
NLR	Narrow-line region
NLSy1	Narrow-line Seyfert galaxy
OVV	Optically violent variable
PSF	Point spread function
QSO	Quasi-stellar object
RA	Right Ascension
SED	Spectral energy distribution
SSC	Synchrotron self Compton
SSRQ	Steep-spectrum radio quasar
SST	Small-sized telescope
Sy1	Seyfert 1
Sy2	Seyfert 2
UHECR	Ultrahigh-energy cosmic ray
VHE	Very high energy
ZA	Zenith angle